
# Improved techniques of impedance calculation and localization in particle accelerators

**Università degli Studi di Roma "La Sapienza"**
Dottorato in Elettromagnetismo
XXVI ciclo

Nicolò Biancacci

**Relatore:**
*Prof. L.Palumbo*

**Correlatori:**
*Dr. M.Migliorati*
*Dr. E.Métral*
*Dr. B.Salvant*

# Acknowledgements

I feel extremely lucky and indebted with so many people that I met during this PhD, that it would be impossible to express in few words what I keep at the end of this journey. I had the possibility of growing both from a professional and human point of view, having met people that have often been much more than just colleagues or supervisors.

The first person I would like to acknowledge is prof. Vittorio G. Vaccaro. He taught me the constancy, the tenacity to the limit of the stubbornness, and at the same time, the patience, the calm understanding and the good will of starting and re-starting again. I learned how to digest series, Bessel functions, convergences and all their friends (... and enemies), and I learned how to give the right weight to Science with respect to friendship, Art, Music, Literature, and so many other fields of knowledge in which prof. Vaccaro has brought me. With him I felt being part of a family that leaves its traces in time, living in the hands and heads of students, researchers and professors, joined together by the great passion for Electromagnetism.

I am indebted with my section leader, Elias Métral for always trusting me, without reserve, and for having given me the possibility of participating in exciting workshops and conferences in which I could share my work. I appreciate his gratuity and openness, constantly felt by each of the students who have the luck of working with him.

I am thankful to Benoît Salvant, for his constant supervision (from Latin *super vedere*, i.e. *looking over*) who was always able to look forward in my work, finding the best opportunities for its development always meeting my insisting interests. The ability of listening during difficult PhD moments, the sustain he gave me during long measurement shifts, the way he discreetly accompanied me in my choices, both involving work and life, make him a great supervisor.

I am also thankful to Mauro Migliorati for his strong scientific support, the constant supervision on my work and the fruitful discussions that accompanied us along these years. His presence, together with the one of prof. L. Palumbo and A. Mostacci, continue making me feel part of a great *roman gang*.

I will never be thankful enough to Gianluigi Arduini for having given me the possibility of starting this great adventure at CERN almost four years ago, already at the time of my Master thesis. I thank him for teaching me the importance of high scientific standards in research and injecting this desire in me to do a quality research. His suggestions, together with the ones of Mauro, have been essential cornerstones of this work.

I acknowledge Simone Gilardoni for supporting the measurements in the PS machine and sharing with me his incredible knowledge, both theoretical and practical, expression of his rare and precious "feeling of the machine".

I would like to thank also Rogelio Tomás for his important help in the optics measurements and result interpretation, and Giovanni Rumolo for his illuminating suggestions and comments on beam dynamics: from both, I also appreciated their contagious good mood.

I am grateful to all the people who spent their precious time in the CERN control room with me. In particular, the OP and BI teams in the PS, SPS and LHC. Among them I would specially like to thank G. Papotti and F. Zimmermann for strongly supporting the measurements in the LHC, and C. Boccard and S. Jackson for their patient help with the SPS beam instrumentation.

I also had the opportunity to interact and collaborate with other international research labs as the USA Brookhaven National Laboratory (BNL). I am grateful to W. Fischer for providing the opportunity of measuring in the BNL accelerator complex, to M. Blaskiewicz, M. Bai, Y. Dutheil, M. Minty, L. Chuyu, K. Mernick and in particular to S. White for the collaboration and sharing of ideas and experiences during the AGS and RHIC measurements. I would also like to thank

N. Wang and U. Niedermayer for the fruitful discussions on impedance we had within frequent web meetings and conferences.

I thank my friend and colleague Cédric Hernalsteens, with whom I shared happiness and difficulties during this PhD time. To him I wish a brilliant conclusion of his PhD.
I thank Carlo Zannini for sharing with me his deep experience and precious time for theoretical discussions on impedance, most of the times triggered by our common source: prof. Vaccaro.
I thank Chiara, Alessia, Alessandro, Serena, Vincenzo, Georges, Cinzia and Gianni, for their daily support and I am also particularly thankful to my office mates Veliko, Stefania and Regina for having sustained me especially in the last months.

I would like to give a special acknowledgement to Vasim Khan, for his closeness to me and for the several discussions on Faith and Science that colored our friendship.

Rivolgo uno speciale ringraziamento ai miei amici del Gruppo Giovani della piccola ma viva Missione Cattolica Italiana di Ginevra, ed ai miei cari amici di vecchia data, Emanuele, Paul e Claudio, sul cui interesse e prezioso sostegno ho sempre potuto contare.

Infine ringrazio la mia famiglia, per aver accolto e sempre sostenuto questo mio percorso, azzerando la distanza fisica con quella spirituale.

Parte integrante di questa avventura è Roberta, senza il cui sostegno e pazienza questo lavoro non sarebbe stato possibile. Con e grazie a lei ho vissuto e assaporato le più gustose miscele di Scienza, Arte e Musica, ho percorso strade dove l'impeto si intreccia con la pazienza, la distanza con la comprensione, la fatica con il sorriso.

# Abstract

In this thesis we mainly focus on particle accelerators applied to high energy physics research where a fundamental parameter, the luminosity, is maximized in order to increase the rate of particle collisions useful to particle physicists. One way to increase this parameter is to increase the intensity of the circulating beams which is limited by the onset of collective effects that may drive the beam unstable and eventually provoke beam losses or reduce the beam quality required by the particle physics experiments.

One major cause of collective effects is the *beam coupling impedance*, a quantity that quantifies the effect of the fields scattered by a beam passing through any accelerator device. The development of an impedance budget is required in those machines that are planning substantial upgrades as shown in this thesis for the CERN PS case.

The main source of impedance in the CERN LHC are the collimators. Within an impedance reduction perspective, in order to reach the goals of the planned upgrades, it was proposed to reduce the collimator impedance by means of their segmentation in the longitudinal direction. This motivated the study of electromagnetic techniques able to take into account the finite length of the device, such as the Mode Matching technique. This technique enabled us to study the impedance dependence on the device length and assess that no evident impedance reduction can be achieved by means of a collimator segmentation.

The developed model allowed also for an accurate study of the impedance resonant-like behavior below the beam pipe cut-off frequency in beam pipe flanges. These insertions are very common in particle accelerator and the resonant effect could drive harmful instabilities within circulating bunches.

The possibility of detecting the high impedance sources by means of beam-based measurements represents another powerful investigation tool. In this thesis we improved the impedance localization technique based on the impedance-induced phase advance beating with intensity. We improved the theoretical background by means of macro particles simulations showing the effect of distributed and localized impedances, we quantified the impact of the noise over signal ratio in the measurement accuracy and we performed impedance localization measurements in the CERN PS, SPS and LHC and in the Brookhaven RHIC accelerators.

# Estratto

Il lavoro descritto in questa tesi è focalizzato sullo studio degli acceleratori di particelle dove un parametro fondamentale, la luminosità, è massimizzato al fine di aumentare il tasso di collisioni utili negli esperimenti di fisica delle particelle. Un modo per aumentare la luminosità è aumentare l'intensità dei fasci circolanti, la quale è a sua volta limitata dal possibile insorgere di instabilità che possono provocare perdite di particelle, rendere i fasci instabili o comprometterne la qualità ai fini degli esperimenti.

Una delle principali cause correlate all'insorgere di instabilità è l'*impedenza di accoppiamento di fascio*, una quantità che racchiude gli effetti dei campi scatterati dai fasci al passaggio attraverso i dispositivi che costituiscono l'acceleratore. Lo sviluppo di un budget d'impedenza di macchina è auspicabile in quegli acceleratori predisposti a futuri upgrades come nel caso del CERN PS trattato in questa tesi.

La più importante sorgente d'impedenza nel CERN LHC è costituita dai collimatori. Al fine di garantire il raggiungimento dei futuri upgrades pianificati per la macchina, è stata proposta la segmentazione longitudinale di tali dispositivi al fine di ridurne l'impedenza associata. Tale proposta ha motivato lo studio di tecniche elettromagnetiche per l'analisi d'impedenza che potessero tener conto della dimensione longitudinale finita dei dispositivi, come la tecnica del Mode Matching. L'impiego di tale tecnica ha consentito lo studio della dipendenza dell'impedenza rispetto alla lunghezza del dispositivo in studio, e, nei limiti del modello sviluppato, ha consentito di stabilire l'inefficacia della segmentazione al fine della riduzione d'impedenza dei collimatori.

Il modello sviluppato ha consentito inoltre uno studio accurato del comportamento risonante dell'impedenza in prossimità delle frequenze di cut-off del tubo di fascio nel caso delle flange. Queste sono inserzioni molto comuni in macchine acceleratrici e l'effetto risonante studiato potrebbe essere causa di instabilità sui fasci circolanti.

La possibilità di localizzare sorgenti di impedenza per mezzo di misure dirette sulla macchina utilizzando i fasci circolanti rappresenta un altro mezzo d'investigazione efficace. In questa tesi abbiamo migliorato la tecnica di localizzazione d'impedenze basata sullo studio della variazione dell'avanzamento di fase delle oscillazioni betatroniche del fascio con l'intensità in corrispondenza dei monitor di osservazione di fascio. Le basi teoriche del metodo sono state derivate in modo sistematico ed originale utilizzando simulazioni di macro particelle e mostrando l'effetto di sorgenti d'impedenza localizzate o distribuite. Abbiamo quantificato e misurato l'effetto del rumore nella misura rispetto al segnale misurato ed abbiamo effettuato misure nelle macchine del CERN PS, SPS e LHC ed in RHIC nel Brookhaven National Laboratory.

# Contents

# Chapter 1

# Introduction

Particle accelerators are nowadays some of the most powerful instruments for scientists in different branches of science. One could think to the high energy physics that recently opened a new research path after the discovery at CERN of a particle compatible with the theorized Higgs boson, or the wide range of studies in synchrotron radiation facilities (biological, chemical, optical studies, etc.) or to the medical applications of the therapy. Particle accelerators are in continuous development in order to meet the always more challenging requirements in beam energy and quality.

Focusing on the high energy physics accelerators, in particular, the potential of new particle discoveries is strongly correlated with the intensity of the circulating particle beams and their size.

The CERN accelerator complex in Fig. 1.1 is an example of the development of accelerators in order to push the frontiers of knowledge towards unexplored high energy boundaries. CERN, the European Organization for Nuclear Research, is currently the world's leading laboratory for particle physics. CERN mission is the fundamental research in physics pushing the frontiers of human knowledge. In support of that mission, CERN drives technology innovation, stimulates international collaboration and inspires a rising generation of scientists. CERN has its headquarters in Geneva. At present, its member states are Austria, Belgium, Bulgaria, the Czech Republic, Denmark, Finland, France, Germany, Greece, Hungary, Israel, Italy, the Netherlands, Norway, Poland, Portugal, Slovakia, Spain, Sweden, Switzerland and the United Kingdom. Romania is a Candidate for Accession. Serbia is Associate member in the pre-stage to membership. India, Japan, the Russian Federation, the United States of America, Turkey, the European Commission and UNESCO have observer status.

In order to understand the challenges of accelerating particle beams in circular accelerators, we can virtually follow the process of acceleration of a particle beam from the source to the high energy of the CERN LHC, the Large Hadron Collider [1, 2]. Hydrogen atoms are taken from a bottle containing hydrogen from which protons are taken by stripping out the orbiting electrons. The protons are then accelerated in the Linac 2 to the kinetic energy $T = 50\,\mathrm{MeV}$. The extracted beam is injected in the PS (Protron Synchrotron) Booster, a piled-ring accelerator built in 1972 in order to provide high intensity beams up to 1.4 GeV to the PS. The PS is one of the oldest machine at CERN, built in 1959, it was the first accelerator designed with strong focusing technique for acceleration [3]. It accelerates particles up to 25 GeV. Particles are then injected in the SPS (Super Protron Synchrotron) where a further acceleration brings them to 450 GeV. The beam is then sent to the LHC through the transfer lines TI2 (clockwise) or TI8 (counter-clockwise). Particles circulate in opposite direction until the energy is increased and the beams are brought into collision.

The amount and quality of beam collisions is of crucial importance in order to provide sufficient data to the experiments. ATLAS and CMS, for example, during the first run of the LHC, were focused on the study of rare events associated with the decay of Higgs-like particles [4,5]. Defined $\sigma_p$ the cross-section of a particular event, the number of interactions per second $\mathrm{d}R/\mathrm{d}t$ is proportional to the Luminosity $\mathcal{L}$ [6]:

$$\frac{\mathrm{d}R}{\mathrm{d}t} = \mathcal{L}\,\sigma_p. \tag{1.1}$$

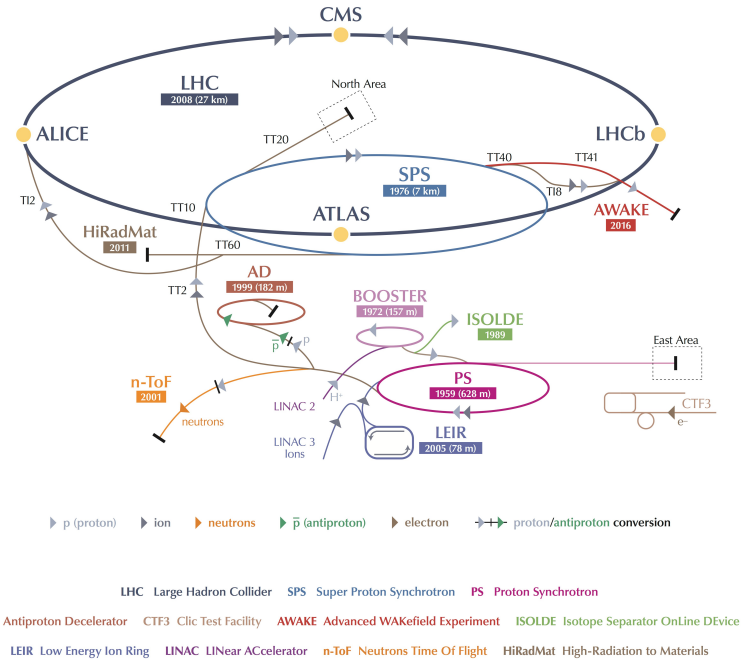


Figure 1.1: The CERN accelerator complex (courtesy of CERN).

For $n_b$ Gaussian bunches circulating at the revolution frequency $f_{rev}$ with same horizontal, vertical and longitudinal beam sizes $\sigma_x$, $\sigma_y$ and $\sigma_b$, and intensity per bunch $N_b$ for the two colliding beams, the luminosity is given by

$$\mathcal{L} = \frac{N_b^2 n_b f_{rev}}{4\pi\sigma_x\sigma_y}. \tag{1.2}$$

As we can see from Eq. (1.2), a high rates of events can be achieved either with small beam sizes or by increasing the number of circulating bunches or their intensity[1]. The increase in beam intensity is often limited by beam instabilities due to the beam interaction with itself, the other beam, electrons or the accelerator devices. The machine beam coupling impedance, for example, is a concept that allows to gather the electromagnetic field interactions with the beam itself and allows for useful stability, or instability, predictions[2]. The knowledge of this parameter is therefore of great importance in order to correctly model and improve the machine performance.

This thesis will introduce into improved calculation and measurement techniques of the beam coupling impedance.

In Chap. 2 we will introduce the concept of beam coupling impedance in a general axisymmetric structure. We will introduce the Mode Matching technique applied to the impedance calculation that will allow to solve the electromagnetic problem associated to the beam scattered fields in a device of finite length. The studied model is a toroidal insert loading a cylindrical cavity. Despite its simplicity, the studied case can model very long devices such as collimators, or beam pipes, or very narrow devices such as flanges, beam pipe gaps or perturbations. The study of the model will be fully characterized in terms of the insert material properties, dimensions and the beam velocity. Interesting trapped modes enhanced close to the beam pipe cut-off frequencies will also be analyzed.

In Chap. 3 we will summarize the effect of the beam coupling impedance on the beam itself particularly focusing on the perturbation of the betatron coherent oscillation frequency, when

[1] N.B. We discarded here other effects that reduce luminosity such as beam collision offset, crossing angle, hour glass effect, etc. [6]

[2] Other instability mechanism are the electron cloud, related to the beam interaction with the extracted electrons from the beam pipe walls, or the beam-beam effect, related with the long range or short range interaction of circulating beams.

increasing the intensity of the circulating beams. This effect, in a circular accelerator, can allow probing the total reactive part of the machine impedance and, even if already studied by other authors, it will be introduced in a simple and original way in Sec. 3.1. The method can be extended to the localization of equipment impedances through the study of the phase advance shift with intensity in accelerators equipped with a distributed multi-turn beam position monitors: this kind of measurement is called the *impedance localization method*. Section 3.2 will give the theoretical background of the measurement technique. Section 3.3 will study the impact of noise on the impedance localization method. Accelerator machines are routinely monitored from the impedance point of view, and impedance models are often one of the core studies before machine upgrades: an example of an impedance model under development is the one of the CERN PS described in Sec. 3.4. Based on this model, the impedance localization method is validated with macroparticle simulations in Sec. 3.5 studying the effect of single (Sec. 3.5.1), distributed (Sec. 3.5.2) and both lumped and distributed impedance sources (Sec. 3.5.3). The chapter is concluded with the introduction of the localization map in Sec. 3.7, a useful representation of the measurement accuracy with respect to the expected impedance measured or modeled signals.

The tools described until now will be applied to machine measurements in Chap. 4. The constraint on the quality of the signal from the beam position monitors, the reliability of the machine optical models, the amount of impedance with respect to the noise background, are all aspects that will be addressed during the description of the measurements done in the CERN PS (Sec. 4.1), SPS (Sec. 4.2) and LHC (Sec. 4.2) and in the AGS and RHIC (Sec. 4.4.1), accelerators located in the Brookhaven National Laboratories (BNL).

In Chap. 5 we will summarize the main results obtained with the Mode Matching technique and the impedance localization method giving an outlook for future possible developments.

# Chapter 2

# Mode Matching for coupling impedance calculations

## 2.1 Wakefields and impedances

The interaction of the surrounding electromagnetic (EM) fields with a particle beam, can be modeled, in first approximation, as the superposition of the external electric $\mathcal{E}^{ext}$ and magnetic $\mathcal{H}^{ext}$ fields[1] like the ones produced in the dipoles, quadrupoles, RF cavities, etc., and the beam induced electric $\mathcal{E}^{wake}$ and magnetic $\mathcal{H}^{wake}$, denoted as *wakefields*.

The external magnetic field induced in the dipoles forces the circulating beam to follow a closed orbit; the field induced by alternating focusing and defocusing quadrupoles controls the amplitude of the transverse betatron oscillation of the beam; the electric field in the RF cavities allows acceleration and RF manipulations; several higher order magnetic and electric fields are used to manipulate the beam, control the beam quality and overcome instabilities.

The self-induced wakefields represent the scattered field excited by the beam interacting with the accelerator devices (beam pipe, cavities, collimators, beam position monitors, etc). These fields can drive the beam unstable behavior which may culminate in partial or total beam loss. Since usually $\mathcal{E}^{wake} << \mathcal{E}^{ext}$ the wakefields and the resulting collective effects on the beam motion can be treated with a perturbative approach ( [7], [8], [9]).

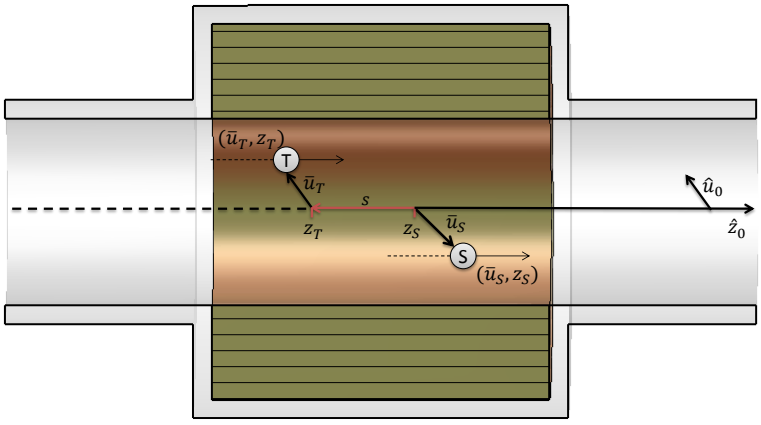


Figure 2.1: Scheme of source (S) and test (T) particle for impedance calculation. The source is displaced by $\bar{u}_S$, and the test by $\bar{u}_T$ from the device reference axis. It is assumed that the two particles maintain the distance $s$ unchanged along the device passage.

Let us now consider the scheme shown in Fig. 2.1: a source particle (S) of charge $Q$ and a

[1]The symbols $\mathcal{E}$ and $\mathcal{H}$ denote fields in time domain.

test particle (T) of charge $q$, travel along the closed orbit across a discontinuity in the accelerator beam pipe. A generic cylindrical coordinate system is adopted with transverse coordinate $\bar{u} = u\hat{u}_0$ and longitudinal coordinate $\bar{z} = z\hat{z}_0$. In particular, if the coordinate system is specified to be Cartesian, we have $u = (x, y)$ and $\bar{u} = x\hat{x}_0 + y\hat{y}_0$, if cylindrical, $u = (r, \phi)$ and $\bar{u} = r\hat{r}_0 + \phi\hat{\phi}_0$.

The test particle is at position $(\bar{u}_T, z_T)$, and it is following at distance $s$ the source particle at position $(\bar{u}_S, z_S = vt)$, where $v = \beta c$ is the particle beam velocity, $\beta$ the relativistic factor, $c$ the speed of light. The source particle represents a current passing in the accelerator device and it excites electromagnetic (EM) fields that act back on the trailing particle. If the velocity of the two particles is constant along the device (i.e. we suppose rigid motion), we can calculate the change in transverse and longitudinal momentum of the test particle to have an indication of the scattered fields impact on longitudinal and transverse dynamics. The source particle excites electric $\bar{\mathcal{E}}(\bar{u}_S, \bar{u}_T, z_T, z_S = vt)$ and magnetic $\bar{\mathcal{H}}(\bar{u}_S, \bar{u}_T, z_T, z_S = vt)$ fields whose strength depends on its position and the coordinates in which they are evaluated (the test particle coordinate in this case). The change in momentum is

$$\Delta\bar{p}(\bar{u}_T, \bar{u}_S, s) = \int_{-\infty}^{\infty} \mathrm{d}t\, \bar{\mathcal{F}}(\bar{u}_S, \bar{u}_T, z_T, z_S = vt)\Big|_{z_T = z_S - s}, \tag{2.1}$$

where $\bar{\mathcal{F}}$ is the Lorentz force $\bar{\mathcal{F}} = q(\bar{\mathcal{E}} + \beta\mu_0 c\hat{z}_0 \times \bar{\mathcal{H}})$ with $\mu_0$ the vacuum permeability. Considering the projections on longitudinal and transverse plane (i.e. $\bar{\mathcal{E}} = \mathcal{E}_l\hat{z}_0 + \mathcal{E}_t\hat{u}_0$, $\bar{\mathcal{H}} = \mathcal{H}_l\hat{z}_0 + \mathcal{H}_t\hat{u}_0$ and $\Delta\bar{p} = \Delta p_l\hat{z}_0 + \Delta p_t\hat{u}_0$) we have

$$\Delta p_l(\bar{u}_T, \bar{u}_S, s) = \int_{-\infty}^{\infty} \mathrm{d}t\, q\, \mathcal{E}_l(\bar{u}_S, \bar{u}_T, z_T, z_S = vt)\Big|_{z_T = z_S + s}, \tag{2.2}$$

$$\Delta p_t(\bar{u}_T, \bar{u}_S, s) = \int_{-\infty}^{\infty} \mathrm{d}t\, \hat{u}_0 \cdot (q\bar{\mathcal{E}}_t(\bar{u}_S, \bar{u}_T, z_T, z_S = vt) + q\mu_0 v\, \hat{z}_0 \times \bar{\mathcal{H}}_t(\bar{u}_S, \bar{u}_T, z_T, z_S = vt))\Big|_{z_T = z_S + s}. \tag{2.3}$$

The *wake function* is defined, respectively for longitudinal and transverse plane, as

$$W_l(\bar{u}_T, \bar{u}_S, s) = -\frac{v}{qQ}\Delta p_l(\bar{u}_T, \bar{u}_S, s), \tag{2.4}$$

$$W_t(\bar{u}_T, \bar{u}_S, s) = -\frac{v}{qQ}\Delta p_t(\bar{u}_T, \bar{u}_S, s). \tag{2.5}$$

The wake function represents the integrated response to the beam impulse excitation, i.e. the equivalent of a Green function. In the following, unless explicitly specified, we will use the term wakefield referring to the wake function. When interested in the effects of wakefield on the longitudinal motion, in first approximation we could neglect the transverse test and source positions, and consider particles aligned on the closed orbit, i.e. $\bar{u}_T = \bar{0}$ and $\bar{u}_S = \bar{0}$. We have

$$W_l(s) = W_l(\bar{0}, \bar{0}, s). \tag{2.6}$$

When interested in the effect of wakefields on the transverse motion, we can Taylor develop the transverse wake along test and source transverse position

$$W_t(\bar{u}_T, \bar{u}_S, s) \approx W_t(\bar{0}, \bar{0}, s) + \nabla_t W_t(\bar{u}_T, \bar{u}_S, s)\Big|_{\bar{u}_T = 0} \bar{u}_S + \nabla_t W_t(\bar{u}_T, \bar{u}_S, s)\Big|_{\bar{u}_S = 0} \bar{u}_T. \tag{2.7}$$

The first term is a constant term, null in axisymmetric structures where the wakefield integration path corresponds to the geometrical symmetry axis; the second term is called *driving* or *dipolar* wakefield since the test particle is driven by the source particle displacement and "feels" a transverse force independent by its position; the third term is called *detuning* or *quadrupolar* wakefield since the test particle "feels" a transverse force linearly proportional to its displacement (like in a quadrupole) being therefore detuned.

The *beam coupling impedance* (or simply impedance) is defined as the Fourier transform of the wakefield:

$$Z_l(\bar{u}_S, \bar{u}_T, \omega) = \int_{-\infty}^{\infty} W_l(\bar{u}_S, \bar{u}_T, s) e^{j\omega s/v} \frac{\mathrm{d}s}{v}, \tag{2.8}$$

$$Z_t(\bar{u}_S, \bar{u}_T, \omega) = -j \int_{-\infty}^{\infty} W_t(\bar{u}_S, \bar{u}_T, s) e^{j\omega s/v} \frac{\mathrm{d}s}{v}. \tag{2.9}$$

Reversely, the wakefields can be expressed in term of the impedance:

$$W_l(\bar{u}_S, \bar{u}_T, s) = \frac{1}{2\pi} \int_{-\infty}^{\infty} Z_l(\bar{u}_S, \bar{u}_T, \omega) e^{-j\omega s/v} \,\mathrm{d}\omega, \tag{2.10}$$

$$W_t(\bar{u}_S, \bar{u}_T, s) = \frac{j}{2\pi} \int_{-\infty}^{\infty} Z_t(\bar{u}_S, \bar{u}_T, \omega) e^{-j\omega s/v} \,\mathrm{d}\omega. \tag{2.11}$$

Depending on the case of study the use of wakefields or impedances might be more appropriate. For example, in linear accelerators, the concept of wakefield is more common, while in circular accelerator, due to periodicity, the frequency domain approach is preferred.

## 2.2 Methods for impedance calculation

In particle accelerators, one is usually interested in evaluating the impedance of beam pipes, cavities, collimators, kickers, etc., in order to evaluate the impact of beam induced scattered fields on the beam dynamics. From an EM point of view, depending on the boundary conditions faced by the beam and the detail accuracy one is interested in, different approaches, analytical or numerical, TD (Time Domain) or FD (Frequency Domain), may be preferred.

### 2.2.1 TD simulations

In TD simulators the bunch is tracked along the device under study and the wakefield is calculated from Eq. (2.2) or (2.3). The impedance can be obtained from the Fourier transformations in Eqs. (2.8) and (2.9). Note that in this case the impedance will be weighted by the longitudinal bunch spectrum since it is not numerically possible to simulate a single particle distribution.

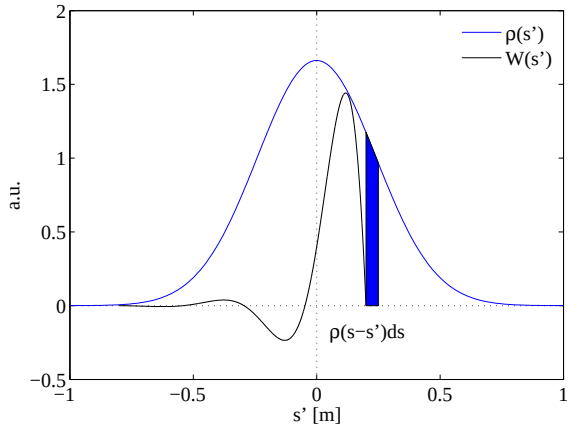


Figure 2.2: Each slice in the bunch produces a wakefield affecting the following particles. The convolution of bunch distribution and wakefield defines the so-called wake potential.

If we consider a Gaussian bunch of *rms* bunch length $\sigma_b$,

$$\rho(s) = \frac{1}{\sqrt{2\pi}\sigma_b} e^{\frac{-s^2}{2\sigma_b^2}}, \tag{2.12}$$

each slice $\rho(s-s')\mathrm{d}s'$ of the bunch passing through a device will excite a wakefield (see Fig. 2.2): the convolution of the generated wakefield and the distribution determines the wake field from the distribution, i.e. the so called *wake potential*

$$W_{pot}(\bar{u}_S, \bar{u}_T, s) = (W * \rho)(s) = \int_{-\infty}^{\infty} \rho(s-s') W(\bar{u}_S, \bar{u}_T, s')\,\mathrm{d}s'. \tag{2.13}$$

The impedance will be therefore the ratio of the Fourier transform of the wake potential and the spectrum of the bunch distribution

$$Z(\bar{u}_S, \bar{u}_T, \omega) = Z_{pot}(\bar{u}_S, \bar{u}_T, \omega)/S(\omega), \tag{2.14}$$

where $S(\omega) = e^{\sigma_b^2\omega^2/2}$. This approach is used by commercial particle simulation tools like CST [10]. The accuracy in the impedance determination at high frequency will be conditioned by the bunch spectrum extension. In CST, the maximal frequency is set to the frequency where $S(\omega)$ falls of $-20\,\mathrm{dB}$, which corresponds to:

$$f_{max} = c\frac{\sqrt{|\log(0.01)|}}{2\pi\sigma_b} \simeq \frac{10^{10}}{\sigma_b[\mathrm{cm}]}. \tag{2.15}$$

### 2.2.2 FD simulations

In FD simulations, Maxwell equations are solved for the device under study and the impedance is calculated directly from the obtained fields. Equations (2.8) and (2.9) can be slightly modified in order to express directly the electric and magnetic fields in frequency domain. The test particle in Fig. 2.1 can be written as a current distribution $\mathcal{J}_T = q\,v\,\delta(\bar{u}-\bar{u}_T)\delta(vt-z+s)$. Considering the longitudinal plane for simplicity, the change in momentum, and therefore the wakefield, can be calculated as

$$\begin{aligned}
W_l(\bar{u}_S, \bar{u}_T, s) &= -\frac{v}{q\,Q}\Delta p_l(\bar{u}_T, \bar{u}_S, s) = -\frac{1}{q\,Q}\int_{-\infty}^{\infty}\mathrm{d}t\int_V \mathrm{d}V\,\mathcal{J}_T\cdot\mathcal{E}_l(\bar{u}_S, \bar{u}, z, z_S = vt) = \\
&= -\frac{v}{q\,Q}\int_{-\infty}^{\infty}\mathrm{d}t\int_V \mathrm{d}V\,q\,\delta(\bar{u}-\bar{u}_T)\delta(vt-z+s)\mathcal{E}_l(\bar{u}_S, \bar{u}, z, z_S = vt) = \\
&= -\frac{v}{Q}\int_{-\infty}^{\infty}\mathrm{d}t\int_{-\infty}^{+\infty}\mathrm{d}z\,\delta(vt-z+s)\mathcal{E}_l(\bar{u}_S, \bar{u}_T, z, z_S = vt) = \\
&= -\frac{1}{Q}\frac{1}{2\pi}\int_{-\infty}^{\infty}\mathrm{d}z\int_{-\infty}^{+\infty}\mathrm{d}\omega\,e^{j\omega(z-s)/v}E_l(\bar{u}_S, \bar{u}_T, z, \omega) = \\
&= -\frac{1}{Q}\frac{1}{2\pi}\int_{-\infty}^{\infty}\mathrm{d}\omega\,e^{-j\omega s/v}\int_{-\infty}^{+\infty}\mathrm{d}z\,e^{j\omega z/v}E_l(\bar{u}_S, \bar{u}_T, z, \omega),
\end{aligned}$$

where we applied the Parseval's theorem

$$\int_{-\infty}^{+\infty}\mathrm{d}t f(t)g(t)^* = \frac{1}{2\pi}\int_{-\infty}^{+\infty}\mathrm{d}\omega F(\omega)G(\omega)^*,$$

to pass from the time domain electric field $\mathcal{E}_l$ to the frequency domain $E_l$. The last expression, together with Eq. (2.10) allows to write the coupling impedance as

$$Z_l(\bar{u}_S, \bar{u}_T, \omega) = -\frac{1}{Q}\int_{-\infty}^{+\infty} \mathrm{d}z\, e^{j\omega z/v} E_z(\bar{u}_S, \bar{u}_T, z, \omega). \tag{2.16}$$

For test and source particle on the closed orbit we recover the usual expression for the longitudinal impedance

$$Z_l(\omega) = -\frac{1}{Q}\int_{-\infty}^{+\infty} \mathrm{d}z\, e^{j\omega z/v} E_z(\bar{u}_S \to \bar{0}, \bar{u}_T \to \bar{0}, z, \omega). \tag{2.17}$$

Analogous analysis can be done for the transverse impedance leading to

$$Z_t(\bar{u}_S, \bar{u}_T, \omega) = \frac{j}{Q}\int_{-\infty}^{+\infty} \mathrm{d}z\, e^{j\omega z/v} \left(\overline{E}(\bar{u}_S, \bar{u}_T, z, \omega) + v\mu_0 \hat{z}_0 \times \overline{H}(\bar{u}_S, \bar{u}_T, z, \omega)\right) \cdot \hat{u}_0. \tag{2.18}$$

In a cylindrical reference system $(\hat{r}_0, \hat{\phi}_0, \hat{z}_0)$ we have

$$Z_t(r_S, \phi_S, r_T, \phi_T, \omega) = \frac{j}{Q}\int_{-\infty}^{+\infty} \mathrm{d}z\, e^{j\omega z/v} (E_r(r_S, \phi_S, r_T, \phi_T, \omega) - v\mu_0\, H_\phi(r_S, \phi_S, r_T, \phi_T, \omega)). \tag{2.19}$$

At first order we can define a dipolar and quadrupolar impedance as done in Sec. 2.1. If, for simplicity, we consider $\phi_S = \phi_T = 0$ (i.e. test and source are on the same azimuthal angle) we have

$$Z_t(r_S, r_T, \omega) \approx \left.\frac{\partial Z_t(r_S, r_T, \omega)}{\partial r_S}\right|_{r_T=0} r_S + \left.\frac{\partial Z_t(r_T, r_S, \omega)}{\partial r_T}\right|_{r_S=0} r_T. \tag{2.20}$$

We therefore define the dipolar and quadrupolar impedance as

$$Z_{dip}(\omega) = \frac{j}{Q\, r_S}\int_{-\infty}^{+\infty} \mathrm{d}z\, e^{j\omega z/v} (E_r(r_S, r_T \to 0, z, \omega) - v\mu_0\, H_\phi(r_S, r_T \to 0, z, \omega)), \tag{2.21}$$

$$Z_{quad}(\omega) = \frac{j}{Q\, r_T}\int_{-\infty}^{+\infty} \mathrm{d}z\, e^{j\omega z/v} (E_r(r_S \to 0, r_T, z, \omega) - v\mu_0\, H_\phi(r_S \to 0, r_T, z, \omega)). \tag{2.22}$$

This approach is frequently used in analytical codes like [11–14], and, with some restriction, in numerical codes like HFSS [15].

Within the FD analytical approaches we can distinguish between those based on *Field Matching* and those based on *Mode Matching*.

### Field Matching and Mode Matching

The *Field Matching* consists in dividing the structure in a certain number of *infinite* sub-domains and representing the electromagnetic fields in these domains by an infinite sum of traveling waves whose unknown coefficients form an infinite vector. A number of functional equations are obtained by matching the tangential component of the fields on the domains boundaries. By means of the Ritz-Galerkin method [16], each functional equation is transformed in an infinite set of equations which link the unknown vectors.

The *Mode Matching* method, represents the EM fields in one of the *finite* sub-domains as sum of eigenmodes whose unknown coefficients form an infinite vector [17, 18]. Afterwards, the procedure is similar to the previous one.

Let us consider as an example 2.3a, where an infinite multi-layer beam pipe is represented: this structure could represent a beam pipe coated with thin layers of material (for example for electron

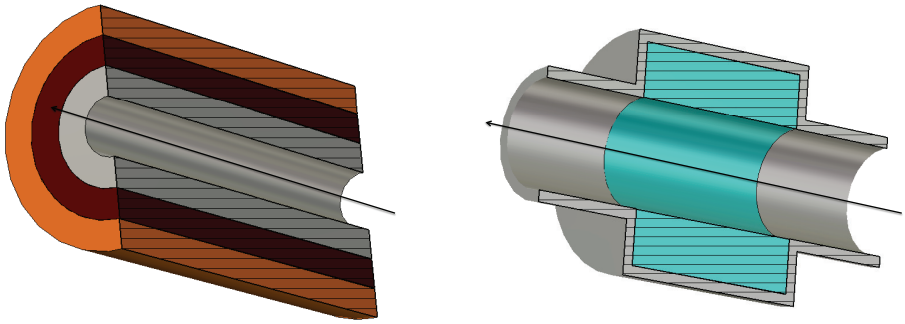

(a) (b)

Figure 2.3: (a) Example of structure solvable with Field Matching. (b) Example of structure solvable with Mode Matching.

cloud mitigation). With a Field Matching approach, each layer is treated as an infinite sub-domain in which Maxwell equations may be solved. The EM tangential component are therefore matched at the boundaries and the problem can be solved [13].

The structure in 2.3b represents a cylindrical cavity loaded with an insert and connected with cylindrical beam pipes. To solve Maxwell equations we could divide the structure in four sub-domains: the beam pipes (I and II), the insert (III) and the cavity (IV). In the finite sub-domain IV, we could assume perfect electric (PEC) boundaries for the field expansion, but this would make the tangential electric field null at the surfaces between the cavity and the beam pipes making difficult a Field Matching approach. We would have similar consequences assuming perfect magnetic (PMC) boundaries. This limit can be overcome representing the EM fields in sub-domain IV as sum of eigenmodes and applying the Mode Matching technique, as will be extensively explained in the next section.

## 2.3 The Mode Matching method

In this section we will show the expressions for the electromagnetic field decomposition in a closed volume. The derived equations are the basis for the Mode Matching method.

Given a volume $V$, enclosed in an ideal surface $S = S_E \cup S_H$, with $S_E$ perfect electric, and $S_H$ perfect magnetic boundary surfaces, the scattered electromagnetic fields $\overline{E}$ and $\overline{H}$ may be decomposed by means of the Helmholtz theorem in summation of irrotational and solenoidal modes which constitute a complete set of orthonormal functions [17, 18]. We can write:

$$\overline{E} = \sum_n \mathbf{V}_n \bar{e}_n + \sum_n \mathbf{F}_n \bar{f}_n \tag{2.23}$$

$$\overline{H} = \sum_n \mathbf{I}_n \bar{h}_n + \sum_n \mathbf{G}_n \bar{g}_n \tag{2.24}$$

where $\bar{e}_n$ and $\bar{h}_n$ are solenoidal and $\bar{f}_n$ and $\bar{g}_n$ irrotational orthonormal eigenvectors. Table 2.1 resumes a set of eigenvectors and the relative differential equations and boundary conditions they satisfy ($\hat{n}_0$ is the unit vector normal to $S$ pointing internally the volume). Since the eigenvectors are determined by the geometry of the structure under study, the problem reduces to finding the coefficients $\mathbf{V}_n$, $\mathbf{F}_n$, $\mathbf{I}_n$, $\mathbf{G}_n$. This can be done by imposing the continuity of the EM field on the boundary surface $S$. In this condition one must also take into account also the impressed field generated by the sources.

On $S_E$, because of the homogeneous boundary condition, which is an intrinsic property of the eigenmodes, it is not possible to perform tout court the matching of the electric field. Analogously this happens on $S_H$ for the magnetic field. This difficulty can be surmounted by resorting to a procedure which will be described in the following. Let $\overline{E}$ be the given imposed electric field on

| Eigenvector | In $V$ | On $S = S_E \cup S_H$ |
|---|---|---|
| $\bar{e}_n$ | $\nabla \times \bar{e}_n = k_n \bar{h}_n$ | $\begin{cases} \hat{n}_0 \times \bar{e}_n = 0; & \text{on } S_E \\ \hat{n}_0 \cdot \bar{e}_n = 0; & \text{on } S_H \end{cases}$ |
| $\bar{f}_n = \nabla \Phi_n$ | $\nabla^2 \Phi_n + \mu_n^2 \Phi_n = 0$ | $\begin{cases} \Phi_n = 0; & \text{on } S_E \\ \partial \Phi_n / \partial n = 0; & \text{on } S_H \end{cases}$ |
| $\bar{h}_n$ | $\nabla \times \bar{h}_n = k_n \bar{e}_n$ | $\begin{cases} \hat{n}_0 \cdot \bar{h}_n = 0; & \text{on } S_E \\ \hat{n}_0 \times \bar{h}_n = 0; & \text{on } S_H \end{cases}$ |
| $\bar{g}_n = \nabla \Psi_n$ | $\nabla^2 \Psi_n + \nu_n^2 \Psi_n = 0$ | $\begin{cases} \partial \Psi_n / \partial n = 0; & \text{on } S_E \\ \Psi_n = 0; & \text{on } S_H \end{cases}$ |

Table 2.1: Eigenvector equations.

the surface $S$ . If we consider the quantity $\nabla \cdot (\overline{E} \times \bar{h}_n^*)$, and resort to simple algebra, we get the following expression:

$$\nabla \cdot (\overline{E} \times \bar{h}_n^*) = \bar{h}_n^* \cdot (\nabla \times \overline{E}) - \overline{E} \cdot (\nabla \times \bar{h}_n^*). \tag{2.25}$$

Into the RHS we use the Maxwell's equation for $\overline{E}$ and Eq. (2.23), then integrate in the volume $V$. Applying the divergence theorem and exploiting the orthonormality of the eigenmodes, we get the following expression:

$$\int_{S_E} (\overline{E} \times \bar{h}_n^*) \cdot \hat{n}_0 \, \mathrm{d}S = -jkZ_o \mathbf{I}_n - k_n \mathbf{V}_n, \tag{2.26}$$

where $\hat{n}_0$ is the unitary vector pointing inward the volume $V$ boundaries, $Z_o$ is the characteristic impedance and $k = \omega/c$ the propagation constant in vacuum. Doing the same for the quantity $\nabla \cdot (\bar{e}_n^* \times \overline{H})$, we have:

$$\int_{S_H} (\bar{e}_n^* \times \overline{H}) \cdot \hat{n}_0 \, \mathrm{d}S = k_n \mathbf{I}_n - jkY_0 \mathbf{V}_n, \tag{2.27}$$

with $Y_0 = 1/Z_o$. Solving the system of Eqs. (2.26) and (2.27) allows us to get the coefficients $\mathbf{I}_n$ and $\mathbf{V}_n$:

$$\mathbf{I}_n = \frac{1}{k^2 - k_n^2} \left( jkY_0 \int_{S_E} (\overline{E} \times \bar{h}_n^*) \cdot \hat{n}_0 \, \mathrm{d}S - k_n \int_{S_H} (\bar{e}_n^* \times \overline{H}) \cdot \hat{n}_0 \, \mathrm{d}S \right), \tag{2.28}$$

$$\mathbf{V}_n = \frac{1}{k^2 - k_n^2} \left( jkZ_o \int_{S_H} (\bar{e}_n^* \times \overline{H}) \cdot \hat{n}_0 \, \mathrm{d}S + k_n \int_{S_E} (\overline{E} \times \bar{h}_n^*) \cdot \hat{n}_0 \, \mathrm{d}S \right). \tag{2.29}$$

Analogously we may proceed for the irrotational fields obtaining:

$$\mathbf{G}_n = j \frac{Y_0}{k} \int_{S_E} (\overline{E} \times \bar{g}_n^*) \cdot \hat{n}_0 \, \mathrm{d}S, \tag{2.30}$$

$$\mathbf{F}_n = -j \frac{Z_o}{k} \int_{S_E} (\overline{H} \times \bar{f}_n^*) \cdot \hat{n}_0 \, \mathrm{d}S. \tag{2.31}$$

The results of the above procedure may appear contradictory. On $S_E$, for example, we have imposed the use of the eigenmodes which satisfy homogeneous boundary conditions: one might be tempted to infer that the expansion coefficients should vanish. There is, indeed, no contradiction:

the result of the LHS of Eqs. (2.28)-(2.31) is obtained integrating on the volume $V$ a positive definite function, while the result of the RHS is obtained integrating on the surface $S$ the "imposed" field $\overline{E}$. However, such an expansion will only be non-uniformly convergent. This behavior will require some caution when truncating the expansion.

## 2.4 Application to a finite length toroidal loaded insert

Structures like 2.3b are common in particle accelerators. Opportunely varying the longitudinal and radial dimensions, or the insert material parameters, the structure could represent a small beam pipe discontinuity, a flange connecting two beam pipes, a beam pipe, a loaded cavity, etc.

The problem has been approached in the past mainly by means of the field matching technique making use of careful approximations where the cavity-like structure was approximated as a thin insert [19–22].

In this section we want to study rigorously the EM fields scattered by a particle beam traveling through a cavity loaded with a linear, isotropic, stationary, dispersive, homogeneous, toroidal material, by means of the Mode Matching method and derive the beam coupling impedance. We will compare our model with the classical thick wall formula for resistive wall impedance, and with CST Particle Studio [10] for low conductivity cases. The impedance dependency on the device length will be also studied in order to assess the validity of the usual "infinite length" approximation. The study of thin inserts will be presented and compared with the theory developed in [22] and the theory developed for small discontinuities [23, p.215]. Since the used approach is non ultra relativistic, we will also study the impedance behavior as a function of the relativistic particle beam velocity.

We will present results both for the longitudinal and transverse dipolar impedance. In particular, the discussion about the longitudinal impedance can be also found in [24].

### 2.4.1 Fields in the sub-domains

The structure we study is a cavity of radius $d$ connected with a beam pipe of radius $b$ and filled with a toroidal insert of thickness $t = d - b$, as shown in Fig. 2.4. We choose a cylindrical reference system $(\hat{r}_0, \hat{\phi}_0, \hat{z}_0)$. The sub-domains I and II represent the cylindrical left and right beam pipes where reflected fields will propagate, sub-domain III is the toroidal insert where radial waves can propagate, and sub-domain IV is the cavity volume where resonances can be excited. Sub-domains I, II and IV are filled with vacuum (permittivity $\varepsilon_0$ and permeability $\mu_0$), sub-domain III with a linear, isotropic, stationary, dispersive, homogeneous material with complex relative permittivity $\varepsilon_f(\omega) = \varepsilon'_f(\omega) + j\varepsilon''_f(\omega)$, conductivity $\sigma_c$ and complex relative permeability $\mu_f(\omega) = \mu'_f(\omega) + j\mu''_f(\omega)$. The surface $S_1$ divides sub-domain I from IV, $S_2$, II from IV, $S_3$, III from IV. The background is chosen to be PEC. Table 2.2 summarizes this information.

| Sub-domain | Geometry | Material |
|---|---|---|
| I (left beam pipe) | $z \in (-\infty, 0), r \in (0, b)$ | $\varepsilon_0$,$\mu_0$ |
| II (right beam pipe) | $z \in (L, \infty), r \in (0, b)$ | $\varepsilon_0$,$\mu_0$ |
| III (material insert) | $z \in (0, L), r \in (b, d)$ | $\varepsilon_0\varepsilon_f(\omega)$, $\mu_0\mu_f(\omega)$, $\sigma_c$ |
| IV (cavity) | $z \in (0, L), r \in (0, b)$ | $\varepsilon_0$,$\mu_0$ |

Table 2.2: Geometry and material definitions.

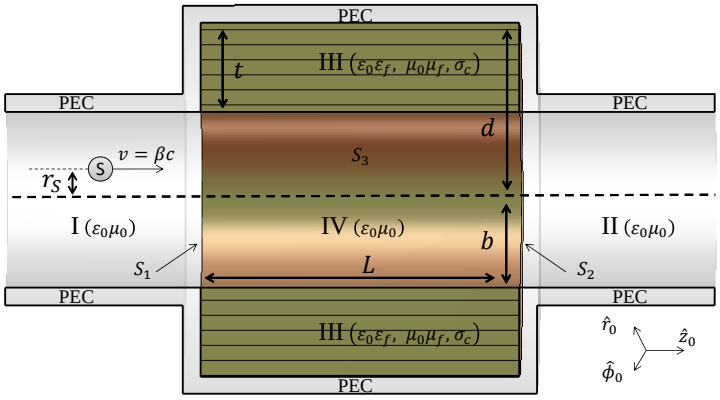


Figure 2.4: Structure under study: loaded cavity connected with two beam pipes.

**Source currents**

Once the geometry is given, we define the source currents for the impedance calculation. Since we are interested in the longitudinal and dipolar impedance, we will consider two beam configurations: both test and source particle at the device center (we suppose that the closed orbit is exactly passing at the center of the device) to calculate the longitudinal impedance (Eq. (2.17)) and test at the center and displaced source particle to calculate the dipolar impedance (Eq. (2.21)).

In cylindrical coordinates, a charged particle $Q$ displaced at $r = r_S$ traveling at velocity $v$ along $\hat{z}_0$ can be written as

$$\mathcal{J}_b(r,\phi,z;t) = Q\,v\delta(\bar{u}-\bar{u}_S)\delta(vt-z) = Q\,v\delta(r-r_S)\frac{\delta(\phi)}{r_S}\delta(vt-z), \tag{2.32}$$

and equivalently, in frequency domain:

$$J_b(r,\phi,z;\omega) = Q\,\delta(r-r_S)\frac{\delta(\phi)}{r_S}e^{-j\omega z/v}, \tag{2.33}$$

Since we work in azimuthal symmetry we can expand the current in a Fourier series:

$$J_b(r,\phi,z) = \sum_{m=0}^{\infty}\rho_{b,m}v = \delta(r-r_S)\sum_{m=0}^{\infty}\frac{Q\,\cos(m\phi)}{\pi r_S(1+\delta_{m0})}e^{-j\omega z/v}. \tag{2.34}$$

In particular, for practical reasons, we rewrite the terms $m = 0$ and $m = 1$ in Tab. 2.3.

| Multipolar term | Current |
|---|---|
| $m = 0$ | $J_b^{long}(r,\phi,z) = \dfrac{Q}{2\pi r_S}\delta(r-r_S)e^{-j\omega z/v}$ |
| $m = 1$ | $J_b^{dip}(r,\phi,z) = \dfrac{Q\,\cos(\phi)}{\pi r_S}\delta(r-r_S)e^{-j\omega z/v}$ |

Table 2.3: Particle source currents.

The term $m = 0$, corresponds to a ring shaped current with radius $r_S$ and will be used as source current for longitudinal impedance calculation. The term $m = 1$ is a $\cos(\phi)$ modulated ring with the same radius, and will be used to calculate the dipolar impedance.

| I | II | III | IV |
|---|---|---|---|
| $\nabla \times \overline{E} = -j\omega\mu_0 \overline{H}$ | $\nabla \times \overline{E} = -j\omega\mu_0 \overline{H}$ | $\nabla \times \overline{E} = -j\omega\mu_0\mu_f \overline{H}$ | $\nabla \times \overline{E} = -j\omega\mu_0 \overline{H}$ |
| $\nabla \times \overline{H} = j\omega\varepsilon_0 \overline{E} + \overline{J}_b$ | $\nabla \times \overline{H} = j\omega\varepsilon_0 \overline{E} + \overline{J}_b$ | $\nabla \times \overline{H} = j\omega\varepsilon_0\varepsilon_f \overline{E} + \sigma_c \overline{E}$ | $\nabla \times \overline{H} = j\omega\varepsilon_0 \overline{E} + \overline{J}_b$ |
| $\nabla \cdot \overline{E} = \frac{\rho_b}{\varepsilon_0}$ | $\nabla \cdot \overline{E} = \frac{\rho_b}{\varepsilon_0}$ | $\nabla \cdot \overline{E} = 0$ | $\nabla \cdot \overline{E} = \frac{\rho_b}{\varepsilon_0}$ |
| $\nabla \cdot \overline{H} = 0$ | $\nabla \cdot \overline{H} = 0$ | $\nabla \cdot \overline{H} = 0$ | $\nabla \cdot \overline{H} = 0$ |

Table 2.4: Maxwell's equations in the sub-domains.

### Source fields

For each of the sub-domains, Maxwell's equations hold as resumed in Tab. 2.4. In I, II and IV the source term is present. The solution in these sub-domains can be written as the superposition of *source fields* and *scattered fields*, i.e.:

$$\overline{E}^{(tot)} = \overline{E}^{(source)} + \overline{E}^{(scattered)}, \tag{2.35}$$

$$\overline{H}^{(tot)} = \overline{H}^{(source)} + \overline{H}^{(scattered)}. \tag{2.36}$$

Since there is only one solution to the EM problem for a given beam excitation, we can choose as source fields, the ones excited by a particle beam traveling in an infinitely long perfectly conducting cylindrical beam pipe of radius $b$. In this way the tangential source fields continuity on $S_1$ and $S_2$ is automatically ensured, simplifying the matching operations[2]. It is understood that the scattered fields must satisfy the source-free Maxwell's equations in all the sub-domains.

The source fields corresponding to the longitudinal and dipolar current excitations of Tab.2.3, have been derived in [25] and are summarized in Tab. 2.5 where

$$F_0(u) = K_0(u) - \frac{I_0(u)K_0(x)}{I_0(x)}, \tag{2.37}$$

$$F_1(u) = K_1(u) - \frac{I_1(u)K_1(x)}{I_1(x)}, \tag{2.38}$$

with $I_\nu(u)$ and $K_\nu(u)$ representing the modified Bessel function of order $\nu$ respectively of first and second kind, $\alpha_b = b\omega/v$, $u = r\alpha_b/(b\gamma)$, $x = \alpha_b/\gamma$, $s = r_S\omega/(\gamma v)$.

### Scattered fields

For symmetry reason, in the longitudinal case, only TM fields can be scattered, while both TE and TM should be considered in the transverse case.

In general, the modes propagating into the beam pipes depend on the radial mode number $p$ and azimuthal mode number $\nu$, the modes in the insert depend on the longitudinal mode number $s$ and $\nu$, the modes in the cavity depend on $p, \nu$ and $s$. We will consider only the scattered modes with azimuthal mode number $\nu = 0$ in the longitudinal case, and the modes with azimuthal mode number $\nu = 1$ in the transverse case[3], and therefore we will suppress the $\nu$ index dependence from the fields expansion.

[2]This approach would not be possible if the entrance beam pipe apertures would be different: in that case one could consider as source fields the one produced by a beam traveling in vacuum. It is, by the way, also possible to formulate the Mode Matching problem considering directly the source current $J_b(r, \phi, z)$ in place of the source fields [17].

[3]This is not a restriction. It could be shown that modes with $\nu \neq 0$ in the longitudinal case, and $\nu \neq 1$ in the transverse, do not couple with the source field and cannot be excited. From another point of view, they do not contribute to the field matching procedure having null projection integrals.

| Source | Longitudinal | Dipolar |
|---|---|---|
| $E_r$ | $-\frac{Q\,Z_o\alpha_b}{2\pi b\beta\gamma}I_0(s)\frac{\partial F_0(u)}{\partial u}e^{-\frac{jz\alpha_b}{b}}$ | $-\frac{Q\,Z_o}{\pi\beta\gamma}\frac{\alpha_b^2}{b^2\gamma}\cos(\phi)I_1(s)\frac{\partial F_1(u)}{\partial u}e^{-\frac{jz\alpha_b}{b}}$ |
| $E_\phi$ | 0 | $\frac{Q\,Z_o}{\pi\beta\gamma}\frac{\alpha_b^2}{b^2\gamma}\sin(\phi)I_1(s)\frac{F_1(u)}{u}e^{-\frac{jz\alpha_b}{b}}$ |
| $E_z$ | $\frac{jQ\,Z_o\alpha_b}{2\pi b\beta\gamma^2}I_0(s)F_0(u)e^{-\frac{jz\alpha_b}{b}}$ | $\frac{jQ\,Z_o}{\pi\beta\gamma^2}\frac{\alpha_b^2}{b^2\gamma}\cos(\phi)I_1(s)F_1(u)e^{-\frac{jz\alpha_b}{b}}$ |
| $H_r$ | 0 | $-\frac{Q}{\pi\gamma}\frac{\alpha_b^2}{b^2\gamma}\sin(\phi)I_1(s)\frac{F_1(u)}{u}e^{-\frac{jz\alpha_b}{b}}$ |
| $H_\phi$ | $-\frac{Q\,\alpha_b}{2\pi b\gamma}I_0(s)\frac{\partial F_0(u)}{\partial u}e^{-\frac{jz\alpha_b}{b}}$ | $-\frac{Q}{\pi\gamma}\frac{\alpha_b^2}{b^2\gamma}\cos(\phi)I_1(s)\frac{\partial F_1(u)}{\partial u}e^{-\frac{jz\alpha_b}{b}}$ |
| $H_z$ | 0 | 0 |

Table 2.5: Source field components for $r > r_S$.

In the longitudinal case, the electric fields in the pipes and the insert (sub-domains I, II and III) can be expressed as:

$$\overline{E}^{(I)} = \sum_p \mathbf{C}_\mathbf{p}^{\mathrm{TM}}\ \overline{E}_p^{(I,\mathrm{TM})}, \tag{2.39}$$

$$\overline{E}^{(II)} = \sum_p \mathbf{D}_\mathbf{p}^{\mathrm{TM}}\ \overline{E}_p^{(II,\mathrm{TM})}, \tag{2.40}$$

$$\overline{E}^{(III)} = \sum_s \mathbf{A}_\mathbf{s}^{\mathrm{TM}}\ \overline{E}_s^{(III,\mathrm{TM})}, \tag{2.41}$$

and analogously for the magnetic fields. In the cavity we have, from Eqs. (2.23) and (2.24) :

$$\overline{E}^{(IV)} = \sum_{p\,s} \mathbf{V}_{\mathbf{p}\,\mathbf{s}}^{\mathrm{TM}}\ \bar{e}_{p\,s}^{(IV,\mathrm{TM})} + \sum_{p\,s} \mathbf{F}_{\mathbf{p}\,\mathbf{s}}\ \bar{f}_{p\,s}^{(IV)}, \tag{2.42}$$

$$\overline{H}^{(IV)} = \sum_{p\,s} \mathbf{I}_{\mathbf{p}\,\mathbf{s}}^{\mathrm{TM}}\ \bar{h}_{p\,s}^{(IV,\mathrm{TM})} + \sum_{p\,s} \mathbf{G}_{\mathbf{p}\,\mathbf{s}}\ \bar{g}_{p\,s}^{(IV)} \tag{2.43}$$

The scattered fields for sub-domains I, II III and IV have been given in Tab. 2.6 where we defined the following parameters:

- $\alpha_p$: $p^{\text{th}}$ zero of the Bessel function $J_\nu(x)$ with $\nu = 0$.
- $\beta_p$: $p^{\text{th}}$ zero of the Bessel function $J'_\nu(x)$ with $\nu = 0$.
- $k_o$: characteristic constant in vacuum $k_o = \omega\sqrt{\mu_o\varepsilon_o}$.
- $k_f$: characteristic constant in the insert material $k_f = \omega\sqrt{\mu_f\varepsilon_f}$.
- $Z_o$: characteristic impedance in vacuum $Z_o = \sqrt{\mu_o/\varepsilon_o}$.
- $Z_f$: characteristic impedance in the insert material $Z_f = \sqrt{\mu_f/\varepsilon_f}$.
- $\alpha_o$: normalized characteristic constant in vacuum $\alpha_o = k_o b$.
- $\alpha_f$: normalized characteristic constant in the insert material $\alpha_f = k_f b$.
- $\tilde{\alpha}_p$: beam pipe normalized propagation constant $\tilde{\alpha}_p = \sqrt{\alpha_o^2 - \alpha_p^2}$.

- $\alpha_s$: longitudinal normalized cavity TM eigenvalue $\alpha_s = s\pi\frac{b}{L}$.
- $\beta_s$: longitudinal normalized cavity TE eigenvalue $\beta_s = \alpha_s$.
- $\tilde{\alpha}_{fs}$: radial normalized propagation constant in the insert $\tilde{\alpha}_{fs} = \sqrt{\alpha_f^2 - \alpha_s^2}$.
- $\alpha_{p\,s}$: cavity TM eigenvalues $\alpha_{p\,s} = \sqrt{\alpha_p^2 + \alpha_s^2}$.
- $\beta_{p\,s}$: cavity TE eigenvalues $\beta_{p\,s} = \sqrt{\beta_p^2 + \beta_s^2}$.
- $\mathcal{W}_{\mathrm{TMs}}$: radial TM wave function in the insert $\mathcal{W}_{\mathrm{TMs}}(r) = H_\nu^{(2)}\left(\frac{r\tilde{\alpha}_{fs}}{b}\right) - \frac{H_\nu^{(2)}\left(\frac{c\tilde{\alpha}_{fs}}{b}\right)}{H_\nu^{(1)}\left(\frac{c\tilde{\alpha}_{fs}}{b}\right)} H_\nu^{(1)}\left(\frac{r\tilde{\alpha}_{fs}}{b}\right)$ calculated in $r = b$ with $\nu = 0$.
- $\mathcal{W}'_{\mathrm{TMs}}$: derivative of $\mathcal{W}_{\mathrm{TMs}}(r)$ with respect to $r$ calculated in $r = b$.
- $\mathcal{V}_{p\,s}^{\mathrm{TM}}$: norm of solenoidal modes $\mathcal{V}_{p\,s}^{\mathrm{TM}} = b\sqrt{\pi}\sqrt{\frac{L}{\epsilon_s}} J_1(\alpha_p)\frac{\alpha_{p\,s}}{\alpha_p}$.
- $\mathcal{V}_{p\,s}^{\mathrm{E}}$: norm of electric irrotational modes $\mathcal{V}_{p\,s}^{\mathrm{E}} = \sqrt{L} J_1(\alpha_p)\,\alpha_{p\,s}$.
- $\mathcal{V}_{p\,s}^{\mathrm{H}}$: norm of magnetic irrotational modes $\mathcal{V}_{p\,s}^{\mathrm{H}} = \sqrt{\pi}\sqrt{\frac{L}{\epsilon_s}} J_0(\beta_p)\,\beta_{p\,s}$.
- $\mathcal{T}_p^{\mathrm{TM}}$: transverse norm $\mathcal{T}_p^{\mathrm{TM}} = \sqrt{\pi}\alpha_p J_1(\alpha_p)$.
- $\mathcal{L}_s^{\mathrm{TM}}$: longitudinal norm $\mathcal{L}_s^{\mathrm{TM}} = \sqrt{L/\epsilon_s}$.

In the transverse case, the electric fields in the pipes and the insert (sub-domains I, II and III) are:

$$\overline{E}^{(I)} = \sum_p \mathbf{C}_{\mathbf{p}}^{\mathrm{TM}}\ \overline{E}_p^{(I,\mathrm{TM})} + \sum_p \mathbf{C}_{\mathbf{p}}^{\mathrm{TE}}\ \overline{E}_p^{(I,\mathrm{TE})}, \tag{2.44}$$

$$\overline{E}^{(II)} = \sum_p \mathbf{D}_{\mathbf{p}}^{\mathrm{TM}}\ \overline{E}_p^{(II,\mathrm{TM})} + \sum_p \mathbf{D}_{\mathbf{p}}^{\mathrm{TE}}\ \overline{E}_p^{(II,\mathrm{TE})}, \tag{2.45}$$

$$\overline{E}^{(III)} = \sum_s \mathbf{A}_{\mathbf{s}}^{\mathrm{TM}}\ \overline{E}_s^{(III,\mathrm{TM})} + \sum_s \mathbf{A}_{\mathbf{s}}^{\mathrm{TE}}\ \overline{E}_s^{(III,\mathrm{TE})}, \tag{2.46}$$

and analogously for the magnetic fields. In the cavity we have:

$$\overline{E}^{(IV)} = \sum_{p\,s} \mathbf{V}_{\mathbf{p\,s}}^{\mathrm{TM}}\ \bar{e}_{p\,s}^{(IV,\mathrm{TM})} + \sum_{p\,s} \mathbf{V}_{\mathbf{p\,s}}^{\mathrm{TE}}\ \bar{e}_{p\,s}^{(IV,\mathrm{TE})} + \sum_{p\,s} \mathbf{F}_{\mathbf{p\,s}}\ \bar{f}_{p\,s}^{(IV)}, \tag{2.47}$$

$$\overline{H}^{(IV)} = \sum_{p\,s} \mathbf{I}_{\mathbf{p\,s}}^{\mathrm{TM}}\ \bar{h}_{p\,s}^{(IV,\mathrm{TM})} + \sum_{p\,s} \mathbf{I}_{\mathbf{p\,s}}^{\mathrm{TE}}\ \bar{h}_{p\,s}^{(IV,\mathrm{TE})} + \sum_{p\,s} \mathbf{G}_{\mathbf{p\,s}}\ \bar{g}_{p\,s}^{(IV)} \tag{2.48}$$

The scattered fields for sub-domains I, II III and IV have been given in Tabs. 2.7, 2.8, 2.9. The parameters used are corresponding to the longitudinal case considering $\nu = 1$ and the following additional ones:

- $\mathcal{W}_{\mathrm{TEs}}$: radial TE wave function in the insert $\mathcal{W}_{\mathrm{TEs}}(r) = H_\nu^{(2)}\left(\frac{r\tilde{\alpha}_{fs}}{b}\right) - \frac{H_\nu'^{(2)}\left(\frac{c\tilde{\alpha}_{fs}}{b}\right)}{H_\nu'^{(1)}\left(\frac{c\tilde{\alpha}_{fs}}{b}\right)} H_\nu^{(1)}\left(\frac{r\tilde{\alpha}_{fs}}{b}\right)$ calculated in $r = b$ with $\nu = 1$.
- $\mathcal{W}'_{\mathrm{TEs}}$: derivative of $\mathcal{W}_{\mathrm{TEs}}(r)$ with respect to $r$ calculated in $r = b$.
- $\mathcal{V}_{p\,s}^{\mathrm{TM}}$: norm of solenoidal modes $\mathcal{V}_{p\,s}^{\mathrm{TM}} = b\sqrt{\frac{\pi}{2}}\sqrt{\frac{L}{\epsilon_s}} J_0(\alpha_p)\frac{\alpha_{p\,s}}{\alpha_p}$.

- $\mathcal{V}_{p\,s}^{\mathrm{TE}}$: norm of solenoidal modes $\mathcal{V}_{p\,s}^{\mathrm{TE}} = b\sqrt{\frac{\pi}{2}}\sqrt{\frac{L}{2}}\sqrt{\beta_p^2 - 1}J_0\left(\beta_p\right)\frac{\beta_{p\,s}}{\beta_p}$.
- $\mathcal{V}_{p\,s}^{\mathrm{E}}$: norm of electric irrotational modes $\mathcal{V}_{p\,s}^{\mathrm{E}} = \frac{1}{2}\sqrt{\pi}\sqrt{L}\alpha_{p\,s}J_0\left(\alpha_p\right)$.
- $\mathcal{V}_{p\,s}^{\mathrm{H}}$: norm of magnetic irrotational modes $\mathcal{V}_{p\,s}^{\mathrm{H}} = \sqrt{\frac{\pi}{2}}\beta_{p\,s}J_0\left(\beta_p\right)\sqrt{\frac{L}{\epsilon_s}}\sqrt{\beta_p^2 - 1}$.
- $\mathcal{T}_p^{\mathrm{TE}}$: transverse norm $\mathcal{T}_p^{\mathrm{TE}} = \sqrt{\frac{\pi}{2}}\beta_p\sqrt{\beta_p^2 - 1}J_0\left(\beta_p\right)$.
- $\mathcal{T}_p^{\mathrm{TM}}$: transverse norm $\mathcal{T}_p^{\mathrm{TM}} = \sqrt{\frac{\pi}{2}}\alpha_p J_0\left(\alpha_p\right)$.
- $\mathcal{L}_s^{\mathrm{TM}}$: longitudinal TM norm $\mathcal{L}_s^{\mathrm{TM}} = \sqrt{L/\epsilon_s}$.
- $\mathcal{L}_s^{\mathrm{TE}}$: longitudinal TE norm $\mathcal{L}_s^{\mathrm{TE}} = \sqrt{L/2}$.

In order to correctly represent the reflected waves in the beam pipes we chose $\alpha_p$ with $Re\left(\alpha_p\right) > 0$ and $Im\left(\alpha_p\right) < 0$: in this way the scattered waves below cut-off get attenuated in both sub-domains I and II. Analogous considerations hold for $\beta_p$.

| | Left pipe (I) | Right pipe (II) | Insert (III) | Cavity (IV) | |
|---|---|---|---|---|---|
| | $\overline{E}_p^{\mathrm{TM}}$, $\overline{H}_p^{\mathrm{TM}}$ | $\overline{E}_p^{\mathrm{TM}}$, $\overline{H}_p^{\mathrm{TM}}$ | $\overline{E}_s^{\mathrm{TM}}$, $\overline{H}_s^{\mathrm{TM}}$ | $\bar{e}_{p\,s}$, $\bar{h}_{p\,s}$ | $\bar{f}_{p\,s}$, $\bar{g}_{p\,s}$ |
| $E_r$ | $-\frac{j\tilde{\alpha}_p J_1\left(\frac{r\alpha_p}{b}\right)}{\alpha_p \mathcal{T}_p^{\mathrm{TM}}} e^{\frac{jz\tilde{\alpha}_p}{b}}$ | $\frac{j\tilde{\alpha}_p J_1\left(\frac{r\alpha_p}{b}\right)}{\alpha_p \mathcal{T}_p^{\mathrm{TM}}} e^{-\frac{j(z-L)\tilde{\alpha}_p}{b}}$ | $-\frac{\alpha_s \mathcal{W}'_{\mathrm{TMs}}\left(\frac{r\tilde{\alpha}_{fs}}{b}\right)}{\tilde{\alpha}_{fs}\mathcal{L}_s^{\mathrm{TM}}} \sin\left(\frac{z\alpha_s}{b}\right)$ | $\frac{\alpha_s J_1\left(\frac{r\alpha_p}{b}\right)}{\alpha_p \mathcal{V}_{p\,s}^{\mathrm{TM}}} \sin\left(\frac{z\alpha_s}{b}\right)$ | $-\frac{\alpha_p J_1\left(\frac{r\alpha_p}{b}\right)}{b\,\mathcal{V}_{p\,s}^{\mathrm{E}}} \sin\left(\frac{z\alpha_s}{b}\right)$ |
| $E_\phi$ | 0 | 0 | 0 | 0 | 0 |
| $E_z$ | $\frac{J_0\left(\frac{r\alpha_p}{b}\right)}{\mathcal{T}_p^{\mathrm{TM}}} e^{\frac{jz\tilde{\alpha}_p}{b}}$ | $\frac{J_0\left(\frac{r\alpha_p}{b}\right)}{\mathcal{T}_p^{\mathrm{TM}}} e^{-\frac{j(z-L)\tilde{\alpha}_p}{b}}$ | $\frac{\mathcal{W}_{\mathrm{TMs}}\left(\frac{r\tilde{\alpha}_{fs}}{b}\right)}{\mathcal{L}_s^{\mathrm{TM}}} \cos\left(\frac{z\alpha_s}{b}\right)$ | $\frac{J_0\left(\frac{r\alpha_p}{b}\right)}{\mathcal{V}_{p\,s}^{\mathrm{TM}}} \cos\left(\frac{z\alpha_s}{b}\right)$ | $\frac{\alpha_s J_0\left(\frac{r\alpha_p}{b}\right)}{b\,\mathcal{V}_{p\,s}^{\mathrm{E}}} \cos\left(\frac{z\alpha_s}{b}\right)$ |
| $H_r$ | 0 | 0 | 0 | 0 | $-\frac{\beta_p J_1\left(\frac{r\beta_p}{b}\right)}{b\,\mathcal{V}_{p\,s}^{\mathrm{H}}} \cos\left(\frac{z\alpha_s}{b}\right)$ |
| $H_\phi$ | $\frac{j\alpha_o J_1\left(\frac{r\alpha_p}{b}\right)}{Z_o\alpha_p \mathcal{T}_p^{\mathrm{TM}}} e^{\frac{jz\tilde{\alpha}_p}{b}}$ | $\frac{j\alpha_o J_1\left(\frac{r\alpha_p}{b}\right)}{Z_o\alpha_p \mathcal{T}_p^{\mathrm{TM}}} e^{-\frac{j(z-L)\tilde{\alpha}_p}{b}}$ | $-\frac{j\alpha_f \mathcal{W}'_s\left(\frac{r\tilde{\alpha}_{fs}}{b}\right)}{Z_f\tilde{\alpha}_{fs}\mathcal{L}_s^{\mathrm{TM}}} \cos\left(\frac{z\alpha_s}{b}\right)$ | $\frac{\alpha_{p\,s} J_1\left(\frac{r\alpha_p}{b}\right)}{\alpha_p \mathcal{V}_{p\,s}^{\mathrm{TM}}} \cos\left(\frac{z\alpha_s}{b}\right)$ | 0 |
| $H_z$ | 0 | 0 | 0 | 0 | $-\frac{\alpha_s J_0\left(\frac{r\beta_p}{b}\right)}{b\,\mathcal{V}_{p\,s}^{\mathrm{H}}} \sin\left(\frac{z\alpha_s}{b}\right)$ |

Table 2.6: Scattered field components for longitudinal impedance calculation.

| Scattered fields TM | Left pipe (I) | Right pipe (II) | Insert (III) |
|---|---|---|---|
| $E_r$ | $-\frac{j\,b\,J_1'\left(\frac{r\alpha_p}{b}\right)\cos(\phi)\tilde{\alpha}_p}{\alpha_p^2\mathcal{T}_s^{\mathrm{TM}}}e^{-\frac{j(z-L)\tilde{\alpha}_p}{b}}$ | $\frac{j\,b\,J_1'\left(\frac{r\alpha_p}{b}\right)\cos(\phi)\tilde{\alpha}_p}{\alpha_p^2\mathcal{T}_s^{\mathrm{TM}}}e^{\frac{jz\tilde{\alpha}_p}{b}}$ | $-\frac{\alpha_s\cos(\phi)\sin\left(\frac{z\alpha_s}{b}\right)\mathcal{W}'_{\mathrm{TMs}}\left(\frac{r\tilde{\alpha}_{fs}}{b}\right)}{\mathcal{L}_s^{\mathrm{TM}}\tilde{\alpha}_{fs}}$ |
| $E_\phi$ | $\frac{j\,b\sin(\phi)\tilde{\alpha}_p J_1\left(\frac{r\alpha_p}{b}\right)}{r\alpha_p^2\mathcal{T}_s^{\mathrm{TM}}}e^{-\frac{j(z-L)\tilde{\alpha}_p}{b}}$ | $-\frac{j\,b\sin(\phi)\tilde{\alpha}_p J_1\left(\frac{r\alpha_p}{b}\right)}{r\alpha_p^2\mathcal{T}_s^{\mathrm{TM}}}e^{\frac{jz\tilde{\alpha}_p}{b}}$ | $\frac{b\,\alpha_s\sin(\phi)\sin\left(\frac{z\alpha_s}{b}\right)\mathcal{W}_{\mathrm{TMs}}\left(\frac{r\tilde{\alpha}_{fs}}{b}\right)}{r\mathcal{L}_s^{\mathrm{TM}}\tilde{\alpha}_{fs}^2}$ |
| $E_z$ | $\frac{\cos(\phi)J_1\left(\frac{r\alpha_p}{b}\right)}{\mathcal{T}_s^{\mathrm{TM}}}e^{-\frac{j(z-L)\tilde{\alpha}_p}{b}}$ | $\frac{\cos(\phi)J_1\left(\frac{r\alpha_p}{b}\right)}{\mathcal{T}_s^{\mathrm{TM}}}e^{\frac{jz\tilde{\alpha}_p}{b}}$ | $\frac{\cos(\phi)\cos\left(\frac{z\alpha_s}{b}\right)\mathcal{W}_{\mathrm{TMs}}\left(\frac{r\tilde{\alpha}_{fs}}{b}\right)}{\mathcal{L}_s^{\mathrm{TM}}}$ |
| $H_r$ | $-\frac{j\,b\,\alpha_o\sin(\phi)J_1\left(\frac{r\alpha_p}{b}\right)}{rZ_o\alpha_p^2\mathcal{T}_s^{\mathrm{TM}}}e^{-\frac{j(z-L)\tilde{\alpha}_p}{b}}$ | $-\frac{j\,b\,\alpha_o\sin(\phi)J_1\left(\frac{r\alpha_p}{b}\right)}{rZ_o\alpha_p^2\mathcal{T}_s^{\mathrm{TM}}}e^{\frac{jz\tilde{\alpha}_p}{b}}$ | $-\frac{j\,b\,\alpha_f\sin(\phi)\cos\left(\frac{z\alpha_s}{b}\right)\mathcal{W}_{\mathrm{TMs}}\left(\frac{r\tilde{\alpha}_{fs}}{b}\right)}{rZ_f\mathcal{L}_s^{\mathrm{TM}}\tilde{\alpha}_{fs}^2}$ |
| $H_\phi$ | $\frac{-j\,b\,\alpha_o\cos(\phi)J_1'\left(\frac{r\alpha_p}{b}\right)}{Z_o\alpha_p^2\mathcal{T}_s^{\mathrm{TM}}}e^{-\frac{j(z-L)\tilde{\alpha}_p}{b}}$ | $\frac{-j\,b\,\alpha_o\cos(\phi)J_1'\left(\frac{r\alpha_p}{b}\right)}{Z_o\alpha_p^2\mathcal{T}_s^{\mathrm{TM}}}e^{\frac{jz\tilde{\alpha}_p}{b}}$ | $-\frac{j\,\alpha_f\cos(\phi)\cos\left(\frac{z\alpha_s}{b}\right)\mathcal{W}'_{\mathrm{TMs}}\left(\frac{r\tilde{\alpha}_{fs}}{b}\right)}{Z_f\mathcal{L}_s^{\mathrm{TM}}\tilde{\alpha}_{fs}}$ |
| $H_z$ | 0 | 0 | 0 |

Table 2.7: TM scattered field components for transverse impedance calculation (sub-domains I, II and III).

| Scattered fields TE | Left pipe (I) | Right pipe (II) | Insert (III) |
|---|---|---|---|
| $E_r$ | $-\frac{j\,b\,\alpha_o\cos(\phi)J_1\left(\frac{r\beta_p}{b}\right)}{rY_0\beta_p^2\mathcal{T}_p^{\mathrm{TE}}}e^{-\frac{j(z-L)\tilde{\beta}_p}{b}}$ | $-\frac{j\,b\,\alpha_o\cos(\phi)J_1\left(\frac{r\beta_p}{b}\right)}{rY_0\beta_p^2\mathcal{T}_p^{\mathrm{TE}}}e^{\frac{jz\tilde{\beta}_p}{b}}$ | $-\frac{j\,b\,\alpha_f\cos(\phi)\sin\left(\frac{z\alpha_s}{b}\right)\mathcal{W}_{\mathrm{TEs}}\left(\frac{r\tilde{\alpha}_{fs}}{b}\right)}{\mathcal{L}_s^{\mathrm{TE}}rY_f\tilde{\alpha}_{fs}^2}$ |
| $E_\phi$ | $-\frac{j\,b\,\alpha_o\sin(\phi)J_1'\left(\frac{r\beta_p}{b}\right)}{Y_0\beta_p^2\mathcal{T}_p^{\mathrm{TE}}}e^{-\frac{j(z-L)\tilde{\beta}_p}{b}}$ | $\frac{j\,b\,\alpha_o\sin(\phi)J_1'\left(\frac{r\beta_p}{b}\right)}{Y_0\beta_p^2\mathcal{T}_p^{\mathrm{TE}}}e^{\frac{jz\tilde{\beta}_p}{b}}$ | $\frac{j\,\alpha_f\sin(\phi)\sin\left(\frac{z\alpha_s}{b}\right)\mathcal{W}'_{\mathrm{TEs}}\left(\frac{r\tilde{\alpha}_{fs}}{b}\right)}{\mathcal{L}_s^{\mathrm{TE}}Y_f\tilde{\alpha}_{fs}}$ |
| $E_z$ | 0 | 0 | 0 |
| $H_r$ | $-\frac{j\,b\,J_1'\left(\frac{r\beta_p}{b}\right)\sin(\phi)\tilde{\beta}_p}{\beta_p^2\mathcal{T}_p^{\mathrm{TE}}}e^{-\frac{j(z-L)\tilde{\beta}_p}{b}}$ | $\frac{j\,b\,J_1'\left(\frac{r\beta_p}{b}\right)\sin(\phi)\tilde{\beta}_p}{\sqrt{2\pi}\beta_p^2\mathcal{T}_p^{\mathrm{TE}}}e^{\frac{jz\tilde{\beta}_p}{b}}$ | $\frac{\alpha_s\sin(\phi)\cos\left(\frac{z\alpha_s}{b}\right)\mathcal{W}'_{\mathrm{TEs}}\left(\frac{r\tilde{\alpha}_{fs}}{b}\right)}{\mathcal{L}_s^{\mathrm{TE}}\tilde{\alpha}_{fs}}$ |
| $H_\phi$ | $-\frac{j\,b\,\cos(\phi)\tilde{\beta}_pJ_1\left(\frac{r\beta_p}{b}\right)}{r\beta_p^2\mathcal{T}_p^{\mathrm{TE}}}e^{-\frac{j(z-L)\tilde{\beta}_p}{b}}$ | $\frac{j\,b\,\cos(\phi)\tilde{\beta}_pJ_1\left(\frac{r\beta_p}{b}\right)}{r\beta_p^2\mathcal{T}_p^{\mathrm{TE}}}e^{\frac{jz\tilde{\beta}_p}{b}}$ | $\frac{b\,\alpha_s\cos(\phi)\cos\left(\frac{z\alpha_s}{b}\right)\mathcal{W}_{\mathrm{TEs}}\left(\frac{r\tilde{\alpha}_{fs}}{b}\right)}{\mathcal{L}_s^{\mathrm{TE}}r\tilde{\alpha}_{fs}^2}$ |
| $H_z$ | $\frac{\sin(\phi)J_1\left(\frac{r\beta_p}{b}\right)}{\mathcal{T}_p^{\mathrm{TE}}}e^{-\frac{j(z-L)\tilde{\beta}_p}{b}}$ | $\frac{\sin(\phi)J_1\left(\frac{r\beta_p}{b}\right)}{\mathcal{T}_p^{\mathrm{TE}}}e^{\frac{jz\tilde{\beta}_p}{b}}$ | $\frac{\sin(\phi)\sin\left(\frac{z\alpha_s}{b}\right)\mathcal{W}_{\mathrm{TEs}}\left(\frac{r\tilde{\alpha}_{fs}}{b}\right)}{\mathcal{L}_s^{\mathrm{TE}}}$ |

Table 2.8: TE scattered field components for transverse impedance calculation (sub-domains I, II and III).

| Scattered fields | Cavity (IV) | | | |
|---|---|---|---|---|
| | Solenoidal TM | Solenoidal TE | Irrotational E | Irrotational H |
| $E_r$ | $-\frac{b\,\alpha_s \cos(\phi) J_1'\left(\frac{r\alpha_p}{b}\right)\sin\left(\frac{z\alpha_s}{b}\right)}{\alpha_p^2 \mathcal{V}_p^{\mathrm{TM}}}$ | $\frac{b\,\beta_{p\,s} \cos(\phi) J_1\left(\frac{r\beta_p}{b}\right)\sin\left(\frac{z\alpha_s}{b}\right)}{r\,\beta_p^2 \mathcal{V}_p^{\mathrm{TE}}}$ | $\frac{\cos(\phi) J_1'\left(\frac{r\alpha_p}{b}\right)\sin\left(\frac{z\alpha_s}{b}\right)}{\mathcal{V}_p^{E}}$ | 0 |
| $E_\phi$ | $\frac{b\,\alpha_s \sin(\phi) J_1\left(\frac{r\alpha_p}{b}\right)\sin\left(\frac{z\alpha_s}{b}\right)}{r\,\alpha_p^2 \mathcal{V}_p^{\mathrm{TM}}}$ | $-\frac{b\,\beta_{p\,s} \sin(\phi) J_1'\left(\frac{r\beta_p}{b}\right)\sin\left(\frac{z\alpha_s}{b}\right)}{\beta_p^2 \mathcal{V}_p^{\mathrm{TE}}}$ | $-\frac{\sin(\phi) J_1\left(\frac{r\alpha_p}{b}\right)\sin\left(\frac{z\alpha_s}{b}\right)}{r\,\mathcal{V}_p^{E}}$ | 0 |
| $E_z$ | $\frac{\cos(\phi) J_1\left(\frac{r\alpha_p}{b}\right)\cos\left(\frac{z\alpha_s}{b}\right)}{\mathcal{V}_p^{\mathrm{TM}}}$ | 0 | $\frac{\alpha_s \cos(\phi) J_1\left(\frac{r\alpha_p}{b}\right)\cos\left(\frac{z\alpha_s}{b}\right)}{b\,\mathcal{V}_p^{E}}$ | 0 |
| $H_r$ | $-\frac{b\,\alpha_{p\,s} \sin(\phi) J_1\left(\frac{r\alpha_p}{b}\right)\cos\left(\frac{z\alpha_s}{b}\right)}{r\,\alpha_p^2 \mathcal{V}_p^{\mathrm{TM}}}$ | $\frac{b\,\alpha_s \sin(\phi) J_1'\left(\frac{r\beta_p}{b}\right)\cos\left(\frac{z\alpha_s}{b}\right)}{\beta_p^2 \mathcal{V}_p^{\mathrm{TE}}}$ | 0 | $\frac{\sin(\phi) J_1'\left(\frac{r\beta_p}{b}\right)\cos\left(\frac{z\alpha_s}{b}\right)}{\mathcal{V}_p^{H}}$ |
| $H_\phi$ | $-\frac{b\,\alpha_{p\,s} \cos(\phi) J_1'\left(\frac{r\alpha_p}{b}\right)\cos\left(\frac{z\alpha_s}{b}\right)}{\alpha_p^2 \mathcal{V}_p^{\mathrm{TM}}}$ | $\frac{b\,\alpha_s \cos(\phi) J_1\left(\frac{r\beta_p}{b}\right)\cos\left(\frac{z\alpha_s}{b}\right)}{r\,\beta_p^2 \mathcal{V}_p^{\mathrm{TE}}}$ | 0 | $\frac{\cos(\phi) J_1\left(\frac{r\beta_p}{b}\right)\cos\left(\frac{z\alpha_s}{b}\right)}{r\,\mathcal{V}_p^{H}}$ |
| $H_z$ | 0 | $\frac{\sin(\phi) J_1\left(\frac{r\beta_p}{b}\right)\sin\left(\frac{z\alpha_s}{b}\right)}{\mathcal{V}_p^{\mathrm{TE}}}$ | 0 | $-\frac{\alpha_s \sin(\phi) J_1\left(\frac{r\beta_p}{b}\right)\sin\left(\frac{z\alpha_s}{b}\right)}{b\,\mathcal{V}_p^{H}}$ |

Table 2.9: Scattered field components for transverse impedance calculation (sub-domain IV).

### 2.4.2 Longitudinal case: matching equations

We will now proceed to the matching procedure in order to find the missing coefficients. In the longitudinal case we have 7 vector unknowns $\mathbf{C}_{\mathbf{p}}^{\mathrm{TM}}$, $\mathbf{D}_{\mathbf{p}}^{\mathrm{TM}}$, $\mathbf{A}_{\mathbf{s}}^{\mathrm{TM}}$, $\mathbf{I}_{\mathbf{ps}}^{\mathrm{TM}}$, $\mathbf{V}_{\mathbf{ps}}^{\mathrm{TM}}$, $\mathbf{G}_{\mathbf{ps}}, \mathbf{F}_{\mathbf{ps}}$ in 7 functional equations: 3 equations can be obtained matching the magnetic field at the surfaces $S_1$, $S_2$ and $S_3$ and the remaining 4 equations are provided by the Mode Matching Eqs. (2.28),(2.29), (2.30),(2.31). By means of an ad-hoc projection (Ritz-Galerkin method [16]) each functional equation may be transformed into an infinite set of linear equations.

We can immediately notice that Eq. 2.31 implies $\mathbf{F}_{\mathbf{ps}} = 0$ since the irrotational electric modes $\overline{f}_{p\,s}$ are null on the sub-domain IV boundaries.

**Magnetic matching on $S_3$**

Between region III and IV we can impose the continuity of longitudinal and azimuthal magnetic field components. In the longitudinal direction we have:

$$H_z^{(III)}\Big|_{r=b} = H_z^{(IV)}\Big|_{r=b}. \tag{2.49}$$

The only longitudinal magnetic component comes from the irrotational modes H, and therefore we have:

$$\mathbf{G}_{\mathbf{ps}} = 0. \tag{2.50}$$

We conclude that the irrotational modes do not couple.

Azimuthally we have:

$$H_\phi^{(source)}\Big|_{r=b} + H_\phi^{(III)}\Big|_{r=b} = H_\phi^{(IV)}\Big|_{r=b}. \tag{2.51}$$

Substituting the azimuthal components in Tabs. 2.5 and 2.6 and projecting over $\cos(\alpha_s z/b)$, we get:

$$\frac{\sqrt{\frac{L}{\epsilon_s}}\sum_p \mathbf{I}_{\mathbf{ps}}^{\mathrm{TM}} J_1(\alpha_p)}{\sqrt{\pi} b} - \frac{j\alpha_b\left(1-(-1)^s e^{-\frac{j(L\alpha_b)}{b}}\right)}{2\pi\left(\alpha_b^2-\alpha_s^2\right) I_0\left(\frac{\alpha_b}{\gamma}\right)} = -\frac{j\mathbf{A}_{\mathbf{s}}^{\mathrm{TM}}\alpha_f\sqrt{\frac{L}{\epsilon_s}}\mathcal{W}'_{\mathrm{TMs}}(\tilde{\alpha}_{fs})}{Z_f\tilde{\alpha}_{fs}}. \tag{2.52}$$

**Magnetic matching on $S_1$**

Between sub-domains I and IV we can impose continuity of the radial magnetic field components:

$$H_r^{(I)}\Big|_{z=0} = H_r^{(IV)}\Big|_{z=0}. \tag{2.53}$$

Substituting the radial components and projecting over $\nabla_t E_{z_q}^{(I)}$ we get:

$$\sum_s \mathbf{I}_{\mathbf{ps}}^{\mathrm{TM}}\sqrt{\epsilon_s} = \frac{j\,\alpha_o\, b\,\mathbf{C}_{\mathbf{p}}^{\mathrm{TM}}\sqrt{L}}{Z_o\,\alpha_p^2}. \tag{2.54}$$

**Magnetic matching on $S_2$**

We perform the same method for sub-domains II and IV and obtain

$$\sum_s \mathbf{I}_{\mathbf{ps}}^{\mathrm{TM}}(-1)^s\sqrt{\epsilon_s} = \frac{j\,\alpha_o\, b\,\mathbf{D}_{\mathbf{p}}^{\mathrm{TM}}\sqrt{L}}{Z_o\,\alpha_p^2}. \tag{2.55}$$

**Electric matching**

According to the assumed expansion in the sub-domain IV, the tangential component of the electric field on the boundary $S = S_1 \cup S_2 \cup S_3 = S_E$ is null by definition and the expansion given by Eqs. (2.42) and (2.43) will not converge uniformly on the boundaries. This difficulty may be circumvented by resorting to the Eqs. (2.28) and (2.29) that simplify in:

$$\mathbf{I}^{\mathrm{TM}}_{\mathbf{p\,s}} = \frac{j\,b\,\alpha_o}{Z_o\,\left(\alpha_o^2 - \alpha_{p\,s}^2\right)} \int_S (\,\overline{E} \times \overline{h}^{*(IV,\mathrm{TM})}_{p\,s}) \cdot \hat{n}_0 \,\mathrm{d}S, \tag{2.56}$$

$$\mathbf{V}^{\mathrm{TM}}_{\mathbf{p\,s}} = -\frac{j\,Z_o\,\alpha_{p\,s}}{\alpha_o} \mathbf{I}^{\mathrm{TM}}_{\mathbf{p\,s}}. \tag{2.57}$$

The surface integral has to be split for $S_1$, $S_2$ and $S_3$. After some algebra it leads to:

$$\mathbf{I}^{\mathrm{TM}}_{\mathbf{p\,s}} = \frac{j\,\alpha_o\,b}{Z_o\,\left(\alpha_o^2 - \alpha_{p\,s}^2\right)} \left( \frac{j\,b\,\mathbf{C}^{\mathrm{TM}}_{\mathbf{p}} \tilde{\alpha}_p}{\alpha_p^2 \sqrt{\frac{L}{\epsilon_s}}} + \frac{j\,b\,\mathbf{D}^{\mathrm{TM}}_{\mathbf{p}} (-1)^s \tilde{\alpha}_p}{\alpha_p^2 \sqrt{\frac{L}{\epsilon_s}}} - 2\sqrt{\pi} \mathbf{A}^{\mathrm{TM}}_{\mathbf{s}} J_1\left(\alpha_p\right) \mathcal{W}_{\mathrm{TMs}}\left(\tilde{\alpha}_{fs}\right) \right). \tag{2.58}$$

Equations (2.52), (2.54), (2.55) and (2.58), constitute four independent vector equations in four vector unknowns. The longitudinal problem is formally solved.

**Matrix manipulation**

One way to simplify the system of equations is to proceed closing the sums that have analytical known solution, either in the longitudinal index $s$ or in the radial index $p$. Appendix A collects the series used along the process: this will reduce the computational load and accelerate the numerical convergence of the solution once this is implemented in a numerical code. Some of the series listed in the appendix are known, other have been derived from the Kneser-Sommerfeld formula following the approach of [26]. Inserting Eq. (2.58) in Eq. (2.52) and summing with Eq. (A.5) we get

$$\mathbf{A}^{\mathrm{TM}}_{\mathbf{s}} = \frac{b\,\alpha_o}{\sqrt{\pi} Z_o \mathcal{H}_s} \left( \sum_p \frac{\tilde{\alpha}_p J_1\left(\alpha_p\right) \mathbf{C}^{\mathrm{TM}}_{\mathbf{p}}}{\alpha_p^2\left(\alpha_o^2 - \alpha_{p\,s}^2\right)} + (-1)^s \sum_p \frac{\tilde{\alpha}_p J_1\left(\alpha_p\right) \mathbf{D}^{\mathrm{TM}}_{\mathbf{p}}}{\alpha_p^2\left(\alpha_o^2 - \alpha_{p\,s}^2\right)} \right) - \frac{j\alpha_b \left( (-1)^s e^{-\frac{jL\alpha_b}{b}} - 1 \right)}{2\pi\left(\alpha_b^2 - \alpha_s^2\right) I_0\left(\frac{\alpha_b}{\gamma}\right) \mathcal{H}_s},$$

where we defined the quantity $\mathcal{H}_s$:

$$\mathcal{H}_s = \frac{j\alpha_f}{Z_f \tilde{\alpha}_{fs}} \sqrt{\frac{L}{\epsilon_s}} \mathcal{W}'_{\mathrm{TMs}}\left(\tilde{\alpha}_{fs}\right) + \frac{j\alpha_o}{Z_o \tilde{\alpha}_s} \sqrt{\frac{L}{\epsilon_s}} \frac{J_1\left(\tilde{\alpha}_s\right)}{J_0\left(\tilde{\alpha}_s\right)} \mathcal{W}_{\mathrm{TMs}}\left(\tilde{\alpha}_s\right).$$

Truncating the number of longitudinal and radial modes to $s_{max} = S$ and $p_{max} = P$, the expression can be put in the matrix formalism

$$\mathbf{A}^{\mathrm{TM}}_{\mathbf{S\times 1}} = \mathrm{N1}_{S\times S} \cdot \mathrm{M1}_{S\times P} \cdot \mathbf{C}^{\mathrm{TM}}_{\mathbf{P\times 1}} + \mathrm{N1}_{S\times S} \cdot \mathrm{II}_{S\times S} \cdot \mathrm{M1}_{S\times P} \cdot \mathbf{D}^{\mathrm{TM}}_{\mathbf{P\times 1}} + B_{S\times 1},$$

with correspondent matrix elements[4]

$$\mathrm{N1}_{s\,s} = \frac{\alpha_o b}{\sqrt{\pi} Z_o \mathcal{H}_s},$$

$$\mathrm{M1}_{s\,p} = \frac{\tilde{\alpha}_p J_1\left(\alpha_p\right)}{\alpha_p^2\left(\alpha_o^2 - \alpha_{p\,s}^2\right)},$$

$$\mathrm{II}_{s\,s} = (-1)^s,$$

$$\mathrm{B}_{s\,1} = -\frac{jQ\, I_0(s)\, \alpha_b \left( (-1)^s e^{-\frac{jL\alpha_b}{b}} - 1 \right)}{2\pi \mathcal{H}_s \left(\alpha_b^2 - \alpha_s^2\right) I_0\left(\frac{\alpha_b}{\gamma}\right)}.$$

[4] A matrix $\mathrm{M}_{S\times P}$ of dimension $S \times P$ has a matrix element generically noted as $\mathrm{M}_{p\,s}$ where $p \in (1 \ldots P)$ and $s \in (1 \ldots S)$ or $s \in (0 \ldots S)$ respectively for TE or TM modes.

It may be noted that the convergence of the method is dependent on the number of longitudinal $S$ and radial $P$ modes we choose for the matrix truncation. As we will see later the number of modes mainly depends on the geometry and the frequency range under study. The term $\mathrm{B}_{s\,1}$ represents the beam driving term. Analogously, inserting Eq. (2.58) in Eq. (2.55) and summing with series (A.1) and (A.2) we get:

$$\mathbf{C}_{\mathbf{p}}^{\mathrm{TM}} \csc(L\tilde{\alpha}_p/b)+\mathbf{D}_{\mathbf{p}}^{\mathrm{TM}} \left(\cot(L\tilde{\alpha}_p/b)+j\right) = -2\,j\,\sqrt{\frac{\pi}{L}}\alpha_p^2 J_1\left(\alpha_p\right)\sum_s \frac{\mathbf{A}_{\mathbf{s}}^{\mathrm{TM}}(-1)^s\sqrt{\epsilon_s}\,\mathcal{W}_{\mathrm{TMs}}\left(\tilde{\alpha}_{fs}\right)}{\alpha_o^2-\alpha_{p\,s}^2}.$$

Inserting Eq. (2.58) in Eq. (2.54) and summing over $s$ with series (A.1) and (A.2) we get:

$$\mathbf{C}_{\mathbf{p}}^{\mathrm{TM}} \left(\cot(L\tilde{\alpha}_p/b)+j\right) + \mathbf{D}_{\mathbf{p}}^{\mathrm{TM}} \csc(L\tilde{\alpha}_p/b) = -2\,j\,\sqrt{\frac{\pi}{L}}\alpha_p^2 J_1\left(\alpha_p\right)\sum_s \frac{\mathbf{A}_{\mathbf{s}}^{\mathrm{TM}}\sqrt{\epsilon_s}\,\mathcal{W}_{\mathrm{TMs}}\left(\tilde{\alpha}_{fs}\right)}{\alpha_o^2-\alpha_{p\,s}^2}.$$

The system can be solved to obtain $\mathbf{C}_{\mathbf{p}}^{\mathrm{TM}}$ and $\mathbf{D}_{\mathbf{p}}^{\mathrm{TM}}$ in function of $\mathbf{A}_{\mathbf{s}}^{\mathrm{TM}}$. After algebraic manipulations we get

$$\mathbf{C}_{\mathbf{P\times 1}}^{\mathrm{TM}} = \mathrm{N2}_{P\times P}\cdot \mathrm{M2}_{P\times S}\cdot \mathbf{A}_{\mathbf{S\times 1}}^{\mathrm{TM}}, \tag{2.59}$$

$$\mathbf{D}_{\mathbf{P\times 1}}^{\mathrm{TM}} = \mathrm{N2}_{P\times P}\cdot \mathrm{M2}_{P\times S}\cdot \mathrm{II}_{S\times S}\cdot \mathbf{A}_{\mathbf{S\times 1}}^{\mathrm{TM}}, \tag{2.60}$$

where we defined the matrix elements

$$N2_{p\,p} = \frac{\sqrt{\pi}\alpha_p^2}{L}J_1\left(\alpha_p\right),$$

$$M2_{p\,p} = \frac{\sqrt{L\epsilon_s}\left((-1)^s e^{-\frac{jL\tilde{\alpha}_p}{b}}-1\right)}{\alpha_o^2-\alpha_{p\,s}^2}\mathcal{W}_{\mathrm{TMs}}\left(\tilde{\alpha}_{fs}\right).$$

Table 2.10 recapitulates the matrix matching equations. Since we have 3 vector equations in 3 independent vector variables, the problem is formally solved and the coefficients $\mathbf{C}_{\mathbf{P\times 1}}^{\mathrm{TM}}$, $\mathbf{D}_{\mathbf{P\times 1}}^{\mathrm{TM}}$ and $\mathbf{A}_{\mathbf{S\times 1}}^{\mathrm{TM}}$ can be found.

| | |
|---|---|
| I) | $\mathbf{A}_{\mathbf{S\times 1}}^{\mathrm{TM}} = \mathrm{N1}_{S\times S}\cdot \mathrm{M1}_{S\times P}\cdot \mathbf{C}_{\mathbf{P\times 1}}^{\mathrm{TM}} + \mathrm{N1}_{S\times S}\cdot \mathrm{II}_{S\times S}\cdot \mathrm{M1}_{S\times P}\cdot \mathbf{D}_{\mathbf{P\times 1}}^{\mathrm{TM}} + B_{S\times 1}$ |
| II) | $\mathbf{C}_{\mathbf{P\times 1}}^{\mathrm{TM}} = \mathrm{N2}_{P\times P}\cdot \mathrm{M2}_{P\times S}\cdot \mathbf{A}_{\mathbf{S\times 1}}^{\mathrm{TM}}$ |
| III) | $\mathbf{D}_{\mathbf{P\times 1}}^{\mathrm{TM}} = \mathrm{N2}_{P\times P}\cdot \mathrm{M2}_{P\times S}\cdot \mathrm{II}_{S\times S}\cdot \mathbf{A}_{\mathbf{S\times 1}}^{\mathrm{TM}}$ |

Table 2.10: Longitudinal vector matching equations.

### 2.4.3 Transverse case: matching equations

In the transverse case we have to include also the TE contribution to the scattered fields that leads to 12 vector unknowns $\mathbf{C}_{\mathbf{p}}^{\mathrm{TM}}$, $\mathbf{D}_{\mathbf{p}}^{\mathrm{TM}}$, $\mathbf{A}_{\mathbf{s}}^{\mathrm{TM}}$, $\mathbf{I}_{\mathbf{ps}}^{\mathrm{TM}}$, $\mathbf{V}_{\mathbf{ps}}^{\mathrm{TM}}$, $\mathbf{C}_{\mathbf{p}}^{\mathrm{TE}}$, $\mathbf{D}_{\mathbf{p}}^{\mathrm{TE}}$, $\mathbf{A}_{\mathbf{s}}^{\mathrm{TE}}$, $\mathbf{I}_{\mathbf{ps}}^{\mathrm{TE}}$, $\mathbf{V}_{\mathbf{ps}}^{\mathrm{TE}}$, $\mathbf{G}_{\mathbf{ps}}, \mathbf{F}_{\mathbf{ps}}$ in 12 functional equations: 6 equations can be obtained matching the magnetic field at the surfaces $S_1$, $S_2$ and $S_3$, 4 equations are provided by the Mode Matching Eqs. (2.28),(2.29) for solenoidal modes and the remaining 2 are provided by Eqs. (2.31),(2.30) for the irrotational modes. Analogously to Section 2.4.2, each functional equation will be transformed into an infinite set of linear equations.

We notice that Eq. 2.31 implies also in this case $\mathbf{F}_{\mathbf{ps}} = 0$.

#### Magnetic matching on $S_3$

Between region III and IV we impose the continuity of longitudinal and azimuthal magnetic field components. In the longitudinal direction we have:

$$H_z^{(III)}\Big|_{r=b} = H_z^{(IV)}\Big|_{r=b}. \tag{2.61}$$

Only the TE solenoidal and H irrotational fields have non-null longitudinal magnetic component. Substituting the longitudinal components from Tabs. 2.8 2.9, and projecting over $\sin(\alpha_s z/b)$, we get:

$$\mathbf{A_s^{TE}} = -\frac{\sqrt{\frac{2}{\pi}}\alpha_s}{b\,\mathcal{W}_{\mathrm{TEs}}\left(\tilde{\alpha}_{f\,s}\right)}\sum_{p=1}^{\infty}\frac{\mathbf{G_{p\,s}}\beta_p}{\sqrt{-1+\beta_p^2}\,\beta_{p\,s}} + \frac{\sqrt{\frac{2}{\pi}}}{b\,\mathcal{W}_{\mathrm{TEs}}\left(\tilde{\alpha}_{f\,s}\right)}\sum_{p=1}^{\infty}\frac{\mathbf{I_{p\,s}^{TE}}\beta_p^2}{\sqrt{-1+\beta_p^2}\,\beta_{p\,s}}. \tag{2.62}$$

In the azimuthal direction we have:

$$H_\phi^{(IV)}\Big|_{r=b} + H_\phi^{(source)}\Big|_{r=b} = H_\phi^{(III)}\Big|_{r=b}. \tag{2.63}$$

The azimuthal components, on the contrary, are non-null also for TM fields. Substituting the field expressions from Tabs. 2.7, 2.8, 2.9 and projecting over $\cos(\alpha_s z/b)$, we get:

$$\begin{aligned}\sqrt{\frac{2}{\pi}}\sqrt{\frac{L}{\epsilon_s}}\frac{1}{b}\sum_{p=1}^{\infty}\frac{\mathbf{G_{p\,s}}\,\beta_p}{\sqrt{\beta_p^2-1}\,\beta_{p\,s}} + \sqrt{\frac{L}{\pi}}\frac{\alpha_s}{b}\sum_{p=1}^{\infty}\frac{\mathbf{I_{p\,s}^{TE}}}{\sqrt{\beta_p^2-1}\,\beta_{p\,s}} + \\ - \sqrt{\frac{2}{\pi}}\sqrt{\frac{L}{\epsilon_s}}\frac{1}{b}\sum_{p=1}^{\infty}\mathbf{I_{p\,s}^{TM}} + \frac{j\alpha_b^2\left((-1)^s e^{-\frac{jL\alpha_b}{b}}-1\right)}{2\pi\, b\gamma\left(\alpha_b^2-\alpha_s^2\right)I_1\left(\frac{\alpha_b}{\gamma}\right)} = \\ = \sqrt{\frac{L}{2}}\frac{\alpha_s\mathcal{W}_{\mathrm{TEs}}\left(\tilde{\alpha}_{fs}\right)}{\tilde{\alpha}_{fs}^2}\mathbf{A_s^{TE}} - \sqrt{\frac{L}{\epsilon_s}}\frac{j\alpha_f\mathcal{W}'_{\mathrm{TMs}}\left(\tilde{\alpha}_{fs}\right)}{Z_f\tilde{\alpha}_{fs}}\mathbf{A_s^{TM}}.\end{aligned} \tag{2.64}$$

**Magnetic matching on $S_1$**

Between sub-domains I and IV we can impose the continuity of the transverse magnetic field components separately for TE and TM modes:

$$\overline{H}_t^{(IV)}\Big|_{z=0} = \overline{H}_t^{(I)}\Big|_{z=0}. \tag{2.65}$$

For TM modes, projecting over $\nabla_t E_{z_q}^{(I)} \times \hat{z}_0$ we get:

$$\sum_{s=0}^{\infty}\sqrt{\epsilon_s}\,\mathbf{I_{p\,s}^{TM}} = \frac{jb\sqrt{L}\,\alpha_o}{Z_o\alpha_p^2}\,\mathbf{C_p^{TM}}. \tag{2.66}$$

For TE modes, projecting over $\nabla_t H_{z_q}^{(I)}$ we get:

$$\sum_{s=0}^{\infty}\frac{\alpha_s\sqrt{2}}{\beta_{p\,s}}\,\mathbf{I_{p\,s}^{TE}} + \sum_{s=0}^{\infty}\frac{\beta_p\sqrt{\epsilon_s}}{\beta_{p\,s}}\mathbf{G_{p\,s}} = \frac{jb\sqrt{L}\,\tilde{\beta}_p}{\beta_p^2}\,\mathbf{C_p^{TE}} \tag{2.67}$$

**Magnetic matching on $S_2$**

Analogously, between sub-domains II and IV, we have, for TM modes,

$$\sum_{s=0}^{\infty}(-1)^s\sqrt{\epsilon_s}\,\mathbf{I_{p\,s}^{TM}} = \frac{jb\sqrt{L}\,\alpha_o}{Z_o\alpha_p^2}\mathbf{D_p^{TM}}, \tag{2.68}$$

and for TE modes:

$$\sum_{s=0}^{\infty}\frac{\sqrt{2}\,(-1)^s\alpha_s}{\beta_{p\,s}}\,\mathbf{I_{p\,s}^{TE}} + \sum_{s=0}^{\infty}\frac{(-1)^s\beta_p\sqrt{\epsilon_s}}{\beta_{p\,s}}\,\mathbf{G_{p\,s}} = -\frac{jb\sqrt{L}\,\tilde{\beta}_p}{\beta_p^2}\mathbf{D_p^{TE}}. \tag{2.69}$$

**Electric matching**

Having adopted the same modal decomposition as in the longitudinal case, we get the following relation between modal coefficients $\mathbf{I_{ps}}$ and $\mathbf{V_{ps}}$:

$$\mathbf{I}_{\mathbf{ps}}^{\mathrm{TM}} = \frac{j\,b\,\alpha_o}{Z_o\left(\alpha_o^2 - \alpha_{p\,s}^2\right)} \int_S (\,\overline{E} \times \bar{h}_{p\,s}^{*(IV,\mathrm{TM})}) \cdot \hat{n}_0 \,\mathrm{d}S, \tag{2.70}$$

$$\mathbf{V}_{\mathbf{ps}}^{\mathrm{TM}} = -\frac{j\,Z_o\,\alpha_{p\,s}}{\alpha_o}\mathbf{I}_{\mathbf{ps}}^{\mathrm{TM}}, \tag{2.71}$$

$$\mathbf{I}_{\mathbf{ps}}^{\mathrm{TE}} = \frac{j\,b\,\alpha_o}{Z_o\left(\alpha_o^2 - \beta_{p\,s}^2\right)} \int_S (\,\overline{E} \times \bar{h}_{p\,s}^{*(IV,\mathrm{TE})}) \cdot \hat{n}_0 \,\mathrm{d}S, \tag{2.72}$$

$$\mathbf{V}_{\mathbf{ps}}^{\mathrm{TE}} = -\frac{j\,Z_o\,\beta_{p\,s}}{\alpha_o}\mathbf{I}_{\mathbf{ps}}^{\mathrm{TE}}. \tag{2.73}$$

This expression are the ones corresponding to Eqs. (2.56) and (2.57), taking into account, this time, the eigenvalues for the transverse plane $\alpha_p$ and $\beta_p$. Solving the integral, we get

$$\mathbf{I}_{\mathbf{ps}}^{\mathrm{TM}} = \frac{jb\,\alpha_o}{Z_o\left(\alpha_o^2 - \alpha_{p\,s}^2\right)} \left( \frac{jb\,\tilde{\alpha}_p}{\alpha_p^2}\sqrt{\frac{\epsilon_s}{L}}\mathbf{C}_{\mathbf{p}}^{\mathrm{TM}} + \frac{jb\,\tilde{\alpha}_p}{\alpha_p^2}(-1)^s\sqrt{\frac{\epsilon_s}{L}}\mathbf{D}_{\mathbf{p}}^{\mathrm{TM}} + \sqrt{2\pi}\,\mathcal{W}_{\mathrm{TMs}}\,(\tilde{\alpha}_{f\,s})\,\mathbf{A}_{\mathbf{s}}^{\mathrm{TM}} \right), \tag{2.74}$$

and

$$\begin{aligned}\mathbf{I}_{\mathbf{ps}}^{\mathrm{TE}} = \frac{jb\alpha_o}{Z_o\left(\alpha_o^2 - \beta_{p\,s}^2\right)} \Bigg( & \frac{jb\,\alpha_o\alpha_s}{Y_0\beta_p^2\beta_{p\,s}}\sqrt{\frac{2}{L}}\,\mathbf{C}_{\mathbf{p}}^{\mathrm{TE}} - \frac{jb\,\alpha_o\alpha_s}{Y_0\beta_p^2\beta_{p\,s}}\sqrt{\frac{2}{L}}(-1)^s\,\mathbf{D}_{\mathbf{p}}^{\mathrm{TE}} + \\ & - \frac{j\sqrt{2\pi}\,\alpha_f\beta_p^2\,(\delta_{\mathrm{s0}} - 1)\,\mathcal{W}'_{\mathrm{TEs}}\,(\tilde{\alpha}_{f\,s})}{Y_f\sqrt{\beta_p^2 - 1}\beta_{p\,s}\tilde{\alpha}_{fs}}\mathbf{A}_{\mathbf{s}}^{\mathrm{TE}} - \frac{\sqrt{\pi}\alpha_s\sqrt{\epsilon_s}\left(\alpha_f^2 - \beta_{p\,s}^2\right)\mathcal{W}_{\mathrm{TMs}}\,(\tilde{\alpha}_{f\,s})}{\sqrt{\beta_p^2 - 1}\,\beta_{p\,s}\,\tilde{\alpha}_{f\,s}^2}\mathbf{A}_{\mathbf{s}}^{\mathrm{TM}} \Bigg).\end{aligned} \tag{2.75}$$

The $\mathbf{G_{ps}}$ coefficients of the irrotational modes H can be derived from Eq.(2.30) which, in this context, may be rewritten as:

$$\mathbf{G}_{\mathbf{ps}} = \frac{jb\,Y_0}{\alpha_o} \int_S (\,\overline{E} \times \bar{g}_{p\,s}^{*}) \cdot \hat{n}_0 \,\mathrm{d}S. \tag{2.76}$$

Solving the integral we have:

$$\begin{aligned}\mathbf{G}_{\mathbf{ps}} = \frac{jbY_0}{\alpha_o} \Bigg( & -\frac{\sqrt{\frac{\pi}{2}}\beta_p\epsilon_s\left((\delta_{\mathrm{s0}} + 1)\,\tilde{\alpha}_{f\,s}^2 + \alpha_s^2\right)\mathcal{W}_{\mathrm{TMs}}\,(\tilde{\alpha}_{fs})}{\sqrt{\beta_p^2 - 1}\,\beta_{p\,s}\,\tilde{\alpha}_{fs}^2}\mathbf{A}_{\mathbf{s}}^{\mathrm{TM}} - \frac{j\sqrt{\pi}\,\alpha_f\beta_p\alpha_s\sqrt{\epsilon_s}\,\mathcal{W}'_{\mathrm{TEs}}\,(\tilde{\alpha}_{f\,s})}{Y_f\sqrt{\beta_p^2 - 1}\beta_{p\,s}\tilde{\alpha}_{f\,s}}\mathbf{A}_{\mathbf{s}}^{\mathrm{TE}} + \\ & + \frac{jb\,\alpha_o}{Y_0\beta_p\beta_{p\,s}}\sqrt{\frac{\epsilon_s}{L}}\mathbf{C}_{\mathbf{p}}^{\mathrm{TE}} - \frac{jb\,(-1)^s\alpha_o}{Y_0\beta_p\beta_{p\,s}}\sqrt{\frac{\epsilon_s}{L}}\mathbf{C}_{\mathbf{p}}^{\mathrm{TE}} \Bigg).\end{aligned} \tag{2.77}$$

Up to this point we collected 9 independent relations given by Eqs. (2.62), (2.64), (2.66), (2.67), (2.68), (2.69), (2.74), (2.75), and (2.77) in 9 variables, $\mathbf{C}_{\mathbf{p}}^{\mathrm{TM}}$, $\mathbf{D}_{\mathbf{p}}^{\mathrm{TM}}$, $\mathbf{A}_{\mathbf{s}}^{\mathrm{TM}}$, $\mathbf{I}_{\mathbf{ps}}^{\mathrm{TM}}$, $\mathbf{C}_{\mathbf{p}}^{\mathrm{TE}}$, $\mathbf{D}_{\mathbf{p}}^{\mathrm{TE}}$, $\mathbf{A}_{\mathbf{s}}^{\mathrm{TE}}$, $\mathbf{I}_{\mathbf{ps}}^{\mathrm{TE}}$, $\mathbf{G_{ps}}$. The $\mathbf{V}_{\mathbf{ps}}^{\mathrm{TM}}$ coefficients are linearly related to the $\mathbf{I}_{\mathbf{ps}}^{\mathrm{TM}}$ with Eq. (2.71) and similarly for the $\mathbf{V}_{\mathbf{ps}}^{\mathrm{TE}}$ ones.

**Matrix manipulation**

We now proceed to the sums saturation analogously to what done in Sec. 2.4.2. Inserting Eq. (2.74) in Eq. (2.66) and summing over the $s$ index with Eqs. (A.7) and (A.8) we get

$$\mathbf{C}_{\mathbf{p}}^{\mathrm{TM}}\left(\cot\left(\frac{L\tilde{\alpha}_p}{b}\right) + j\right) + \mathbf{D}_{\mathbf{p}}^{\mathrm{TM}}\csc\left(\frac{L\tilde{\alpha}_p}{b}\right) = j\sqrt{\frac{2\pi}{L}}\alpha_p^2\sum_{s=0}^{\infty}\frac{\sqrt{\epsilon_s}\,\mathcal{W}_{\mathrm{TMs}}\,(\tilde{\alpha}_{f\,s})}{\alpha_o^2 - \alpha_{p\,s}^2}\mathbf{A}_{\mathbf{s}}^{\mathrm{TM}}. \tag{2.78}$$

Inserting Eq. (2.74) in Eq. (2.68) we get:

$$\mathbf{C}_{\mathbf{p}}^{\mathrm{TM}} \csc\left(\frac{L\tilde{\alpha}_p}{b}\right) + \mathbf{D}_{\mathbf{p}}^{\mathrm{TM}} \left(\cot\left(\frac{L\tilde{\alpha}_p}{b}\right) + j\right) = j\sqrt{\frac{2\pi}{L}}\alpha_p^2 \sum_{s=0}^{\infty} \frac{(-1)^s \sqrt{\epsilon_s}\, \mathcal{W}_{\mathrm{TMs}}\left(\tilde{\alpha}_{f\,s}\right)}{\alpha_o^2 - \alpha_{p\,s}^2} \mathbf{A}_{\mathbf{s}}^{\mathrm{TM}}. \quad (2.79)$$

Solving the system in the two variables $\mathbf{C}_{\mathbf{p}}^{\mathrm{TM}}$ and $\mathbf{D}_{\mathbf{p}}^{\mathrm{TM}}$ and passing to a matrix representation, we have

$$\mathbf{C}_{\mathbf{P}\times\mathbf{1}}^{\mathrm{TM}} = \mathrm{N1}_{P\times P} \cdot \mathrm{M1}_{P\times S} \cdot \mathbf{A}_{\mathbf{S}\times\mathbf{1}}^{\mathrm{TM}},$$
$$\mathbf{D}_{\mathbf{P}\times\mathbf{1}}^{\mathrm{TM}} = \mathrm{N1}_{P\times P} \cdot \mathrm{M1}_{P\times S} \cdot \mathrm{II}_{S\times S} \cdot \mathbf{A}_{\mathbf{S}\times\mathbf{1}}^{\mathrm{TM}},$$

with matrix elements

$$\mathrm{N1}_{p\,p} = \sqrt{\frac{\pi}{2}}\frac{\alpha_p^2}{L},$$
$$\mathrm{M1}_{p\,s} = \frac{\sqrt{L\,\epsilon_s}\left(1 - (-1)^s e^{-\frac{jL\tilde{\alpha}_p}{b}}\right)\mathcal{W}_{\mathrm{TMs}}\left(\tilde{\alpha}_{fs}\right)}{\alpha_o^2 - \alpha_{p\,s}^2},$$
$$\mathrm{II}_{s\,s} = (-1)^s.$$

another system can be obtained inserting Eqs. (2.75) and (2.77) respectively in Eqs. (2.67) and (2.69). Summing over the $s$ index with Eqs. (A.9)-(A.12) we get

$$\mathbf{C}_{\mathbf{P}\times\mathbf{1}}^{\mathrm{TE}} = \mathrm{N2}_{P\times P} \cdot \mathrm{M2}_{P\times S} \cdot \mathbf{A}_{\mathbf{S}\times\mathbf{1}}^{\mathrm{TE}} + \mathrm{N2}_{P\times P} \cdot \mathrm{M3}_{P\times S} \cdot \mathbf{A}_{\mathbf{S}\times\mathbf{1}}^{\mathrm{TM}},$$
$$\mathbf{D}_{\mathbf{P}\times\mathbf{1}}^{\mathrm{TE}} = \mathrm{N2}_{P\times P} \cdot \mathrm{M2}_{P\times S} \cdot \mathrm{II}_{S\times S} \cdot \mathbf{A}_{\mathbf{S}\times\mathbf{1}}^{\mathrm{TE}} + \mathrm{N2}_{P\times P} \cdot \mathrm{M3}_{P\times S} \cdot \mathrm{II}_{S\times S} \cdot \mathbf{A}_{\mathbf{S}\times\mathbf{1}}^{\mathrm{TM}},$$

with matrix elements

$$\mathrm{N2}_{p\,p} = -\frac{j\sqrt{\pi}\beta_p^2}{4\sqrt{L}\,Y_f\,\alpha_o Z_o \sqrt{\beta_p^2 - 1}\,\tilde{\beta}_p \left(\cot\left(\frac{L\tilde{\beta}_p}{b}\right) + j\right)},$$
$$\mathrm{M2}_{p\,s} = \frac{2\alpha_f \beta_p^2 \alpha_s \epsilon_s \left(\beta_{p\,s}^2 - \alpha_o^2 \delta_s\right) \mathcal{W}'_{\mathrm{TEs}}\left(\tilde{\alpha}_{f\,s}\right)\left(\cot\left(\frac{L\tilde{\beta}_p}{b}\right) - (-1)^s \csc\left(\frac{L\tilde{\beta}_p}{b}\right) + j\right)}{\beta_{p\,s}^2 \tilde{\alpha}_{f\,s}\left(\beta_{p\,s}^2 - \alpha_o^2\right)},$$
$$\mathrm{M3}_{p\,s} = \frac{2j\sqrt{2\epsilon_s}\,Y_f\,\left(\alpha_o^2\alpha_s^2 - \alpha_f^2\tilde{\beta}_p^2\right)\mathcal{W}_{\mathrm{TMs}}\left(\tilde{\alpha}_{f\,s}\right)\left(\cot\left(\frac{L\tilde{\beta}_p}{b}\right) - (-1)^s \csc\left(\frac{L\tilde{\beta}_p}{b}\right) + j\right)}{\tilde{\alpha}_{f\,s}^2\left(\alpha_o^2 - \beta_{p\,s}^2\right)}.$$

Inserting Eqs. (2.74), (2.75) and (2.77) in Eq. (2.64) and summing over the index $p$ making use of Eqs. (A.19)-(A.23) we get

$$\begin{aligned}
&\mathrm{B}_{S\times 1} + \mathrm{F1}_{S\times S} \cdot \mathbf{A}_{\mathbf{S}\times\mathbf{1}}^{\mathrm{TE}} + \mathrm{F2}_{S\times S} \cdot \mathbf{A}_{\mathbf{S}\times\mathbf{1}}^{\mathrm{TM}} - (\mathrm{T1}_{S\times S} \cdot \mathrm{G1}_{S\times P} + \mathrm{T2}_{S\times S} \cdot \mathrm{G2}_{S\times P}) \cdot \mathbf{C}_{\mathbf{P}\times\mathbf{1}}^{\mathrm{TE}} + \\
&+ \mathrm{II}_{S\times S} \cdot (\mathrm{T1}_{S\times S} \cdot \mathrm{G1}_{S\times P} + \mathrm{T2}_{S\times S} \cdot \mathrm{G2}_{S\times P}) \cdot \mathbf{D}_{\mathbf{P}\times\mathbf{1}}^{\mathrm{TE}} + \mathrm{T3}_{S\times S} \cdot \mathrm{G3}_{S\times P} \cdot \mathbf{C}_{\mathbf{P}\times\mathbf{1}}^{\mathrm{TM}} + \\
&+ \mathrm{II}_{S\times S} \cdot \mathrm{T3}_{S\times S} \cdot \mathrm{G3}_{S\times P} \cdot \mathbf{D}_{\mathbf{P}\times\mathbf{1}}^{\mathrm{TM}} = 0, \quad (2.80)
\end{aligned}$$

and the matrix elements

$$\mathrm{B}_{s\,1} = -\frac{jQ\,I_1(s)\alpha_b^2\left(1-(-1)^s e^{-\frac{jL\alpha_b}{b}}\right)}{\pi b\gamma\left(\alpha_b^2-\alpha_s^2\right)I_1\left(\frac{\alpha_b}{\gamma}\right)},$$

$$\mathrm{T1}_{s\,s} = b\sqrt{\frac{2}{\pi}},$$

$$\mathrm{T2}_{s\,s} = \sqrt{\frac{2}{\pi}}\alpha_o^2\alpha_s^2,$$

$$\mathrm{T3}_{s\,s} = \sqrt{\frac{2}{\pi}}\frac{\alpha_o}{Z_o},$$

$$\mathrm{G1}_{s\,p} = \frac{1}{\sqrt{\beta_p^2-1}\beta_{p\,s}^2},$$

$$\mathrm{G2}_{s\,p} = \frac{1}{\beta_p^2\sqrt{\beta_p^2-1}\beta_{p\,s}^2\left(\alpha_o^2-\beta_{p\,s}^2\right)},$$

$$\mathrm{G3}_{s\,p} = \frac{\tilde{\alpha}_p}{\alpha_p^2\left(\alpha_o^2-\alpha_{p\,s}^2\right)},$$

$$\mathrm{F1}_{s\,s} = \frac{\sqrt{L}\alpha_f\alpha_s\left(I_0\left(\alpha_s\right)-I_2\left(\alpha_s\right)\right)\mathcal{W}'_{\mathrm{TEs}}\left(\tilde{\alpha}_{fs}\right)}{\sqrt{2}Y_f\alpha_o Z_o\left(I_0\left(\alpha_s\right)+I_2\left(\alpha_s\right)\right)\tilde{\alpha}_{fs}} - \frac{\sqrt{L}\alpha_s\mathcal{W}_{\mathrm{TEs}}\left(\tilde{\alpha}_{fs}\right)}{\sqrt{2}\tilde{\alpha}_{fs}^2},$$

$$\mathrm{F2}_{s\,s} = -\frac{j\sqrt{L}}{2}\Big(\frac{1}{\alpha_o Z_o}\Big(\frac{\sqrt{2}\alpha_o^2\alpha_s^2 J_2(\tilde{\alpha}_s)}{\tilde{\alpha}_s\left(\alpha_f^2-\alpha_s^2\right)(\tilde{\alpha}_s J_0(\tilde{\alpha}_s)-J_1(\tilde{\alpha}_s))} - \frac{2\alpha_o^2 J_2(\tilde{\alpha}_s)}{\sqrt{\epsilon_s}\tilde{\alpha}_s J_1(\tilde{\alpha}_s)} + \frac{\sqrt{2}(I_0(\alpha_s)-I_2(\alpha_s))\left(\alpha_f^2\delta_s-\alpha_s^2(\delta_s-1)\right)}{\left(\alpha_f^2-\alpha_s^2\right)(I_0(\alpha_s)+I_2(\alpha_s))} + \frac{4\sqrt{\epsilon_s}\left(\alpha_f^2(I_1(\alpha_s)-\alpha_s I_0(\alpha_s))\left(\left(\alpha_o^2+\alpha_s^2\right)J_1(\tilde{\alpha}_s)-\alpha_o^2\tilde{\alpha}_s J_0(\tilde{\alpha}_s)\right)+\alpha_s^2\left(\alpha_o^2-\alpha_s^2\right)I_1(\alpha_s)(J_1(\tilde{\alpha}_s)-\tilde{\alpha}_s J_0(\tilde{\alpha}_s))\right)}{\alpha_s\tilde{\alpha}_s\left(\alpha_s^2-\alpha_f^2\right)(\alpha_s^2-\alpha_o^2)(I_0(\alpha_s)+I_2(\alpha_s))(J_0(\tilde{\alpha}_s)-J_2(\tilde{\alpha}_s))}\Big)\mathcal{W}_{\mathrm{TMs}}(\tilde{\alpha}_{fs}) + - \frac{2\alpha_f}{Z_f\sqrt{\epsilon_s}\tilde{\alpha}_{fs}}\mathcal{W}'_{\mathrm{TMs}}(\tilde{\alpha}_{fs})\Big).$$

Inserting Eqs. (2.75) and (2.77) in Eq. (2.62) making use of Eqs. (A.20) and (A.23)-(A.25) we get

$$\begin{aligned}&\mathrm{F3}_{S\times S}\cdot\mathbf{A}^{\mathrm{TE}}_{\mathbf{S\times 1}} + \mathrm{F4}_{S\times S}\cdot\mathbf{A}^{\mathrm{TM}}_{\mathbf{S\times 1}} - \left(\mathrm{T4}_{S\times S}\cdot\mathrm{G4}_{S\times P} - \mathrm{T5}_{S\times S}\cdot\mathrm{G5}_{S\times P}\right)\cdot\mathbf{C}^{\mathrm{TE}}_{\mathbf{P\times 1}} + \\ &+ \mathrm{II}_{S\times S}\cdot\left(\mathrm{T4}_{S\times S}\cdot\mathrm{G4}_{S\times P} - \mathrm{T5}_{S\times S}\cdot\mathrm{G5}_{S\times P}\right)\cdot\mathbf{D}^{\mathrm{TE}}_{\mathbf{P\times 1}} = 0.\end{aligned} \tag{2.81}$$

where the matrix elements are

$$\mathrm{T4}_{s\,s} = b\,\alpha_s\sqrt{\frac{2}{\pi}}\sqrt{\frac{\epsilon_s}{L}},$$

$$\mathrm{T5}_{s\,s} = \frac{2\,b\,\alpha_o^2\alpha_s}{\sqrt{\pi}\sqrt{L}},$$

$$\mathrm{G4}_{s\,p} = \frac{1}{\sqrt{\beta_p^2-1}\,\beta_{p\,s}^2},$$

$$\mathrm{G5}_{s\,p} = \frac{1}{\sqrt{\beta_p^2-1}\,\beta_{p\,s}^2\left(\alpha_o^2-\beta_{p\,s}^2\right)},$$

$$\mathrm{F3}_{s\,s} = \frac{\alpha_f\left(\delta_s-1\right)\tilde{\alpha}_s^2\left(J_0\left(\tilde{\alpha}_s\right)+J_2\left(\tilde{\alpha}_s\right)\right)}{Y_f\alpha_o Z_o\tilde{\alpha}_{fs}\left(J_0\left(\tilde{\alpha}_s\right)-J_2\left(\tilde{\alpha}_s\right)\right)}\mathcal{W}'_{\mathrm{TEs}}\left(\tilde{\alpha}_{fs}\right) + \mathcal{W}_{\mathrm{TEs}}\left(\tilde{\alpha}_{fs}\right),$$

$$\mathrm{F4}_{s\,s} = \frac{j\alpha_s\left(\alpha_o^2-\alpha_f^2\right)\left(J_0\left(\tilde{\alpha}_s\right)+J_2\left(\tilde{\alpha}_s\right)\right)}{\alpha_o Z_o\tilde{\alpha}_{fs}^2\left(J_0\left(\tilde{\alpha}_s\right)-J_2\left(\tilde{\alpha}_s\right)\right)}\mathcal{W}_{\mathrm{TMs}}\left(\tilde{\alpha}_{fs}\right).$$

Table 2.11 recapitulates the matrix matching equations. We have 6 vector equations in 6 independent vector variables, the problem is formally solved and the coefficients $\mathbf{C}^{\mathrm{TM}}_{\mathbf{P\times 1}}$, $\mathbf{D}^{\mathrm{TM}}_{\mathbf{P\times 1}}$, $\mathbf{C}^{\mathrm{TE}}_{\mathbf{P\times 1}}$, $\mathbf{D}^{\mathrm{TE}}_{\mathbf{P\times 1}}$, $\mathbf{A}^{\mathrm{TM}}_{\mathbf{S\times 1}}$ and $\mathbf{A}^{\mathrm{TE}}_{\mathbf{S\times 1}}$ can be found.

| | |
|---|---|
| I) | $\mathbf{C}^{\mathrm{TM}}_{\mathbf{P\times 1}} = \mathrm{N1}_{P\times P}\cdot \mathrm{M1}_{P\times S}\cdot \mathbf{A}^{\mathrm{TM}}_{\mathbf{S\times 1}}$ |
| II) | $\mathbf{D}^{\mathrm{TM}}_{\mathbf{P\times 1}} = \mathrm{N1}_{P\times P}\cdot \mathrm{M1}_{P\times S}\cdot \mathrm{II}_{S\times S}\cdot \mathbf{A}^{\mathrm{TM}}_{\mathbf{S\times 1}}$ |
| III) | $\mathbf{C}^{\mathrm{TE}}_{\mathbf{P\times 1}} = \mathrm{N2}_{P\times P}\cdot \mathrm{M2}_{P\times S}\cdot \mathbf{A}^{\mathrm{TE}}_{\mathbf{S\times 1}} + \mathrm{N2}_{P\times P}\cdot \mathrm{M3}_{P\times S}\cdot \mathbf{A}^{\mathrm{TM}}_{\mathbf{S\times 1}}$ |
| IV) | $\mathbf{D}^{\mathrm{TE}}_{\mathbf{P\times 1}} = \mathrm{N2}_{P\times P}\cdot \mathrm{M2}_{P\times S}\cdot \mathrm{II}_{S\times S}\cdot \mathbf{A}^{\mathrm{TE}}_{\mathbf{S\times 1}} + \mathrm{N2}_{P\times P}\cdot \mathrm{M3}_{P\times S}\cdot \mathrm{II}_{S\times S}\cdot \mathbf{A}^{\mathrm{TM}}_{\mathbf{S\times 1}}$ |
| V) | $\mathrm{F1}_{S\times S}\cdot \mathbf{A}^{\mathrm{TE}}_{\mathbf{S\times 1}} + \mathrm{F2}_{S\times S}\cdot \mathbf{A}^{\mathrm{TM}}_{\mathbf{S\times 1}} - (\mathrm{T1}_{S\times S}\cdot \mathrm{G1}_{S\times P} + \mathrm{T2}_{S\times S}\cdot \mathrm{G2}_{S\times P})\cdot \mathbf{C}^{\mathrm{TE}}_{\mathbf{P\times 1}} +$ $+\mathrm{II}_{S\times S}\cdot (\mathrm{T1}_{S\times S}\cdot \mathrm{G1}_{S\times P} + \mathrm{T2}_{S\times S}\cdot \mathrm{G2}_{S\times P})\cdot \mathbf{D}^{\mathrm{TE}}_{\mathbf{P\times 1}} + \mathrm{T3}_{S\times S}\cdot \mathrm{G3}_{S\times P}\cdot \mathbf{C}^{\mathrm{TM}}_{\mathbf{P\times 1}} +$ $+\mathrm{II}_{S\times S}\cdot \mathrm{T3}_{S\times S}\cdot \mathrm{G3}_{S\times P}\cdot \mathbf{D}^{\mathrm{TM}}_{\mathbf{P\times 1}} + \mathrm{B}_{S\times 1} = 0$ |
| VI) | $\mathrm{F3}_{S\times S}\cdot \mathbf{A}^{\mathrm{TE}}_{\mathbf{S\times 1}} + \mathrm{F4}_{S\times S}\cdot \mathbf{A}^{\mathrm{TM}}_{\mathbf{S\times 1}} - (\mathrm{T4}_{S\times S}\cdot \mathrm{G4}_{S\times P} - \mathrm{T5}_{S\times S}\cdot \mathrm{G5}_{S\times P})\cdot \mathbf{C}^{\mathrm{TE}}_{\mathbf{P\times 1}} +$ $+\mathrm{II}_{S\times S}\cdot (\mathrm{T4}_{S\times S}\cdot \mathrm{G4}_{S\times P} - \mathrm{T5}_{S\times S}\cdot \mathrm{G5}_{S\times P})\cdot \mathbf{D}^{\mathrm{TE}}_{\mathbf{P\times 1}} = 0$ |

Table 2.11: Transverse vector matching equations.

### 2.4.4 Impedance calculation

In the longitudinal case, the impedance can be calculated by means of Eq. (2.17). Dividing the calculation for the 3 sub-domains I, II and IV, we have

$$Z_l(\omega) = -\frac{1}{Q}\int_{-\infty}^{+\infty} \mathrm{d}z\, e^{j\alpha_b z/b} E_z = -\frac{1}{Q}\int_{-\infty}^{0} \mathrm{d}z\, e^{j\alpha_b z/b} E_z^{(I)} - \frac{1}{Q}\int_{0}^{L} \mathrm{d}z\, e^{j\alpha_b z/b} E_z^{(IV)} - \frac{1}{Q}\int_{L}^{+\infty} \mathrm{d}z\, e^{j\alpha_b z/b} E_z^{(II)}. \tag{2.82}$$

Here we only consider the scattered fields produced by the longitudinal source current of Tab. 2.3. For $r_S = 0$ we can simplify the source matrix $\mathrm{B}_{s\,1}$ since $I_0(s) = 1$ and we can normalize over the charge $Q$. In sub-domain I we have:

$$Z_l^{(I)}(\omega) = -\int_{-\infty}^{0} \mathrm{d}z\, e^{j\alpha_b z/b} \sum_{p=1}^{\infty} \mathbf{C}^{\mathrm{TM}}_{\mathbf{p}}\, E^{(I)}_{z_p} = -\sum_{p=1}^{\infty}\left(\int_{-\infty}^{0} \mathrm{d}z\, e^{j\alpha_b z/b}\, \mathbf{C}^{\mathrm{TM}}_{\mathbf{p}}\, E^{(I)}_{z_p}\right).$$

Substituting $E^{(I)}_{z_p}$ from Tab. 2.6 and integrating, we get

$$Z_l^{(I)}(\omega) = -\sum_{p=1}^{\infty} \frac{jb\,\mathbf{C}^{\mathrm{TM}}_{\mathbf{p}}}{\sqrt{\pi}\alpha_p J_1(\alpha_p)(\tilde{\alpha}_p + \alpha_b)}.$$

Truncating at $p_{max} = P$ the number of radial modes we have

$$Z_l^{(I)}(\omega) = Z^{I,C_{\mathrm{TM}}}_{1\times P}\cdot \mathbf{C}^{\mathrm{TM}}_{\mathbf{P\times 1}}, \tag{2.83}$$

where we defined the matrix element

$$Z^{I,C_{\mathrm{TM}}}_{1\,p} = \frac{j\,b}{\sqrt{\pi}\alpha_p J_1(\alpha_p)(\tilde{\alpha}_p + \alpha_b)}. \tag{2.84}$$

Analogously, in sub-domain II we have

$$Z_l^{(II)}(\omega) = Z^{II,D_{\mathrm{TM}}}_{1\times P}\cdot \mathbf{D}^{\mathrm{TM}}_{\mathbf{P\times 1}}, \tag{2.85}$$

with matrix element

$$Z^{II,D_{\mathrm{TM}}}_{1\,p} = -\frac{j\,b\,e^{\frac{jL\alpha_b}{b}}}{\sqrt{\pi}\alpha_p J_1(\alpha_p)(\alpha_b - \tilde{\alpha}_p)}. \tag{2.86}$$

In the cavity sub-domain IV we have

$$Z_l^{(IV)}(\omega) = -\sum_{p\,s}^{\infty}\left(\int_0^L \mathrm{d}z\, e^{j\alpha_b z/b}\,\mathbf{V}^{\mathrm{TM}}_{\mathbf{p\,s}}\, e^{(IV)}_{z_{p\,s}}\right).$$

We can pass from the $\mathbf{V}^{\mathrm{TM}}_{\mathbf{p\,s}}$ to the $\mathbf{I}^{\mathrm{TM}}_{\mathbf{p\,s}}$ coefficients applying Eq. (2.57). Separating the radial $p$ and longitudinal $s$ indexes dependence by means of Eq. (2.75), the impedance $Z_l^{(IV)}(\omega)$ can be split into 3 contributions as function of $\mathbf{C}^{\mathrm{TM}}_{\mathbf{p}}$, $\mathbf{D}^{\mathrm{TM}}_{\mathbf{p}}$ and $\mathbf{A}^{\mathrm{TM}}_{\mathbf{s}}$. Summing in $p$ with Eq. (A.6) and $s$ with Eqs. (A.3) and (A.4), we get

$$Z_l^{(IV)}(\omega) = Z^{IV,C_{\mathrm{TM}}}_{1\times P}\cdot\mathbf{C}^{\mathrm{TM}}_{\mathbf{P}\times\mathbf{1}} + Z^{IV,D_{\mathrm{TM}}}_{1\times P}\cdot\mathbf{D}^{\mathrm{TM}}_{\mathbf{P}\times\mathbf{1}} + Z^{IV,A_{\mathrm{TM}}}_{1\times S}\cdot\mathbf{A}^{\mathrm{TM}}_{\mathbf{S}\times\mathbf{1}}, \tag{2.87}$$

where we truncated at $p_{max} = P$ and $s_{max} = S$. The matrix elements are

$$Z^{IV,C_{\mathrm{TM}}}_{1\,p} = \frac{b\left(\alpha_b \csc\left(\frac{L\tilde{\alpha}_p}{b}\right)\left(\cos\left(\frac{L\tilde{\alpha}_p}{b}\right) - e^{\frac{jL\alpha_b}{b}}\right) + j\tilde{\alpha}_p\right)}{\sqrt{\pi}\alpha_p J_1(\alpha_p)\left(\alpha_b^2 - \tilde{\alpha}_p^2\right)}, \tag{2.88}$$

$$Z^{IV,D_{\mathrm{TM}}}_{1\,p} = -\frac{b\left(\alpha_b \csc\left(\frac{L\tilde{\alpha}_p}{b}\right)\left(e^{\frac{jL\alpha_b}{b}}\cos\left(\frac{L\tilde{\alpha}_p}{b}\right) - 1\right) - j\tilde{\alpha}_p\, e^{\frac{jL\alpha_b}{b}}\right)}{\sqrt{\pi}\alpha_p J_1(\alpha_p)\left(\alpha_b^2 - \tilde{\alpha}_p^2\right)}, \tag{2.89}$$

$$Z^{IV,A_{\mathrm{TM}}}_{1\,s} = \frac{j\,b\,\alpha_b \mathcal{W}_{\mathrm{TMs}}(\tilde{\alpha}_{fs})\left((-1)^s e^{\frac{jL\alpha_b}{b}} - 1\right)}{\left(\alpha_b^2 - \alpha_s^2\right)\sqrt{\frac{L}{\epsilon_s}}\,J_0(\tilde{\alpha}_s)}. \tag{2.90}$$

The longitudinal impedance is therefore calculated summing the contribution of Eqs. (2.83), (2.85) and (2.87):

$$Z_l(\omega) = Z_l^{(I)}(\omega) + Z_l^{(II)}(\omega) + Z_l^{(IV)}(\omega). \tag{2.91}$$

The same procedure is followed to calculate the transverse dipolar impedance. From Eq. (2.21) we have

$$Z_{dip}(\omega) = \frac{j}{Q\,r_S}\int_{-\infty}^{+\infty}\mathrm{d}s\, e^{j\omega s/v}(E_r(r_S, r_T = 0, s, \omega) - \beta c\mu_0 H_\phi(r_S, r_T = 0, s, \omega)). \tag{2.92}$$

From now on we will consider a small source displacement, i.e. $r_S \to 0$, so that we can simplify the source matrix $\mathrm{B}_{s\,1}$ since $I_1(s)/r_S \to 1/2$ and we will normalize over the charge $Q$.
In sub-domain I we have

$$\begin{aligned} Z_{dip}^{(I)}(\omega) = {} & j\int_{-\infty}^{0}\mathrm{d}z\, e^{j\alpha_b z/b}\sum_{p=1}^{\infty}\mathbf{C}^{\mathrm{TM}}_{\mathbf{p}}\,(E^{(I,\mathrm{TM})}_{r_p} - \beta c\mu_0 H^{(I,\mathrm{TM})}_{\phi_p}) + \\ & + j\int_{-\infty}^{0}\mathrm{d}z\, e^{j\alpha_b z/b}\sum_{p=1}^{\infty}\mathbf{C}^{\mathrm{TE}}_{\mathbf{p}}\,(E^{(I,\mathrm{TE})}_{r_p} - \beta c\mu_0 H^{(I,\mathrm{TE})}_{\phi_p}). \end{aligned}$$

Substituting the fields components from Tabs. 2.7 and 2.8 and integrating, we get

$$Z_{dip}^{(I)}(\omega) = \sum_{p=1}^{\infty}\frac{jb\,\mathbf{C}^{\mathrm{TM}}_{\mathbf{p}}(\tilde{\alpha}_p + \beta\alpha_o)}{\sqrt{2\pi}\alpha_p^2 J_0(\alpha_p)(\tilde{\alpha}_p + \alpha_b)} + \sum_{p=1}^{\infty}\frac{-jb\,\mathbf{C}^{\mathrm{TE}}_{\mathbf{p}}\left(\beta\tilde{\beta}_p + \alpha_o\right)}{\sqrt{2\pi}Y_o\beta_p^2\sqrt{\beta_p^2 - 1}J_0(\beta_p)\left(\tilde{\beta}_p + \alpha_b\right)}. \tag{2.93}$$

Analogously we can do for sub-domain II getting

$$Z_{dip}^{(II)}(\omega) = \sum_{p=1}^{\infty}\frac{-jb\,\mathbf{D}^{\mathrm{TM}}_{\mathbf{p}}e^{\frac{jL\alpha_b}{b}}(\beta\alpha_o - \tilde{\alpha}_p)}{\sqrt{2\pi}\alpha_p^2 J_0(\alpha_p)(\alpha_b - \tilde{\alpha}_p)} + \sum_{p=1}^{\infty}\frac{jb\,\mathbf{D}^{\mathrm{TE}}_{\mathbf{p}}e^{\frac{jL\alpha_b}{b}}\left(\alpha_o - \beta\tilde{\beta}_p\right)}{\sqrt{2\pi}Y_o\beta_p^2\sqrt{\beta_p^2 - 1}J_0(\beta_p)\left(\alpha_b - \tilde{\beta}_p\right)} \tag{2.94}$$

Truncating at $p_{max} = P$ radial modes we have

$$Z_{dip}^{(I)} = Z_{1\times P}^{C_{\mathrm{TM}}} \cdot \mathbf{C}_{\mathbf{P}\times\mathbf{1}}^{\mathrm{TM}} + Z_{1\times P}^{C_{\mathrm{TE}}} \cdot \mathbf{C}_{\mathbf{P}\times\mathbf{1}}^{\mathrm{TE}}, \tag{2.95}$$

$$Z_{dip}^{(II)} = Z_{1\times P}^{D_{\mathrm{TM}}} \cdot \mathbf{D}_{\mathbf{P}\times\mathbf{1}}^{\mathrm{TM}} + Z_{1\times P}^{D_{\mathrm{TE}}} \cdot \mathbf{D}_{\mathbf{P}\times\mathbf{1}}^{\mathrm{TE}}, \tag{2.96}$$

with matrix elements

$$Z_{1\,p}^{I,C_{\mathrm{TM}}} = \frac{jb\left(\tilde{\alpha}_p + \beta\alpha_o\right)}{\sqrt{2\pi}\alpha_p^2 J_0\left(\alpha_p\right)\left(\tilde{\alpha}_p + \alpha_b\right)}, \tag{2.97}$$

$$Z_{1\,p}^{I,C_{\mathrm{TE}}} = \frac{-jb\left(\beta\tilde{\beta}_p + \alpha_o\right)}{\sqrt{2\pi}Y_o\beta_p^2\sqrt{\beta_p^2-1}J_0\left(\beta_p\right)\left(\tilde{\beta}_p + \alpha_b\right)}, \tag{2.98}$$

$$Z_{1\,p}^{II,D_{\mathrm{TM}}} = \frac{-jb\,e^{\frac{jL\alpha_b}{b}}\left(\beta\alpha_o - \tilde{\alpha}_p\right)}{\sqrt{2\pi}\alpha_p^2 J_0\left(\alpha_p\right)\left(\alpha_b - \tilde{\alpha}_p\right)}, \tag{2.99}$$

$$Z_{1\,p}^{II,D_{\mathrm{TE}}} = \frac{jb\,e^{\frac{jL\alpha_b}{b}}\left(\alpha_o - \beta\tilde{\beta}_p\right)}{\sqrt{2\pi}Y_o\beta_p^2\sqrt{\beta_p^2-1}J_0\left(\beta_p\right)\left(\alpha_b - \tilde{\beta}_p\right)}. \tag{2.100}$$

In the cavity sub-domain IV, the fields are given by Eqs. (2.47) and (2.48). We will consider separately the contribution of TM, TE and irrotational modes to the impedance.
Starting from the TM contribution we have:

$$Z_{dip}^{(IV_{\mathrm{TM}})}(\omega) = \sum_{p\,s}^{\infty} j \int_0^L \mathrm{d}z\, e^{j\alpha_b z/b}\left(\mathbf{V}_{\mathbf{p}\mathbf{s}}^{\mathrm{TM}}\, e_{r_{p\,s}}^{(IV,\mathrm{TM})} - \beta Z_o \mathbf{I}_{\mathbf{p}\mathbf{s}}^{\mathrm{TM}}\, h_{\phi_{p\,s}}^{(IV,\mathrm{TM})}\right).$$

To solve this expression we can write the coefficients $\mathbf{V}_{\mathbf{p}\mathbf{s}}^{\mathrm{TM}}$ as function of $\mathbf{I}_{\mathbf{p}\mathbf{s}}^{\mathrm{TM}}$ resorting to Eq. (2.71) and substitute the $\mathbf{I}_{\mathbf{p}\mathbf{s}}^{\mathrm{TM}}$ by means of Eq. (2.74) in order to recollect the known coefficients $\mathbf{C}_{\mathbf{p}}^{\mathrm{TM}}$, $\mathbf{D}_{\mathbf{p}}^{\mathrm{TM}}$ and $\mathbf{A}_{\mathbf{s}}^{\mathrm{TM}}$. Substituting the field expressions from Tab. 2.9 and summing over the $p$ and $s$ indexes respectively using Eqs. (A.26), (A.13) and (A.14) we get

$$Z_{dip}^{(IV_{\mathrm{TM}})} = Z_{1\times P}^{IV_{\mathrm{TM}},C_{\mathrm{TM}}} \cdot \mathbf{C}_{\mathbf{P}\times\mathbf{1}}^{\mathrm{TM}} + Z_{1\times P}^{IV_{\mathrm{TM}},D_{\mathrm{TM}}} \cdot \mathbf{D}_{\mathbf{P}\times\mathbf{1}}^{\mathrm{TM}} + Z_{1\times S}^{IV_{\mathrm{TM}},A_{\mathrm{TM}}} \cdot \mathbf{A}_{\mathbf{S}\times\mathbf{1}}^{\mathrm{TM}},$$

where we truncated at $p_{max} = P$ and $s_{max} = S$. The matrix elements are

$$Z_{1\,p}^{IV_{\mathrm{TM}},C_{\mathrm{TM}}} = \frac{b\left(\alpha_b\alpha_p^2\left(-\cot\left(\frac{L\tilde{\alpha}_p}{b}\right) + e^{\frac{jL\alpha_b}{b}}\csc\left(\frac{L\tilde{\alpha}_p}{b}\right)\right) + j\tilde{\alpha}_p\left(\alpha_b^2 - \alpha_o^2\right)\right)}{\sqrt{2\pi}\alpha_b\alpha_p^2 J_2\left(\alpha_p\right)\left(\alpha_b^2 - \alpha_o^2 + \alpha_p^2\right)}, \tag{2.101}$$

$$Z_{1\,p}^{IV_{\mathrm{TM}},D_{\mathrm{TM}}} = \frac{b\left(j\tilde{\alpha}_p e^{\frac{jL\alpha_b}{b}}\left(\alpha_b^2 - \alpha_o^2\right) + \alpha_b\alpha_p^2\left(-\csc\left(\frac{L\tilde{\alpha}_p}{b}\right) + e^{\frac{jL\alpha_b}{b}}\cot\left(\frac{L\tilde{\alpha}_p}{b}\right)\right)\right)}{\sqrt{2\pi}\alpha_b\alpha_p^2 J_2\left(\alpha_p\right)\left(\alpha_b^2 - \alpha_o^2 + \alpha_p^2\right)}, \tag{2.102}$$

$$Z_{1\,s}^{IV_{\mathrm{TM}},A_{\mathrm{TM}}} = \frac{jb\left(-1 + (-1)^s e^{\frac{jL\alpha_b}{b}}\right)}{\left(\alpha_b^2 - \alpha_s^2\right)\sqrt{\frac{L}{\epsilon_s}}}\left(\frac{\tilde{\alpha}_s}{2J_1\left(\tilde{\alpha}_s\right)} - 1\right)\mathcal{W}_{\mathrm{TMs}}\left(\tilde{\alpha}_{fs}\right). \tag{2.103}$$

In a similar way we can derive the TE contribution

$$Z_{dip}^{(IV_{\mathrm{TE}})}(\omega) = \sum_{p\,s}^{\infty} j \int_0^L \mathrm{d}z\, e^{j\alpha_b z/b}\left(\mathbf{V}_{\mathbf{p}\mathbf{s}}^{\mathrm{TE}}\, e_{r_{p\,s}}^{(IV,\mathrm{TE})} - \beta Z_o \mathbf{I}_{\mathbf{p}\mathbf{s}}^{\mathrm{TE}}\, h_{\phi_{p\,s}}^{(IV,\mathrm{TE})}\right).$$

The $\mathbf{V}_{\mathbf{p}\mathbf{s}}^{\mathrm{TE}}$ coefficients can be expressed in function of $\mathbf{I}_{\mathbf{p}\mathbf{s}}^{\mathrm{TE}}$ resorting to Eq. (2.73) and we can substitute the $\mathbf{I}_{\mathbf{p}\mathbf{s}}^{\mathrm{TE}}$ by means of Eq. (2.75) in order to recollect the known coefficients $\mathbf{C}_{\mathbf{p}}^{\mathrm{TE}}$, $\mathbf{D}_{\mathbf{p}}^{\mathrm{TE}}$, $\mathbf{A}_{\mathbf{s}}^{\mathrm{TM}}$, and $\mathbf{A}_{\mathbf{s}}^{\mathrm{TE}}$. We get:

$$Z_{dip}^{(IV_{\mathrm{TE}})} = Z_{1\times P}^{IV_{\mathrm{TE}},C_{\mathrm{TE}}} \cdot \mathbf{C}_{\mathbf{P}\times\mathbf{1}}^{\mathrm{TE}} + Z_{1\times P}^{IV_{\mathrm{TE}},D_{\mathrm{TE}}} \cdot \mathbf{D}_{\mathbf{P}\times\mathbf{1}}^{\mathrm{TE}} + Z_{1\times S}^{IV_{\mathrm{TE}},A_{\mathrm{TM}}} \cdot \mathbf{A}_{\mathbf{S}\times\mathbf{1}}^{\mathrm{TM}} + + Z_{1\times S}^{IV_{\mathrm{TE}},A_{\mathrm{TE}}} \cdot \mathbf{A}_{\mathbf{S}\times\mathbf{1}}^{\mathrm{TE}}.$$

It may be interesting to notice the presence of the cross-coupling term $\mathbf{A_s^{TM}}$. Substituting the field expressions and summing over the $p$ and $s$ index using Eqs. (A.27), (A.28), (A.15) and (A.16) we get

$$Z_{1\,p}^{IV_{\mathrm{TE}},C_{\mathrm{TE}}} = \frac{b\sqrt{L}\alpha_o\left(j\alpha_b + \beta_p \mathrm{csch}\left(\frac{L\beta_p}{b}\right)\left(\cosh\left(\frac{L\beta_p}{b}\right) - e^{\frac{jL\alpha_b}{b}}\right)\right)}{\sqrt{2\pi}Y_o\beta_p^2\sqrt{L\left(\beta_p^2-1\right)}J_0\left(\beta_p\right)\left(\alpha_b^2+\beta_p^2\right)}, \tag{2.104}$$

$$Z_{1\,p}^{IV_{\mathrm{TE}},D_{\mathrm{TE}}} = -\frac{b\alpha_o\left(L\beta_p \mathrm{csch}\left(\frac{L\beta_p}{b}\right) + jLe^{\frac{jL\alpha_b}{b}}\left(\alpha_b + j\beta_p\coth\left(\frac{L\beta_p}{b}\right)\right)\right)}{\sqrt{2\pi}\sqrt{L}Y_o\beta_p^2\sqrt{L\left(\beta_p^2-1\right)}J_0\left(\beta_p\right)\left(\alpha_b^2+\beta_p^2\right)}, \tag{2.105}$$

$$Z_{1\,s}^{IV_{\mathrm{TE}},A_{\mathrm{TE}}} = \frac{\sqrt{2}b\alpha_f\alpha_s\left(\delta_{\mathrm{s0}}-1\right)\left(-1+(-1)^s e^{\frac{jL\alpha_b}{b}}\right)\mathcal{W}'_{\mathrm{TEs}}\left(\tilde{\alpha}_{fs}\right)}{\sqrt{L}Y_f\left(\alpha_s^2-\alpha_b^2\right)\left(I_0\left(\alpha_s\right)+I_2\left(\alpha_s\right)\right)\tilde{\alpha}_{fs}}, \tag{2.106}$$

$$Z_{1\,s}^{IV_{\mathrm{TE}},A_{\mathrm{TM}}} = \frac{jb\sqrt{\epsilon_s}\left(-1+(-1)^s e^{\frac{jL\alpha_b}{b}}\right)\left(\alpha_f^2\left(\frac{1}{I_0(\alpha_s)+I_2(\alpha_s)}-1\right)+\alpha_s^2\right)\mathcal{W}_{\mathrm{TMs}}\left(\tilde{\alpha}_{fs}\right)}{\sqrt{L}\left(\alpha_b^2-\alpha_s^2\right)\tilde{\alpha}_{fs}^2}. \tag{2.107}$$

The last impedance term is the one coming from the irrotational modes. Since we found $\mathbf{F_{ps}} = 0$, we will calculate only the contribution from the modes H, i.e. involving the $\mathbf{G_{ps}}$ coefficients. We have:

$$Z_{dip}^{(IV_H)}(\omega) = \sum_{p\,s}^{\infty} j\int_0^L \mathrm{d}z\, e^{j\alpha_b z/b}\left(-\beta Z_o \mathbf{G_{ps}}\, g_{\phi_{p\,s}}\right).$$

Substituting Eq. (2.77) we can write $\mathbf{G_{ps}}$ as function of the known coefficients $\mathbf{C_p^{TE}}$, $\mathbf{D_p^{TE}}$, $\mathbf{A_s^{TM}}$, and $\mathbf{A_s^{TE}}$. We get:

$$Z_{dip}^{(IV_H)} = Z_{1\times P}^{IV_H,C_{\mathrm{TE}}}\cdot\mathbf{C^{TE}_{P\times 1}} + Z_{1\times P}^{IV_H,D_{\mathrm{TE}}}\cdot\mathbf{D^{TE}_{P\times 1}} + Z_{1\times S}^{IV_H,A_{\mathrm{TM}}}\cdot\mathbf{A^{TM}_{S\times 1}} + Z_{1\times S}^{IV_H,A_{\mathrm{TE}}}\cdot\mathbf{A^{TE}_{S\times 1}}.$$

Substituting the field expressions and summing over the $p$ and $s$ index using Eqs. (A.27), (A.17) and (A.18) we get

$$Z_{1\,p}^{IV_H,C_{\mathrm{TE}}} = \frac{b\alpha_o Z_o\left(\alpha_b \mathrm{csch}\left(\frac{L\beta_p}{b}\right)\left(-\cosh\left(\frac{L\beta_p}{b}\right)+e^{\frac{jL\alpha_b}{b}}\right)+j\beta_p\right)}{\sqrt{2\pi}\alpha_b\beta_p\sqrt{\beta_p^2-1}J_0\left(\beta_p\right)\left(\alpha_b^2+\beta_p^2\right)}, \tag{2.108}$$

$$Z_{1\,p}^{IV_H,D_{\mathrm{TE}}} = \frac{b\beta Z_o\left(\alpha_b \mathrm{csch}\left(\frac{L\beta_p}{b}\right) - e^{\frac{jL\alpha_b}{b}}\left(\alpha_b\coth\left(\frac{L\beta_p}{b}\right)+j\beta_p\right)\right)}{\sqrt{2\pi}\beta_p\sqrt{\beta_p^2-1}J_0\left(\beta_p\right)\left(\alpha_b^2+\beta_p^2\right)}, \tag{2.109}$$

$$Z_{1\,s}^{IV_H,A_{\mathrm{TE}}} = -\frac{b\beta^2\alpha_f\alpha_s\beta_s^2\epsilon_s\left(-1+(-1)^s e^{\frac{jL\alpha_o}{b\beta}}\right)\mathcal{W}'_{\mathrm{TEs}}\left(\tilde{\alpha}_{fs}\right)}{\sqrt{2}\sqrt{L}Y_f\left(2\beta_s I_1\left(\beta_s\right)-2\beta_s^2 I_0\left(\beta_s\right)\right)\tilde{\alpha}_{fs}\left(\beta^2\alpha_s^2-\alpha_o^2\right)}, \tag{2.110}$$

$$Z_{1\,s}^{IV_H,A_{\mathrm{TM}}} = -\frac{jb\beta\alpha_b\beta_s^2\epsilon_s\left(-1+(-1)^s e^{\frac{jL\alpha_b}{b}}\right)\left(\left(\delta_{\mathrm{s0}}+1\right)\tilde{\alpha}_{fs}^2+\alpha_s^2\right)\mathcal{W}_{\mathrm{TMs}}\left(\tilde{\alpha}_{fs}\right)}{2\alpha_o\left(\alpha_b^2-\alpha_s^2\right)\sqrt{\frac{L}{\epsilon_s}}\left(2\beta_s I_1\left(\beta_s\right)-2\beta_s^2 I_0\left(\beta_s\right)\right)\tilde{\alpha}_{fs}^2}. \tag{2.111}$$

The impedance can therefore be written as:

$$Z_{dip}(\omega) = Z_{dip}^{(I)}(\omega) + Z_{dip}^{(II)}(\omega) + Z_{dip}^{(IV_{\mathrm{TM}})}(\omega) + Z_{dip}^{(IV_{\mathrm{TE}})}(\omega) + Z_{dip}^{(IV_H)}(\omega). \tag{2.112}$$

## 2.5 Impedance benchmark and applications

In order to benchmark the procedure explained in the previous section for longitudinal and transverse impedance calculations, we will study the Mode Matching convergence as function of the matrix truncation parameters $S$ and $P$, as well as the computed impedance for different conductivities, length and thickness and finally the "resonant-like" behavior at cut-off. We will conclude

studying the behavior for non ultra relativistic beams. During the benchmark we will pay particular attention to those effects related to the device's *finite length*, i.e. that could not be studied within the usual *infinite length* approximation.

### 2.5.1 Convergence tests

The convergence of the Mode Matching depends on the number of longitudinal $S$ modes and radial $P$ modes used in the matrix computation. We defined $S$ and $P$ as the maximum number of longitudinal and radial cavity modes, differently from $s$ and $p$, longitudinal and radial mode indexes: once $S$ and $P$ are fixed, the modal index will be $p \in (1, \ldots, P)$ and $s \in (0, \ldots, S-1)$ for TM modes and $s \in (1, \ldots, S)$ for TE modes. This is also the convention implemented in the Matlab [27] code we implemented. A rule of thumb for a first estimation on the number of modes required to study a given structure is given by Eq. (2.113). Given the geometry in terms of beam pipe radius $b$, cavity thickness $t$ and insert length $L$ we can estimate the maximum number of modes $P$ and $S$ needed in order to reach the maximum frequency $f_{max}$ we are interested in simulating. Figure 2.5a shows the impedance calculation for the case of a resistive insert with

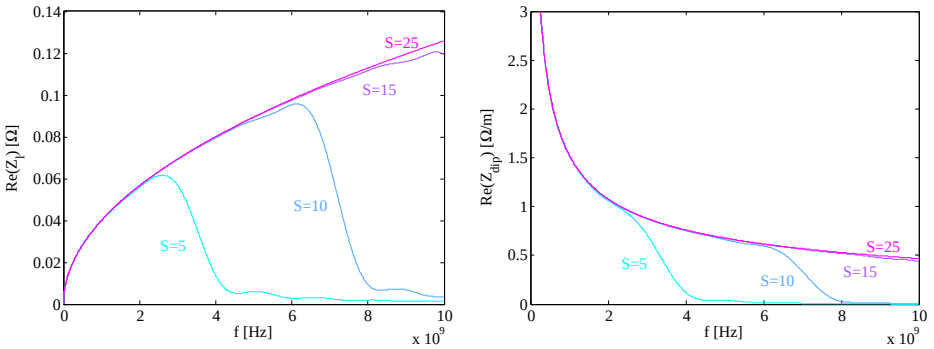


(a) (b)

Figure 2.5: Convergence of Mode Matching as a function of the number of longitudinal modes $S$, longitudinal (a) and transverse (b) case. Mode Matching parameters: $b = 5\,\text{cm}$, $t = 25\,\text{cm}$, $L = 20\,\text{cm}$, $\sigma_c = 10^6\,\text{S/m}$, $\beta = 1$.

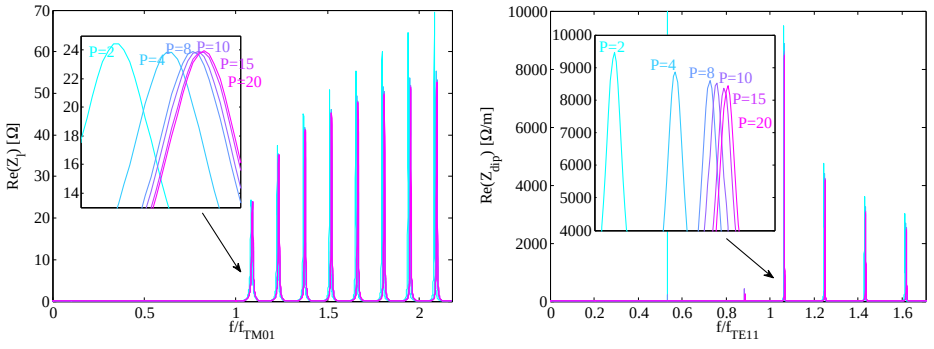


(a) (b)

Figure 2.6: Convergence of Mode Matching as a function of the number of longitudinal modes $P$, longitudinal (a) and transverse (b) case. Frequency is normalized over the first beam pipe propagating mode, the $\text{TM}_{01}$ in (a) and the $\text{TE}_{11}$ in (b). Mode Matching parameters: $b = 5\,\text{cm}$, $t = 45\,\text{cm}$, $L = 2\,\text{mm}$, $\sigma_c = 10^{-10}\,\text{S/m}$, $\beta = 1$.

$\sigma_c = 10^6\,\text{S/m}$. Different choices of $S$ are shown ($S$=5, 10, 15, 25) for the same number of radial modes ($P$=5). If, for example, we consider the case ($S$=5, $P$=5), the mode frequencies calculated

| $f_{0,p,s}$ | ss=1 | ss=2 | ss=3 | ss=4 | ss=5 |
|---|---|---|---|---|---|
| pp=1 | 0.3825 | 0.8414 | 1.547 | 2.2807 | 3.0222 |
| pp=2 | 0.8779 | 1.1543 | 1.7371 | 2.4138 | 3.1238 |
| pp=3 | 1.3763 | 1.5672 | 2.035 | 2.6362 | 3.2988 |
| pp=4 | 1.8754 | 2.0196 | 2.4008 | 2.9279 | 3.5362 |
| pp=5 | 2.3747 | 2.4902 | 2.8082 | 3.2703 | 3.8245 |

Table 2.12: Resonant frequencies (in GHz) excited for different number of modes $ss$ and $pp$.

with Eq. (2.113) are shown in Tab. 2.12. For $ss = pp = 5$, the maximum frequency $f_{max} = f_{0,5,4}$ can be seen at the bottom-right corner and is 3.8245 GHz: Figure 2.5a shows a "decay" in the impedance around $f_{max}$ as expected, sign of lack of modes.
Similar considerations hold for the transverse case. In case of S=25 we fully cover the frequency span we are interested in. It is interesting to note that, in this case, the number of radial modes P is not relevant since the current flows mainly on the insert surface and therefore radial resonances are not expected.
For low conductivity, resonant modes start to appear and the role of $P$ modes become evident. Figure 2.6 shows the case for a very narrow empty cavity ($\sigma_c = 10^{-10}\,\mathrm{S/m}$). In this case $S = 1$ is sufficient to cover the range of interest while, due to the thickness, we have to consider $P = 20$ in order to appreciate a reasonable convergence.

### 2.5.2 Empty cavity: mode excitation

As described in Sec. 2.4.1, the TM modes excited in the pillbox cavity have azimuthal number $\nu = 0$ for the longitudinal impedance, and are given by

$$f^{\mathrm{TM}}_{0,p,s} = \frac{c}{2\pi b}\sqrt{\alpha^2_{0,p} + \alpha^2_s}, \quad \text{with s}\in(0,1,\dots) \text{ and p}\in(1,2,\dots). \tag{2.113}$$

The TM and TE modes for the transverse dipolar impedance calculation ($\nu = 1$), are given by:

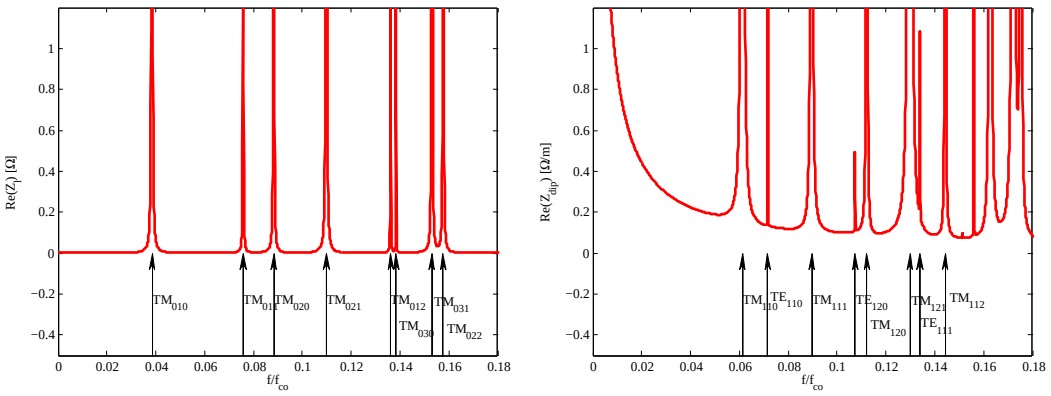


(a) (b)

Figure 2.7: (a) TM modes in longitudinal impedance and (b) TM and TE modes excited in the dipolar impedance. Mode Matching parameters: $b = 1\,\mathrm{cm}$, $t = 25\,\mathrm{cm}$, $L = 20\,\mathrm{cm}$, $\sigma_c = 10^{-7}\,\mathrm{S/m}$, $\beta = 1$, $P = 10$, $S = 10$.

$$f^{\mathrm{TM}}_{1,p,s} = \frac{c}{2\pi b}\sqrt{\alpha^2_{1,p} + \alpha^2_s}, \quad \text{with s}\in(0,1,\dots) \text{ and p}\in(1,2,\dots) \tag{2.114}$$

$$f^{\mathrm{TE}}_{1,p,s} = \frac{c}{2\pi b}\sqrt{\beta^2_{1,p} + \alpha^2_s}, \quad \text{with s}\in(1,2,\dots) \text{ and p}\in(1,2,\dots). \tag{2.115}$$

In order to perform this benchmark we choose a small beam pipe radius with respect to the cavity thickness ($b = 1\,\mathrm{cm}$ and $t = 25\,\mathrm{cm}$): in this way we can push the beam pipe cut-off

frequency $f_{co}$ well above the first cavity resonant mode avoiding the resonant frequency shift due to the coupling with the beam pipes. The conductivity $\sigma_c$, moreover, has been set to $\sigma_c = 10^{-7}\,\mathrm{S/m}$ in order to be able to appreciate the resonant shape in the real part of the impedance (a null conductivity would give rise to Dirac functions at resonant frequencies). Figure 2.7 shows the real part of the longitudinal and transverse dipolar impedance. Arrows are placed at the frequencies calculated with Eq. (2.113) for the longitudinal impedance, and Eqs. (2.114), (2.115) for the transverse one. A good agreement for the resonant frequency location is observed between these predictions and the mode matching modes.. We note that, even if in the transverse case the beam represents a TM-like excitation (there is no magnetic field component in z-direction), the TE modes are anyway excited. The slow impedance growth towards low frequencies is due to the fact that we had to choose a small, but non-zero, conductivity $\sigma_c$ in order to make the modes visible: this does not anyway affect the mode location whose frequency implies $\omega\varepsilon_0 >> \sigma_c$.

### 2.5.3 Empty cavity: low frequency

The case of empty cavity impedance represents a classical study already analyzed by other authors. In particular, here, we will compare the Mode Matching longitudinal and transverse impedance with formulas given in [23] for the low frequency regime.

The longitudinal impedance of an empty cavity, at low frequency can be approximated by

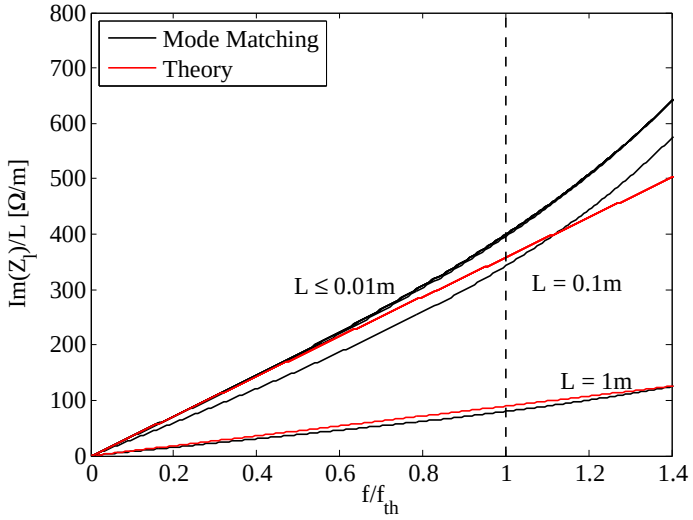


Figure 2.8: Comparison of Mode Matching with the classical low frequency longitudinal impedance behavior in an empty cavity. $f_{th} = \frac{c}{2\pi(b+t)}$. Mode Matching parameters: $b = 5\,\mathrm{cm}$, $t = 25\,\mathrm{cm}$, $L \in (10^{-6}, 10^{-5}, \ldots, 0.1, 1)\,\mathrm{m}$, $\sigma_c = 10^{-12}\,\mathrm{S/m}$, $\beta = 1$.

$$Z_l^{low.freq.} = \frac{j\,Z_o L\omega}{2\pi c}\ln\left(1+\frac{t}{b}\right), \quad \text{if } L << 2t, \tag{2.116}$$

$$Z_l^{low.freq.} = \frac{j\,Z_o t\omega}{2\pi c}\ln\left(1+\frac{t}{b}\right), \quad \text{if } L >> 2t. \tag{2.117}$$

The frequency regime in which we can apply the approximation is $f < f_{th} = c/(2\pi(b+t))$, i.e. below the first cavity resonant mode. Figure 2.8 shows the comparison of Mode Matching and Eqs. (2.116) and (2.117): the agreement is good below $f_{th}$ as expected, and we can distinguish the two cases correspondent to $L << 2t$ and $L >> 2t$. Since $2t = 50\,\mathrm{cm}$, when $L < 1\,\mathrm{cm}$ we are closer to Eq. (2.116), when $L < 1\,\mathrm{cm}$ we are closer to Eq. (2.117), while, for $L = 10\,\mathrm{cm}$ we are in an intermediate range in between the given formulas. We note that, for $L < 1\,\mathrm{cm}$ all the curves overlap being normalized over the insert length: in this range, therefore, the impedance scales linearly with length.

In the transverse case, the impedance at low frequency is [23]

$$Z_{dip}^{low.freq.} = -j\frac{Z_0 L}{\pi b^2}\frac{S^2-1}{S^2+1}, \tag{2.118}$$

valid for $L < \pi^2 \frac{b}{32}$ [28] and $f < f_{\mathrm{TM}_{010}}$ with $S = (b+t)/b$. Figure 2.9 shows the convergence to the theoretical value for small cavity length: from $L < 0.001$ the condition $L < \pi^2 \frac{b}{32}$ is fulfilled with 6% and Mode Matching and theory are closer. We note that at low frequency the impedance does not scale linearly with the insert length.

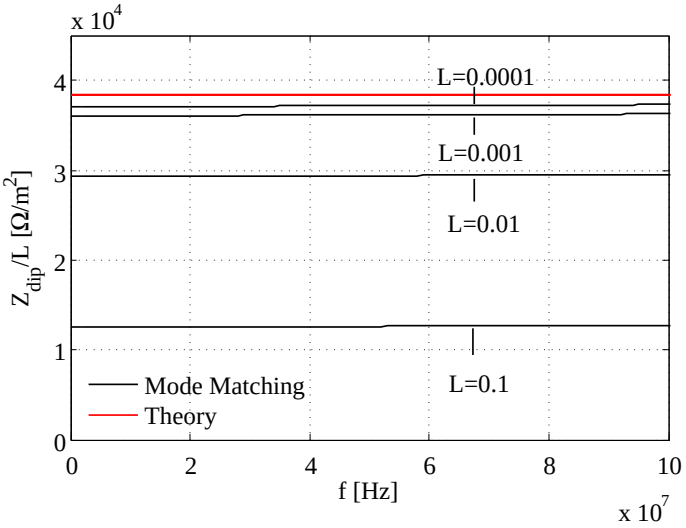


Figure 2.9: Comparison of Mode Matching with the classical low frequency longitudinal impedance behavior in an empty cavity. Mode Matching parameters: $b = 5\,\mathrm{cm}$, $t = 10\,\mathrm{cm}$, $L \in (10^{-4}, \ldots, 0.1)\,\mathrm{m}$, $\sigma_c = 10^{-12}\,\mathrm{S/m}$, $\beta = 1$.

### 2.5.4 Conductive insert: benchmark on length, thickness and conductivity

The list of benchmarks performed on a conductive insert can be summarized in Tab. 2.13. We

| Frequency range | $L > b, t < b$ | $L < b, t > b$ | $L < b, t < b$ | $L > b, t > b$ |
|---|---|---|---|---|
| $f < f_c\ ,\ f < f_{skin}$ | Rewall-LF | 2D-Axi | 2D-Axi | 2D-Axi |
| $f < f_c\ ,\ f > f_{skin}$ | Rewall-IF | Rewall-IF | SCT | Rewall-IF |
| $f > f_c$ | - | CST | TMT | CST |

Table 2.13: Table of benchmarks performed in order to test the Mode Matching with the finite length insert method for different frequency ranges and insert dimensions.

introduced the frequency parameters $f_c$, $f_{co}$ and $f_{skin}$. The parameter $f_c$ is the frequency limit at which a metal with a given conductivity $\sigma_c$ can be treated as a good conductor ($\sigma_c > \omega\varepsilon_0$) and is defined as

$$f_c = \frac{\sigma_c}{2\pi\varepsilon_0}. \tag{2.119}$$

We define $f_{co}$ as the beam pipe cut-off frequency and depends on the impedance under study: for the longitudinal impedance, only TM modes are excited and we define

$$f_{co}^{\mathrm{TM}} = \alpha_{0,1}\frac{c}{b}, \tag{2.120}$$

where $\alpha_{0,1} \simeq 2.4048$ is the eigenvalue correspondent to the $\mathrm{TM}_{01}$ propagating mode; for the transverse impedance, both TE and TM modes are excited and we define

$$f_{co}^{\mathrm{TE}} = \beta_{0,1} \frac{c}{b}, \tag{2.121}$$

where $\beta_{0,1} \simeq 1.8411$ is the eigenvalue correspondent to the $\mathrm{TE}_{11}$ propagating mode. The parameter $f_{skin}$ is the frequency at which the skin depth $\delta_{skin} = \sqrt{2/(\omega\mu\sigma_c)}$ equals the insert thickness $t$. It is important to notice that we can define a $f_{skin}$ only in the hypothesis of good conductor, i.e. $\sigma_c > \omega\varepsilon_0$ or $f < f_c$. "Rewall" refers to the classical thick wall impedance formulas derived in [9], [23] for intermediate frequencies IF ($f > f_{skin}$) and low frequencies LF ($f < f_{skin}$), "2D-Axi" refers to the numerical code for multilayer beam pipes developed in [13], "SCT" refers to the Shobuda-Chin-Takata model for the longitudinal impedance of small inserts [22], "TMT" refers to the trapped mode theory developed in [29], "CST" refers to the commercial time domain numerical simulator [10].

**Case $f < f_c$ and $t < b$, $L > b$**

For long devices and thin conducting layer the resistive wall theory can be applied both at LF and IF. The classical resistive wall formulas in these regimes are summarized in the following Tab. 2.14. Figure (2.10) shows the comparison between Mode Matching and the classical theory of resistive

| | LF | IF |
|---|---|---|
| $Z_l^{Rewall}$ | $\dfrac{j\,Z_o t\omega}{2\pi b\,c} L$ | $\dfrac{1+j}{2\pi b\,\sigma_c \delta_{skin}} L$ |
| $Z_{dip}^{Rewall}$ | $\dfrac{j\,Z_o t}{\pi b^3} L$ | $\dfrac{\beta c}{\omega} \dfrac{1+j}{\pi \sigma_c \delta_{skin} b^3} L$ |

Table 2.14: Classical resistive wall formulas as from [23].

wall impedance: the agreement is good within a wide range of frequencies and we can recover both the LF and IF regimes.

**Case $f < f_c$ and $t < b$, $L < b$**

Decreasing the insert length we can compare our model for longitudinal impedance with Shobuda-Chin-Takata's one (SCT) one. In the SCT's model the PEC boundary layer around the insert (the layer around sub-domain III in Fig. 2.4) is not present and the field can propagate in free space. Moreover, following the approximation of short insert length in the SCT theory, the longitudinal field variation along $\hat{z}_0$ has been neglected. The regime in which the two models are expected to agree is above $f_{skin}$. This behavior is shown in Fig. 2.11a where we compared the two models varying the conductivity from $\sigma_c \in (10^2\,\mathrm{S/m}, \ldots, 10^4\,\mathrm{S/m})$. Below the $f_{skin}$ the two models start to differ: in our case, the transverse field approaches the cavity's boundary and is reflected, in SCT it is radiated to the external vacuum region. From $f_{skin}$ the two models start to converge to the same impedance value. However, one may notice that the Mode Matching impedance slightly oscillates around SCT's one before converging to the same curve. A closer view of the oscillation can be obtained from Fig. 2.11b. The discrepancy between the two models can be understood considering that around $f_{skin}$ the skin depth is comparable with the insert thickness. This implies that the backward wave slightly interferes with the outgoing wave producing a modest standing wave pattern in the insert, therefore affecting the impedance. With increasing frequency, the backward wave amplitude becomes smaller and smaller and this pattern vanishes. The discrepancy at high frequency has to be compared with the impedance absolute value which becomes larger and larger.

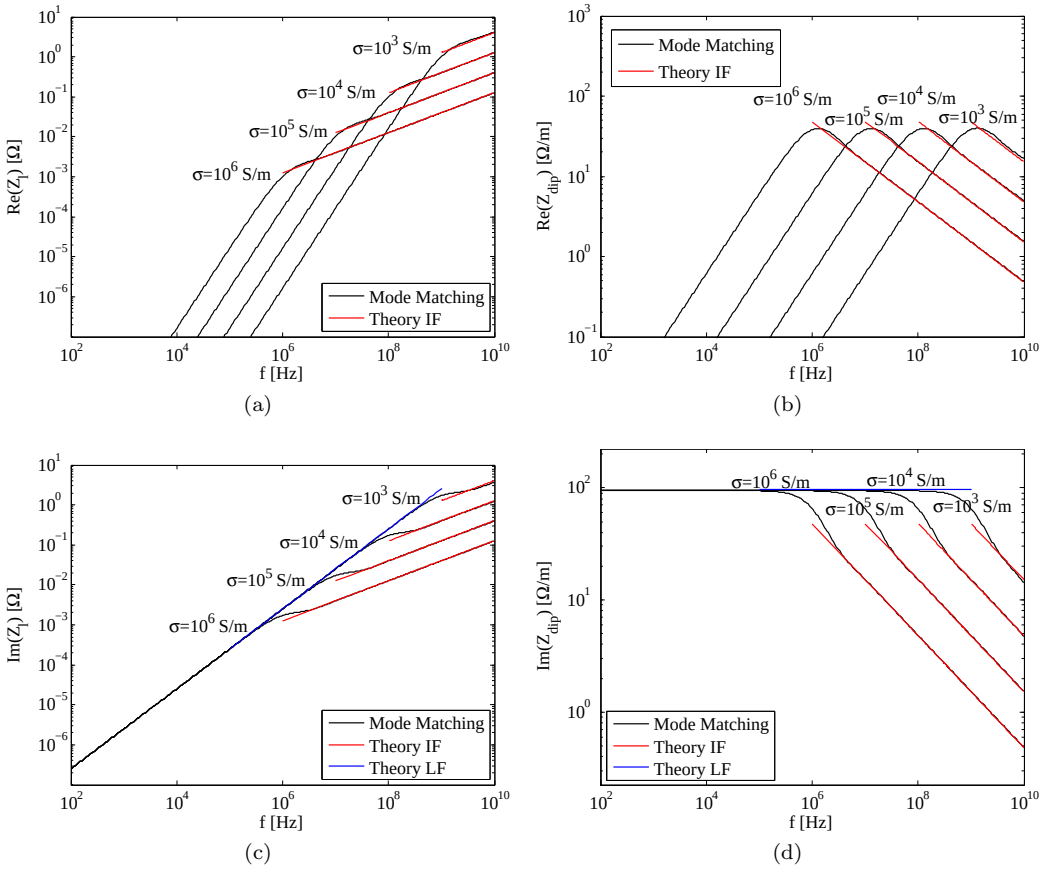


Figure 2.10: Comparison between Mode Matching and the classical theory of resistive wall, real (a) and imaginary (c) part of longitudinal impedance, real (b) and imaginary (d) part of transverse impedance. Mode Matching parameters: $b = 5\,\mathrm{cm}$, $t = 500\,\mu\mathrm{m}$, $L = 20\,\mathrm{cm}$, $\sigma_c \in (10^3, \ldots, 10^6)\,\mathrm{S/m}$, $\beta = 1$, $P = 10$, $S = 20$.

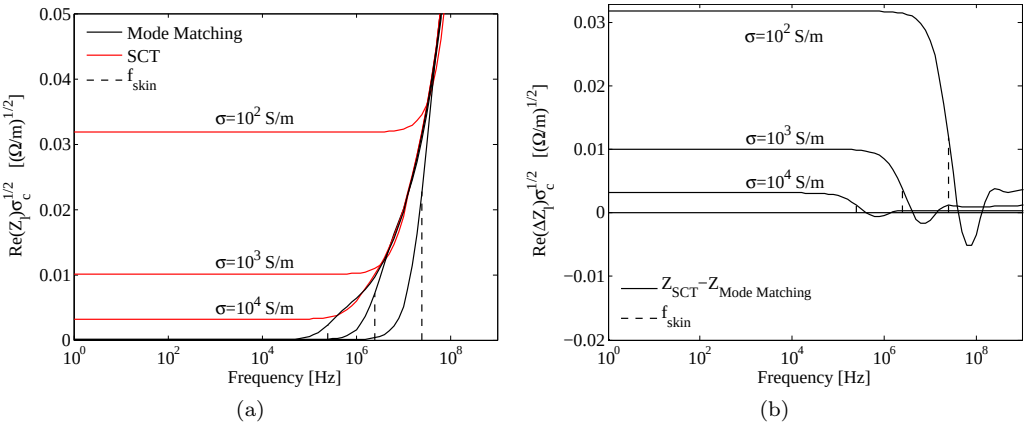


Figure 2.11: Comparison between Mode Matching and SCT model for longitudinal impedance of short inserts (a) and impedance model difference (c). Mode Matching parameters: $b = 5\,\mathrm{cm}$, $t = 1\,\mathrm{cm}$, $L = 0.1\,\mathrm{cm}$, $\sigma_c \in (10^2, \ldots, 10^4)\,\mathrm{S/m}$, $\beta = 1$, $P = 40$, $S = 40$.

### Case $f < f_c$ and $t > b$

In case the thickness becomes comparable or greater with respect to the beam pipe radius, the LF resistive wall formula does not hold any more since assumes $t << b$. In order to cover this

range of frequencies we can compare our model with the "2D-Axi" code. The code was developed at CERN in order to study multilayer beam pipes with particular attention to coatings and thin conducting layers commonly used for impedance and electron cloud mitigation. The model is developed within the *infinite length* approximation. Important notice is that "2D-Axi" does not allow for the moment PEC layers: in order to simulate our boundary condition we chose therefore an ideally highly conductive material with $\sigma_c = 10^{10}\,\mathrm{S/m}$ and infinite thickness.

When $L < b$, the transverse LF impedance in the Mode Matching *finite length* model becomes higher up to a factor 2 with respect to the 2D-Axi *infinite length* model, as shown for the imaginary part in Fig. 2.12. This effect, due to the fields at the edge of the structure, can be considered not of particular concern being apparent only for short inserts at very low frequencies ($10 - 100\,\mathrm{Hz}$).

No evidence of this effect is instead present in the longitudinal impedance as shown for the real part in Fig. 2.13. This is probably due to the small effect of the edges on the longitudinal electric field on axis $E_z$.

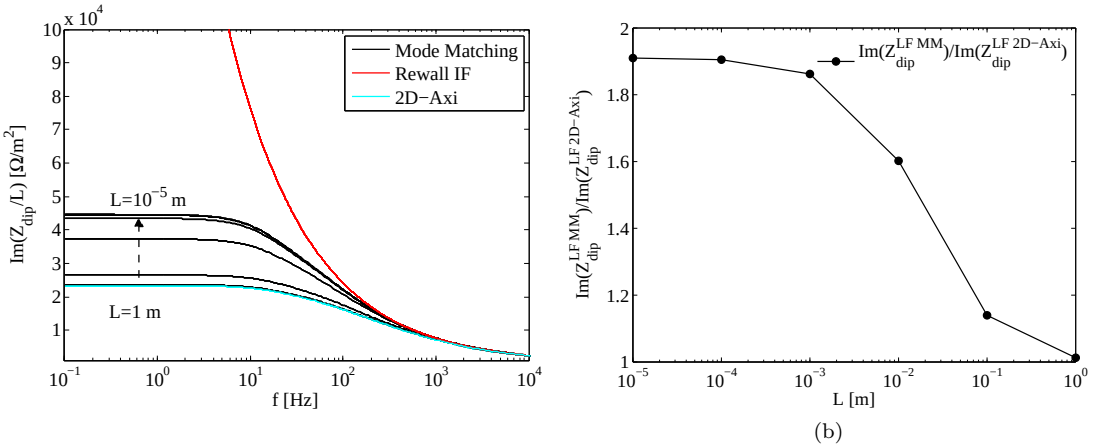


(b)

Figure 2.12: Comparison between Mode Matching and the 2D-Axi model for the imaginary part of the LF dipolar impedance. Mode Matching parameters: $b = 5\,\mathrm{cm}$, $t = 25\,\mathrm{cm}$, $\sigma_c = 10^6\,\mathrm{S/m}$, $\beta = 1$, $P = 10$, $S = 10$.

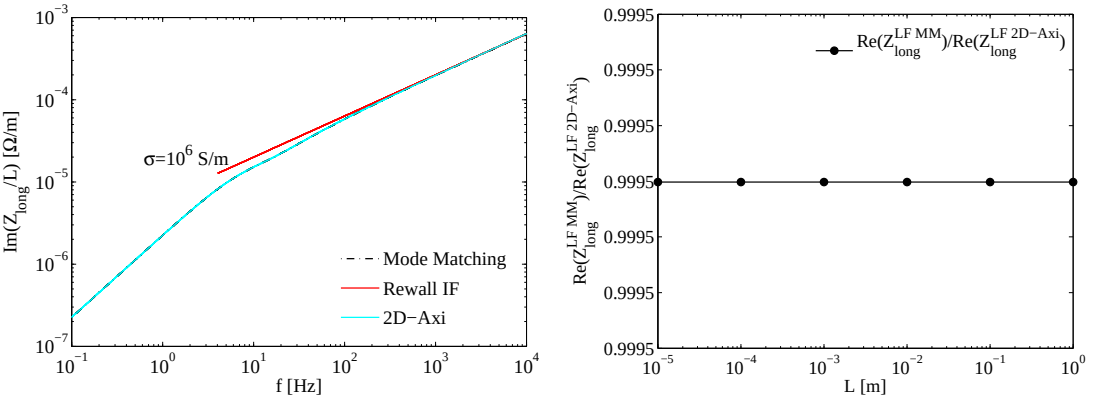


Figure 2.13: Comparison between Mode Matching and the 2D-Axi model for the real part of the LF longitudinal impedance. Mode Matching parameters: $b = 5\,\mathrm{cm}$, $t = 25\,\mathrm{cm}$, $\sigma_c = 10^6\,\mathrm{S/m}$, $\beta = 1$, $P = 10$, $S = 10$.

Highly conductive materials like copper or graphite are used in the LHC collimators (an example is shown in Fig. 2.14). These are one of the main impedance sources in the whole machine and efforts have been taken for their impedance reduction. One of the possible strategy consist in the device longitudinal segmentation in shorter modules [30]. Within the limitations of our model, by

the way, there is not an evident gain in impedance reduction as depicted in Fig. 2.12b.

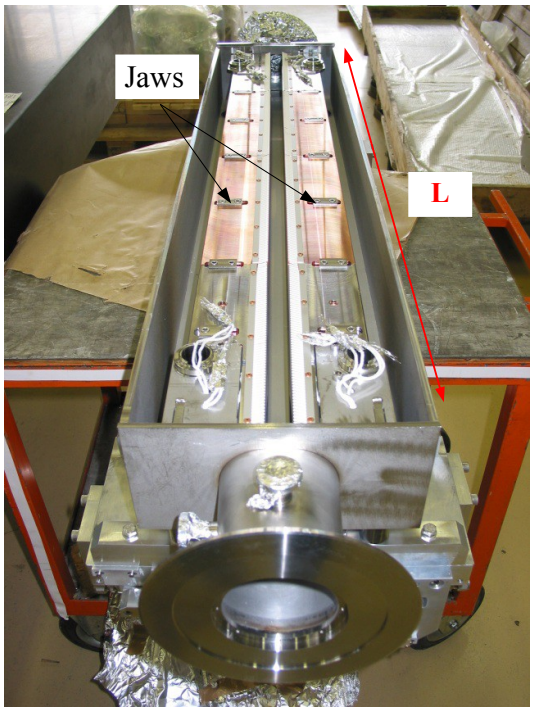


Figure 2.14: Example of collimator. The two jaws are made of highly conductive material and approach very closely the beam trajectory introducing high beam coupling impedance.

**Case $f > f_c$ and $L < b$, $t < b$**

Further reducing the cavity size, we can study the effect of small beam pipe perturbations to the longitudinal impedance. When the thickness $t$ and length $L$ are small with respect to the radius $b$, the first cavity resonant mode $\mathrm{TM}_{010}$ starts to approach the first beam pipe propagating mode $\mathrm{TM}_{01}$. This cavity resonance is usually defined as a "trapped mode" extending the definition of trapped modes to those ones slightly below cut-off [23]. The trapped mode frequency $f_{trap}$ can be estimated as $f_{trap} \simeq f_{\mathrm{TM}_{01}} + \Delta f_{\mathrm{TM}_{01}}$ with [29]

$$\Delta f_{\mathrm{TM}_{01}} = -f_{\mathrm{TM}_{01}} \frac{\alpha_{0,1}^2}{2} \left(\frac{A^2}{b}\right)^2, \tag{2.122}$$

where $A = L\,t$ is the longitudinal cross sectional area of the cavity. The approximation is found to be valid for $A\alpha_{0,1}^2/b^2 << 1$. In order to validate our method, we choose a series of cavity areas $A$, detect the trapped mode below cut-off, and compare with Eq. (2.122). Figure 2.15a shows the case of a longer than thicker cavity protrusion: the beam pipe radius is $b = 5\,\mathrm{cm}$, the thickness has been set to $2\,\mathrm{mm}$ and $L \in (1\,\mathrm{mm}, \ldots, 5\,\mathrm{cm})$. The agreement between theory and Mode Matching is good until the length of the cavity reaches the value of the beam pipe radius: longer cavities require the inclusion of higher order modes in the impedance calculation.

The case of a thicker than longer cavity discontinuity is shown in Fig. 2.15b where the length has been fixed to $2\,\mathrm{mm}$ and the thickness $t \in (1\,\mathrm{mm}, \ldots, 2\,\mathrm{cm})$. The agreement is good within a shorter range with respect to the previous case. This is due to the approximations used in [29] where the electric field dependence on the radial position is expressed as

$$E_z \propto J_0\left(\alpha_{0,1}\frac{r}{b}\right), \tag{2.123}$$

and at the boundary $r = c \simeq b$, at first order,

$$E_z \propto -\frac{\alpha_{0,1}}{b} J_1\left(\alpha_{0,1}\right) t. \tag{2.124}$$

For thickness close to the beam pipe radius ($t \simeq 1\,\text{cm}$ in our case), this approximation becomes inaccurate and the field penetration in the cavity space needs to be taken into account.

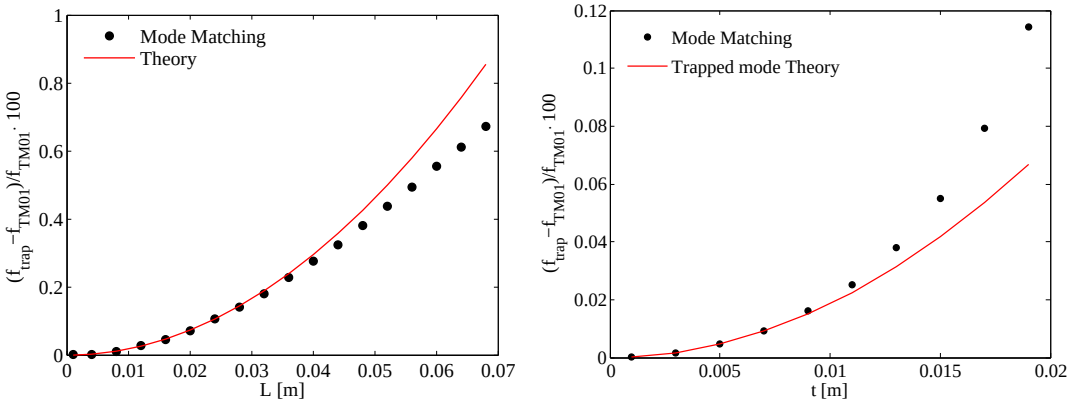


Figure 2.15: Comparison of trapped mode theory for longitudinal impedance and Mode Matching for (a) longer than thicker cavities, and (b) thicker than longer ones. Mode Matching parameters: $b = 5\,\text{cm}$, $\sigma_c = 10^{-8}\,\text{S/m}$, $\beta = 1$, $P = 5$, $S = 5$.

**Case $f > f_c$ and $L > b$, $t > b$**

In case of low conductivities, i.e. $\sigma_c \in \left(10^{-5}, \ldots, 10^{5}\right)\,\text{S/m}$, we can benchmark the Mode Matching with CST Particle Studio Wakefield Solver [10]. As already introduced in Sec. 2.2.1, CST is a time domain code in which a truncated Gaussian particle distribution $\rho(s)$ can be tracked along the device under test. The bunch length settles the maximum frequency simulated by means of Eq. (2.15). For example, with a bunch length of $\sigma_b = 3\,\text{cm}$ we can reach $f_{max} \simeq 3.5\,\text{GHz}$.

Figure 2.16 shows the Mode Matching benchmark with CST for $\sigma_c = 10^{-2}\,\text{S/m}$ both for longitudinal and transverse case. The agreement is good along the chosen frequency range even if

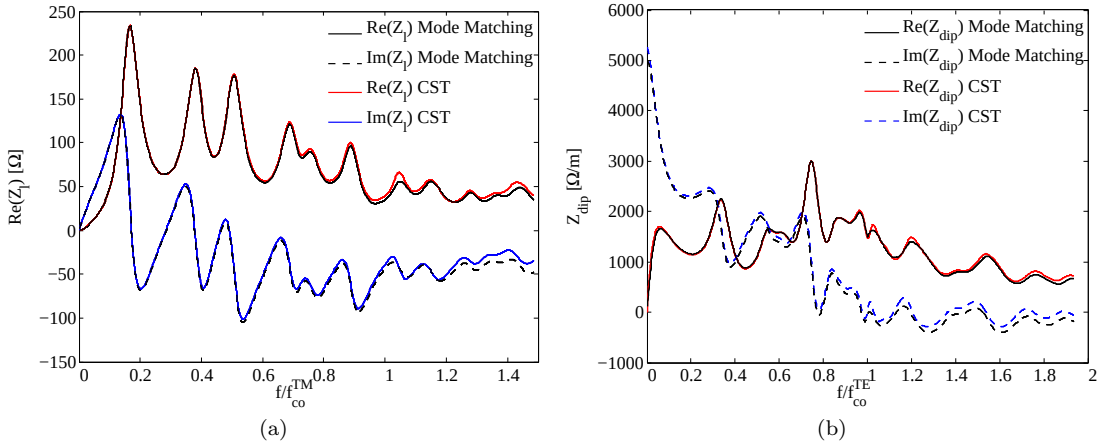


Figure 2.16: Comparison of Mode Matching and CST for (a) longitudinal and (b) transverse impedance. Mode Matching parameters: $b = 5\,\text{cm}$, $t = 25\,\text{cm}$, $L = 20\,\text{cm}$, $\sigma_c = 10^{-2}\,\text{S/m}$, $\beta = 1$, $P = 15$, $S = 15$. CST parameters: $\sigma_b = 3\,\text{cm}$, $L_{wake} = 20\,\text{m}$, $N_{mesh} = 1.1 \cdot 10^6$.

a small but increasing mismatch tends to appear for higher frequencies. This is due to the chosen bunch length: at $f_{max}$ the bunch power spectrum has reduced to 1% making the impedance more sensitive to the numerical noise. Choosing a smaller bunch length we can reduce this effect at the expense of a longer simulation time due to the increased mesh number necessary to sample

the bunch profile. Figure 2.17 shows the comparison between a $\sigma_b = 3\,\text{cm}$ and $\sigma_b = 2\,\text{cm}$ case. For lower conductivities, e.g. $\sigma_c = 10^{-3}$ in Fig. 2.18a, the losses in the insert get smaller when

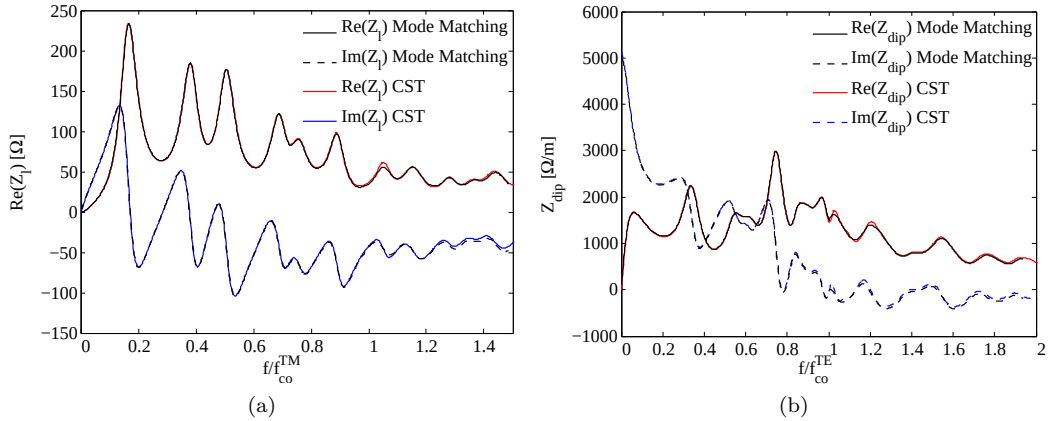


(a) (b)

Figure 2.17: Comparison of Mode Matching and CST for (a) longitudinal and (b) transverse impedance. Mode Matching parameters: $b = 5\,\text{cm}$, $t = 25\,\text{cm}$, $L = 20\,\text{cm}$, $\sigma_c = 10^{-2}\,\text{S/m}$, $\beta = 1$, $P = 15$, $S = 15$. CST parameters: $\sigma_b = 2\,\text{cm}$, $L_{wake} = 20\,\text{m}$, $N_{mesh} = 3.8 \cdot 10^6$.

the resonance height in the cavity structure increases. As explained in Sec. 2.2.1 the impedance calculated in CST is the Fourier transform of the wake potential induced by the bunch: if the wake oscillation is not completely damped, the typical *sinc*-like oscillations start to appear around the resonance frequencies. We therefore need a longer wake (i.e. longer simulation time) in order to bring the wake oscillation to the noise level and correctly model the resonance. Figure 2.18b shows the merit factor $Q$ convergence for the first resonant mode in function of the wake length: as we can see resonances for low conductivities are difficult to calculate in CST-PS. A more suitable solver for this purpose is the CST Eigenmode solver. The benchmark studies are therefore restricted to

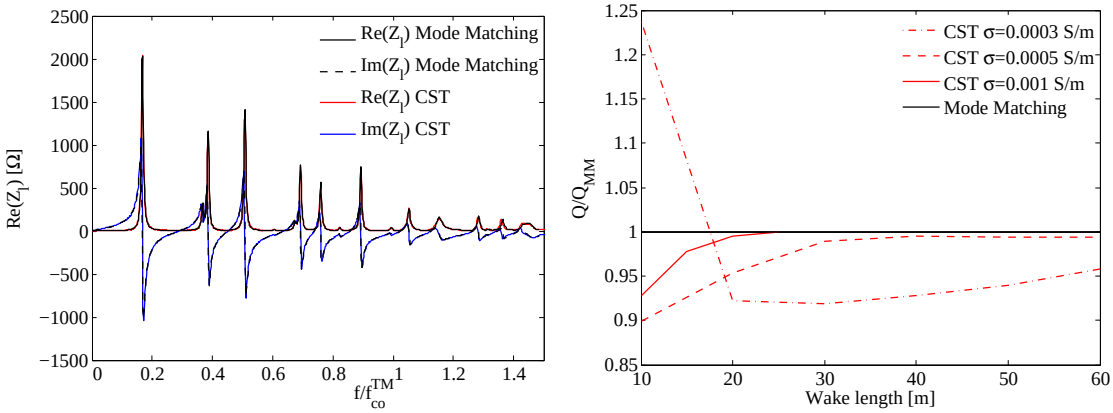


(a) (b)

Figure 2.18: Comparison of Mode Matching and CST for (a) longitudinal impedance with $\sigma_c = 10^{-3}\,\text{S/m}$ and (b) Q saturation of first impedance peak Vs simulated wake length for lower conductivities. Mode Matching parameters: $b = 5\,\text{cm}$, $t = 25\,\text{cm}$, $L = 20\,\text{cm}$, $\beta = 1$, $P = 15$, $S = 15$. CST parameters: $\sigma_b = 2\,\text{cm}$, $N_{mesh} = 3.8 \cdot 10^6$

a short range of conductivities: if in the lower bound we are limited by the wake length to simulate in order to cover the resonance damping time, for higher conductivities the wake field becomes smaller and closer to the CST numerical noise. As an example we simulated a conductivity of $\sigma_c = 10^2\,\text{S/m}$: as shown in Fig. 2.19 a considerable discrepancy appears due to the small wake potential amplitude.

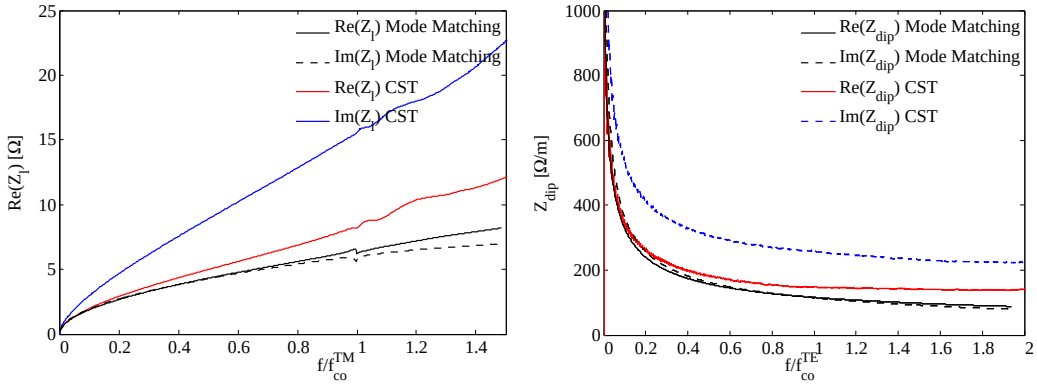


(a) (b)

Figure 2.19: Comparison of Mode Matching and CST for (a) longitudinal and (b) transverse impedance. Mode Matching parameters: $b = 5\,\text{cm}$, $t = 25\,\text{cm}$, $L = 20\,\text{cm}$, $\sigma_c = 10^2\,\text{S/m}$, $\beta = 1$, $P = 15$, $S = 15$. CST parameters: $\sigma_b = 2\,\text{cm}$, $L_{wake} = 20\,\text{m}$, $N_{mesh} = 3.8 \cdot 10^6$.

**Case $f > f_c$ and $L < b$, $t > b$)**

For short inserts and low conductivities we can compare our results with CST. Analogously to what was done in Sec. 2.5.3 we can simulate a narrow insertion at low frequencies. Since we are interested in low frequencies we can increase the bunch length to 20 cm to cover a range up to 350 MHz. Figure 2.20 shows a comparison with Mode Matching for different cavity length: the agreement is good within a 5% of accuracy.

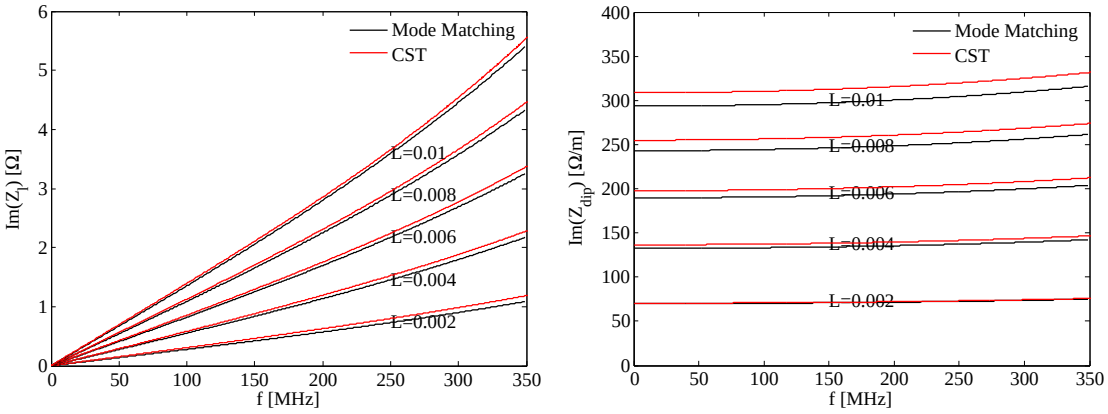


(a) (b)

Figure 2.20: Comparison of Mode Matching and CST for low frequencies and short inserts impedance. Mode Matching parameters: $b = 5\,\text{cm}$, $t = 10\,\text{cm}$, $\sigma = 10^{-8}\,\text{S/m}$, $\beta = 1$, P=5, S=5. CST parameters: $\sigma_b = 20\,\text{cm}$, $L_{wake} = 1\,\text{m}$, $N_{mesh} = 2.3 \cdot 10^6$.

### 2.5.5 Impedance kink at cut-off

An interesting effect we are going to separately explain, is the resonance-like kink appearing around the cut-off frequency for short inserts. The impedance of a circular resistive insert can be studied, in first approximation, with a 2D model, i.e. assuming infinite length and scaling the impedance per meter to the device length [7], [25]. We have already shown that the approximation is not valid for good conductors ($f < f_c$) when the insert length $L$ is smaller than the beam pipe radius $b$ in the low frequencies regime, and intuitively for dielectrics ($f > f_c$) where longitudinal resonances depend on the device length. Independently on the conductivity, when $L < \lambda_{co}/2$ with $\lambda_{co} = c/f_{co}$ wavelength at cut-off frequencies, we can have a resonance-like peak just below the cut-off frequency. Figure 2.21 shows a longitudinal impedance kink at the first cut-off frequency mode $\mathrm{TM}_{01}$. For lower conductivities the effect becomes more evident. It is interesting to notice, for example in Fig. 2.22, that the kink amplitude at cut-off frequency can also vanish if it is placed in correspondence to the descending slope of the nearby resonance.

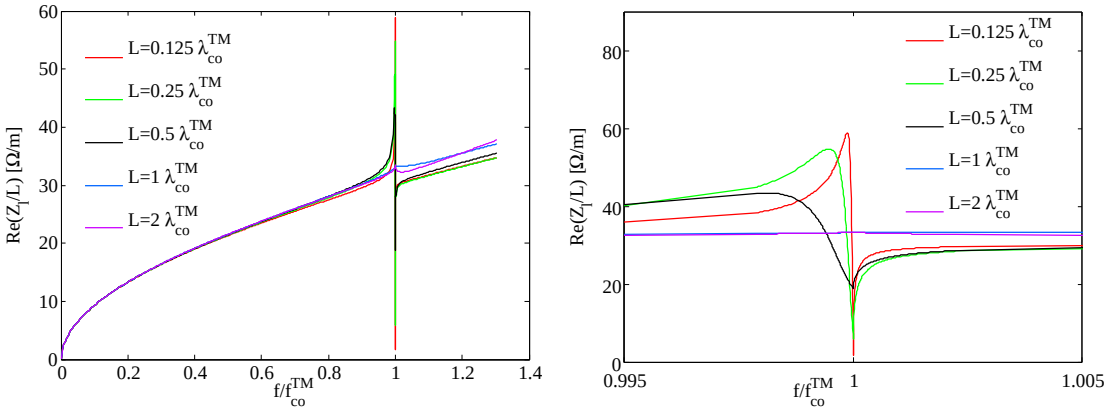


Figure 2.21: Kink in the longitudinal impedance at the $\mathrm{TM}_{01}$ mode cut-off frequency (a) and zoomed view around cut-off (b). Mode Matching parameters: $b = 5\,\mathrm{cm}$, $t = 25\,\mathrm{cm}$, $L \in (1/8, 1/4, 1/2, 1, 2)\lambda_{co}^{\mathrm{TM}}$, $\sigma = 10^2\,\mathrm{S/m}$, $\beta = 1$, P=5, S=25.

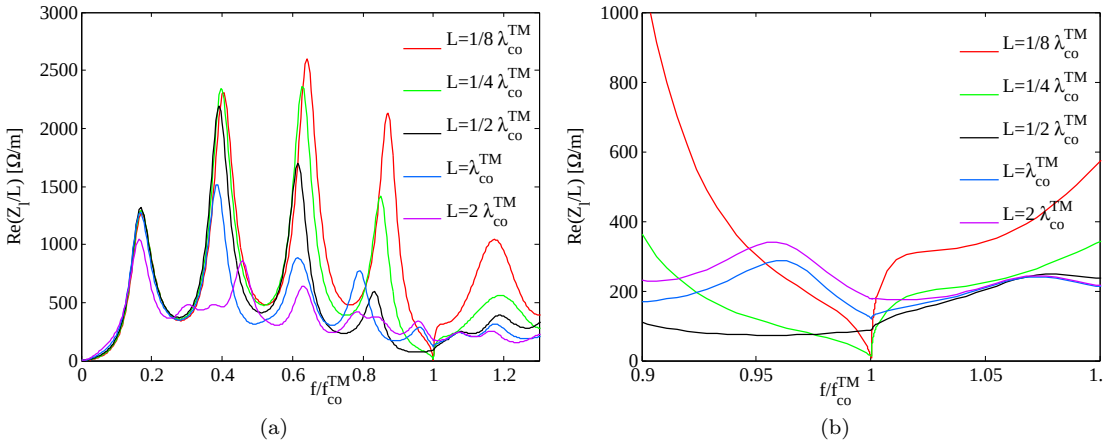


Figure 2.22: Kink in the longitudinal impedance at the $\mathrm{TM}_{01}$ mode cut-off frequency (a) and enlargement around cut-off (b). Mode Matching parameters: $b = 5\,\mathrm{cm}$, $t = 25\,\mathrm{cm}$, $L \in (1/8, \cdots, 2)\lambda_{co}^{\mathrm{TM}}$, $\sigma = 10^{-2}\,\mathrm{S/m}$, $\beta = 1$, P=5, S=25.

In order to explain the observations we resort to a representation of the device with a transmission line model. Below cut-off a semi-infinite pipe exhibits reactive input impedance which, for

TM modes, is capacitive [31]: $Z_{pipe}^{\mathrm{TM}} = 1/j\,\omega C_p$ where

$$C_p = \frac{Y_o}{2\,\pi\sqrt{f_{co}^2 - f^2}} \tag{2.125}$$

is the equivalent beam pipe capacity with $f_{co}$ the cut-off frequency of the TM mode propagating in the beam pipe. The impedance vanishes at cut-off and becomes resistive above it ($Z_{pipe}^{\mathrm{TM}} = R_p$). According to the circuital representation in Fig. 2.23 the two pipe impedances are in parallel to the "impedance of the insert", where the quoted expression indicates the impedance of the insert calculated replacing the two pipes with two PEC circular plates, which seal the insert and form a closed cavity. Being $L < \lambda_{co}/2$, the insert impedance can be treated as a lumped impedance in parallel to the beam pipes [16]. The definition of the parameters for the lumped element would require a rigorous and complex study that deviates from the purposes of this thesis: we will proceed with a semi-empirical explanation that, nevertheless, can give the reader a complete understanding of the phenomenon. Since the longitudinal beam coupling impedance represents power loss from conductivity (real part) and power exchanged with the cavity insert (imaginary part) we assume that the lumped impedance element coincides with the beam coupling impedance $Z_i = R_i + jX_i = Z_l$.

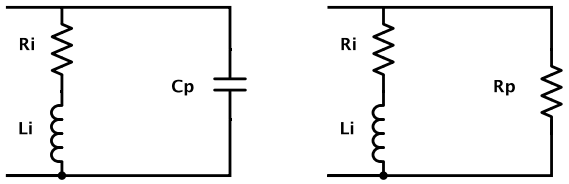


Figure 2.23: Transmission line model for kink at cut-off frequency. The insert $Z_i = R_i + jX_i$ represents the inductive resistive wall, the pipes are capacitive below cut-off (a), and resistive above cut-off (b).

Focusing on Fig. 2.21, we may infer that the dissipation is such that we are in the regime of resistive wall behavior, which is inductive ($Z_i = R_i + j\omega L_i$): the surface impedance is very small and its phase angle is steadily $\pi/4$. At a certain frequency, just a bit smaller than $f_{co}^{\mathrm{TM}}$, the capacitive reactance of the pipe $C_p$ becomes so small to equal the inductive reactance of the wall $L_i$. In this case we have the typical behavior of a parallel RLC circuit and that explains the resonance sharp peaks appearing slightly before cut-off. At the cut-off frequency the pipe impedance vanishes since $C_p \to \infty$ and the TL model is short-circuited.

Note that the Q-factor does not only depend on the amount of power losses but also on the fast change of the capacitive reactance in the narrow domain close to $f_{co}$. However, the Q-factor decreases according to the increase of the power losses, namely according to the increase of the insert length and, up to a certain extent, according to the decrease of the conductivity.

When the conductivity of the insert becomes smaller than a certain amount, since the skin depth becomes comparable or larger than the sector thickness, the behavior of the insert changes: the resonances of the insert itself, which are due to the interference of outgoing and reflected waves, become apparent as depicted in Fig. 2.22.
The circuital model is valid only if the length $L < \lambda_{co}/2$. This may explain why from $L \geq \lambda_{co}/2$ in Fig. 2.22 the effect becomes less and less evident.
One may notice that at cut-off frequency, the resonant behavior has disappeared, and only the cliff to zero is apparent for the first 3 curves. One could infer that this phenomenon depends on the conductivity. Figures 2.24 and 2.25 show that the possibility of two different states may happen also in the case of constant conductivity and different thickness. Changing the value of $t$, the standing wave pattern changes and the cut-off frequency moves from the left to the right of the

closest resonance. A resonance is represented by

$$Z(\omega) = \frac{R_s}{1 + j\,Q\left(\dfrac{\omega_r}{\omega} - \dfrac{\omega}{\omega_r}\right)}, \tag{2.126}$$

where $R_s$, $Q$, and $\omega_r = 2\pi f_r$ are respectively the shunt impedance, quality factor and resonance frequency. For $f < f_r$ the behavior is inductive, while for $f > f_r$ it is capacitive. In the first case we are just in the same condition as Fig. 2.21 since the closest resonance appears inductive, while, in the second case, the kink flips from the resonant behavior to the opposite polarity because the insert appears capacitive $Z_i = R_i + 1/j\omega C_i$ and therefore there is no inductance to produce a resonance with the capacitive beam pipe impedance $C_p$.

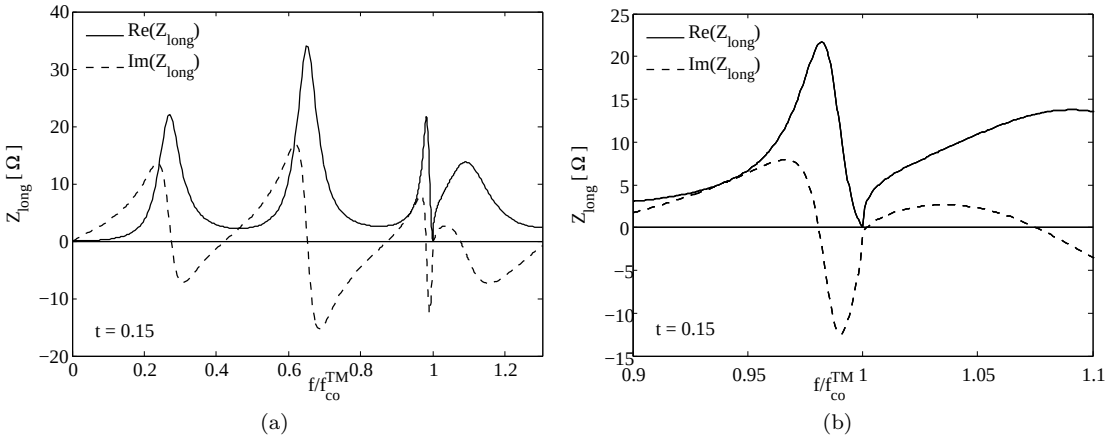


Figure 2.24: Kink in the longitudinal impedance at the $\mathrm{TM}_{01}$ mode cut-off frequency (a) and enlargement around cut-off (b) for thickness $t = 15\,\mathrm{cm}$. Mode Matching parameters: $b = 5\,\mathrm{cm}$, $t = 15\,\mathrm{cm}$, $L = 1/16\,\lambda_{co}^{\mathrm{TM}}$, $\sigma = 10^{-2}\,\mathrm{S/m}$, $\beta = 1$, P=5, S=25.

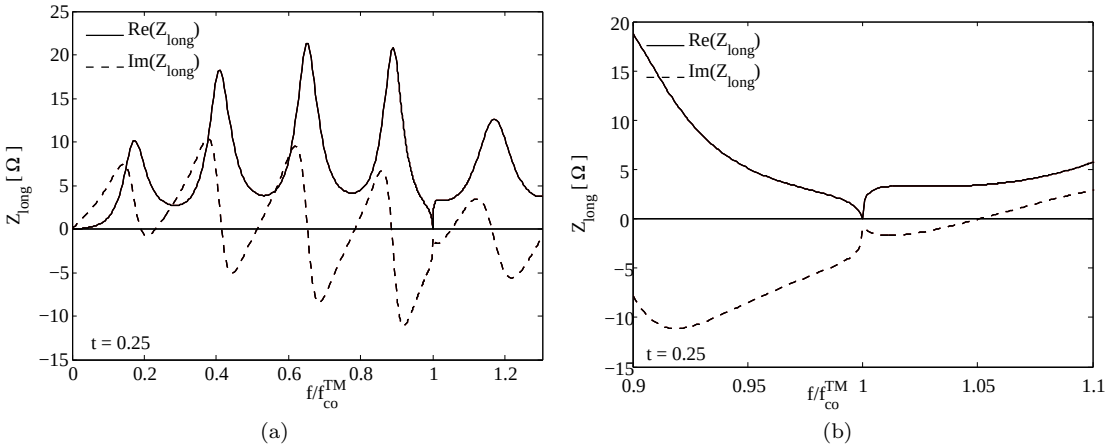


Figure 2.25: Kink in the longitudinal impedance at the $\mathrm{TM}_{01}$ mode cut-off frequency (a) and enlargement around cut-off (b) for thickness $t = 25\,\mathrm{cm}$. Mode Matching parameters: $b = 5\,\mathrm{cm}$, $t = 25\,\mathrm{cm}$, $L = 1/16\,\lambda_{co}^{\mathrm{TM}}$, $\sigma = 10^{-2}\,\mathrm{S/m}$, $\beta = 1$, P=5, S=25.

Similar considerations can be done for the transverse impedance. The lowest beam pipe cut-off frequency $f_{co}$ is this time the one corresponding to the $\mathrm{TE}_{11}$ mode whose transmission line impedance below cut-off is $Z_p = j\omega L_p$ with

$$L_p = \frac{Z_o}{2\pi\sqrt{f_{co}^2 - f^2}}, \tag{2.127}$$

and $Z_p = R_p$ above cut-off. The insert lumped impedance, associated with beam losses, can be obtained from the transverse impedance via the Panofsky-Wenzel theorem [9]: $Z_i = \omega/c\, Z_{dip}$. Figure 2.26 shows the classical resistive wall transverse impedance: the behavior appears capacitive, but the corresponding insert lumped impedance is inductive and therefore a resonance cannot be established at the $\mathrm{TE}_{11}$ cut-off. For lower conductivities, Figures 2.27 and 2.28 show the possibility

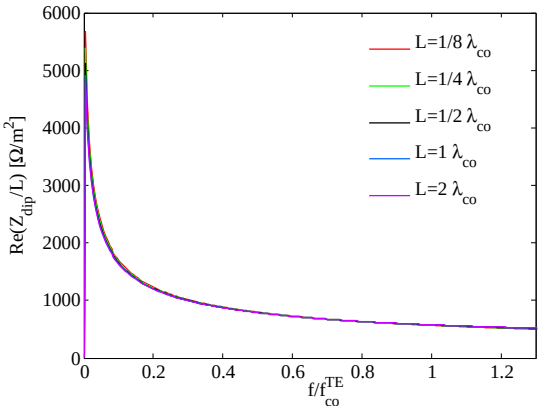


Figure 2.26: Dipolar impedance normalized at the $\mathrm{TE}_{11}$ mode cut-off frequency. Mode Matching parameters: $b = 5\,\mathrm{cm}$, $t = 25\,\mathrm{cm}$, $L \in (1/8, \cdots, 2)\lambda_{co}^{TM}$, $\sigma = 10^{-2}\,\mathrm{S/m}$, $\beta = 1$, P=5, S=25.

of having a resonance slightly below cut-off. We may note that at exactly the cut-off frequency, i.e. $f/f_{co}^{\mathrm{TE}} = 1$ in Figs. 2.27b and 2.28b the impedance appears unperturbed: this is not unexpected since the pipe inductance given in Eq. 2.127 goes to infinity becoming an open circuit.
We notice also that in Fig. 2.27a the pipe inductance is in parallel to the inductive slope of the closest resonance $f_r$, while in Fig. 2.28a it is in parallel to the capacitive slope: we would therefore expect a resonant behavior only in the second case, not in the first. This effect, from one side settles the limitations in describing with a simple lumped circuit model a distributed system, and on the other side confirms the Mode Matching as a valuable technique for studying very narrow and localized resonances on the impedance.

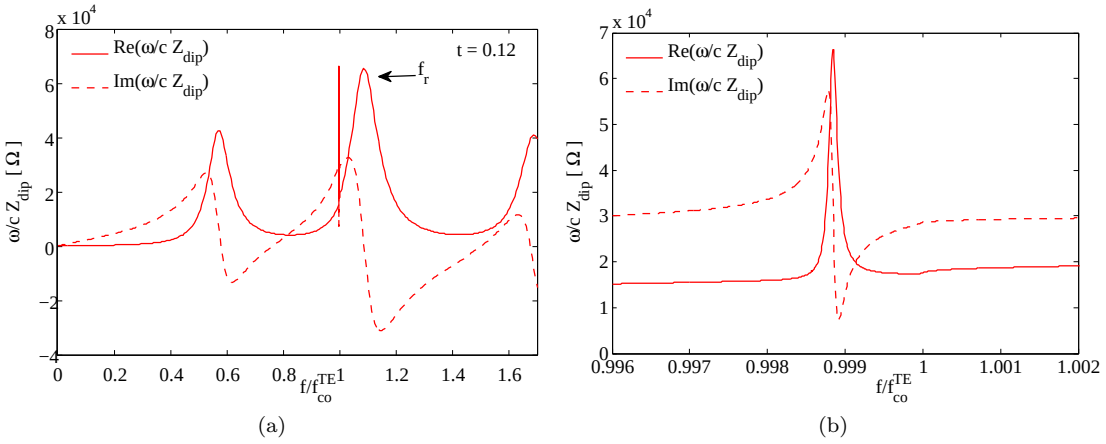


Figure 2.27: Kink in the dipolar impedance at the $\mathrm{TE}_{11}$ mode cut-off frequency (a) and enlargement around cut-off (b) for thickness $t = 12\,\mathrm{cm}$. Mode Matching parameters: $b = 5\,\mathrm{cm}$, $t = 12\,\mathrm{cm}$, $L = 1/8\,\lambda_{co}^{\mathrm{TE}}$, $\sigma = 10^{-2}\,\mathrm{S/m}$, $\beta = 1$, P=5, S=25.

These examples have enlightened the potentialities of the Mode Matching technique and are not academical. A recent interest arose at CERN for materials with low losses. This is witnessed by the study of the dielectric properties at high frequency of SiC ($\varepsilon_r = 10$ and $\tan\delta = 0.2$), oriented to its use in accelerator devices: recently this material has been characterized [32]; its equivalent

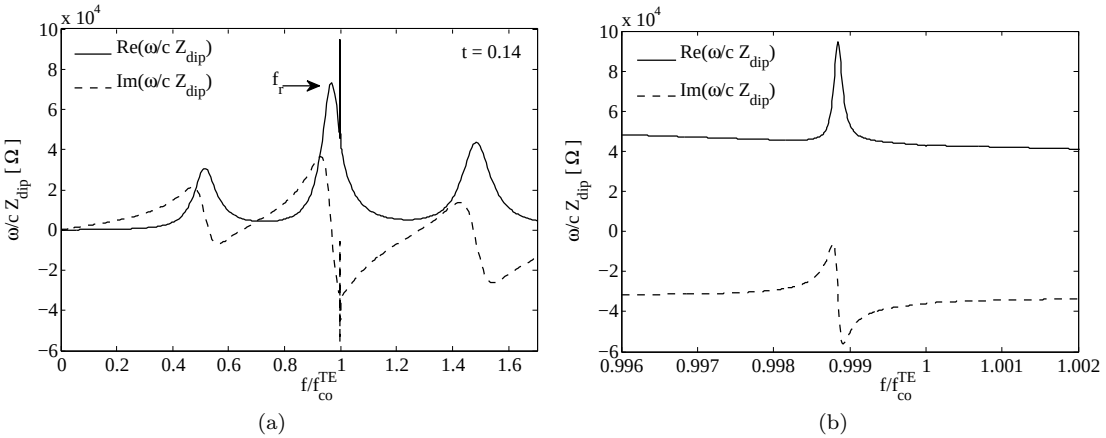


Figure 2.28: Kink in the dipolar impedance at the $\mathrm{TE}_{11}$ mode cut-off frequency (a) and enlargement around cut-off (b) for thickness $t = 14\,\mathrm{cm}$. Mode Matching parameters: $b = 5\,\mathrm{cm}$, $t = 14\,\mathrm{cm}$, $L = 1/8\,\lambda_{co}^{\mathrm{TE}}$, $\sigma = 10^{-2}\,\mathrm{S/m}$, $\beta = 1$, P=5, S=25.

conductivity would be estimated as $\sigma_{eq} = \omega_0 \varepsilon_0 \varepsilon_r \tan\delta = 0.1\,\mathrm{S/m}$ at $f = 1\,\mathrm{GHz}$ which is in the range of our examples. Furthermore, allowing for Alumina 96% ($\varepsilon_r = 9.4$ and $\tan\delta = 10^{-4}$), its equivalent conductivity is $\sigma_{eq} \simeq 5{\cdot}10^{-4}\,\mathrm{S/m}$ at $f \simeq 2.2948\,\mathrm{GHz}$ the cut-off frequency of a beam pipe with radius $b = 5\,\mathrm{cm}$. Figure 2.29a shows the longitudinal impedance correspondingly to a 8 mm long alumina insert that could represent a beam pipe flange: the characteristic resonance close to cut-off can be appreciated at $f \simeq 2.2946$ GHz in the zoomed view of Fig. 2.29b. The presence of the resonance at cut-off can be explained as it is the cut-off on the inductive impedance slope of the most nearby resonance that corresponds in this case to the $\mathrm{TM}_{0,15,0}$ mode.

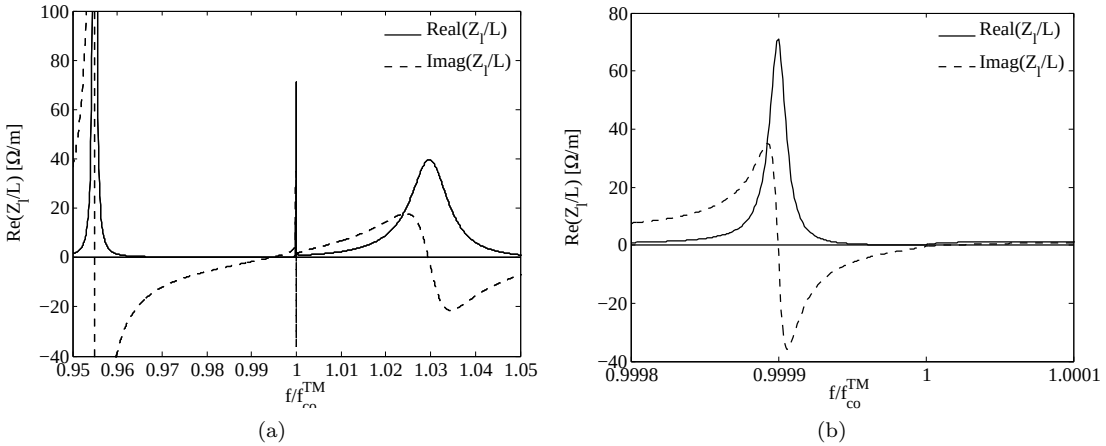


Figure 2.29: Presence of cut-off resonance in a short accelerator beam pipe flange (a) and zoomed view (b). Mode Matching parameters: $b = 5\,\mathrm{cm}$, $t = 30\,\mathrm{cm}$, $L = 8\,\mathrm{mm}$, insert in Alumina 96% ($\varepsilon_r = 9.4$ and $\tan\delta = 10^{-4}$), P=25, S=25.

Tests have been done also with CST-Eigenmode Solver, in order to verify if this behavior is the signature of a trapped mode. Figure 2.30a shows a simple model simulated: an 8 mm long alumina insert between two $L_{pipe}$ long beam pipes, sealed by PEC plates on both ends. The structure exhibits a $\mathrm{TM}_{0,15,0}$-like mode at 2.2955 GHz as shown in Fig. 2.30a which confirms the Mode Matching expected mode of Fig. 2.29b. The small discrepancy in frequency could be explained by the finite beam pipe length that we have chosen ($L_{pipe} = 120$ cm on both ends) in the CST simulation: close to cut-off, the EM field expands into the pipes; therefore, by increasing the beam pipe length, this discrepancy could be slowly reduced as shown in Figure 2.30b.

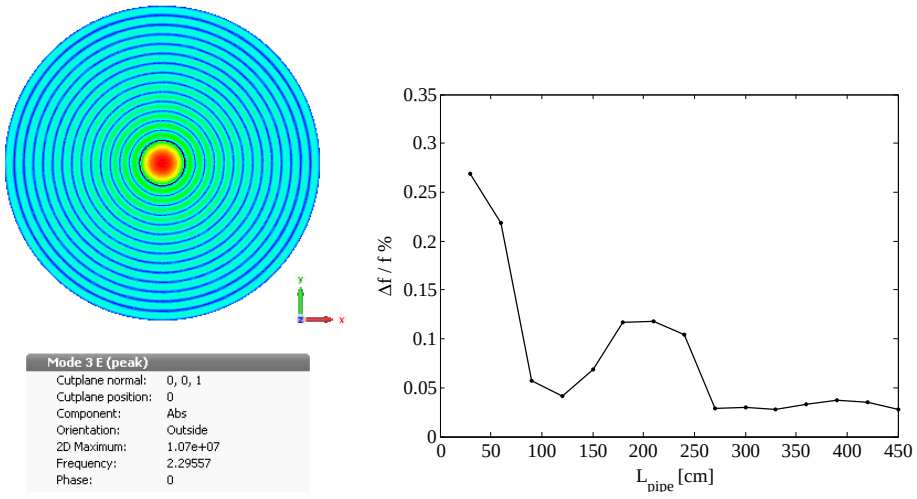


(a) (b)

Figure 2.30: CST-Eigenmode Solver simulation for the resonance near cut-off in a short accelerator beam pipe flange (a) and convergence of the mode frequency in function of the beam pipe length $L_{pipe}$ (b). CST parameters: $b = 5\,\text{cm}$, $t = 30\,\text{cm}$, $L = 8\,\text{mm}$, $L_{pipe} = 120\,\text{cm}$, insert in Alumina 96% ($\varepsilon_r = 9.4$ and $\tan\delta = 10^{-4}$), $N_{mesh} = 25000$ tetrahedrons.

### 2.5.6 Impedance dependence on relativistic $\beta$

We are going now to benchmark the Mode Matching method for impedance calculation in case of not ultra relativistic beam velocities, i.e. $\beta < 1$. This problem is of relevant importance for machines that work at the first stages of beam acceleration. For example, in the CERN PS-Booster (PSB), the proton beam is first injected at 50 MeV and accelerated to 1.4 GeV kinetic energy, that corresponds to $\beta_{inj} = 0.314$ and $\beta_{ext} = 0.916$. At low $\beta$, effects like the *space charge* (SC) become relevant in particle dynamics and play a key role in the overall beam stability.

The resistive wall impedance of circular vacuum chambers in low $\beta$ regime was already studied in the past in [7] and [33] and generalized within the "2D-Axi" code [13]. These approaches are all valid for infinitely long beam pipes, i.e. where edges effects and/or cavity resonances are not expected to appear. The Mode Matching approach does not present these limitations. We will, nevertheless, proceed to the benchmark with the "2D-Axi" code in order to prove the method reliability.

Since we considered as source fields for the impedance calculations, the fields produced by a beam traveling in a perfectly conducting beam pipe (Tab. 2.5), the impedance calculated with the Mode Matching in Sec. 2.4 does not take into account the *direct* and *indirect* space charge (DSC and ISC): the DSC represents the direct interaction of the source particle field with the test particle, the ISC the interaction of the perfectly conducting beam pipe scattered fields. Since in the "2D-Axi" code the ISC impedance is included in the impedance calculation, we will add the $Z^{ISC}$ term to the impedance calculated with the Mode Matching. The ISC longitudinal impedance per meter unit of round beam pipe of radius b is given by [25]

$$Z_l^{ISC} = \frac{j\,\omega I_0^2(s) Z_o}{2\pi c \beta^2 \gamma^2} \frac{K_0(x)}{I_0(x)}, \tag{2.128}$$

and the transverse impedance per meter unit by

$$Z_{dip}^{ISC} = \frac{j\,I_1^2(s) Z_o}{\beta \gamma^2 \pi r_S^2} \frac{K_1(x)}{I_1(x)}, \tag{2.129}$$

where we remind that $\alpha_b = b\,\omega/v$, $x = \alpha_b/\gamma$, $s = r_S\omega/(\gamma v)$. For $r_S \to 0$ the expressions simplify

to:

$$Z_l^{ISC} = \frac{j\,\omega\,Z_o}{2\pi\,c\beta^2\gamma^2}\frac{K_0(x)}{I_0(x)}, \tag{2.130}$$

$$Z_{dip}^{ISC} = \frac{j\,\omega^2\,Z_o}{4\pi\,c^2\beta^3\gamma^4}\frac{K_1(x)}{I_1(x)}. \tag{2.131}$$

For small argument $x$ we recover the well known formulas showing the $1/\gamma^2$ dependence:

$$Z_l^{ISC} = \frac{-j\,\omega\,Z_o}{2\pi\,c\beta^2\gamma^2}\ln(x), \tag{2.132}$$

$$Z_{dip}^{ISC} = \frac{j\,Z_o}{2\pi\beta\gamma^2}\frac{1}{b^2}. \tag{2.133}$$

Figures 2.31a and 2.31b show the comparison between the "2D-Axi" code and the Mode Matching for a high conductivity material ($\sigma_c = 10^6\,\mathrm{S/m}$) that could model a collimator module.

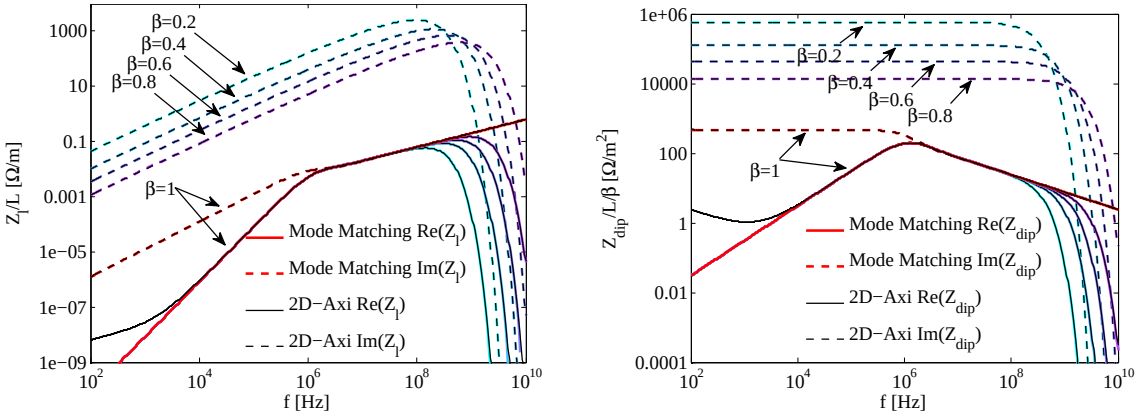


(a) (b)

Figure 2.31: Comparison between the Mode Matching and the "2D-Axi" code for different relativistic $\beta$ longitudinal (a) and transverse (b) impedance. The thick line is the real part, the dashed line the imaginary part of the impedance. The transverse impedance is normalized over $\beta$. Mode Matching parameters: $b = 0.05\,\mathrm{m}$, $t = 0.5\,\mathrm{mm}$, $L = 20\,\mathrm{cm}$, $\sigma = 10^6\,\mathrm{S/m}$, $\beta = (0.2, 0.4, 0.6, 0.8, 1)$, P=25, S=25.

The ultra relativistic beam approximation, commonly used in impedance calculations, constitutes, in the case of the real part of the impedance, the worst-case scenario. It is interesting to notice that the resistive wall transverse impedance scales with an additional $\beta$ with respect to the longitudinal case (see Tab. 2.14). The imaginary part of the impedance grows quadratically with $\beta\gamma$.

The discrepancy at low frequencies is due to the PEC model in the "2D-Axi" code which is a layer with high, but finite, conductivity (in the case under study we put $\sigma_c^{(2D-Axi)} = 10^{14}\,\mathrm{S/m}$).

The decrease of the impedance at high frequency can be understood resorting to a perturbative method which assumes that the longitudinal current on the insert is just equal to the one circulating on a PEC pipe, i.e. in Leontovich approximation. According to Tab. 2.5 in an infinite smooth pipe the magnetic field on the wall is given by the formula

$$H_\phi^{source} = \frac{Q}{2\pi\,b\,I_0(\omega b/(\beta\gamma c))}e^{-\frac{jz\alpha_b}{b}}, \tag{2.134}$$

which suggests that the maximum of the surface current is for frequencies which satisfy the following approximate equation:

$$f_{max} \simeq 0.7\frac{\beta\gamma c}{2\pi b}. \tag{2.135}$$

The frequencies corresponding to the longitudinal impedance maxima, calculated with Eq. 2.135, are indicated in Fig. 2.32a by vertical black lines and the intercepts with the impedance curves by the corresponding colored dots. This approximation is found to be good also in the transverse

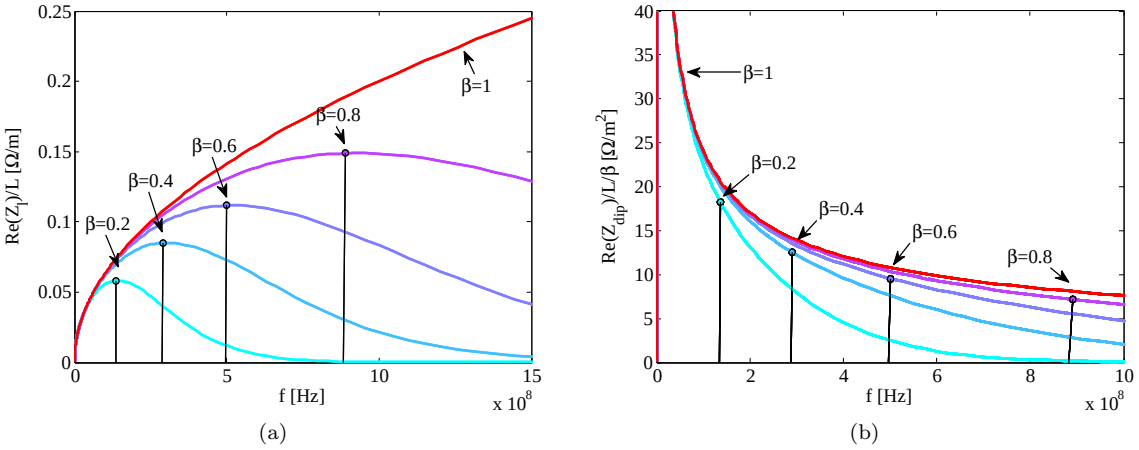


Figure 2.32: Deviation of the non ultra relativistic beam impedance from the ultra relativistic case and corresponding $f_{max}$ frequencies. The transverse impedance is normalized over $\beta$. Mode Matching parameters: $b = 0.05\,\mathrm{m}$, $t = 0.5\,\mathrm{mm}$, $L = 20\,\mathrm{cm}$, $\sigma = 10^6\,\mathrm{S/m}$, $\beta = (0.2, 0.4, 0.6, 0.8, 1)$, P=25, S=25.

case (Fig. 2.32b). A simple interpretation for this behavior is the following: since the impedance is the electromagnetic response to the beam excitation, a short beam (i.e. for $\beta \simeq 1$) will excite a high frequency spectrum while a long beam (i.e. for $\beta << 1$) will excite only a smaller part of it.

However, this behavior is no longer kept for lower conductivities, where resonances may appear and the perturbative approximation in Eq. (2.135) cannot be used anymore.

# Chapter 3

# Transverse impedance localization: simulations

Having a reliable model of the beam coupling impedance is a mandatory requirement in circular particle accelerators, and in particular for the CERN accelerator complex where the High Luminosity programme [34–36] implies new challenges in terms of beam performance and stability.

In addition to theoretical estimations based on numerical codes or analytical formulas as the ones described in the previous chapter, impedance measurements can be done in order to monitor and compare the machine status with the impedance model. Measuring the betatron coherent frequency shift with intensity, for example, gives informations on the total reactive transverse impedance according to Sacherer's theory [37]. An extension of this method for measuring the reactive part of transverse localized impedances was proposed the first time in 1995 at CERN [38]: measuring the impedance-induced *betatron phase advance shift with intensity*, the LEP RF sections were found to be important impedance contributors. Figure 3.1 shows the measured phase advance between beam position monitors (BPMs) in the horizontal (left) and vertical (right) planes: two considerably big jumps in the accelerator phase advance that could be correlated with high transverse impedance in the RF sections.

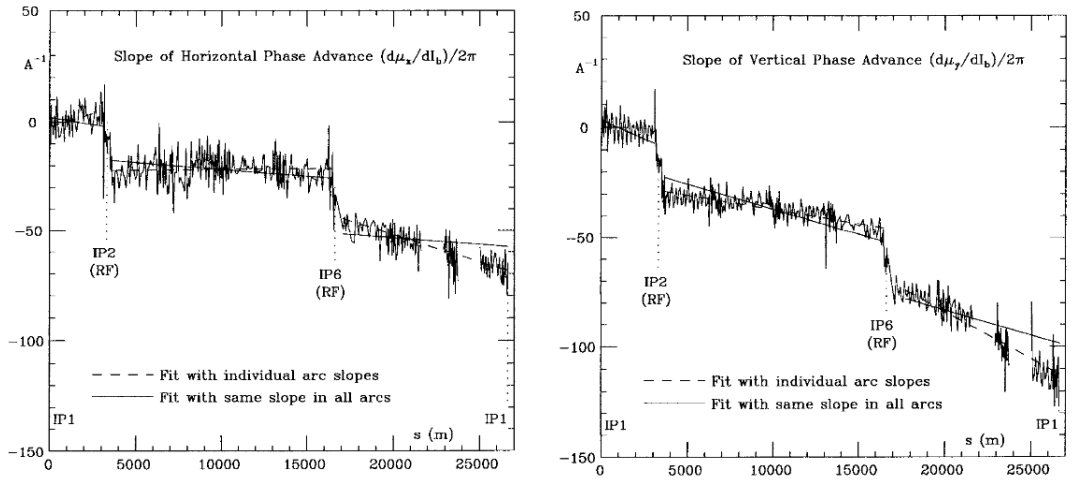


(a) (b)

Figure 3.1: LEP impedance localization: the steps can be correlated with high impedance in the RF sections. (Courtesy of [38])

A similar method, based on the impedance-induced *orbit shift with intensity*, was proposed in 1999 in the Novosibirsk VEPP-4M electron-positron storage ring [39] and in 2001 in the Argonne

APS synchrotron accelerator [40]. Later in 2002, the same method was tried in the Grenoble ESRF [41].

The CERN research on the impedance localization method using phase advance shift with intensity, was continued in 2004 in the SPS [42,43] and in BNL RHIC [44]. Even if the measurement was proved to work, the results were of difficult interpretation and the impedance locations were not univocally reconstructed.

In this and the following chapter, we will review the measurement technique and present the simulations and measurements in the CERN machines, in particular PS, SPS and LHC, and in the BNL RHIC. Even if the method is not new, the difference with the authors who already gave a contribution to this type of measurement can be summarized in

1. quantification of the noise impact in the measurement,
2. refinement of the reconstruction technique,

both essential in order to establish the measurement feasibility and improve the results interpretation.

## 3.1 Theoretical background

The connection between transverse beam coupling impedance and main accelerators observables such as tune, phase advance between BPMs and orbit position was done starting from the work of F.Sacherer [37] and J.L. Laclare [45].

The beam circulating in an accelerator executes the so-called transverse *betatron* oscillations whose frequency $\omega_\beta$, the *betatron frequency*, is given by the magnetic focusing force in the lattice. We define the *coherent betatron tune* as the number of betatron oscillation of the center of mass per turn, $Q_o = \omega_\beta/\omega_o$ where $\omega_o = \beta c/R$ with $R$ radius of the accelerator machine.

On top of this oscillation, each particle in the beam executes longitudinal oscillations whose frequency, the *synchrotron frequency*, is determined by the accelerator RF system.

Particles with different longitudinal momentum $p_l' = p_l + \Delta p_l$ will have slightly different betatron tune with respect to the center of mass $Q' = Q_o + \Delta Q_o$. The relative ratio between $\Delta Q_o$ and $\Delta p_l$ is defined as *chromaticity*:

$$\xi = \frac{\Delta Q_o/Q_o}{\Delta p_l/p_l}. \tag{3.1}$$

The chromaticity sets a further relation between transverse and longitudinal motion that results in a shift of the beam spectrum accordingly to the sign of $\xi$. The chromaticity can be set up adjusting the current in the accelerator sextupoles. For the stability of the centroid motion against the resistive wall impedance, chromaticity is usually set to be positive for machine operating above transition, or negative below transition.

The natural beam oscillations may be considerably influenced by the beam interaction with impedances. According to Eqs. (2.4) and (2.5) each particle in a beam experiences a kick proportional to the wake potential and the total charge carried by the beam in the longitudinal and transverse momentum. A positive transverse momentum kick $\Delta p_t$, for example, can be seen as an equivalent additional defocusing in the lattice that provokes a reduction of the betatron frequency, i.e. a negative shift of $\omega_\beta$.

### 3.1.1 Impedance-induced coherent tune shift with intensity

A complete study of the beam frequency shift with intensity, involving azimuthal $l$ and radial $n$ bunch oscillation modes decomposition, can be found in [9, 37, 46]. The tune corresponds to the mode with $l = n = 0$. A simplified model for the tune shift with intensity with chromaticity $\xi = 0$ will be given in the following.

Let us consider a bunch distribution $\rho(s)$ traveling at speed $v = \beta c$ along the accelerator closed orbit. The $i^{th}$ particle in the bunch executes betatron oscillations given by [47]

$$\frac{d}{d^2 s} y_i(s) + K_o(s) y_i(s) = 0, \tag{3.2}$$

where $K_o(s) = B_1(s)/B\rho$ is the effective focusing function[1] for the ideal lattice, $B\rho$ is the so called beam rigidity, with $B$ the main dipole field strength and $\rho$ bending radius, $y$ denotes, for example, the vertical coordinate. Applying a Floquet transformation we can find the Hill's solution of Eq. (3.2) in the form

$$y_i(s) = \sqrt{\epsilon_y \beta_y(s)} \cos(\psi_y(s) + \theta_i), \tag{3.3}$$

where $\beta_y$ is the betatron function (or $\beta$ function) fixed by the lattice properties, $\epsilon_y$ is the single particle invariant, $\theta_i$ is the betatron phase at $t = 0$ and $\psi_y(s)$ the betatron phase advance given by:

$$\psi_y(s) = \int_0^s \frac{1}{\beta_y(s)}\, \mathrm{d}s. \tag{3.4}$$

where the integral goes from $s = 0$, a conventional accelerator starting point. We define the tune as the number of particle oscillation per turn given by

$$Q_y = \frac{1}{2\pi} \int_0^C \frac{1}{\beta_y(s)}\, \mathrm{d}s, \tag{3.5}$$

with $C$ the accelerator circumference. Having $\xi = 0$ the particle motion is completely decoupled from the synchrotron motion. When the particle motion is perturbed by the interaction with a beam coupling impedance Eq. (3.2) becomes

$$\frac{d}{d^2 s} y_i(s) + K_o(s) y_i(s) = \frac{< F_i >}{\beta^2 E_o}, \tag{3.6}$$

where $< F_i >$ is the average force experienced by the particle $i^{th}$ at distance $s_i$ from the center of the bunch, $E_o = \gamma m_p c^2$ is the energy of the traveling proton particle with $m_p$ the proton rest mass.

Defining an average force $< F_i >$ acting on each bunch particle is a consequence of the *rigid beam* approximation in the impedance definition of Sec. 2.1: the test particle passing through a device of length $L$ preserves its distance from the source particle. We can therefore express the transverse momentum change $\Delta p_{t,i}$ as $\Delta p_{t,i} =< F_i > L/v$. Recurring to Eqs. (2.5) and (2.13), setting the source beam charge at the center of mass $\bar{y}$ we write Eq.(3.6) in terms of the wake potential $W_{pot}$

$$\frac{d}{d^2 s} y_i(s) + K_o(s) y_i(s) = \frac{-q^2}{L\beta^2 E_o} W_{pot}(s_i) = \frac{-q^2}{L\beta^2 E_o} \left(W * \rho\right)(s_i), \tag{3.7}$$

where $W(s)$ is the wake function. Expanding the wake term at first order over test particle position $y_i$ and the beam center of mass $\bar{y}$ as in Eq. (2.7), we have:

$$\frac{d}{d^2 s} y_i(s) + K_o(s) y_i(s) = \frac{-q^2}{L\beta^2 E_o} \left((W_{dip}\bar{y}(s) + W_{quad} y_i(s)) * \rho\right)(s_i), \tag{3.8}$$

Since we are interested to the motion of the center of mass, we sum over the number of particles to get:

$$\frac{d}{d^2 s} \bar{y}(s) + K_o(s) \bar{y}(s) = \frac{1}{N_p} \sum_{i=1}^{N_p} \frac{-q^2}{L\beta^2 E_o} \left((W_{dip}\bar{y}(s) + W_{quad} y_i(s)) * \rho\right)(s_i), \tag{3.9}$$

where

$$\bar{y}(s) = \frac{1}{N_p} \sum_{i=1}^{N_p} y_i(s). \tag{3.10}$$

[1]Here we assume that all the particles *see* the same focusing function $K_o(s)$ discarding secondary effects due to the magnetic field imperfections.

**Tune shift from the indirect space charge with $\xi = 0$: smooth approximation**

Let us now particularize for the case of the indirect space charge impedance (ISC) in a round perfectly conducting beam pipe of radius $b$. The dipolar wake field can be derived from Eq. (2.133) with a Fourier inverse transformation as defined in Eq. (2.11). We get

$$W_{dip}^{ISC}(s) = -v\beta\delta(s) Im(Z_{dip}^{ISC}) C. \tag{3.11}$$

It is important to notice that the ISC can be derived also using an *image current* approach, as commonly depicted in literature [8], [46]: in this case the fields scattered by a source beam displaced by $\bar{y}_1$ from the center, can be calculated as the ones provoked by an image current set at distance $\bar{y}_2 = b^2/\bar{y}_1$ from the center. The quadrupolar impedance is therefore null: the image current of a beam traveling at the center of the pipe will be pushed to infinity since $\bar{y}_1 \to 0$ and a test particle will experience no scattered field.
Substituting the wakefield in Eq. (3.9) we have

$$\frac{d}{d^2 s}\bar{y}(s) + K_o(s)\bar{y}(s) = \frac{q^2 v}{N_p \beta E_o} Im(Z_{dip}^{ISC})\bar{y}(s) \sum_{i=1}^{N_p} (\delta * \rho)(s_i). \tag{3.12}$$

Expanding the convolution integral we have:

$$\sum_{i=1}^{N_p} (\delta * \rho)(s_i) = \sum_{i=1}^{N_p} \int_{-\infty}^{+\infty} \delta(s - s_i)\rho(s)\, \mathrm{d}s. \tag{3.13}$$

To solve the integral we can divide the longitudinal particle distribution in $2\,M$ slices of width $\Delta s$ as depicted in Fig. 3.2. The $j^{th}$ slice counts $N_j$ particles of the entire ensemble and is centered in $s_j$. The longitudinal beam distribution $\rho(s_j)$ can be seen as:

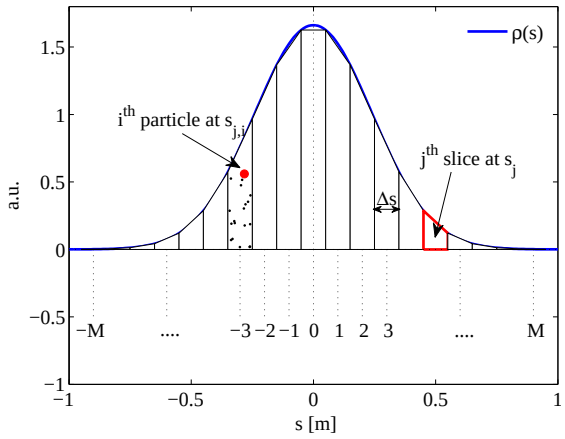


Figure 3.2: Model used for the coherent tune shift computation: the bunch distribution $\rho(s)$ is divided in $2\,M$ slices. The $j^{th}$ slice has width $\Delta s$ and is centered in $s_j$. In each slice $N_j$ particles of the total ensemble are contained. Each particle in the $j_{th}$ slice has a corresponding longitudinal position $s_{j,i}$.

$$\rho(s_j) = \lim_{\Delta s \to 0} \frac{N_j}{\Delta s} = \lim_{\Delta s \to 0} \frac{1}{\Delta s} \sum_{i=1}^{N_j} \int_{-\infty}^{+\infty} \delta(s - s_{j,i})\, \mathrm{d}s. \tag{3.14}$$

Equation (3.13) can be rewritten as:

$$\sum_{j=-M}^{M} \sum_{i=1}^{N_j} \int_{-\infty}^{+\infty} \delta(s - s_{j,i})\rho(s_j)\, \mathrm{d}s = \sum_{j=-M}^{M} N_j \rho(s_j). \tag{3.15}$$

Multiplying and dividing by the slice width we have

$$\sum_{j=-M}^{M} \frac{N_j}{\Delta s}\rho(s_j)\Delta s = \sum_{j=-M}^{M} \rho(s_j)^2 \Delta s, \tag{3.16}$$

and taking the limit for $\Delta s \to 0$ we get:

$$\lim_{\Delta s \to 0} \sum_{j=-M}^{M} \rho(s_j)^2 \Delta s = \int_{-\infty}^{+\infty} \rho(s)^2 \, \mathrm{d}s. \tag{3.17}$$

Equation (3.12) than becomes:

$$\frac{d}{d^2 s}\bar{y}(s) + K_o(s)\bar{y}(s) = \frac{q^2 v}{N_p \beta E_o} Im\left(Z_{dip}^{ISC}\right) \bar{y}(s) \int_{-\infty}^{+\infty} \rho(s)^2 \, \mathrm{d}s. \tag{3.18}$$

In the smooth approximation $K_o(s) \simeq Q_{yo}^2/R^2$ and we can write

$$\frac{d}{d^2 s}\bar{y}(s) + \left(\frac{Q_{yo}}{R}\right)^2 \bar{y}(s) = \frac{q^2 v}{N_p \beta E_o} Im\left(Z_{dip}^{ISC}\right) \bar{y}(s) \int_{-\infty}^{+\infty} \rho(s)^2 \, \mathrm{d}s. \tag{3.19}$$

If we consider now an equivalent focusing function $K(s)$, including the effect of the impedance, we can write

$$\frac{d}{d^2 s}\bar{y}(s) + K(s)\bar{y}(s) = 0, \tag{3.20}$$

where $K(s) = K_o(s) + \Delta K(s)$. In the smooth approximation $K(s) \simeq Q_y^2/R^2$ where $Q_y = Q_{yo} + \Delta Q_y$. Equation (3.20) reduces to

$$\frac{d}{d^2 s}\bar{y}(s) + \left(\frac{Q_y}{R}\right)^2 \bar{y}(s) = 0. \tag{3.21}$$

Expanding and neglecting the quadratic term in $\Delta Q_y$ we have

$$\frac{d}{d^2 s}\bar{y}(s) + \left(\frac{Q_{yo}}{R}\right)^2 \bar{y}(s) = -2\frac{Q_{yo}\Delta Q_y}{R^2}. \tag{3.22}$$

Comparing with Eq. (3.19) we get the tune shift $\Delta Q_y$

$$\Delta Q_y = -\frac{q^2 R^2 v}{2 N_p Q_{yo} \beta E_o} Im\left(Z_{dip}^{ISC}\right) \int_{-\infty}^{+\infty} \rho(s)^2 \, \mathrm{d}s. \tag{3.23}$$

For a *uniform* distribution we have

$$\rho(s) = \frac{N_p}{2\hat{z}} rect_{2\hat{z}}(s), \tag{3.24}$$

where $\hat{z} = v\hat{\tau}$ is the half bunch length. This will produce a tune shift equal to

$$\Delta Q_y = \frac{-N_p q^2 R^2}{2 Q_{yo} \beta E_o} Im\left(Z_{dip}^{ISC}\right) \frac{1}{2\hat{\tau}}. \tag{3.25}$$

Defining the average beam current as $\bar{I} = qN_p/T_o$ we have

$$\Delta Q_y = -\frac{q\bar{I} T_o R}{8\pi Q_{yo} \beta E_o \hat{\tau}} Im\left(Z_{dip}^{ISC}\right) C. \tag{3.26}$$

This is the same result one could obtain following the Vlasov approach of [37] and [45] in the particular case of transverse azimuthal mode 0 oscillation. This is expected since we are studying

a particular case of *rigid* dipole oscillation and constant inductive impedance where the complete set of bunch oscillations can be represented by Legendre modes. The calculated tune shift for a uniform distribution is the same one could obtain with the *image current* approach described in literature [8], [46].

For a *Gaussian* distribution we have

$$\rho(s) = \frac{N_p}{\sqrt{2\pi}\sigma_z} e^{-\frac{s^2}{2\sigma_z^2}}, \tag{3.27}$$

where $\sigma_z = v\sigma_\tau$ is the *rms* bunch length. This will produce a tune shift equal to:

$$\Delta Q_y = -\frac{q\bar{I}T_o R}{8\pi^{3/2} Q_{yo}\beta E_o \sigma_\tau} Im\left(Z_{dip}^{ISC}\right) C. \tag{3.28}$$

Again, this result represents a particular case of the Vlasov formalism in the case of *rigid* dipole oscillation and constant inductive impedance where the complete set of bunch oscillations can be represented by Hermite modes.

This approach enables us to make estimations with measured bunch distributions with wall current monitors, an alternative to the acquisition of the bunch spectrum.

**Tune shift from the indirect space charge with $\xi = 0$: general case**

If we do not consider a smooth approximation, we can calculate the tune shift applying the theory of lattice imperfections [47] from which we have that a small perturbation $\Delta K(s_k)$ in the focusing function at longitudinal position $s_k$ with length $\mathrm{d}s_k$ perturbs the focusing function by $K(s) = K_o(s) + \Delta K(s_k)$ and provokes a tune shift equal to

$$\Delta Q_{y_k} = \frac{1}{4\pi}\beta_k(s_k)\Delta K(s_k)\mathrm{d}s_k \tag{3.29}$$

In our case we have

$$\Delta K(s_k) = \frac{-q^2 v}{N_p \beta E_o} Im\left(Z_{dip}^{ISC}\right) \int_{-\infty}^{+\infty} \rho(s)^2 \,\mathrm{d}s. \tag{3.30}$$

that provokes a tune shift

$$\Delta Q_{y_k} = \frac{1}{4\pi}\beta_k(s_k)\frac{-q^2 v}{N_p \beta E_o} Im\left(Z_{dip}^{ISC}\right) \mathrm{d}s_k \int_{-\infty}^{+\infty} \rho(s)^2 \,\mathrm{d}s \tag{3.31}$$

integrating over the whole circumference and defining the average betatron function $\bar{\beta}_y$

$$\bar{\beta}_y = \frac{1}{C}\oint_C \beta(s)\mathrm{d}s, \tag{3.32}$$

we have:

$$\Delta Q_y = \frac{1}{4\pi}\frac{-q^2 v}{N_p \beta E_o} Im\left(Z_{dip}^{ISC}\right) C\bar{\beta}_y \int_{-\infty}^{+\infty} \rho(s)^2 \,\mathrm{d}s. \tag{3.33}$$

Equation (3.26) is modified in

$$\Delta Q_y = -\frac{q\bar{I}T_o\bar{\beta}_y}{8\pi\beta E_o\hat{\tau}} Im\left(Z_{dip}^{ISC}\right) C, \tag{3.34}$$

and Eq. (3.28) in

$$\Delta Q_y = -\frac{q\bar{I}T_o\bar{\beta}_y}{8\pi^{3/2}\beta E_o\sigma_\tau} Im\left(Z_{dip}^{ISC}\right) C. \tag{3.35}$$

These expressions become the ones obtained in the smooth approximation case specifying $\bar{\beta}_y = R/Q_{y_o}$.

The approach here described was derived in the case of a constant inductive impedance. It is possible to extend it in a general way defining the *effective impedance* as will be introduced in the following section.

**Tune shift from a generic impedance with $\xi = 0$**

Let us consider now a generic impedance $Z(\omega)$ and calculate the induced tune shift at a given intensity. Since we are interested in real tune shifts, we will consider only the reactive part of the impedance[2].

From the convolution in Eq. (3.7) we have that

$$\mathcal{F}\left(W * \rho\right)(s) = Z(\omega)S(\omega), \tag{3.36}$$

where $\mathcal{F}$ denotes the Fourier transformation and $S(\omega)$ the beam spectrum. If the impedance is broad enough over the beam spectrum, we can define an *effective impedance* as

$$Z^{eff} = \frac{\displaystyle\int_{-\infty}^{+\infty} Z(\omega)\|S(\omega)\|^2 \,\mathrm{d}\omega}{\displaystyle\int_{-\infty}^{+\infty} \|S(\omega)\|^2 \,\mathrm{d}\omega}, \tag{3.37}$$

where $\|S(\omega)\|^2$ is the beam power spectrum. For a Gaussian beam distribution we have

$$\|S(\omega)\|^2 = e^{-\omega^2\sigma_\tau^2}. \tag{3.38}$$

Approximating now $Z(\omega)$ with $Z^{eff}$ the impedance will be constant over the spectrum as in the previous case of the $Z_{dip}^{ISC}$.

The quadrupolar impedance can be included in this frame considering that in a kicked beam performing betatron oscillation $y_i(s) \simeq \bar{y}(s)$. Therefore (3.8) becomes

$$\frac{d}{d^2s}y_i(s) + K(s)y_i(s) \simeq \frac{-q^2}{L\beta E_o}\,\bar{y}\left(\left(W_{dip} + W_{quad}\right) * \rho\right)(s_i). \tag{3.39}$$

Equation (3.31) is modified substituting $Z_{dip}^{ISC} \to Z^{eff} = Z_{dip}^{eff} + Z_{quad}^{eff}$. Having, for example, a series of lumped impedances of devices with length $L_k$ along which the betatron function $\beta_{y_k}$ can be assumed to be constant, we can calculate a tune shift of

$$\Delta Q_y = \frac{1}{4\pi}\frac{-q^2 v}{N_p\beta E_o}\left(\sum_k \beta_{y_k}(s_k) Im\left(Z_k^{eff}\right) L_k\right)\int_{-\infty}^{+\infty}\rho(s)^2\,\mathrm{d}s \tag{3.40}$$

where we considered only the imaginary part of $Z^{eff}$ since in this work we are interested only in tune shifts and not in rise times. For distributed impedances, like the resistive wall, the sum is replaced by an integral

$$\Delta Q_y = \frac{1}{4\pi}\frac{-q^2 v}{N_p\beta E_o}\left(\oint_C \beta(s) Im\left(Z^{eff}\right)\mathrm{d}s\right)\int_{-\infty}^{+\infty}\rho(s)^2\,\mathrm{d}s \tag{3.41}$$

Particularizing for a constant distribution we have:

$$\Delta Q_y = \begin{cases} -\dfrac{q\bar{I}T_o}{8\pi\beta E_o\hat{\tau}}\sum_k \beta_{y_k}(s_k) Im\left(Z_k^{eff}\right) L_k, & \text{for } k \text{ lumped impedances} \\ \\ -\dfrac{q\bar{I}T_o}{8\pi\beta E_o\hat{\tau}}\displaystyle\oint_C \beta_y(s) Im\left(Z^{eff}\right)\mathrm{d}s. & \text{for distributed impedances} \end{cases} \tag{3.42}$$

For a Gaussian distribution we have

$$\Delta Q_y = \begin{cases} -\dfrac{q\bar{I}T_o}{8\pi^{3/2}\beta E_o\sigma_\tau}\sum_k \beta_{y_k}(s_k) Im\left(Z_k^{eff}\right) L_k, & \text{for } k \text{ lumped impedances} \\ \\ -\dfrac{q\bar{I}T_o}{8\pi^{3/2}\beta E_o\sigma_\tau}\displaystyle\oint_C \beta_y(s) Im\left(Z^{eff}\right)\mathrm{d}s. & \text{for distributed impedances} \end{cases} \tag{3.43}$$

From these expressions we can see how the tune shift with intensity constitutes the first global parameter used to estimate the total machine effective impedance of an accelerator.

[2]Our approach could easily be extended to include the real part of the impedance and calculate the rise time of an instability.

## 3.2 Impedance-induced phase advance shift with intensity

From Eq. (3.30) we learned how the impedance effect could be treated as an additional defocusing quadrupolar strength from which the tune shift could be calculated. In the general case, an impedance $Z_k^{eff}$ of length $L_k$ meters long placed at position $s_k$ in the accelerator, has an equivalent quadrupolar strength

$$\Delta K = \frac{-q^2 v}{N_p \beta E_o} Im\left(Z_k^{eff}\right) \int_{-\infty}^{+\infty} \rho(s)^2 \, \mathrm{d}s, \tag{3.44}$$

From a global point of view, this perturbation provokes a tune shift as given in Eqs. (3.42) and (3.43), while, from a *local* point of view, it provokes a beating in the betatron function $\beta_y(s)$, the so called *betatron beating* (or $\beta$ beating).

The $\beta$ beating induced by a quadrupole error is given by [47], [48]:

$$\frac{\Delta\beta_y(s)}{\beta_{y_o}} = -\frac{\beta_k}{2\sin(2\pi Q_{y_o})} \cos(2|\psi_y(s) - \psi_y(s_k)| - 2\pi Q_{y_o}) \Delta K L_k, \tag{3.45}$$

where $\beta_y(s)$ and $\psi_y(s)$ are the perturbed beta and phase functions, while the subscript "$o$" refers to the unperturbed ones, $\Delta\beta_y(s) = \beta_y(s) - \beta_{y_o}(s)$ and $\beta_k = \beta_{y_o}(s_k)$ is the beta function at the impedance (or kick) location. To compute the phase advance beating at the $s$ location we solve

$$\psi_y(s) = \int_0^s \frac{1}{\beta_y(\tau)} \, \mathrm{d}\tau + \psi_y(0). \tag{3.46}$$

Setting the initial phase $\psi_y(0) = 0$ and developing the $\beta_y(\tau)$ function at first order, we get

$$\begin{aligned} \psi_y(s) &= \int_0^s \frac{1}{\beta_{y_o}(\tau)\left(1 + \Delta\beta_y/\beta_{y_o}(\tau)\right)} \, \mathrm{d}\tau = \\ &= \int_0^s \frac{1}{\beta_{y_o}(\tau)} \, \mathrm{d}\tau - \int_0^s \frac{\Delta\beta_y(\tau)}{\beta_{y_o}^2(\tau)} \, \mathrm{d}\tau = \\ &= \psi_{y_o}(s) + \Delta\psi_y(s), \end{aligned} \tag{3.47}$$

where $\Delta\psi_y(s) = \psi_y(s) - \psi_{y_o}(s)$. Inserting (3.45) in (3.47) we obtain

$$\begin{aligned} \Delta\psi_y(s) &= \int_0^s \frac{\beta_{y_o}(s_k)\Delta K L_k}{2\sin(2\pi Q_{y_o})} \frac{1}{\beta_{y_o}(\tau)} \cos(2|\psi_{y_o}(\tau) - \psi_k| - 2\pi Q_{y_o}) \, \mathrm{d}\tau = \\ &= \frac{\beta_k \Delta K L_k}{4\sin(2\pi Q_{y_o})} \int_0^s 2\dot{\psi}_{y_o}(\tau) \cos(2|\psi_{y_o}(\tau) - \psi_k|) \cos(2\pi Q_{y_o}) \, \mathrm{d}\tau + \\ &+ \frac{\beta_k \Delta K L_k}{4\sin(2\pi Q_{y_o})} \int_0^s 2\dot{\psi}_{y_o}(\tau) \sin(2|\psi_{y_o}(\tau) - \psi_k|) \sin(2\pi Q_{y_o}) \, \mathrm{d}\tau = \qquad (3.48) \\ &= C(s) + S(s), \qquad (3.49) \end{aligned}$$

where $\psi_k = \psi_{y_o}(s_k)$. Naming $(C)$ the cosine part of the integral and $(S)$ the sine one, we can develop separately the equation for cases $\psi_{y_o}(s) > \psi_k$ and $\psi_{y_o}(s) < \psi_k$.

When $\psi_{y_o}(s) > \psi_k$ for the $(C)$ part we obtain

$$(C) = \frac{\beta_k \Delta K}{2\sin(2\pi Q_{y_o})} \cos(2\pi Q_{y_o}) \sin(\psi_{y_o}(s)) \cos(\psi_{y_o}(s) - 2\psi_k). \tag{3.50}$$

For the sine part (S), we split the integration as

$$\begin{aligned} (S) &= \frac{\beta_k \Delta K L_k}{4} \int_0^s 2\dot{\psi}(\tau) \sin(2|\psi_{y_o}(\tau) - \psi_k|) \, \mathrm{d}\tau = \\ &= \frac{\beta_k \Delta K L_k}{4} \left\{ -\int_0^{s_k} 2\dot{\psi}_{y_o}(\tau) \sin(2(\psi_{y_o}(\tau) - \psi_k)) \, \mathrm{d}\tau + \int_{s_k}^s \dot{\psi}_{y_o}(\tau) \sin(2(\psi_{y_o}(\tau) - \psi_k)) \, \mathrm{d}\tau \right\} = \\ &= \cdots = \frac{\beta_k \Delta K L_k}{4} \left(2 - \cos(2\psi_k) - \cos(2(\psi_{y_o}(s) - \psi_k)\right) = \\ &= \frac{\beta_k \Delta K L_k}{2} - \frac{\beta_k \Delta K L_k}{2} \cos(\psi_{y_o}(s)) \cos(2\psi_k - \psi_{y_o}(s)). \end{aligned} \tag{3.51}$$

Summing (3.50) and (3.51) we get

$$\Delta\psi_y(s) = \frac{\beta_k \Delta K L_k}{2} + \frac{\beta_k \Delta K L_k}{2\sin(2\pi Q_{y_o})} \cos(2\psi_k - \psi_{y_o}(s)) \sin(\psi_{y_o}(s) - 2\pi Q_{y_o}). \tag{3.52}$$

For $\psi_{y_o}(s) < \psi_k$, following the same procedure as before, we obtain

$$\Delta\psi_y(s) = \frac{\beta_k \Delta K L_k}{2\sin(2\pi Q_{y_o})} \sin(\psi_{y_o}(s)) \cos(\psi_{y_o}(s) - 2\psi_k + 2\pi Q_{y_o}). \tag{3.53}$$

Considering the normalized phase $\mu(s) = \psi(s)/2\pi$ we get

$$\Delta\mu_y(s, s_k) = \begin{cases} \dfrac{\beta_k \Delta K L_k}{4\pi} + \dfrac{\beta_k \Delta K L_k}{4\pi\sin(2\pi Q_{y_o})} \cos(2\psi_k - \psi_{y_o}(s)) \sin(\psi_{y_o}(s) - 2\pi Q_{y_o}), & \text{for } s \geq s_k, \\ \dfrac{\beta_k \Delta K L_k}{4\pi\sin(2\pi Q_{y_o})} \sin(\psi_{y_o}(s)) \cos(\psi_{y_o}(s) - 2\psi_k + 2\pi Q_{y_o}), & \text{for } s < s_k. \end{cases} \tag{3.54}$$

Recognizing the definition of tune shift from Eq. (3.29) we get

$$\Delta\mu_y(s, s_k) = \begin{cases} \Delta Q_{y_k} + \dfrac{\Delta Q_{y_k}}{\sin(2\pi Q_{y_o})} \cos(2\psi_k - \psi_{y_o}(s)) \sin(\psi_{y_o}(s) - 2\pi Q_{y_o}), & \text{for } s \geq s_k, \\ \dfrac{\Delta Q_{y_k}}{\sin(2\pi Q_{y_o})} \sin(\psi_{y_o}(s)) \cos(\psi_{y_o}(s) - 2\psi_k + 2\pi Q_{y_o}), & \text{for } s < s_k. \end{cases} \tag{3.55}$$

A quadrupole error, therefore, produces a phase beating wave whose amplitude is given by the corresponding tune shift, and presents a step equal to the tune shift at the impedance location. The step will be positive for focusing errors, or negative for defocusing ones. In most of the cases an impedance behaves as a defocusing quadrupole error giving rise to a descending step into the beating wave at the impedance location.

The analytical formula in Eq. (3.54) has been benchmarked with MAD-X [49]. Figure 3.3 shows the phase advance step and wave provoked by a quadrupole error in section 71 in the PS as seen from the 40 beam position monitors: a good agreement between the analytical approach and MAD-X can be appreciated.

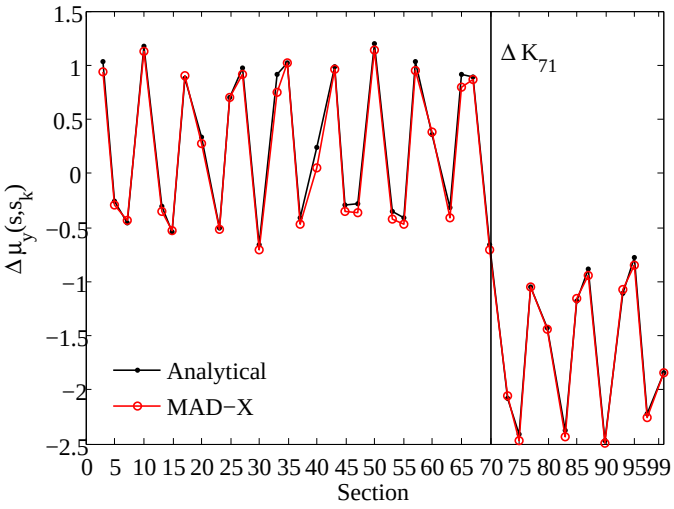


Figure 3.3: Phase advance beating provoked by a quadrupole error in section 71 in the PS calculated with MAD-X and the analytical formula.

A distributed impedance like the resistive wall and the space charge, on the contrary, will produce a smooth descent in the beating wave. Since the impedance is distributed, we can calculate

the response in phase $\Delta\mu_y(s)$ taking the limit of Eq. (3.54) for $L_k \to \mathrm{d}s_k$. We have

$$\mathrm{d}\mu_y(s,s_k) = \begin{cases} \mathrm{d}Q(s_k) + \dfrac{\mathrm{d}Q(s_k)}{\sin(2\pi Q_{y_o})}\cos(2\psi_y(s_k) - \psi_{y_o}(s))\sin(\psi_{y_o}(s) - 2\pi Q_{y_o})\,\mathrm{d}s_k, & \text{for } s \geq s_k, \\ \dfrac{\mathrm{d}Q(s_k)}{\sin(2\pi Q_{y_o})}\sin(\psi_{y_o}(s))\cos(\psi_{y_o}(s) - 2\psi_y(s_k) + 2\pi Q_{y_o})\,\mathrm{d}s_k, & \text{for } s < s_k, \end{cases} \tag{3.56}$$

with

$$\mathrm{d}Q(s_k) = \frac{\beta_y(s_k)\Delta K^{distr}}{4\pi}\mathrm{d}s_k. \tag{3.57}$$

The phase advance beating is therefore calculated as

$$\Delta\mu_y(s) = \oint_C \mathrm{d}\mu_y(s,s_k). \tag{3.58}$$

## 3.3 Noise impact on the phase advance measurement

Before proceeding to the reconstruction algorithm, we are interested in the accuracy reachable in case of real phase advance measurements, where the unavoidable presence of noise sets a lower limit in the magnitude of the impedance that can be localized with this technique.

We will consider a simple model in which the measured signal presents an additive Gaussian noise $n(t)$ of standard deviation $\sigma_n$. The phase advance is measured between two beam position monitor from sinusoidal signals $s_1$ and $s_2$ of same frequency $Q_o$, amplitude $A$ and normalized phases $\mu_1$ and $\mu_2$:

$$\mathrm{BPM}_1 \to s_1(N) = A\cos(2\pi Q_o N T_o + 2\pi\mu_1) + n(NT_o), \tag{3.59}$$

$$\mathrm{BPM}_2 \to s_2(N) = A\cos(2\pi Q_o N T_o + 2\pi\mu_2) + n(NT_o), \tag{3.60}$$

where $N$ is the number of recorded turns and $T_o$ the revolution period.
We can define the *Noise over Signal Ratio* $NSR$, as $NSR = \sigma_n/A$.

Since we are interested in the betatron tune shift with intensity, that is in the order of $\Delta Q \simeq 0.01$ or less, we need sufficient frequency resolution. A classical FFT will resolve $\Delta Q^{min} \propto 1/N$ while accurate iterative methods like SUSSIX [50] and NAFF [51] can give higher resolution up to $\Delta Q^{min} \propto 1/N^4$ in case of pure sinusoidal signals filtered with Hanning window.

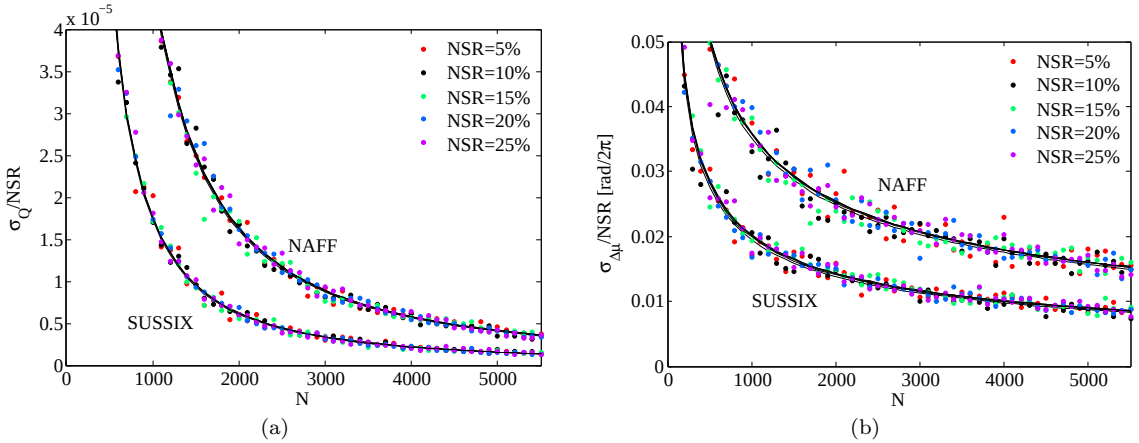


Figure 3.4: Normalized standard deviation of tune (a) and phase advance (b) measurements with NAFF and SUSSIX. The algorithm runs over 100 measurements for $N$ up to 5500 turns with additive Gaussian noise with $NSR \in (5\%, 10\%, 15\%, 20\%, 25\%)$. Dots are the simulated data, lines are the fit.

In the case of noisy signals, the accuracy becomes poorer but still higher than a normal FFT: Figures 3.4a and 3.4b show the reconstructed tune and phase advance for increasing number of

turns and noise levels. As we can see the two codes are comparable with a better accuracy for SUSSIX that will be therefore used for the phase advance measurements. Fitting the curves we get

$$\sigma_Q = F_Q \frac{NSR}{N\sqrt{N}}, \tag{3.61}$$

for the accuracy in tune determination,

$$\sigma_{\Delta\mu} = F_{\Delta\mu} \frac{NSR}{\sqrt{N}}, \tag{3.62}$$

for the accuracy in phase advance determination, and, in analogous way

$$\sigma_a = F_a \frac{NSR}{\sqrt{N}}, \tag{3.63}$$

for the accuracy in amplitude. The $F$ coefficients depend on the noise distribution and the method adopted for the parameter accuracy determination: in SUSSIX $F_Q \simeq 0.55$, $F_{\Delta\mu} \simeq 0.63$ and $F_a \simeq 1.01$; in NAFF $F_Q \simeq 1.46$, $F_{\Delta\mu} \simeq 1.12$ and $F_a \simeq 2.11$.

What we are interested in, by the way, is not only the accuracy in phase advance measurements, but the accuracy of the phase advance *slope* with intensity. If we imagine to have a set of $M$ phase advance measurements at different intensities $X \in (X_1, X_2, \ldots, X_M)$ with negligible uncertainty in the intensity measurement, assuming the same accuracy in phase advance for each measurement as given in (3.62), the accuracy in the phase advance slope with intensity $\sigma_{\Delta\mu/\Delta N_b}$ will be given by [52]

$$\sigma_{\Delta\mu/\Delta N_b} = F_{\Delta\mu} \frac{NSR}{\sigma_X \sqrt{M}\sqrt{N}}, \tag{3.64}$$

where $\sigma_X$ is the standard deviation of the intensity scan $X$. This equation deserves some comments. In order to increase the resolution on phase advance (i.e. reduce $\sigma_{\Delta\mu/\Delta N_b}$) one could:

- Increase the number of turns $N$. This can be done settling the chromaticity $\xi$ very close to zero and reducing detuning with amplitude if necessary (with octupoles). In this way a kicked beam will oscillate at almost constant amplitude and the BPM system can acquire the transverse oscillations up to a limit given by the data storage memory. For example, the maximum number of turns that can be stored in the CERN-PS machine is $N = 5000$.

- Increase the number of measurements $M$. If the machine refill time is negligible, this parameter can be pushed typically up to $M = 100$. A too long measurement time could be affected by the machine parameter drift with time.

- Increasing the intensity scan $\sigma_X$. This is limited, at low intensity, by the BPM gain that needs always to be adjusted to the intensity range under study, at high intensity, by machine non-linearities that would affect the beam betatron motion, or by beam instabilities (TMCI, etc.).

- Decreasing the $NSR$. This can be done up to some extent using an SVD noise reduction to clean the noise correlated between BPMs, or enhancing the signal amplitude (kicking more). This last option is limited by the machine physical aperture and non-linearities such as detuning with amplitude.

- Decreasing the $F_{\Delta\mu}$. This factor is related to the noise distribution coming from the BPM system, and to the method used to perform the FFT. The former can hardly be reduced being linked to the machine hardware, as well as the second, related to the specific method used to calculate the FFT.

## 3.4 The impedance database: example of the PS machine

Modern accelerator machines are carefully monitored from the impedance point of view. We present here the PS impedance database developed in order to keep track of the machine impedance and compare the impedance measurements and the expectations.

Taking the example of a Gaussian beam, we defined the tune shift induced by an impedance source in Eq. (3.43). Taking the derivative with respect to the intensity scan we can define the *tune shift with intensity* $\Delta Q_{y_k}/\Delta N_b$ as

$$\Delta Q_{y_k}/\Delta N_b = -\frac{q^2}{8\pi^{3/2}\beta E_o \sigma_\tau}\beta_{y_k}(s_k) Im\left(Z_k^{eff}\right) L_k, \tag{3.65}$$

and for distributed impedances,

$$\Delta Q_y/\Delta N_b = -\frac{q^2}{8\pi^{3/2}\beta E_o \sigma_\tau}\oint_C \beta_y(s) Im\left(Z^{eff}\right) \mathrm{d}s. \tag{3.66}$$

We estimated the phase advance signal induced from a localized impedance source in Eq. (3.55) and we can define $A_k$ as the impedance-induced phase advance beating amplitude as

$$A_k = \frac{\Delta Q_{y_k}/\Delta N_b}{\sin(2\pi Q_{y_o})} = \frac{\beta_k \Delta K/\Delta N_b L_k}{4\pi \sin(2\pi Q_{y_o})}. \tag{3.67}$$

If the impedance, on the other side, is distributed, the impedance-induced phase advance beating signal will be a superposition of distributed sources whose result, as we will see later on, is a decreasing slope in the phase advance versus intensity.

The amplitude $A_k$ should be directly compared to the measurement accuracy $A_{th} = \sigma_{\Delta\mu/\Delta N_b}$ in order to predict the measurement feasibility. At the same way, considering both Eqs. (3.67) and (3.65) we can define an impedance threshold $Z_{th}$ as

$$Z_{th} = -A_{th}\frac{8\pi^{3/2}\beta E_o \sigma_\tau}{\beta_y(s)\, q^2}\sin(2\pi Q_{y_o}), \tag{3.68}$$

where we immediately notice the inverse proportionality with the $\beta$ function: increasing the $\beta$ function increases the impedance-induced phase advance signal, reducing the corresponding impedance threshold.

The impedance budget has been calculated for different energies: injection, ($T = 1.4\,\mathrm{GeV}$), flat bottom ($T = 2\,\mathrm{GeV}$) and extraction ($T = 25\,\mathrm{GeV}$). We might notice that at different energies the impedance changes accordingly to the relativistic $\beta$, and the indirect space charge, in particular, can become a relevant source of distributed impedance.

The accelerator lattice parameters, such as the horizontal and vertical tunes $Q_{x,y}$, the *twiss* functions (phase advance $\mu(s)$, $\beta$ function $\beta_{x,y}(s)$, dispersion $D_{x,y}(s)$, etc.) change depending on the energy and the lattice configuration. In particular, the variation of the $\beta$ function can directly affect the effect of the impedance on the transverse beam dynamics. Table B.1 resumes the most important parameters relevant for the 2 GeV lattice.

The detrimental effect of the impedance is related to the spectrum sampled by the beam. Recalling the effective impedance definition in Eq. (3.37), for a Gaussian beam we have

$$\rho(t) = \frac{1}{\sqrt{2\pi}\sigma_t} e^{-\frac{t^2}{2\sigma_t^2}}, \tag{3.69}$$

from which the spectrum

$$S(\omega) = e^{-\frac{(\omega\sigma_t)^2}{2}} \tag{3.70}$$

A typical beam used for high intensity scans is the *TOF* beam whose parameters are summarized in the following table:

Once energy and beam parameters are defined the effective impedance corresponding to each element in the accelerator lattice, lumped or distributed, can be quantified. In the following we present the main elements that have been so far evaluated. The energy of interest is $T = 2\,\mathrm{GeV}$ as it is the one adopted for the transverse impedance localization measurements.

| TOF beam | Parameter | Value |
|---|---|---|
| Momentum spread | $\mathrm{d}p/p_o$ | $2 \cdot 10^{-3}$ |
| Bunch length | $4 \cdot \sigma_t$ | 90 ns |
| Horizontal emittance | $\varepsilon_x$ | 15 $\mu$rad |
| Vertical emittance | $\varepsilon_y$ | 8 $\mu$rad |

Table 3.1: TOF beam parameters used in the PS impedance budget.

**Resistive wall and indirect space charge**

The resistive wall impedance has been evaluated taking into account the different materials that constitute the beam pipe: 20% of the machine beam pipe is made of 1.5 mm thick Inconel Alloy X750 (conductivity $\sigma_c = 8.3 \cdot 10^5$ S/m) and 70% of 2mm thick stainless steel (conductivity $\sigma_c = 1.3 \cdot 10^6$ S/m). The remaining 10% is constituted by insertion devices treated separately. The vacuum chamber, that has the so-called *racetrack* shape, has been considered to be round with a radius of 35 mm or flat. The transverse effective impedance is about the same for the two geometries: 0.29 MΩ/m and 0.35 MΩ/m for respectively the round chamber (35 mm of radius) and parallel plates. For the parallel plates, the dipolar and quadrupolar impedance contributions are of same sign for the vertical plane and the total vertical impedance is increased by a factor 1.2 with respect to the round chamber case, but for the horizontal plane the parallel plates model gives zero total impedance due to the perfect compensation of dipolar and quadrupolar components of the impedance. The impedance has been evaluated with the $2D - Axi$ code [13] taking into account the indirect space charge contribution. In table 3.2 we have summarized the results of the indirect space charge contribution for injection ($T = 1.4$ GeV), flat bottom ($T = 2$ GeV) and extraction (25 GeV) kinetic energies. We assume that the parallel plates and the smaller round chamber can be used for the vertical plane, while an intermediate value between the two round pipes can be used for the horizontal plane. Focusing at 2 GeV, Figure 3.5 shows the vertical (i.e. equal to the

| Kinetic energies | 1.4 GeV | 2 GeV | 25 GeV |
|---|---|---|---|
| Flat chamber | 6.0 MΩ/m | 3.7 MΩ/m | <0.5 MΩ/m |
| Round chamber (r=35 mm) | 4.9 MΩ/m | 3.0 MΩ/m | <0.5 MΩ/m |
| Round chamber (r=73 mm) | 1.1 MΩ/m | 0.7 MΩ/m | <0.1 MΩ/m |

Table 3.2: Indirect space charge contributions to the total transverse effective impedance at different kinetic energies for round chamber and parallel plates.

horizontal) dipolar and quadrupolar impedance calculated with the $2D - Axi$ code. Operating a Fourier transform we get the wakefields corresponding to the calculated impedances. Figure 3.6 shows both the calculated dipolar and quadrupolar wakefields.

**Steps, vacuum ports, bellows**

Other elements, such as bellows, connections between the beam pipe and the vacuum pumps and other beam pipe step transitions have been evaluated because, notwithstanding their low impedance, due to their number, the total contribution cannot be ignored. For the machine impedance budget it has been evaluated the contribution of 200 bellows, 100 vacuum pumps and 60 vacuum chamber steps.

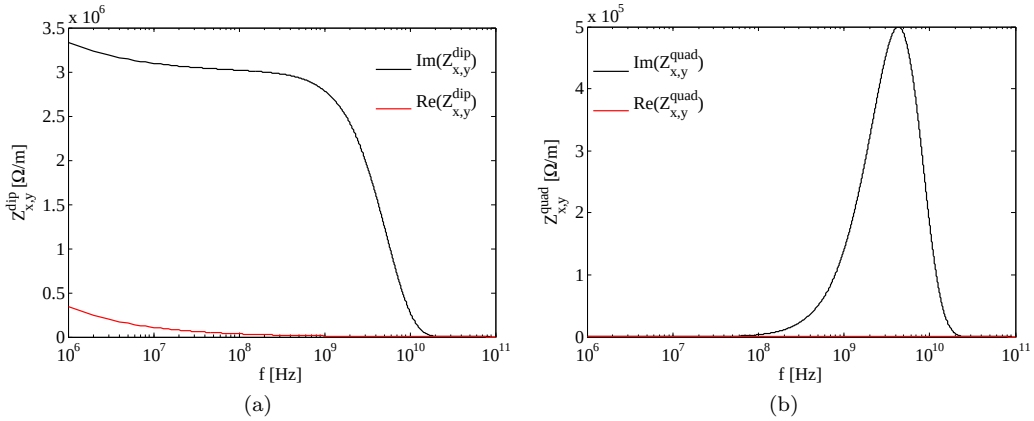


Figure 3.5: Total dipolar (a) and quadrupolar (b) resistive wall impedance calculated for the PS accelerator. The impedance includes the indirect space charge contribution at 2 GeV.

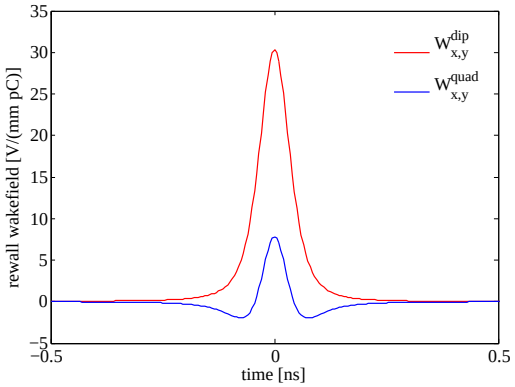


Figure 3.6: Total resistive wall wakefield for the PS accelerator. The wakefield includes the indirect space charge contribution at 2 GeV.

### Kickers

Another important source of impedance is represented by the kickers. There are different kinds of kickers which give different contributions to the transverse effective impedance. Some of them (delay-line kickers) have a segmented ferrite inside, while others not. These kickers have been simulated with CST Microwave Studio [10] and compared with measurements [53] revealing a very good agreement in particular for the vertical plane. Also the other segmented kickers have been simulated in the same way, while, at the moment, for the lumped inductance kickers, which are not segmented, the impedance has been evaluated by using the field matching technique [11] also taking into account the quadrupolar impedance component [54]. The contribution of all the kickers is less than 0.03 MΩ/m in the horizontal plane, and about 1.4 MΩ/m in the vertical one.

### Cavities

RF cavities have been also taken into account, but a first estimate of the contribution of the 10 MHz cavities does not seem to indicate a strong impact in the transverse plane.

### Septa

Finally, a first estimate of the septa contribution (electrostatic and magnetic) does not seem to dramatically change the total budget, giving an effective impedance of some kΩ/m.

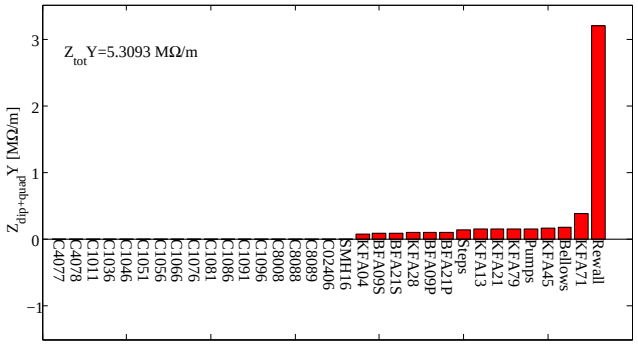


Figure 3.7: Vertical effective impedance for elements in the PS impedance model. Cavities are called C, kickers KFA or BFA, septa SMH or SES.

According to the above analysis Figure 3.7 shows the calculation of the effective impedance $Z_k^{eff}$ for each element (its length $L_k$ is included). The full impedance model is reported in App. C. As already introduced, most of the impedance is dominated by the indirect space charge (in the ReWall contribution) and the kickers. Figures 3.7 and 3.8 summarize the effective impedance and the corresponding tune shift for the vertical plane.

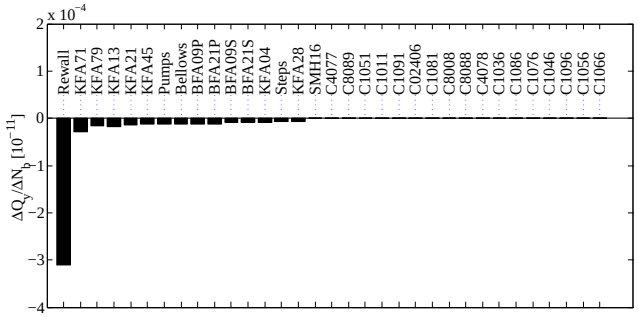


Figure 3.8: Vertical tune shift with intensity normalized to $10^{11}$ ppb for each element in the PS impedance model.

Figure 3.9 shows the total impedance calculated summing the impedances of each element as a function of frequency up to 1 GHz.

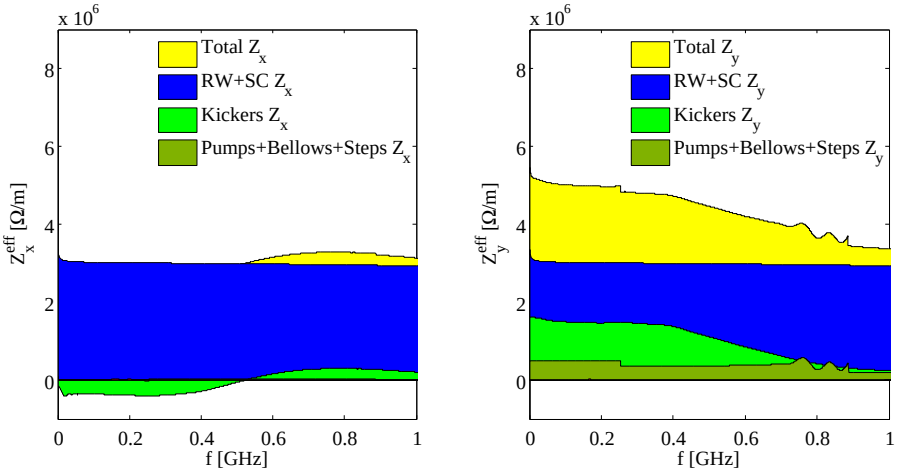


Figure 3.9: Total horizontal (left) and vertical (right) PS impedance at 2 GeV in function of frequency.

## 3.5 The HEADTAIL code

HEADTAIL is a macro particle code in which the interaction of a beam with an impedance is simulated. The existent version of HEADTAIL [55, 56] has been extended [57] in order to include the possibility of having distributed impedance kicks in different accelerator locations: this is important if one is interested in the study of the phase advance variation with intensity between consecutive BPMs.

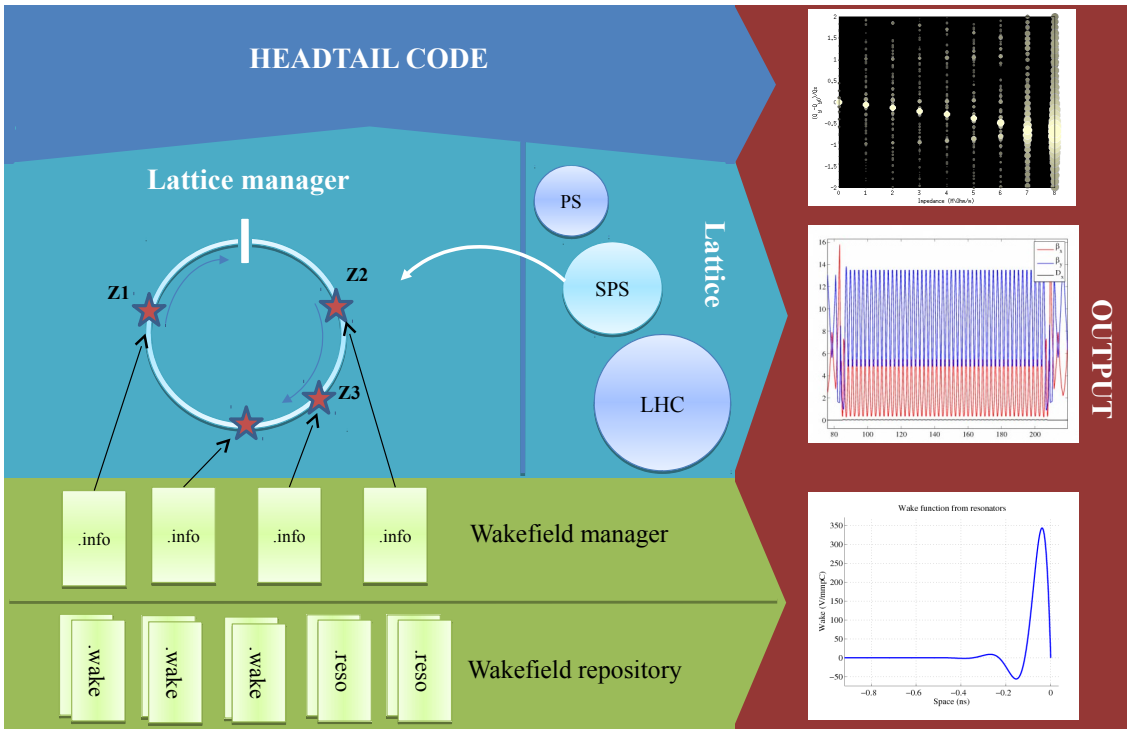


Figure 3.10: Structure of the HEADTAIL code interface with wakefield manager and lattice manager.

Figure 3.10 shows the HEADTAIL structure interface: the wakefields are stored in a *wakefield repository* where these are managed and inserted in the accelerator lattice by a *wakefield manager*. The *lattice repository* allows the user to choose between different accelerator machine and the corresponding MAD-X descriptions. Once the machine and the wakefields are defined, the HEADTAIL simulation can be executed and the output collected. A specific description of each module will be given in the following.

- **Wakefield Repository:** The wake repository consists of a collection of *.wake* and *.reso* files that respectively describe a generalized or a resonator wakefield: a generalized wakefield, following the convention initiated in [58], is described by 9 columns (time $T$[ns], dipolar wakes $W_x^{dip}$ [V/(mm pC)] and $W_y^{dip}$ [V/(mm pC)], quadrupolar wakes $W_x^{quad}$ [V/(mm pC)] and $W_y^{quad}$ [V/(mm pC)], coupled terms $W_{x,y}^{dip}$ [V/(mm pC)] and $W_{x,y}^{quad}$ [V/(mm pC)], constant terms $W_x^{const}$ [V/pC] and $W_y^{const}$ [V/pC], and longitudinal wake $W^{long}$ [V/pC]), over which a subset can be chosen for simulation as specified in the *wake manager*; a resonator impedance is given by the definition of the transverse and longitudinal quality factor, resonant frequency and shunt impedance.

- **Wakefield Manager:** In order to be able to run simulations with different impedances (resistive wall, kickers, cavities, etc.), placed in different locations, the *wakefield manager* will read a *.info* file that contains information about the impedance we want to place in the lattice. As resumed in the example of Tab. 3.3 the wake specified by `NAME` can be placed in an arbitrary `POSITION` in the lattice. Specified the kind of `INTERACTION` and the

TABLE_TYPE ("0" for a resonator, "1" for a wake table with columns specified by TABLE_TYPE) the wake can be scaled to match specified $\beta$ functions (useful for wakes that represent lumped description of long devices) or multiplied by a multiplication coefficient. In the given example

| | |
|---|---|
| NAME: | REWALL |
| POSITION: | 201.06 |
| INTERACTION: | IMPEDANCE |
| TYPE: | 1 |
| TABLE_TYPE: | 4 |
| SCALE: | 1 |
| BETX: | 17.35 |
| BETY: | 16.88 |
| MULTIPLY: | 0 |
| MULTIPLY_COEFF: | - |

Table 3.3: Wake manager description for a resistive wall kick: example of a *REWALL.info* file.

the *REWALL.info* file will point to the *REWALL.wake* file where the wake table is given. Specifying a different value for TABLE_TYPE it is possible to select a subset of the 9 columns required for the generalized wakefield description. Table 3.4 specifies the components selected corresponding to each choice of TABLE_TYPE.

| TABLE TYPE | Columns in the *.wake* file |
|---|---|
| 1 | $T$, $W^{long}$ |
| 2 | $T$, $W_x^{dip}$, $W_y^{dip}$ |
| 3 | $T$, $W_x^{dip}$, $W_y^{dip}$, $W^{long}$ |
| 4 | $T$, $W_x^{dip}$, $W_y^{dip}$, $W_x^{quad}$, $W_y^{quad}$ |
| 5 | $T$, $W_x^{dip}$, $W_y^{dip}$, $W_x^{quad}$, $W_y^{quad}$, $W_{x,y}^{dip}$, $W^{long}$ |
| 6 | $T$, $W_x^{dip}$, $W_y^{dip}$, $W_x^{quad}$, $W_y^{quad}$, $W_{x,y}^{dip}$, $W_{x,y}^{quad}$ |
| 7 | $T$, $W_x^{dip}$, $W_y^{dip}$, $W_x^{quad}$, $W_y^{quad}$, $W_{x,y}^{dip}$, $W_{x,y}^{quad}$, $W^{long}$ |
| 8 | $T$, $W_x^{dip}$, $W_y^{dip}$, $W_x^{quad}$, $W_y^{quad}$, $W_{x,y}^{dip}$, $W_{x,y}^{quad}$, $W_x^{const}$, $W_y^{const}$ |
| 9 | $T$, $W_x^{dip}$, $W_y^{dip}$, $W_x^{quad}$, $W_y^{quad}$, $W_{x,y}^{dip}$, $W_{x,y}^{quad}$, $W_x^{const}$, $W_y^{const}$, $W^{long}$ |

Table 3.4: Different table selection for wakefield components.

- **Lattice repository:** HEADTAIL is interfaced with MAD-X for the lattice generation and machine parameters matching (like tune and chromaticity). The machine lattices are kept inside a specific folder with the name of the machine. Once a machine is specified, HEADTAIL will perform the following operations:

  1. Reading the *.info* files specified in the configuration file.
  2. Placing the impedances along the lattice and, if needed, installing new element in the lattice.
  3. Making a structure of each element to handle the twiss parameters easily.
  4. Constructing the transport matrices from one element to the other.
  5. If the impedances have to be lumped at one point in the ring, summing the total wakefield and using the one turn map for transport.

  Four types of elements are present at the moment:

  – START: always present, it is the starting point of the machine.

- `H/VMONITOR`: horizontal (H) or vertical (V) monitors corresponding to the BPM specified in the MAD-X lattice.
- `IMPEDANCE`: element corresponding to the wakefield interaction point.
- `AC DIPOLE`: AC dipole beam excitation element.

Every element in the lattice is treated as a structure object: the lattice manager creates a structure in HEADTAIL with all its optic functions. Once the lattice is created, each element is characterized by a 4-D matrix associated to the optic transport from its point in the lattice to the following one. HEADTAIL therefore transports the particles for the specified number of turns updating synchrotron motion, chromaticity and octupole detuning as a rotation at the end of each turn.

The process of lumping impedances in one location from different ring positions deserves further explanation. From Eq. (3.65) we understand that the tune shift $\Delta Q_{y_k}/\Delta N_b$ is proportional to the $\beta_{y_k}(s_k)$ function in the kick point $s_k$ and the impedance itself $\left(Z_k^{eff}\right) L_k$. We can therefore write:

$$\Delta Q_{y_k}/\Delta N_b \propto \beta_{y_k} Z_k L_k. \tag{3.71}$$

Lumping the $Z_k$ impedance at the `START` where the $\beta$ function is $\beta_o$ we would have

$$\Delta Q_{y_o}/\Delta N_b \propto \beta_{y_o} Z_k L_k. \tag{3.72}$$

To have the same effect of the impedance in $s_k$ we need to scale $Z_k$ at `START` by

$$Z_o = \beta_{y_k}/\beta_{y_o} Z_k L_k. \tag{3.73}$$

For an homogeneous distribution of impedance along the ring we would have

$$Z_o = \oint_C \beta_y(s)/\beta_{y_o} Z \mathrm{d}s = ZC\bar{\beta}/\beta_{y_o}, \tag{3.74}$$

where $\bar{\beta}$ is the average $\beta$ function in the plane of interest.[3]

- **HEADTAIL:** The core part of the code is shown in Fig. 3.11. The simulation setup is listed in a configuration (*.cfg*) file, where information like number of turns to be simulated, wake manager directives, machine lattice, tune and chromaticities, etc., are specified (see App. D.1 for an example of the PS HEADTAIL model at 2 GeV). After the file opening and the lattice and bunch distribution initialization, the loop over the number of turns starts. For each turn all the elements are processed and particles are transported between them. Before each turn iteration the bunch is sliced in a specified number of slices and the macro particles distributed among them. If the `START` element is processed, the *prt.dat* file is written with useful centroid motion information. A restricted set of centroid motion information is written on separate files when an element `H/VMONITOR` is processed. When an `IMPEDANCE` interaction is modeled, the wake kick is calculated for each of the slice and then applied to each particle in the bunch. When an `AC DIPOLE` excitation is set up the beam interacts is excited at the AC dipole driving frequency (see Sec. 4.3 for more details).

- **OUTPUT:** All the simulation informations and results are collected in a specific folder in which the following list of files are collected:

  1. `HDTL_average_lattice.dat`: This file contains a MAD-X twiss file for the complete machine simulated.
  2. `HDTL_selected_lattice.dat`: This file contains a MAD-X file for the elements that were selected for the tracking.
  3. `Prb.dat`: This file contains a snapshot of the phase space (id, $x$,$x'$,$y$,$y'$,$z$,$z'$) at the turns selected in the configuration file. 100 particles are taken randomly along the first bunch.

[3] One should note that $\bar{\beta}$ is different from the $\hat{\beta} = R/Q$ of the smooth approximation. In the SPS, for example, with an integer tune of 26 in the vertical plane we get $\hat{\beta} = 41$m and $\bar{\beta} = 52$m, i.e. 25% more.

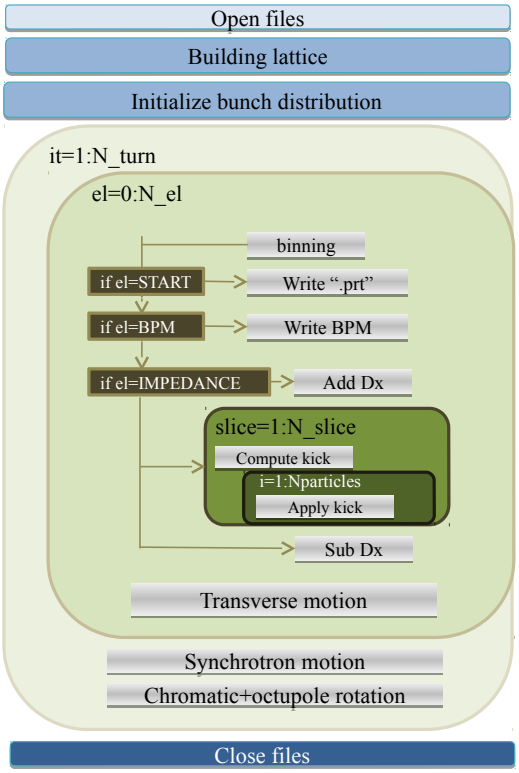


Figure 3.11: Internal structure of the HEADTAIL code.

4. `Pini.dat`: This file contains a snapshot of the initialized phase space ($x$,$x'$,$y$,$y'$,$z$,$z'$), 1000 particles are taken randomly.
5. `Bunchds.dat`: This file contains a snapshot of the longitudinal distribution in space $s$ [m] and particle density $N_p(s)$ for the bunch after all the interaction have been made at the turns selected in the configuration file. The bunch extends from -5$\sigma_b$ to +5$\sigma_b$ where $\sigma_b$ is the rms bunch length.
6. `Prt.dat`: General tracking information files referring to the `START` point in the lattice. The columns are given by:
   (a) Time step: sampled time in which the beam passes at START.
   (b) $\bar{X}$: average centroid $X$ [m].
   (c) $\bar{X'}$: average centroid $X'$ [rad].
   (d) $\bar{Y}$: average centroid $Y$ [m].
   (e) $\bar{Y'}$: average centroid $Y'$ [rad].
   (f) $\bar{Z}$: average centroid $Z$ [m].
   (g) $\bar{\mathrm{d}p/p}$: average centroid p/$p$.
   (h) $\bar{\sigma}_x$: average horizontal beam size [m][4].
   (i) $\bar{\sigma}_y$: average vertical beam size [m][4].
   (j) $\bar{\sigma}_z$: average longitudinal beam extension [m].
   (k) $\bar{\sigma}_{\mathrm{d}p/p}$: average beam momentum spread.
   (l) $\varepsilon_{x_n}$: beam normalized horizontal emittance [mm mrad][5].
   (m) $\varepsilon_{y_n}$: beam normalized vertical emittance [mm mrad][5].
   (n) $\varepsilon_l$: beam longitudinal emittance [eV s][5].

[4]since the starting point can have $\alpha_{x,y} \neq 0$, $< \sigma_{x,y} >$ are not generally referred to a flat ellipse.
[5]Calculated as $\varepsilon_y = \sqrt{< y^2 >< y'^2 > - < y >< y' >^2}$ for a centered beam.

(o) $J_x$: Horizontal action variable [m][6].
(p) $J_y$: Vertical action variable [m][6].
(q) $\varepsilon_l = 4\pi\sigma_l\sigma_{\Delta E}$: beam longitudinal emittance [eV s][7].
(r) $\rho_{y,z}$: Y-Z correlation.
(s) Effective number of particles $(N_{tot} - N_{lost})/N_{tot}$.

7. `*.track`: File containing the wake used in the simulated interactions sampled at each slice where the interaction is calculated.
8. `Sample.dat`: Net bunch energy loss per turn in case of longitudinal impedance. The file contains the turn number the energy loss per turn $\mathrm{d}p_{turn}$ [MeV], referred to the bunch under study.
9. `Hdtl.dat`: Headtail monitor emulator.
10. `Inph.dat`: Collects informations about the longitudinal matching number, total number of macro particles, bunch and slices used in the simulation, the percent of beam loss and the pipe average apertures.
11. `lumped.wake`: if the lump option is chosen, in this file will be printed the total wake weighted at `START`.

### 3.5.1 Example: single impedance source

A first simple case was simulated in HEADTAIL: a single PS kicker impedance source corresponding to the kicker KFA71 was placed at its position at 447.03 m from the `START` conventionally located at the reference BPM named `PR_UHV00`. The PS is divided in 100 sections and the $71^{th}$ corresponds to the one hosting the KFA71 kicker.

A TOF bunch was simulated with the parameters reported in Tab. 3.1, over an intensity scan from $2 \cdot 10^{11}$ to $2 \cdot 10^{12}$ ppb. The HEADTAIL configuration file is listed in App. D.1. The phase advance from the reference BPM has been therefore measured for each intensity and the phase advance shift calculated.

The black curve in Fig. 3.12 shows the phase advance shift with intensity. A clear step in the phase beating signal is visible corresponding to the KFA71 location.

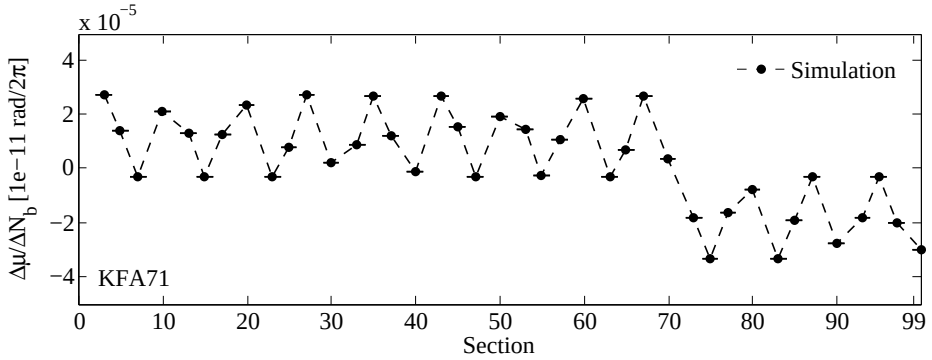


Figure 3.12: Phase advance shift with intensity simulated with HEADTAIL in the case of the KFA71 impedance.

We reconstruct the impedance position recurring to a least square matrix inversion using the response matrix calculated with Eq. (3.54). Given a $N_{BPM}$ number of BPMs and $N_k$ number of reconstruction points where an impedance kick $\Delta K/\Delta N_b$ could be given, we define $S$ as the $N_{BPM} \times N_k$ response matrix calculated with Eq. (3.54). In our case $N_{BPM} = 42$, the total number of simulated BPMs, and we placed the impedance reconstruction points in each of the 100 machine sections, so that $N_k = 100$ and $S$ has dimensions $42 \times 100$. We define the vector $\vec{B}$ the vector

[6]Calculated as $J_x = \frac{1}{2\beta_x}(x^2 + (\beta x' + \alpha_x x)^2)$.

[7]This is an approx. for a beam whose dimension in longitudinal phase space are smaller in comparison to the bucket dimension.

containing the values of the phase advance shift with intensity at the BPM locations, and $\Delta\vec{K}/\Delta N_b$ the vector of the impedance kick strength $\Delta K/\Delta N_b$ at the reconstruction points. We therefore have

$$\vec{B} = S \cdot \Delta K/\vec{\Delta} N_b, \tag{3.75}$$

and the problem of the impedance localization reduces to the pseudo-inversion of the matrix $S$ in order to get the correct value of $\Delta\vec{K}/\Delta N_b$.

We can constraint the problem solution with the following observations coming from the physics of beam-impedance interaction:

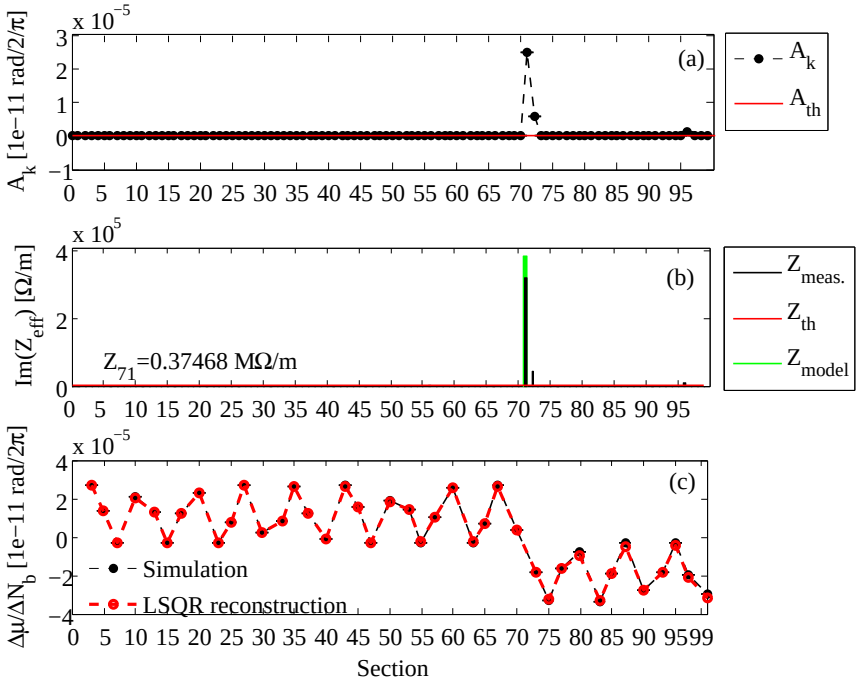


Figure 3.13: Reconstruction of the kicker KFA71 impedance simulated with HEADTAIL. (a) shows the reconstructed impedance-induced phase advance beating amplitude (in black) and the accuracy threshold (in red); (b) shows the reconstructed impedance (in black), the expected from the impedance model (in green) and the threshold by the Gaussian noise added to the BPM signals (in red) which is zero in this case; (c) shows the simulated phase advance slope with intensity at the BPM locations (in black) and the slope from the reconstructed impedance positions (in red).

1. **Defocusing impedance**: the observed tune shift negative is (at least in the vertical plane) for a kicker device, we can constraint the reconstruction since imposing $\Delta K/\Delta N_b > 0$ which means a defocusing impedance effect[8]. Imposing a $\Delta K^{max}/\Delta N_b$ corresponding to the impedance of 1 MΩ/m we can also set an upper limit to the values of $\Delta K/\Delta N_b$.

2. **Total impedance**: The sum of the strength of each reconstructor should be close to the total machine impedance measured with the tune shift measurement.

3. **Impedance model**: The reconstruction location can be constrained excluding those positions in which a high impedance is not expected to be present (drifts, dipoles, etc.).

Figure 3.13(a) shows with the black curve, the reconstructed impedance-induced phase advance beating amplitude $A_k$, and with the red curve, the threshold of the measured accuracy, set in this case to zero since we performed a noise-free simulation. Figure 3.13(b) shows the impedance reconstructed values at the reconstructed positions (in black), together with the model expectation (in green) and the measurement threshold (in red). The impedance is correctly found in section 71

[8]Conventionally $\Delta K < 0$ corresponds to a defocusing element, here it is intended *with* sign.

and the magnitude is close to the expected one from the impedance model (`PE.KFA71` in App. C). The good quality of the reconstruction can be appreciated in Fig. 3.13(c) comparing the simulated (in black) and reconstructed (in red) phase advance slope.

Having virtually no noise in the simulation, the impedance threshold given by the accuracy reachable in the phase advance measurement is zero. Artificially introducing additive Gaussian noise to the measured BPM turn by turn signals, we can simulate the typical measured signal from a BPM, and crosscheck accuracy and reconstruction from Eqs. (3.64) and (3.68) where we considered for simplicity the machine average $\beta$ function. In the following we will show the study of the impedance reconstruction adding Gaussian noise with increasing standard deviation $\sigma_n$ ($0\,\mu$m, $10\,\mu$m, $30\,\mu$m and $50\,\mu$m) to the simulated BPM tracking signals.

Most of the information involved in the impedance localization measurement can be gathered in a *localization map* where we directly compare the accuracy in the phase advance measurement $\sigma_{\Delta\mu/\Delta N_b}$ and the impedance induced phase advance amplitude $A_k$. Figure 3.14 shows the illustrated cases of $\sigma_n \in (0\,\mu\text{m}, 10\,\mu\text{m}, 30\,\mu\text{m}$ and $50\,\mu\text{m})$: in the first two cases, the accuracy reachable is below the amplitude $A_k$ calculated for the section 71 (i.e. hosting the kicker KFA71) and the impedance, as shown in Fig. 3.15, can be localized; in the third case the accuracy starts to be comparable with the impedance and the reconstruction is not obvious; in the last case, the accuracy is not enough and the impedance cannot be localized. It is important to notice that:

1. The predicted and measured (from simulations) accuracy are in good agreement.

2. Having added a constant $\sigma_n$ does not imply a constant $NSR$ since the BPM signal amplitude varies with the $\beta$ function at the BPM locations.

3. The accuracy points lie on a line which is defined by Eq. (3.64) when $NSR$ is the independent variable. If we imagine to fix the impedance to be localized, i.e. we fix the amplitude $A_k$, we should set the number of measurements $M$, turns $N$, and the scan width $\sigma_X$, in a way that the accuracy in phase advance slope is below the amplitude $A_k$. If we imagine to fix, on the other side, the machine BPM system $NSR$, as it is often the case, we could infer the maximum amplitude (and therefore the maximum impedance), that could be localized.

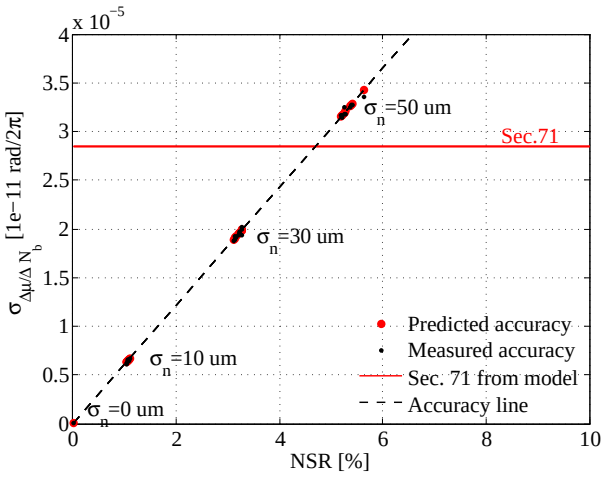


Figure 3.14: Localization Map showing the impedance induced phase advance amplitude for the kicker in section 71, the predicted and estimated phase accuracy in the different cases $\sigma_n \in (0\,\mu\text{m}, 10\,\mu\text{m}, 30\,\mu\text{m}$ and $50\,\mu\text{m})$ and the accuracy line. If the phase accuracy is below the red line, the impedance can be localized.

The localization map allows to quickly make predictions about the measurement requirements unifying the information about the machine impedance model and the machine BPM characteristics. For example we may infer that the maximum NSR allowed to localize the KFA71 kicker is $NSR \simeq 4\%$.

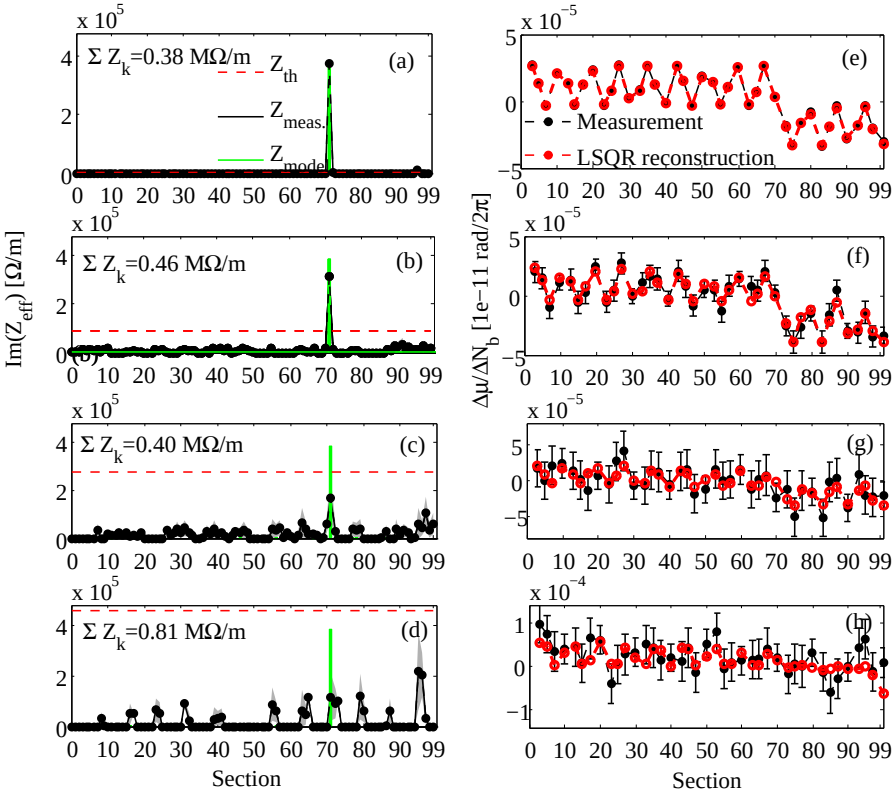


Figure 3.15: Impedance localization (left side) and reconstruction (right side) for $\sigma_n = 0\,$um (a,e), $\sigma_n = 10\,\mu$m (b,f), $\sigma_n = 30\,\mu$m (c,g) and $\sigma_n = 50\,\mu$m (d,h). Below $\sigma_n = 50\,\mu$m the impedance can still be reconstructed.

Figure 3.15, shows on the right side the phase advance slope in the four cases with the corresponding reconstruction curve. The phase measured can still be reconstructed for $\sigma_n = 10\,$um and $\sigma_n = 30\,$um while it appears to be corrupted in the last case. On the left side the corresponding impedance reconstruction is shown with the same conclusions.

### 3.5.2 Example: resistive wall

In accelerator machines, especially at relatively low energies, the resistive wall and indirect space charge impedance represent the major contribution to the machine impedance budget. The effect on the impedance localization measurement is not negligible. If we consider the previous case of Fig. 3.13 in which an impedance source was provoking a step at its impedance location, we can imagine that a distribute impedance will provoke a monotonic downward slope in the measured phase advance shift with intensity. This is illustrated in Fig. 3.16 where 100 kicks of resistive wall impedance and indirect space charge (see Fig. 3.6) were simulated with HEADTAIL.

The choice of 100 kicks implies an impedance kick roughly every 6 m in the PS machine with an average resistive wall kick given by $3\,\mathrm{M\Omega/m}/100 = 30\,\mathrm{k\Omega/m}$.

The reconstruction method is for this case slightly different. Since we have only distributed impedance, the condition $\Delta K/\Delta N_b > 0$ is over constrained and would lead to long calculation time for the minimization of the least square problem in Eq. (3.75). We can, instead, process the measured phase advance slope subtracting the signal provoked by an homogeneously distributed impedance. Given a value of $Z^{distr}$, we can calculate the equivalent $\Delta K^{distr}/\Delta N_b$ from Eq. (3.44). In particular, for a Gaussian bunch, we get

$$\frac{\Delta K^{distr}}{\Delta N_b} = -\frac{q^2}{2\sqrt{\pi}\beta E_o \sigma_\tau} Im\left(Z^{distr}\right). \tag{3.76}$$

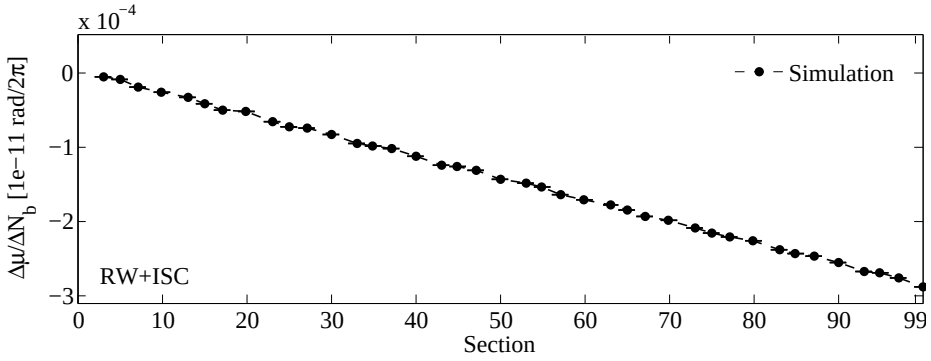


Figure 3.16: Phase advance shift with intensity simulated in HEADTAIL in the case of resistive wall and indirect space charge impedances.

Using this equivalent strength, we can calculate the response matrix from the whole accelerator to calculate $\Delta\mu^{distr}(s)/\Delta N_b$ from Eq. (3.58). Once the phase advance calculated from distributed sources is subtracted from the simulated one, the residual $|\vec{B} - S \cdot \Delta\vec{K}^{distr}/\Delta N_b|$ can be inverted following the procedure described in Sec. 3.5.1 where we set a maximum number of iterations of $T_{max} = 1000$ in the least square inversion. Figure 3.17 shows the values of the residual norm (a) and the least square iterations (b) varying $Z^{distr}$. For values smaller than 2.8 MΩ/m the convergence time sharply saturates to $T_{max}$, while it is constant for higher values. On the other side, the residual norm grows from 2.8 MΩ/m. Figure 3.18 shows the reconstruction of the phase ad-

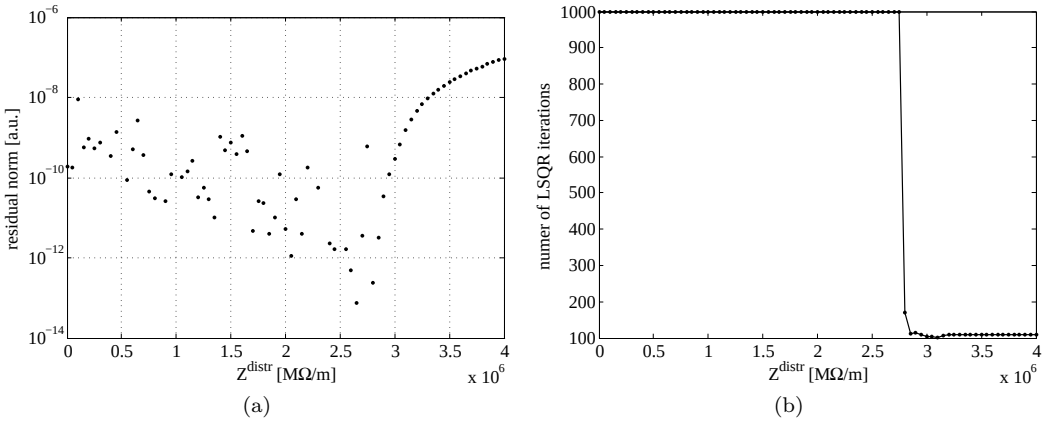


(a) (b)

Figure 3.17: Evolution of the residual norm (a) and number of least square iterations (b) for different values of $Z^{distr} = 2.8\,\mathrm{M\Omega/m}$. The distributed impedance reconstruction is optimized at the curve minimum between number of iterations and residual norm value.

vance slope (b) with the corresponding impedance distribution (a): the total impedance measured with the tune shift ($Z_{tot} = 3.09\,\mathrm{M\Omega/m}$), is in good agreement with the reconstructed impedance ($\sum Z_k = 2.98\,\mathrm{M\Omega/m}$) which is the sum of the distributed impedance and the one calculated from the residual. This value is close to the $3.2\,\mathrm{M\Omega/m}$ calculated in App. C.

We may note that, with respect to the simulation, we cannot exactly reconstruct the 100 impedance kicks placed in the accelerator but we have a good approximation as sum of the distributed impedance and lumped residual one. This is not a limitation since the lumped residual kicks are comparable in amplitude with the distributed impedance. The small discrepancy comes from the discrete behavior of the simulated impedance which is only *conceptually* referring to the distributed resistive wall since consists in 100 kicks in specific locations. In reality we are in the case of really distributed impedance.

We will now simulate a more general case involving both lumped impedances and distributed

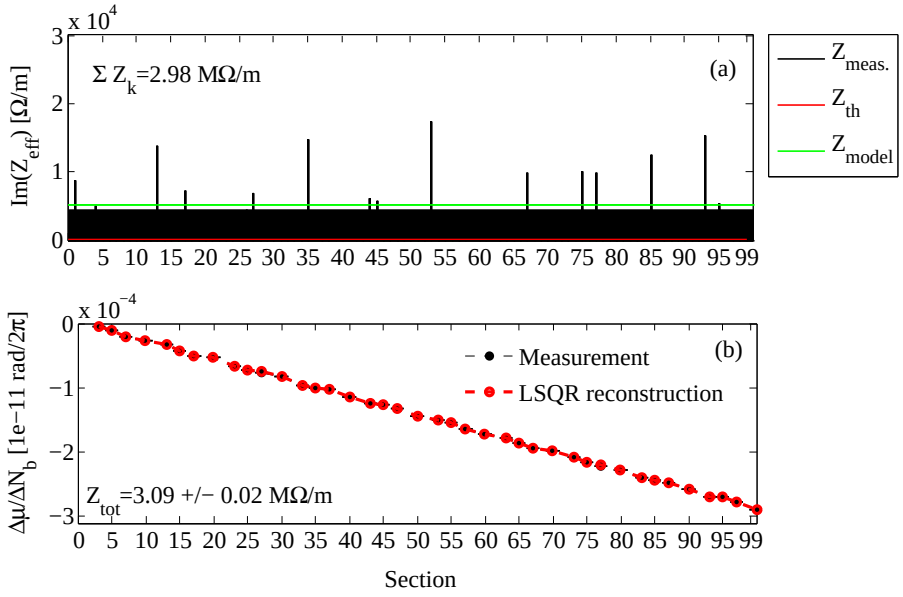


Figure 3.18: Impedance reconstruction in the case of 100 resistive wall and indirect space charge kicks HEADTAIL simulation.

ones.

### 3.5.3 Example: multiple impedance sources and resistive wall

The last example deals with the impedance localization of multiple impedance sources with resistive wall and indirect space charge contribution. We simulated with HEADTAIL all the kicker impedance sources in the PS, which wakefields were calculated for simplicity with the Tsutsui's [11] model[9].

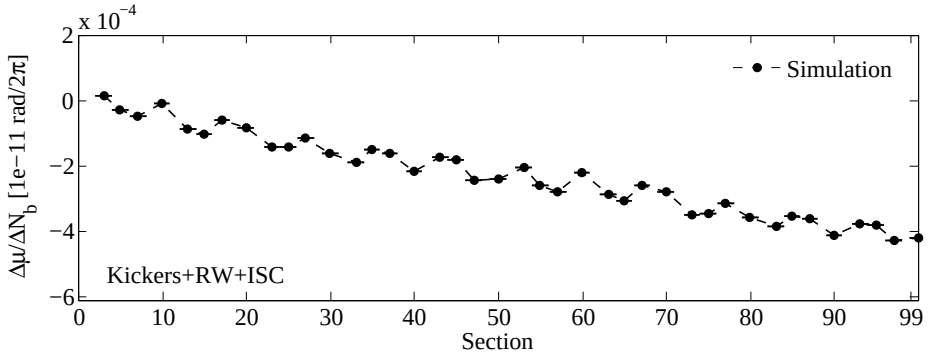


Figure 3.19: Phase advance shift with intensity simulated in HEADTAIL in the case of kickers, resistive wall and indirect space charge impedances.

The resistive wall impedance, and its indirect space charge component were simulated with 100 kicks equally spaced in the machine. The phase advance slope in Fig. 3.19, exhibits the contribution coming from distributed kicks $\Delta K^{distr}/\Delta N_b$ and a series of lumped kicks $\Delta K^{lump}/\Delta N_b$, in this case corresponding to the kickers.

Trying to isolate the contribution of the distributed impedance like in the previous example is this time not effective. As shown in Fig. 3.20 many different values for distributed impedance correspond to acceptable values of the residual norm and number of least square iterations: when the distributed impedance is not enough to describe the phase advance, the lumped impedance

[9]Some kicker have been simulated in CST to take into account the segmentation contribution (see App. C)

overcomes the limitation and vice versa. This is, by the way, not a strong limitation for the purpose of the measurement: a model is often available for the resistive wall and indirect space charge impedance, that constitutes a starting point for the distributed impedance estimation and the localization studies.

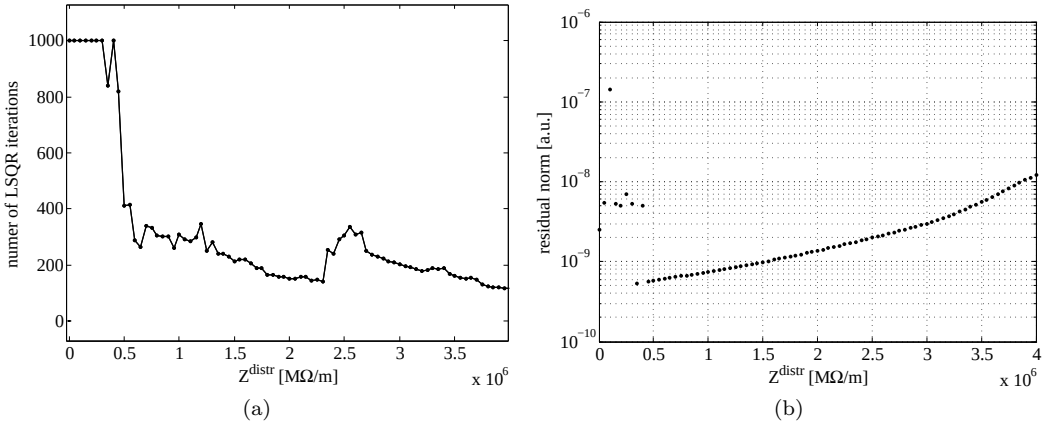


Figure 3.20: Evolution of the residual norm (a) and number of least square iterations (b) for different values of $Z^{distr}$. The interplay between many lumped impedances and the distributed impedance does not allow for a not unique choice of $Z^{distr}$.

We show the impedance reconstruction in Fig. 3.21 allowing for the distributed impedance value of $Z^{distr} = 3\,\mathrm{M\Omega/m}$: both total and summed impedance are in good agreement as well as the lumped impedance amplitude with the model.

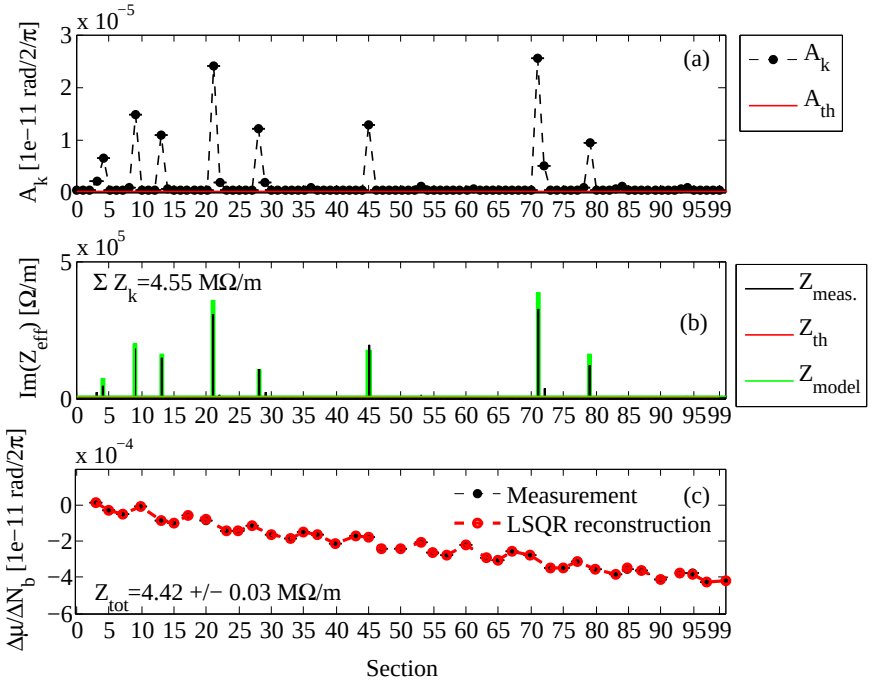


Figure 3.21: Impedance reconstruction in the case of all the kickers, resistive wall and indirect space charge kicks HEADTAIL simulation.

Adding a Gaussian noise of $\sigma_n = 5\,\mathrm{um}$ to the BPM data, we can study the reconstruction problem in case of distributed impedance and lumped ones. The amount of noise we add is sufficient to localize the highest kicker impedance sources in sections 21 and 71 as shown in the

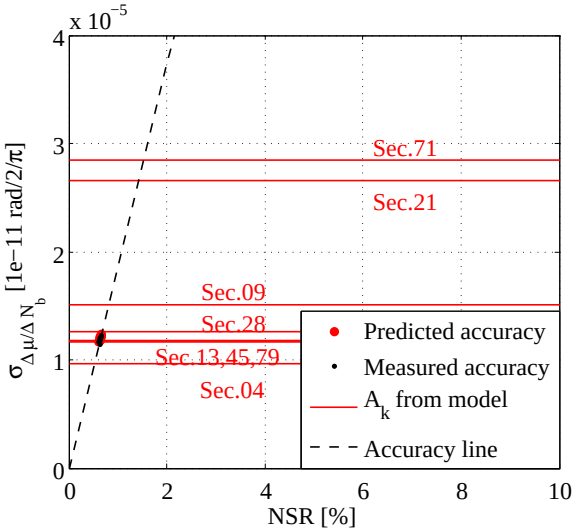


Figure 3.22: Localization Map showing the impedance induced phase advance amplitude for all the kickers together with the predicted and estimated phase accuracy in the case of $NSR$ 0.5% and the accuracy line. If the phase accuracy is below the red line, the impedance can be localized.

localization map in Fig. 3.22. We may notice that the accuracy line is steeper than the one shown in Fig. 3.14. This is because in the first case we have all the machine impedance model (restricted to all the kickers and the wall impedance), while in the second case, only one of the machine kickers: in the first case the increased impedance moves down the intensity threshold due to Transverse Mode Coupling Instability (TMCI) therefore restricting the intensity scan available. As a consequence, as shown in Eq. (3.64), restricting the intensity scan decreases the measurement accuracy resulting in a steeper accuracy line. This effect, in reality, would be partially compensated by the direct space charge: the center of mass oscillation (i.e. the tune) is not perturbed by the direct space charge force being affected by internal forces, while the other modes are shifted downwards increasing the TMCI threshold [8].

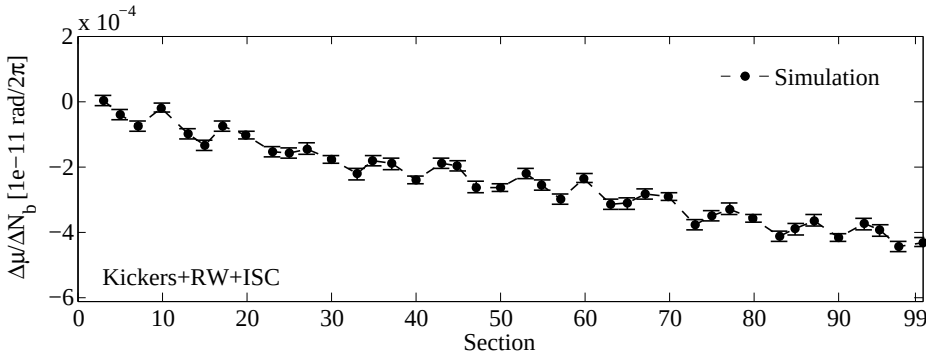


Figure 3.23: Phase advance shift with intensity simulated in HEADTAIL in the case of kickers, resistive wall and indirect space charge impedances with additive Gaussian Noise of $\sigma_n = 5$ um.

After the calculation of the phase advance shift with intensity from the BPMs shown in Fig 3.23, we can reconstruct the impedance following the procedure of the noise-free case. We notice that, in this case, the simulated phase advance slope $\vec{B}$ exhibits error bars $\Delta\vec{B}$ according to Eq. (3.64). In order to take into account also the error bar information, we perform a sensitivity analysis of the least square inversion perturbing $\vec{B}$ with a phase signal extracted by a Gaussian aleatory process with standard deviation $\Delta\vec{B}$ and null average. The result of the inversion and the statistical inversion is shown in Fig. 3.24 where we chose a distributed impedance of 3 MΩ/m. As we observe, the kickers in sections 21 and 71 could be localized, and some hint of impedance is visible for the

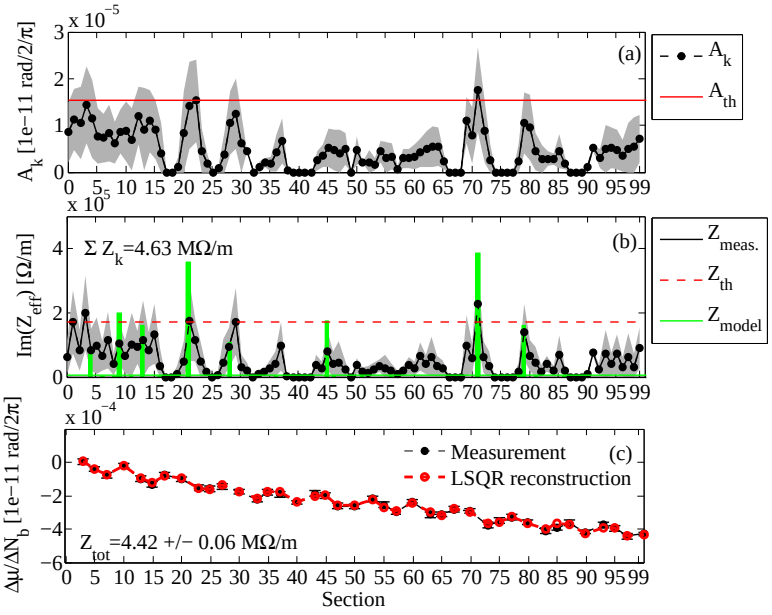


Figure 3.24: Impedance reconstruction in the case of all the kickers, resistive wall and indirect space charge kicks HEADTAIL simulation and additive Gaussian noise. The distributed impedance is set to 3 MΩ/m.

kicker in section 28. The kickers in the first sections are instead of small amplitude and could not be uniquely localized.

We conclude the study noticing that, varying the distributed impedance from 3 MΩ/m to 2.5 MΩ/m and 3.5 MΩ/m, the picture gets basically unchanged for the impedance position point of view, as reported in Fig. 3.25.

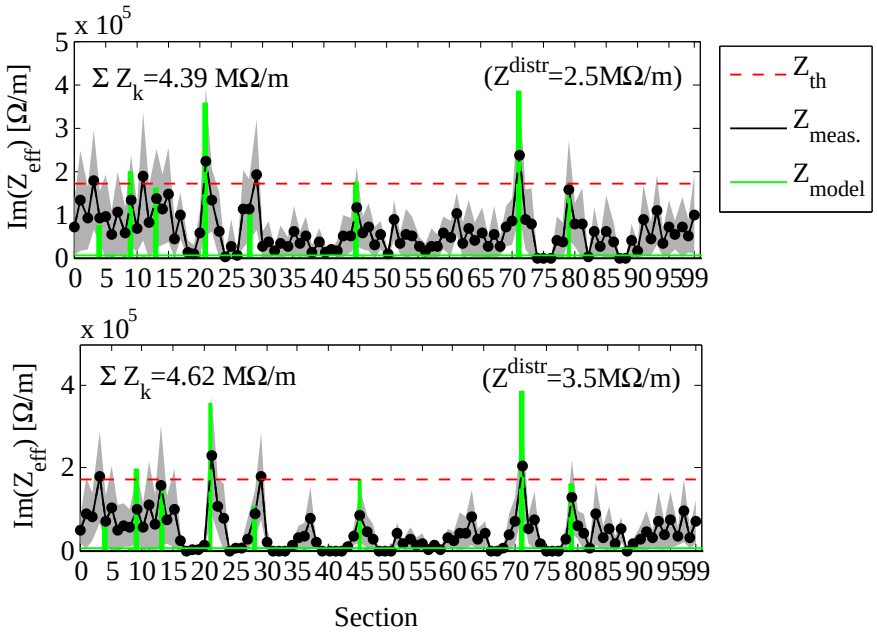


Figure 3.25: Impedance reconstruction in the case of all the kickers, resistive wall and indirect space charge kicks HEADTAIL simulation and additive Gaussian noise, changing the background impedance from 3 MΩ/m to 2.5 MΩ/m and 3.5 MΩ/m.

## 3.6 0-current optics

As a direct consequence of our analysis, we can derive the machine optic model virtually at $N_b = 0$ ppb. The impedance localization measurement, in fact, searches for *intensity dependent* errors that provoke a linear tune and phase shift with intensity. Extrapolating the intercept at $N_b = 0$ ppb we recollect the machine optics and the *static* errors that are unavoidably present.

The knowledge of the model is essential in order to correctly perform the impedance reconstruction. As we have shown in Eq. 3.54, knowing the measured phase at 0-current allows us to construct the response matrix $S$ for the problem inversion. Figure 3.26a shows the measured (from simulation) phase advance for the last analyzed case of multiple impedance sources, resistive wall, indirect space charge and additive noise. The comparison with the optic model reveals a phase beating of $\simeq 5\%$ between the simulated and the MAD-X optical model. Since Eq. 3.54 takes into account the phase advance at the BPM positions, we can directly use the measured phase advance in place of the MAD-X one: this is very useful in case optical errors (like quadrupole misalignment, field errors, etc.) are not taken into account in the MAD-X model. Moreover, the interpolation of the measured model over the reconstructor positions allows to have a better estimation of the phase advance at the kick position.

Figure 3.26b shows the measured (from simulation) $\beta$ function and the comparison with MAD-X. The $\beta$ function is calculated using the 3-BPM method as in [59]. The comparison with the optic model reveals a phase beating of $\simeq 5\%$ between the simulated and the MAD-X optical model, which is expected since the method derives the $\beta$ function from the phase advance between BPMs. Unfortunately deriving the $\beta$ function is not model independent, in the sense that a knowledge of the MAD-X machine optics is required. Nevertheless, also the measured $\beta$ functions can be plugged into Eq. 3.54 allowing for an accurate description of the machine model and the $S$ response matrix.

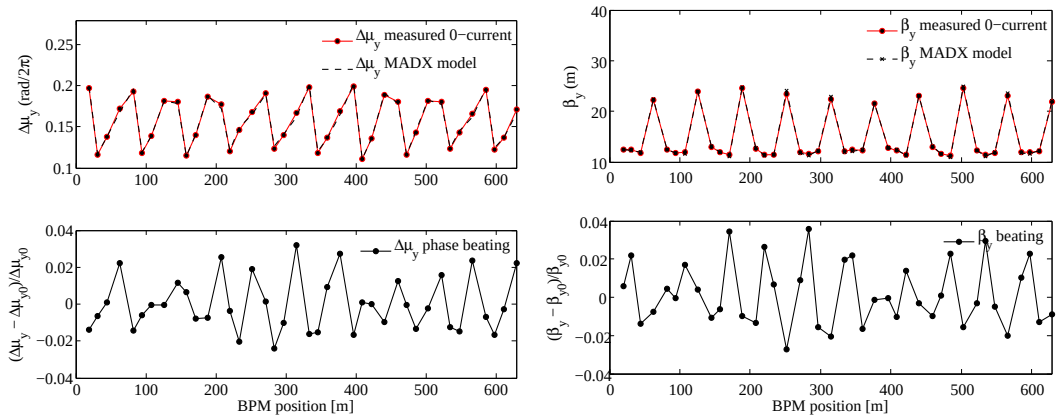


(a) (b)

Figure 3.26: Measured (from simulation) phase beating (a) and $\beta$ beating (b) in the case of of all the kickers, resistive wall and indirect space charge kicks HEADTAIL simulation and additive Gaussian noise.

## 3.7 The PS localization map

We conclude the chapter showing the localization map calculated for the kicker impedance sources in the PS for a Gaussian bunch as in Tab. 3.1. The typical number of turns that can be recorded by the BPM system is $N = 5000$, while typically $M = 150$ measurements can be done during one measurement time slot. Figure 3.27 shows the accuracy line allowing for an intensity scan from $10^{11}$ to $10^{12}$ ppb (set by the BPM resolution downward, and by instabilities upward): in order to localize the PS impedances we should have a noise level of the order of $NSR \simeq 2\%$. In the

machine $NSR \simeq 5\%$ or slightly less is usually achieved, that allows only for the localization of the impedance sources in sections 21 and 71 as we saw in the simulations.

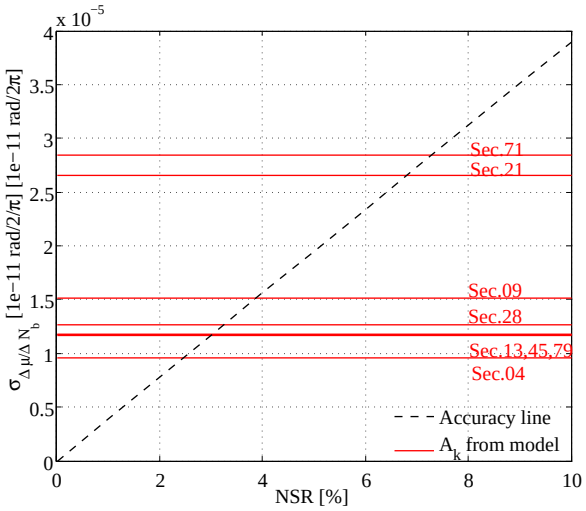


Figure 3.27: Accuracy line for the PS machine with $N = 5000$, $M = 150$, and intensity scan from $1 \cdot 10^{12}$ to $2 \cdot 10^{12}$ ppb in function of the machine noise level.

Another way to enhance the possibility of reconstructing impedances, is to increase the impedance signal $A_k$. From Eq.(3.67), it is clear that this can be done either increasing the tune shift, for example by means of a shorter bunch length, or moving the working point close to the half integer. In this last case, one could argue that operating close to the half integer would make the least square inversion very difficult because of the machine optic model that usually gets more approximate due to the machine errors enhancement (see for example [48]). Nevertheless, as we commented in the previous sections, the optic model at 0-current can be inferred from the measurements themselves allowing for an *almost* model independent analysis, as we will show in the next chapter.

# Chapter 4

# Transverse impedance localization: measurements

We present now the method benchmark and application in the CERN PS, SPS and LHC machines and in the BNL AGS and RHIC accelerators.

We will start presenting the status of the total transverse PS machine impedance for different energies. This will motivate the studies for the impedance localization method , in particular at 2 GeV energy.

The impedance localization method is then validated with an equivalent experiment done varying the current in two quadrupoles to provoke a tune shift analogous to the one provoked by an increase of beam current.

In the following, two measurements at 2 GeV are presented with the corresponding impedance reconstruction. The quality of the reconstruction will lead us to the study and the analysis of the method performance at different working points in order to enhance the impedance signal.

## 4.1 Measurements in the PS

In order to assess the total transverse impedance in the PS, a first tune shift with intensity measurement was done at different energies. If the bunch length remains approximately unchanged with intensity, Eq. (3.43) predicts a linear tune shift with the bunch current, with a slope proportional to the transverse total effective impedance.

Considering past analysis, several measurements of betatron tune shift as a function of beam intensity have been reported: at $T = 1.4\,\mathrm{GeV}$ injection energy [60], at $T = 2\,\mathrm{GeV}$ flat bottom [61], and at extraction energy [60, 61].

At injection, a horizontal total effective impedance of $3.5\,\mathrm{M\Omega/m}$ and a vertical one of $12.5\,\mathrm{M\Omega/m}$ were obtained in Ref. [60], where also a discussion and a comparison with older measurements can be found.

At 2 GeV, other measurements, made only in the vertical plane during recent machine development sessions in 2012-2013, give $Z_y^{eff} = (9.6 \pm 1.0)\ \mathrm{M\Omega/m}$.

The observed difference in the vertical plane between these two sets of measurements could be explained by the effect of the indirect space charge. If we approximate the PS vacuum chambers as a round chamber of 35 mm of radius, we get 4.9 MΩ/m at injection energy and 3 MΩ/m at 2 GeV.

At the extraction energy of 25 GeV, as shown in Fig. 4.1 the contribution to the impedance of the space charge becomes negligible. Indeed, at this energy, we are mainly dominated by resistive wall and geometrical impedances. The measurements of Ref. [60] give $Z_x^{eff} < 1\ \mathrm{M\Omega/m}$ and $Z_y^{eff} = 6.1\,\mathrm{M\Omega/m}$, while our measurements give $Z_x^{eff} \simeq 0.43\,\mathrm{M\Omega/m}$ and $Z_y^{eff} \simeq 4.7\,\mathrm{M\Omega/m}$.

We summarize in Tab. 4.1 the observations collected until now for the transverse vertical impedance of the machine. The PS transverse impedance is therefore mainly dominated by the space charge at injection and 2 GeV energies, but includes a not negligible contribution of $\simeq 5\,\mathrm{M\Omega/m}$ which is due to pure resistive wall and insertion devices. Accounting for $\simeq 1.4\,\mathrm{M\Omega/m}$ from

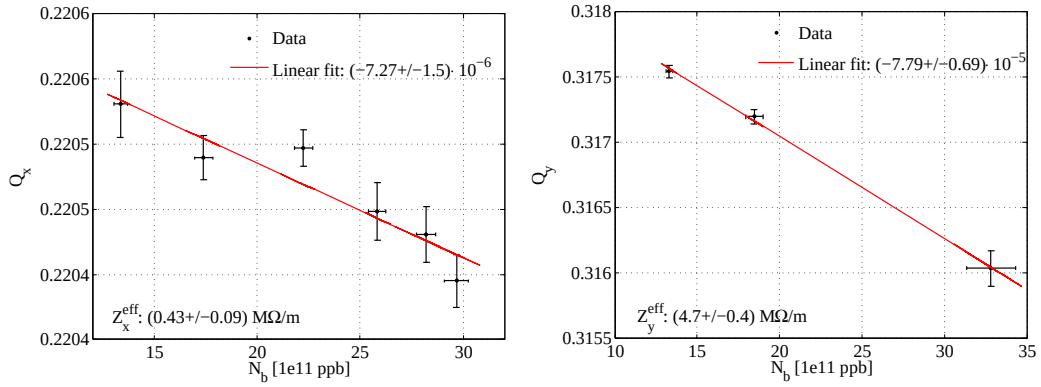


Figure 4.1: Measurements of tune shift in the two planes (X and Y) at the kinetic energy of 25 GeV.

| Kinetic energies | 1.4 GeV | 2 GeV | 25 GeV |
|---|---|---|---|
| Round chamber (r=35 mm) | 4.9 MΩ/m | 3.0 MΩ/m | ≤0.5 MΩ/m |
| Measured $Z_y^{eff}$ | 12.5 MΩ/m | $(9.6 \pm 1.0)$ MΩ/m | $(5.3 \pm 0.8)$ MΩ/m |

Table 4.1: Indirect space charge contributions to the total transverse effective impedance at different kinetic energies for round chamber and vertical total effective impedance.

the kicker of the impedance model, we miss $\simeq 3.5\,\mathrm{M\Omega/m}$. The transverse impedance localization method is therefore an essential method in order to get hints of possible high impedance locations.

### 4.1.1 Impedance localization test

Before applying the transverse impedance localization method to the machine, we made a test in order to asses the method feasibility in a simpler well controlled case: we changed the current in two equal quadrupoles (QLSF in section 29 and QSE in section 87) to provoke a *tune shift with quadrupole current* and tried to reconstruct the quadrupole location.

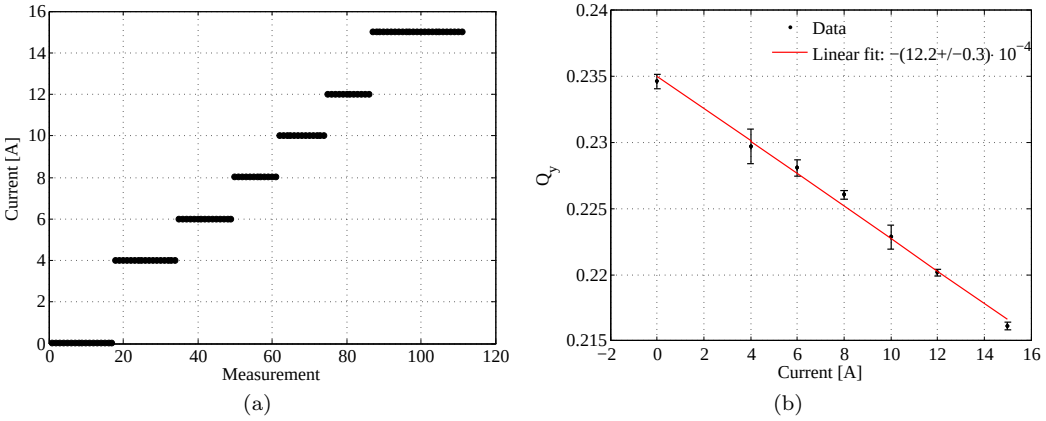


Figure 4.2: Current sweep in QSE and QLSF quadrupoles (a) and corresponding vertical tune shift with current.

The current was increased from 0 to 15 A and provoked a tune shift of 0.02 as shown in

Fig. 4.2. The tune shift induced by the quadrupoles is $\Delta Q_y/\Delta I \simeq 12 \cdot 10^{-4}\mathrm{A}^{-1}\mathrm{rad}/2\pi$. Since the two quadrupoles are equal we expect to be able to reconstruct the induced tune shift as half of the total one. Calculating the phase advance shift with current we recollect the phase advance slope signal[1], which could be inverted as shown in Fig 4.3. The inversion leads to a value very close to the expectation for the two quadrupoles: $\Delta Q_{y_k}/\Delta I \simeq 6 \cdot 10^{-4}\mathrm{A}^{-1}\mathrm{rad}/2\pi$. The third spurious kick could be due to the fact that we do not reconstruct the quadrupole kick at exactly its position but in the middle of the straight section: this can lead to some small phase mismatch in the reconstruction, which is compensated by the least-square algorithm adding a third kick.

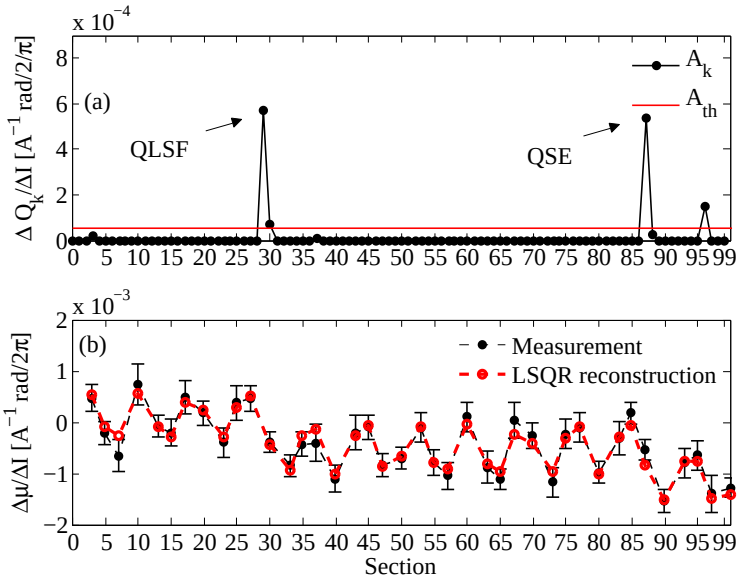


Figure 4.3: Measurement of the two quadrupoles equivalent tune shift (a) from the reconstructed phase advance slope with current (b).

### 4.1.2 Impedance localization measurements

We performed two sets of measurements on 05-02-2013 injecting a TOF beam, whose main characteristics are listed in Tab. 4.2. The main machine parameters used in the measurement are listed in App. B.1. After orbit correction, the beam was kicked at 2 GeV kinetic energy with the help of a transverse feedback damper (ADT), a fast transverse kicker used for damping unwanted unstable coherent motion: the device is able to excite the beam oscillations at a single frequency which was set carefully close to the tune. Figure 4.4a shows the performed intensity scan and and Fig. 4.4b the bunch excitation at low and high intensity: we observe the linear ramp on the coherent oscillation due to the locking of the ADT exciting signal to the bunch coherent tune. The BPM system counts 40 BPMs and is able to store up to $N = 5000$ coherent oscillation points.

#### NSR estimation

The turn-by-turn data were stored and analyzed for each intensity. The noise information can be obtained both from time domain (TD) looking at the *rms* of the first 500 points in the coherent oscillation, and from frequency domain (FD), applying the Parseval theorem. Figure 4.5 shows the comparison between the two methods that are in good agreement. The noise level is set at $\sigma_n \simeq 0.1\,\mathrm{mm}$. The frequency analysis on the BPM data was performed using SUSSIX [50].

A first measurement selection is therefore done deleting those measurements whose $NSR$ is higher than a certain threshold. Figure 4.6 shows the $NSR$ in function of the beam intensity and the BPM position along the accelerator: setting a cut at $NSR_{th} = 25\%$ we restricted the set

[1] We remark that the last point in the slope, corresponding to the machine circumference, calculates the phase advance shift between the reference BPM and itself, and therefore represents the tune shift with intensity.

| TOF beam | Parameter | Set1 | Set 2 |
|---|---|---|---|
| Intensity | $N_b$ | $5 \cdot 10^{11} \rightarrow 13 \cdot 10^{11}$ ppb | $5 \cdot 10^{11} \rightarrow 13 \cdot 10^{11}$ ppb |
| Momentum spread | $\mathrm{d}p/p_o$ | $2 \cdot 10^{-3}$ | $2 \cdot 10^{-3}$ |
| Bunch length | $\sigma_t$ | 94 ns | 112 ns |
| Horizontal emittance | $\varepsilon_x$ | $\simeq 15\mu$rad | $\simeq 15\mu$rad |
| Vertical emittance | $\varepsilon_y$ | $\simeq 8\mu$rad | $\simeq 8\mu$rad |

Table 4.2: TOF beam parameters used in the two set of PS transverse impedance localization measurements.

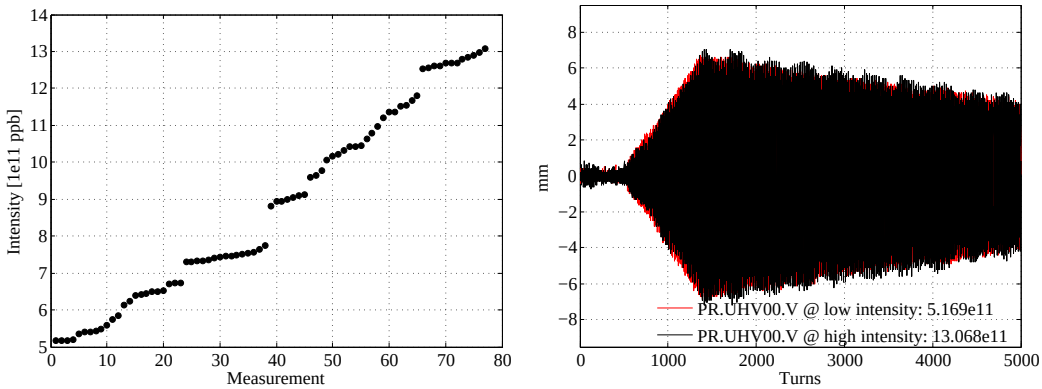


Figure 4.4: (a) Intensity scan performed during the impedance localization measurements. (b) Typical traces from a BPM for low and high intensity: the linear part is when the ADT locks the beam coherent tune oscillation.

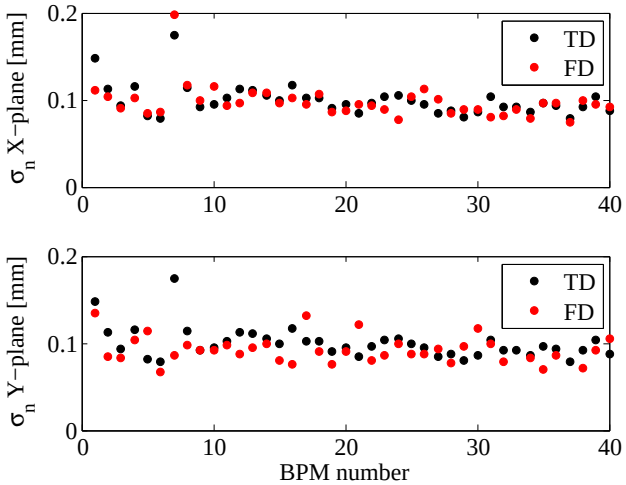


Figure 4.5: Measurements of noise standard deviation $\sigma_n$ in the two planes, from time domain (TD) and frequency domain (FD).

of measurements before the final processing on the phase. We may note also, that the $NSR$ on average settles around $NSR \simeq 5\%$ excluding those intensities where the measurement turned out to be too noisy.

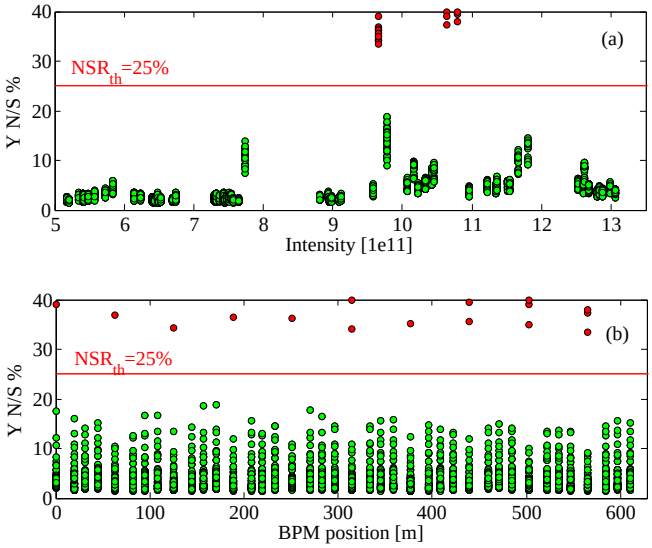


Figure 4.6: Measurement of the $NSR$ as a function of the beam intensity (a) and BPM position (b).

### Phase advance shift with intensity

Once the measurements are deemed clean enough, the phase advance slope with intensity can be calculated expecting the accuracy given by Eq. (3.64). A further threshold of $NSR = 5\%$ was introduced before fitting the phase drift, preserving again a reasonable set of data points. Figure 4.7a shows the localization map corresponding to the first set of measurements: the accuracy looks to be enough for the localization of the impedance in sections 21 and 71. Furthermore, a small gain could be achieved with noise clean reduction through the SVD eigenvalue analysis [62, 63] in order to reduce the correlated noise between BPMs as shown in Fig. 4.7b.

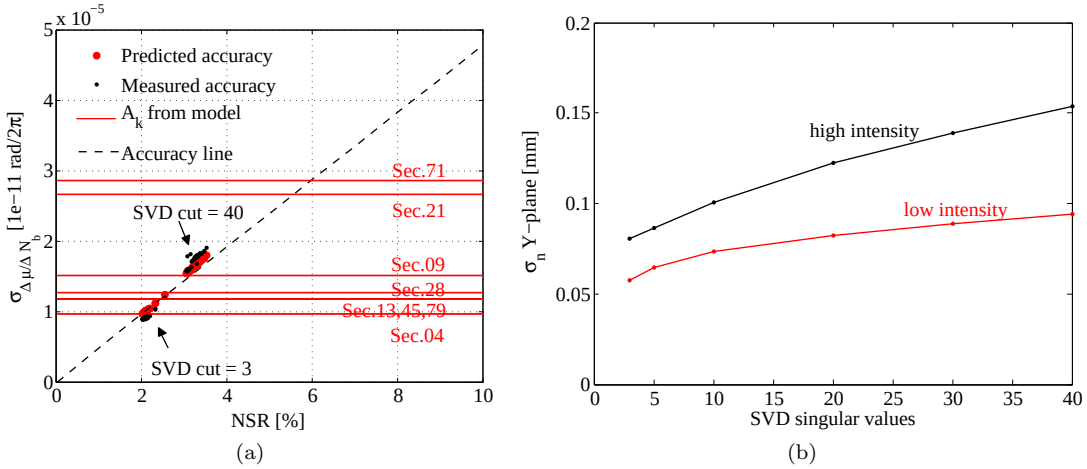


Figure 4.7: (a) PS localization map for the first set of measurements. The SVD cleaning allows the NSR reduction and consequently the improvement of the measurement accuracy. (b) SVD noise reduction for high and low intensities.

The phase advance slope was calculated considering the integrated phase advance from a reference BPM, namely the `PR.UHV00` one. Figure 4.8 shows the phase advance shift with intensity for the two sets of measurements. We immediately notice the effect of the shorter bunch length in the first measurement set, which provokes a steeper phase drift and consequently a bigger tune shift. The slope shows a decreasing behavior similar to what we simulated in Sec. 3.5.2 suggest-

ing a strong contribution of distributed impedance. Moreover we expect a not negligible effect of the indirect space charge, whose contribution to the total vertical tune shift (see Fig. 3.8) was estimated to be $\Delta Q^{ISC}/\Delta N_b \simeq 3 \cdot 10^{-4}$.

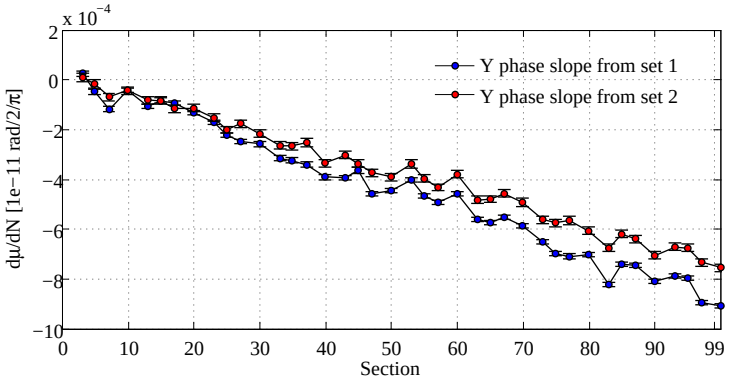


Figure 4.8: Integrated phase shift with intensity for the two sets of measurements: the impact of the shorter bunch length in the first set, enhances the tune shift.

### Tune shift with intensity

Figures 4.9a and 4.9b show the tune shift with intensity and the bunch profiles corresponding to the two sets of measurements. The total impedance can be therefore estimated from Eq. (3.33) using the measured profiles or from Eq. (3.35) in the Gaussian fit approximation. In the following we will use the Gaussian fit approximation for consistency with the estimations in the impedance model and the HEADTAIL simulations. We list the main results in Tab. 4.3. The variation of the effective impedance is within the error bars for the two sets of measurements: as expected, varying the bunch length, we linearly vary the tune shift. This means that the effective impedance is almost constant within the bunch spectrum. This can be crosschecked in Fig. 3.9 where we can see that the imaginary part of the impedance is constant up to $\simeq 300\,\mathrm{MHz}$ while the bunch spectrum extend up to $\sigma_f = 1/\sigma_t \simeq 40\,\mathrm{MHz}$.

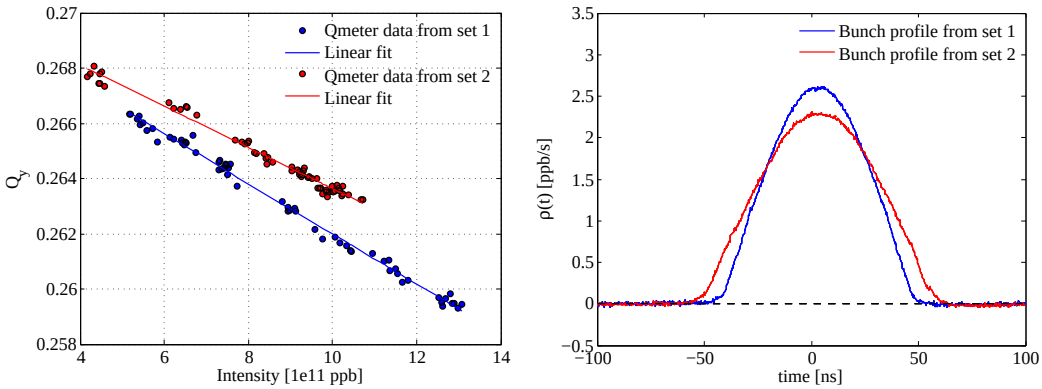


(a) (b)

Figure 4.9: (a) Vertical tune shifts for the two sets of measurements in the PS at 2 GeV kinetic energy, and (b) corresponding bunch profiles.

### 0-current model

As a direct consequence of our analysis, we can derive the machine optic model virtually at $N_b = 0\,\mathrm{ppb}$. Figure 4.10 shows the phase advance and $\beta$ beating for the first set of measurement (it is similar for the second one). The measured beta beating is $\simeq 10\%$ which allows for a

| | Bunch length $[4\,\sigma_t]$ | $\Delta Q_y/\Delta N_b$ | $Z_y^{eff}$ [$\Omega$/m] |
|---|---|---|---|
| Set 1 | $\sigma_t = 94$ ns | $(-8.98 \pm 0.08)10^{-4}$ | $(9.24 \pm 0.09)$ M$\Omega$/m |
| Set 2 | $\sigma_t = 112$ ns | $(-7.68 \pm 0.26)10^{-4}$ | $(9.39 \pm 0.31)$ M$\Omega$/m |

Table 4.3: Measured PS vertical effective impedance at 2 GeV.

good estimation of the $\beta$ function from phase advance measurements. The response matrix $S$, as we commented in Sec. 3.6, can be constructed with the measured phase advances and $\beta$ function. The only dependence on the model is associated to the measurement of the $\beta$ function for which the 3-BPMs method requires the machine MAD-X model.

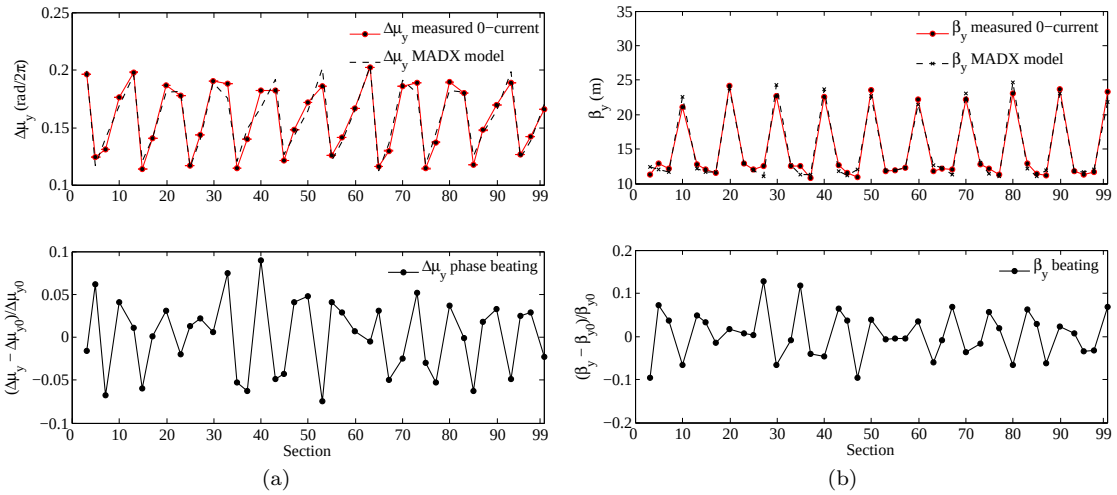


(a) (b)

Figure 4.10: Measured phase beating (a) and $\beta$ beating (b) in the first set of measurement. The beating is $\simeq 10\%$.

### Impedance reconstruction

We reconstruct the distributed and lumped impedances starting from a set of 100 equally spaced reconstructors, each one placed in each of the 100 PS sections. Following the discussion of Sec. 3.5.3 we solve the least square problem

$$\min_{\{\Delta K^{lump}/\Delta N_b\}} |\vec{B} - S \cdot (\Delta K/\vec{\Delta N_b})|, \tag{4.1}$$

after having subtracted from the measured phase advance slope the contribution of the distributed impedance $Z^{distr} \simeq 3\,\mathrm{M}\Omega/\mathrm{m}$ estimated from the PS impedance model. The reconstruction for the first and second set of measurements is shown in Fig. 4.11. The first measurement shows a lower impedance threshold with respect to the second one, which is consistent with the shorter bunch length of the first case. This is calculated by means of Eq. (3.68) considering for simplicity the machine average $\beta$ function. The gray error bounds are calculated as in Sec. 3.5.3. The level of noise and the error bounds are quite high in the second measurements and only the kicker in section 71 seems to be correctly localized. In the first set the same kicker and the ones in sections 21 and 28 are visible while the ones in sections 4 and 9 appear with higher amplitude and displaced. Some clear peak appears between sections 55 and 65 that might be correlated with the presence of a localized impedance source.

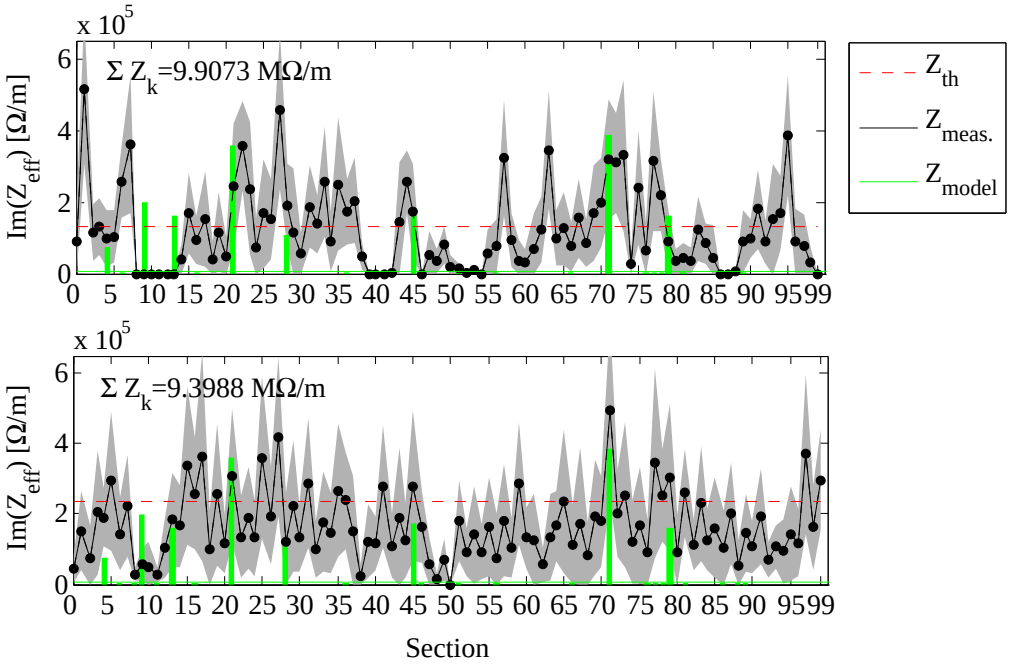


Figure 4.11: Measurement of localized impedance sources in the PS for the first (top) and second (bottom) set of measurements.

### 4.1.3 Measurements close to the half integer

The measurements shown in the previous paragraph showed a strong impact of noise in the impedance reconstruction.

As depicted in Eq. (3.64), the interplay of number of measurements, intensity scan width, time available, kick amplitude and noise background make often the measurements challenging. A way to overcome this difficulty is to enhance the impedance signal moving the fractional part of the tune close to the half integer, as we commented also in Sec. 3.7. This was tried in another measurement setting $Q_{y_o} \simeq 0.47$ in order to enhance the $\beta$ beating and therefore the impedance signal of a factor $1/\sin(2\pi Q_{y_o}) \simeq 5$. Unfortunately, the closer to the half integer, the worst become the MAD-X optic model if the machine errors are not known: while the phase advance response can be measured, the $\beta$ functions rely on the model accuracy.

The reconstruction result is shown in Fig. 4.12. The $A_k$ in Fig. 4.12a are basically a normalized tune shift with intensity (cfr. with Eq. (3.67)), therefore proportional to $\beta_k Z_k^{eff}$. Since, close to the half integer errors are enhanced, the $\beta$ function can have significant excursions: we therefore calculated the response matrix referring to the average $\beta$ function in the PS lattice without errors, which is $\bar{\beta}_y \simeq 16.68\,\mathrm{m}$. This means that the amplitude of the impedance peaks in Fig. 4.12b may be improperly scaled and some caution should be taken when looking at the plot. Some strong impedance seems to be localized, in fact, close to sections 16, 64 and 92 where respectively a magnetic septum (SMH16), a wirescanner (MBP64) and a 20 MHz cavity (C2092) are located. The kicker positions are localized even if not perfectly centered.

The sections localized in the impedance localization measurements are being currently investigated considering the output of the measurements presented in this and the last sections. Limitations come, in the first case, from the knowledge of the $\beta$ function along the machine, in the second, from the high level of noise introduced in the measurement.

Other impedance localization measurements are therefore planned for the post-LS1 period attempting to reach a lower $NSR$. In particular, tests are planned at injection, flat bottom and top energy in order to evaluate the effect of the indirect space charge impedance contribution. The measurements at top energy should minimize the space charge contribution: if this is the main source of homogeneously distributed impedance along the machine, the reconstruction of localized impedance sources could improve.

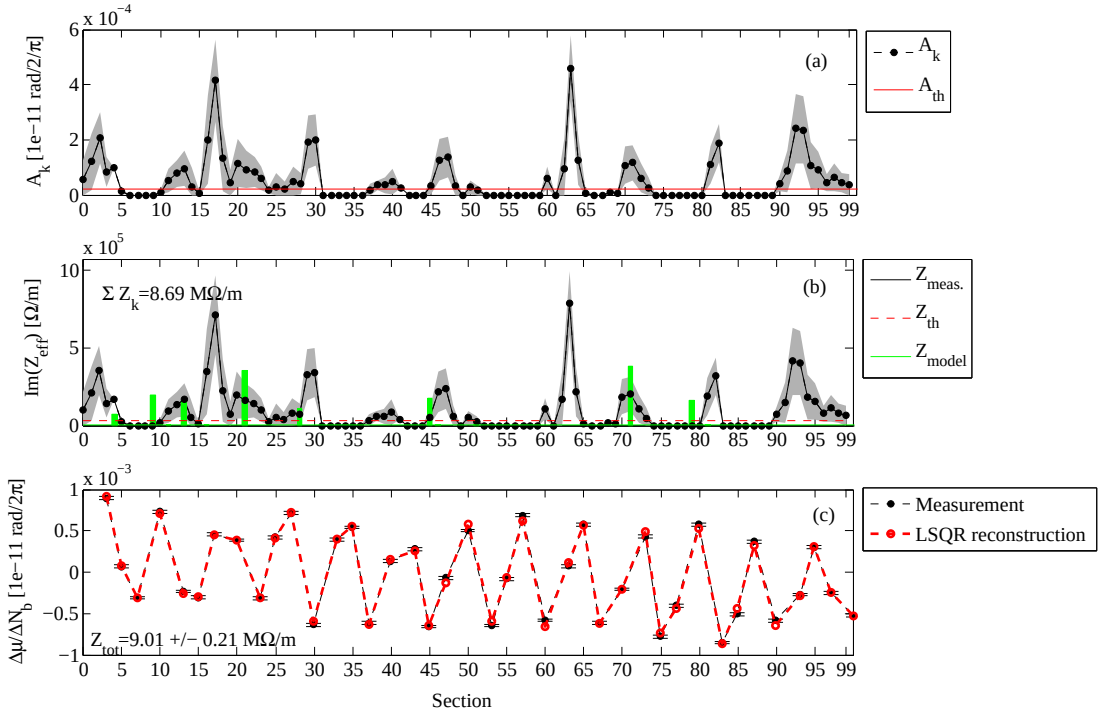


Figure 4.12: Measurement of localized impedance sources in the PS close to the half integer.

## 4.2 Measurements in the SPS

The SPS machine is an accelerator of $\simeq 6.9\,\mathrm{km}$ that serves as the LHC injector accelerating the beam ejected from the PS up to the total energy of $E = 450\,\mathrm{GeV}$.

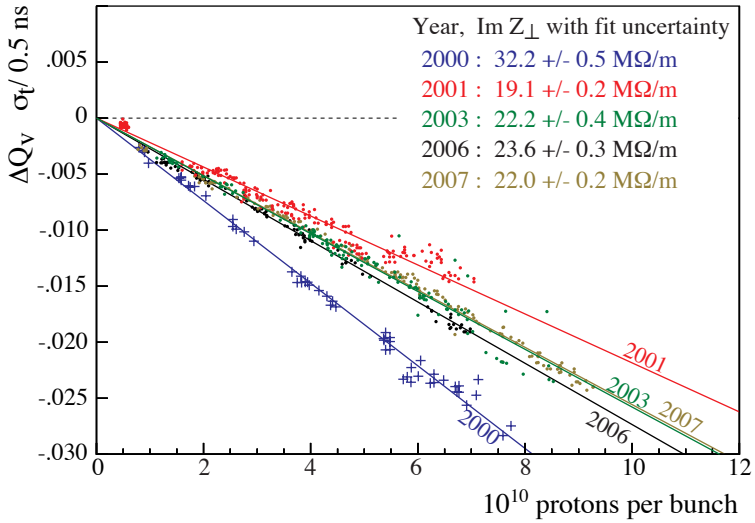


Figure 4.13: SPS impedance status from 2000 to 2007. The impedance reduction campaign of 2000 and the serigraphy on the MKE kickers show a strong impact on the total SPS transverse impedance budget (courtesy of H.Burkhardt).

The tight beam parameters constraints required from the LHC and in the future, from the High Luminosity LHC, motivated deep studies of the machine impedance and actions for the impedance reduction. As shown in Fig. 4.13, starting from 2000, an impedance removal campaign was started: this implied for example the removal of old lepton cavities and the shielding of the numerous

pumping ports. The reduction effect can be appreciated from the tune shift curve of 2001 where the impedance estimated was reduced to 22 MΩ/m. The following installation of 9 MKE kickers, 5 in 2003, and other 4 in 2006, increased again the impedance motivating the surface serigraphy in order to reduce their impedance contribution. The kicker serigraphy has been progressively continued along the years and it will be completed for the run after the first long shutdown (LS1). Already from 2006 to 2007 the beneficial effect can be appreciated.

Figures 4.14a and 4.14b show the updated impedance budget for the SPS in the horizontal and vertical planes. The horizontal tune shift measurements were taken on 15-01-2013 and shows a small positive tune shift due to the contribution of the detuning impedance of the kickers [64]. The vertical tune shift measurement was taken on 22-01-2013 showing a reduction of the impedance budget according to the kicker serigraphy. We note here, that the effective impedance is evaluated with the smooth approximation for back-compatibility to the older measurements shown in Fig. 4.13: the average vertical $\beta$ function $\bar{\beta}_y$ is different from the $\hat{\beta}_y = R/Q$ of the smooth approximation. In the SPS Q26 optics[2] in the vertical plane we get $\hat{\beta}_y \simeq 41$m and $\bar{\beta}_y \simeq 54$m, i.e. 25% more. This means that the real effective impedance accounting for the machine optics would scale to $\simeq 15.5\,\mathrm{M\Omega/m}$.

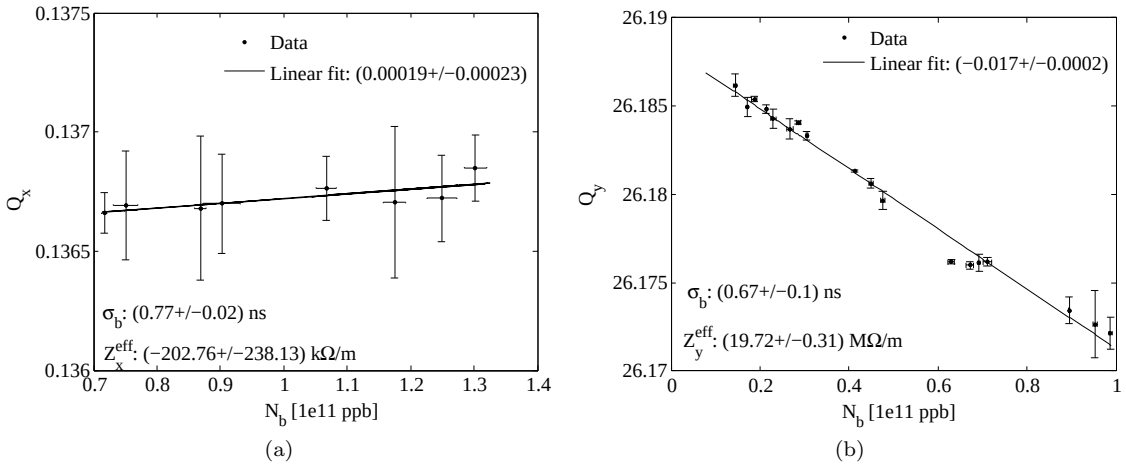


Figure 4.14: Tune shift measurements in horizontal (a) and vertical (b) plane for the SPS.

The transverse machine impedance budget includes a $\simeq 40\%$ of the impedance coming from the kickers, $\simeq 25\%$ from the wall, indirect space charge, cavities and BPMs. The remaining 35% was still unknown until recent developments showed that the numerous step transitions could explain almost the totality of the missing impedance [66].

The impedance localization measurement was tried in the SPS in order to establish the method itself and contribute to the machine impedance identification. Unfortunately, in spite of the joint efforts of the beam instrumentation experts and machine operators, the machine BPM system could not operate in good condition, affecting the quality of the measured phase advance slope.

As an example, we describe the measurement operated in 22-01-2013 where a LHC-type of beam whose characteristic are resumed in Tab. 4.4 was injected and excited with a tune kicker at the injection energy of 26 GeV. The machine parameters used in the measurement are listed in App. B.2. The vertical chromaticity was carefully set the closest to 0 as possible in order to ensure a sufficiently high number of betatron oscillations as shown in Fig. 4.15a. After calibration, the BPM system was set up and 1024 turns recorded. The multi-turn data acquisition have been therefore processed and Fourier transformed and the phase advance calculated. Figure 4.15b shows an example of phase advance drift with intensity from the reference BPM `BPV.60108` from which the phase advance is calculated to the `BPV.12708` BPM.

[2]The name "Q26" refers to the integer art of the tune which is 26. This is specifically mentioned to distinguish from an other optics, the "Q20" that has been recently developed in order to increase the slip factor $\eta$, parameter involved in various intensity limiting effects, such as the TMCI threshold, and now in operation [65].

| LHC-INDIV beam | Parameter | |
|---|---|---|
| Intensity | $N_b$ | $1 \cdot 10^{10} \rightarrow 1 \cdot 10^{11}$ ppb |
| Momentum spread | $\mathrm{d}p/p_o$ | $\simeq 3 \cdot 10^{-3}$ |
| Bunch length | $\sigma_t$ | $\simeq 0.7$ ns |
| Horizontal emittance | $\varepsilon_x$ | $\simeq 2\mu$rad |
| Vertical emittance | $\varepsilon_y$ | $\simeq 2\mu$rad |

Table 4.4: INDIV beam parameters used in the SPS transverse impedance localization measurements.

Analogously to the PS case, only those measurement with a low $NSR$ were kept during the analysis: typically, a NSR$\simeq 5-10\%$ could be achieved in the SPS measurements.

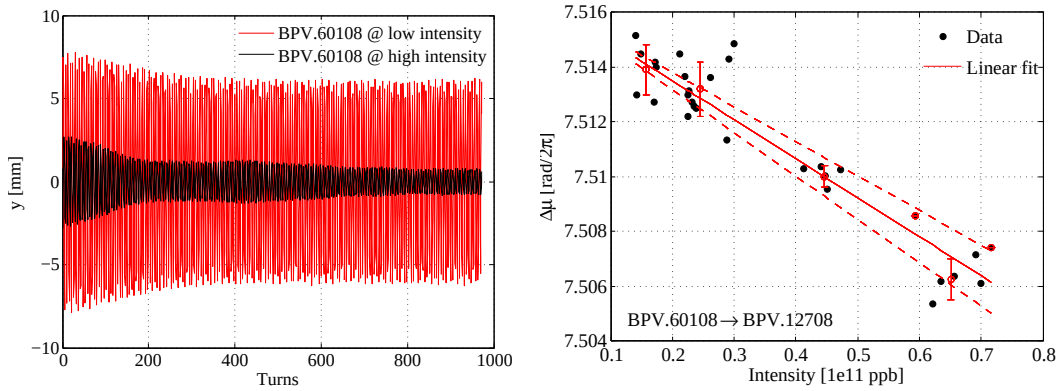


(a) (b)

Figure 4.15: Example of coherent beam center of mass oscillation excited by the kicker at low and high intensity.

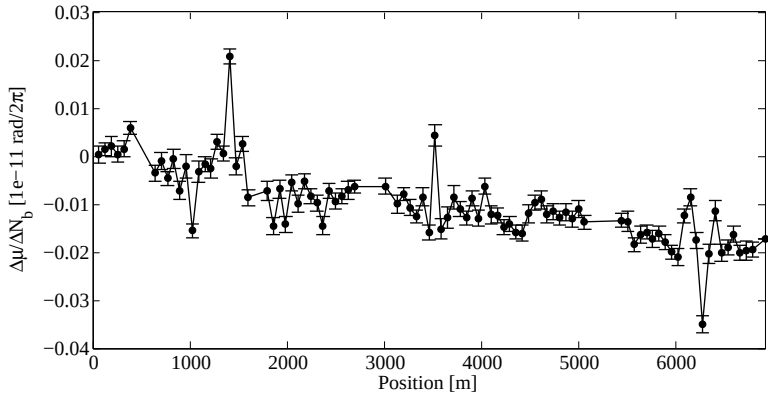


Figure 4.16: Integrated phase shift with intensity measured in the SPS with Q26 optics.

According to these considerations the phase advance slope along the machine was calculated and it is shown in Fig. 4.16. With respect to the PS case, there is not a smoothly decreasing slope, but some spikes are visible and points in which the phase slope tends to rise up. This behavior could be due to some intensity dependent additional effects either coming from the BPM system calibration, or from beam dynamics effects not yet considered.

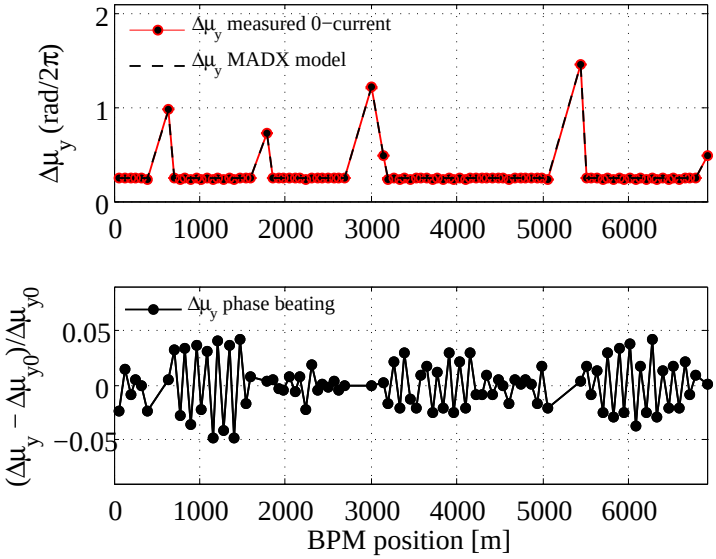


Figure 4.17: Phase advance beating measured in the SPS with Q26 optics.

A first inversion was anyway attempted. Figure 4.17 shows the phase beating in the machine at $\simeq 5\%$ level: a good indication of the optic model description of the machine. As distributed impedance we adopted $Z^{distr} \simeq 9\,\mathrm{M\Omega/m}$ as from the most recent estimations accounting for resistive wall, indirect space charge and step transitions opportunely weighted by the lattice average vertical beta function [66].

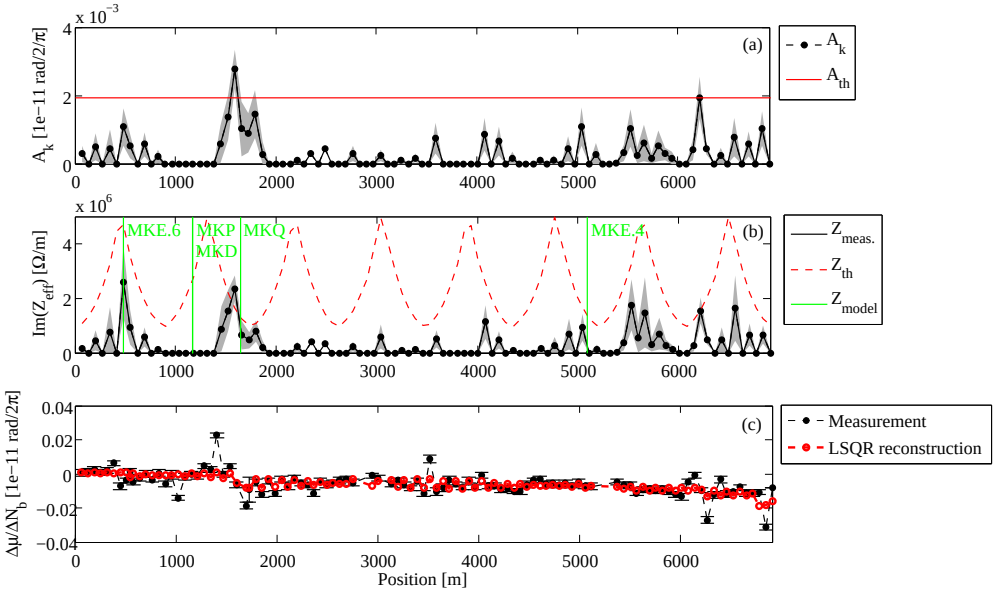


Figure 4.18: Reconstruction of the SPS impedance sources (b) and corresponding induced phase advance beating amplitude (a) for the measured phase advance shift with intensity (c). The kicker positions are noted with green vertical lines. The distributed impedance is set to $9\,\mathrm{M\Omega/m}$.

The inversion is shown in Fig. 4.18: as we can see at the bottom the quality of the reconstruction is poor due to the distorted signal. Some impedance peak is by the way visible close to the MKE and MKP kicker position: among the kickers, which contribute for $7\,\mathrm{M\Omega/m}$ to machine impedance budget, the MKP and MKE give the highest impedance contribution. This suggests that the method could be potentially able to localize impedance sources in the SPS, in particular after the LS1 long shutdown when part of the BPM system is planned to be upgraded.

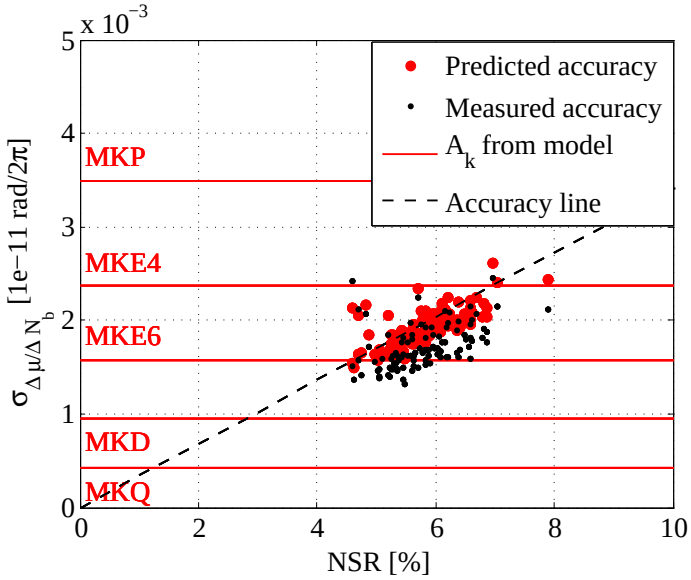


Figure 4.19: SPS localization map: MKP and MKE are close to the measurement accuracy threshold.

We conclude the paragraph showing the localization map in Fig. 4.19 where, analogously to the PS case, we compare the impedance-induced phase advance amplitude and the accuracy obtained in the measurement. Again, we could be able to localize at least the MKP if the signal quality could be improved.

## 4.3 Measurements in the LHC

The impedance localization technique was as well applied to the LHC. Since the AC dipole was used as exciter, we briefly introduce the advantage of this device with respect to the beam kick as applied in the PS or the SPS.

### 4.3.1 Driven oscillations with an AC dipole

An AC dipole is a radio frequency dipole that produces an oscillating field that excites driven oscillations in the beam. While a normal kick would naturally excite the coherent tune oscillation and sidebands, with an AC dipole it is possible to drive the beam oscillation at different frequencies so that to avoid emittance growth and maintain coherent oscillations for many turns therefore improving the quality reproducibility of the optics measurement.

The AC dipole was first introduced and studied in the AGS in the Brookhaven National Laboratories [67]. Studies on the linear and non linear particle motion in the presence of an AC dipole were done in [68,69]. First measurements of resonance driving terms were done in the SPS [70] and RHIC [71]. The device was applied for accurate optics measurements in Tevatron [72], RHIC [73] and recently in the LHC [74].

The concept behind the use of an AC dipole is the following: if an equivalent accelerator optics at a driven frequency $Q_d$ (in tune units) can be measured, it is possible to reproduce with *some* transformation the natural accelerator optics at $Q_{nat}$. Figure 4.20a shows the typical excitation pattern of a driven oscillation at frequency $Q_d$ simulated in HEADTAIL: the ramp before and after the flat oscillation allows for reduced emittance growth and accurate optics measurements. Figure 4.20b shows the driven $Q_d$ and the natural $Q_{nat}$ frequencies. As we can see the signal corresponding to the driven frequency is much stronger than the natural tune.

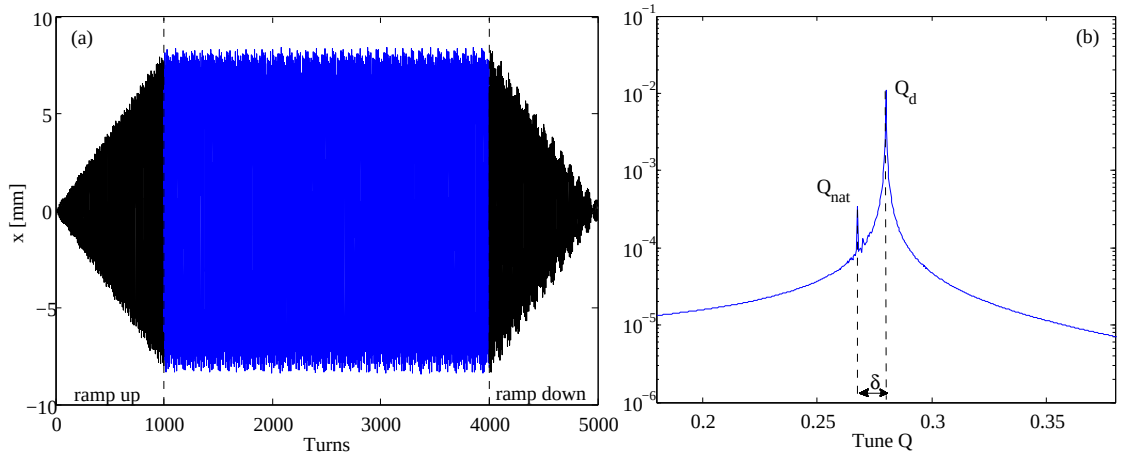


Figure 4.20: (a) Typical excitation pattern of a driven oscillation at frequency $Q_d$ as simulated in HEADTAIL: the signal presents a ramp before and after the flat oscillation allowing for small losses and emittance growth; (b) FFT of the AC dipole signal showing driven $Q_d$ and natural $Q_{nat}$ tunes.

The AC dipole frequency of operation defines the parameter $\delta = Q_d - Q_{nat}$, the distance between natural and driven frequencies. It can be proved [75] that once the accelerator optics is measured at the driving frequency, it is possible to reconstruct the optics at the natural frequency applying the following relation

$$\tan(2\pi\mu_d - \pi Q_d) = \frac{1+\lambda_d}{1-\lambda_d}\tan(2\pi\mu_{nat} - \pi Q_{nat}) \tag{4.2}$$

where $\mu_d$ is the measured phase advance (in tune units) from the AC dipole location at the driven

frequency and $\mu_{nat}$ the phase advance at the natural frequency, and $\lambda_d$ is given by

$$\lambda_d = \frac{\sin(\pi(Q_d - Q_{nat}))}{\sin(\pi(Q_d + Q_{nat}))}. \tag{4.3}$$

Analogously, the optics at the driven frequency, can be modeled as the natural optics including a quadrupole error of strength $\Delta K_{ACd}$ at the AC dipole location. The strength $\Delta K_{ACd}$ is given by [75]

$$\Delta K_{ACd} = 2\frac{\cos(2\pi Q_{nat}) - \cos(2\pi Q_d)}{\beta_{ACd}\sin(2\pi Q_{nat})} \tag{4.4}$$

with $\beta_{ACd}$ the beta function at the AC dipole location.

### 4.3.2 Tune shift measurements with AC dipole

As we showed in Fig. 4.20a, it is possible to measure very clean and highly coherent signals at the driven frequency of an AC dipole. This is particularly important in large accelerators like the LHC were it is difficult to achieve the same oscillation quality with a kicked beam due to very stringent machine protection constraints, beam losses and chromaticity set up. Figure 4.20b shows also that it is difficult to correctly detect the natural tune when a driven oscillation takes place and in particular the tune shift with intensity. This is particularly true for machines like the LHC where the total tune shift is very small (on the order of $1.5 \cdot 10^{-3}$) and the one induced by each impedance source even smaller (collimators in the LHC induce a tune shift on the order of $10^{-4}$). This would complicate the turn by turn analysis since, in Eqs. (4.2) and (4.3) we would need a very accurate information on the tune for each step of the intensity scan. One could think to perform a kick excitation before the AC dipole in order to detect the correct tune, but this would provoke losses spoiling the beam quality for the following AC dipole excitation.

Part of these issues can be overcome focusing on Eq. (4.4). At virtually 0-current, i.e. $N_b = 0\,\text{ppb}$, the AC dipole would interfere with the natural optics as a quadrupole error with a strength

$$\Delta K^0_{ACd} = 2\frac{\cos(2\pi Q^0_{nat}) - \cos(2\pi Q_d)}{\beta_{ACd}\sin(2\pi Q^0_{nat})}. \tag{4.5}$$

Increasing the intensity by $\Delta N_b$ a linear tune shift with intensity would modify the coherent natural tune as

$$Q_{nat} = Q^0_{nat} + \frac{\Delta Q_{nat}}{\Delta N_b}\Delta N_b. \tag{4.6}$$

Plugging this information in Eq. (4.4) we have

$$\Delta K_{ACd} = 2\frac{\cos(2\pi(Q^0_{nat} + \frac{\Delta Q_{nat}}{\Delta N_b}\Delta N_b)) - \cos(2\pi Q_d)}{\beta_{ACd}\sin(2\pi(Q^0_{nat} + \frac{\Delta Q_{nat}}{\Delta N_b}\Delta N_b))} \simeq \tag{4.7}$$

$$\simeq 2\frac{\cos(2\pi Q^0_{nat}) - 2\pi\sin(2\pi Q^0_{nat})\frac{\Delta Q_{nat}}{\Delta N_b}\Delta N_b - \cos(2\pi Q_d)}{\beta_{ACd}\sin(2\pi Q^0_{nat}) + \beta_{ACd}2\pi\cos(2\pi Q^0_{nat})\frac{\Delta Q_{nat}}{\Delta N_b}\Delta N_b} \tag{4.8}$$

where we considered small tune shifts $\frac{\Delta Q_{nat}}{\Delta N_b}$. In the denominator appears the quantity

$$\sin(2\pi Q^0_{nat}) + 2\pi\cos(2\pi Q^0_{nat})\frac{\Delta Q_{nat}}{\Delta N_b}\Delta N_b. \tag{4.9}$$

Considering a working point $Q^0_{nat}$ close to 0.25 and a small tune shift, then

$$\sin(2\pi Q^0_{nat}) \gg 2\pi\cos(2\pi Q^0_{nat})\frac{\Delta Q_{nat}}{\Delta N_b}\Delta N_b \tag{4.10}$$

and Eq. (4.7) can be approximated as

$$\Delta K_{ACd} \simeq \Delta K^0_{ACd} - \frac{4\pi}{\beta_{ACd}} \frac{\Delta Q_{nat}}{\Delta N_b} \Delta N_b. \tag{4.11}$$

Considering the variation over the intensity, we have

$$\frac{\Delta K_{ACd}}{\Delta N_b} = -\frac{4\pi}{\beta_{ACd}} \frac{\Delta Q_{nat}}{\Delta N_b}. \tag{4.12}$$

Equation (4.12) says that measuring at the fixed natural tune $Q^0_{nat}$, whatever tune variation will be compensated at the AC dipole location. From Eq. (3.55) the step in the phase advance beating at the AC dipole location $s_{ACd}$ will therefore be

$$\frac{\Delta\mu(s, s_{ACd})}{\Delta N_b} = -\frac{\Delta Q_{nat}}{\Delta N_b} = -\sum_k \frac{\Delta Q^{imp}_k}{\Delta N_b}, \tag{4.13}$$

where

$$\frac{\Delta\mu(s, s_{ACd})}{\Delta N_b} = \frac{\beta_{ACd}}{4\pi} \frac{\Delta K_{ACd}}{\Delta N_b}. \tag{4.14}$$

This result was benchmarked with HEADTAIL. The B1 ring was modeled as in the configuration file in App. D.2 We placed a broadband resonator close to the IP7 in the LHC lattice model whose tune shift was expected around $5 \cdot 10^{-3}$ per $10^{11}$ ppb. It was first simulated with a kick excitation, and after with an AC dipole excitation as shown in Fig. 4.20a. Figure 4.21 shows the phase advance measured at the natural tune in the case of a kick (a) or AC dipole (b) excitation. In the first case the procedure to derive the phase advance is the same used in chapter 3, in the second case we used Eq. (4.2) to calculate the natural phase advance from the AC dipole driven one. The amplitude of the oscillation which is roughly the tune shift is close to what expected ($5 \cdot 10^{-3}$). The step in the phase advance at the impedance location is compensated as expected in the case of using an AC dipole as exciter. This can be intuitively understood also considering that we are measuring at the AC dipole frequency and calculating the effect at the natural tune $Q^0_{nat}$, therefore not allowing for any tune shift.

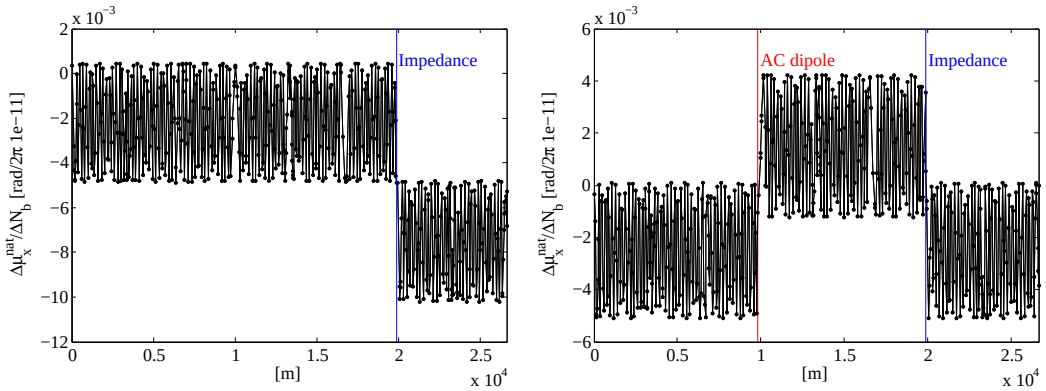


Figure 4.21: HEADTAIL simulations of a broadband impedance placed close to the IP7 in LHC at 19900 m, with a kick (a) and AC dipole (b) excitation. The AC dipole tune shift compensation is visible.

### 4.3.3 Estimations for the LHC

The considerations suggest a method for measuring both impedance and total tune shift in circular accelerator with an AC dipole. The machine could be filled with a certain number of bunches with

different intensities, the tune could be measured for the lowest intense one, coherent oscillation excited with the AC dipole and the oscillations acquired for all the bunches at the same time. Alternatively, a single high intensity bunch could be scraped progressively in order to scan different intensities. Ensuring a reasonable amount of measurement points, the impedance-induced phase advance tune shift could be calculated and observed as depicted in the previous section.

In this frame, a first measurement was done on 28-11-2012 in the LHC for the determination of the measurement accuracy from multi-turn data acquisition. The machine parameters used in the measurement are listed in App. B.3. A single high intensity bunch of $N_b \simeq 3 \cdot 10^{11}$ ppb was progressively scraped to $N_b \simeq 10^{11}$ ppb with $M = 14$ AC dipole induced oscillations. Figures 4.22a and 4.22b show the steps in the beam intensity together with the shortening of the bunch length from the scraping. The measurement was done at injection energy $E = 450\,\text{GeV}$ over 20 minutes. The machine natural tunes were $Q^0_{nat,y} = 0.3085$ and $Q^0_{nat,x} = 0.2743$ and the AC dipole oscillations were driven at $Q_{d,y} = 0.32$ and $Q_{d,x} = 0.27$. A number of $N = 2200$ of coherent driven oscillations was recorded by the BPM system. Figure 4.23 shows the localization map where the accuracy

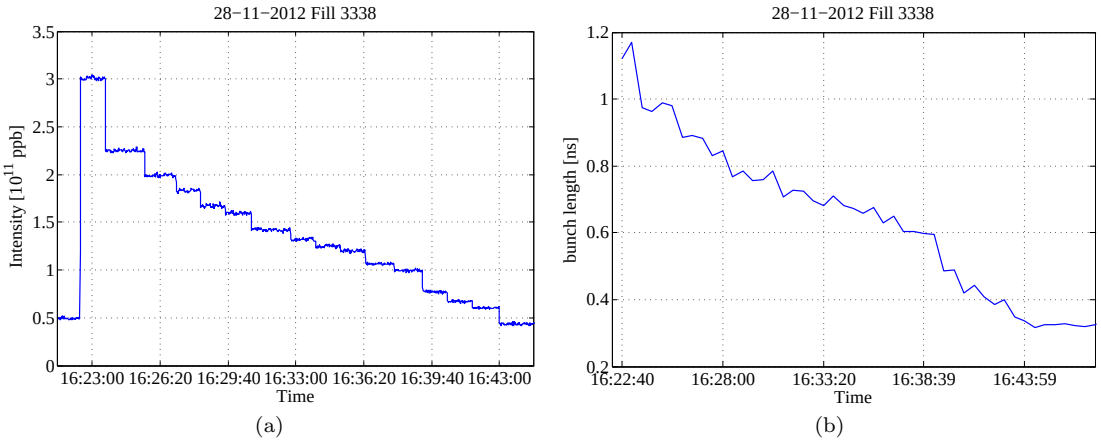


(a) (b)

Figure 4.22: Scraping of a single bunch (a) and bunch length reduction (b) during multi-turn data acquisition with an AC dipole.

predicted and measured from the measured phase advances is compared with the impedance-induced phase advance amplitude of Eq. (3.67) from the current impedance model of the most relevant collimators at the interaction points (IPs) both for the horizontal and vertical planes. As we can see a good measurement accuracy is potentially achievable and the impedance of the collimators could, in principle, be localized in dedicated future measurements.

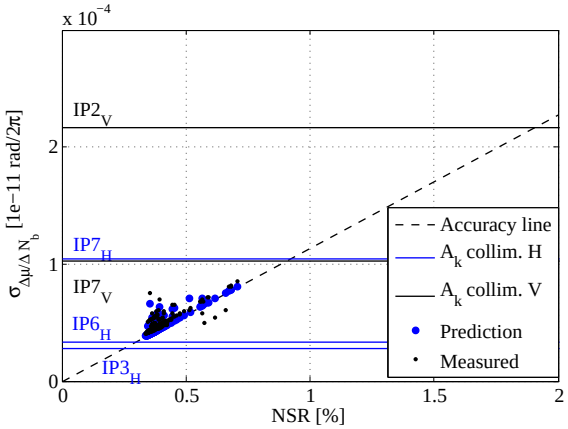


Figure 4.23: Localization map for the LHC.

Particular care should be taken in the correction of the tune drift with time which is in the

order of 0.005 every $\simeq 15$ minutes especially at injection [76]. Since we are measuring signals which amplitude is one order of magnitude less, this effect becomes important and can overcome the impedance signal as we will also show in more detail in the next section.

## 4.4 Measurements in the AGS and RHIC machines

### 4.4.1 Introduction to the BNL particle accelerators

The RHIC luminosity upgrade program [77] aims for an increase of the polarized proton luminosity by a factor 2. To achieve this goal a significant increase in the beam intensity is foreseen. The beam coupling impedance represents a source of detrimental effects for beam quality and stability at high bunch intensities. In this section, we evaluate the global transverse impedance in both the AGS and RHIC with recent measurements of tune shift as a function of bunch intensity. Attempts of impedance localization measurements are shown as well.

The Brookhaven accelerator complex is showed in Fig. 4.24. The accelerator machines operate primarily with gold ions and with polarized protons. Focusing on the proton operations, the particles are injected into the Linac and accelerated through the Booster and the AGS up to the total energy of about 25 GeV.

The AGS machine can be considered as the CERN-PS twin accelerator where the concept of alternate gradient focusing had its origin through the pioneering work of E. Courant, M. S. Livingston, and H. Snyder. Built in 1960, the AGS accelerator has served the Physics community through the discovery of subatomic particles such as the muon neutrino and the J/$\Psi$ particles. It is today, with the AGS booster, part of the injector accelerator system for RHIC.

The extracted beams are therefore injected into RHIC. The RHIC collider consists of two 3.8 km circumference hexagonally shaped rings, named Blue and Yellow. Each ring is constituted of six straight sections and six arcs, where particles circulate through 1740 superconducting magnets. The main purpose of the collider is to provide collisions at 100 GeV per beam of heavy gold ions into the two main experiments, STAR and PHENIX. These are located at the straight sections enumerated by clock positions, respectively at 6 o'clock (injection point) and 8 o'clock. RHIC provides also collisions for lighter ions down to protons at the energy of 250 GeV.

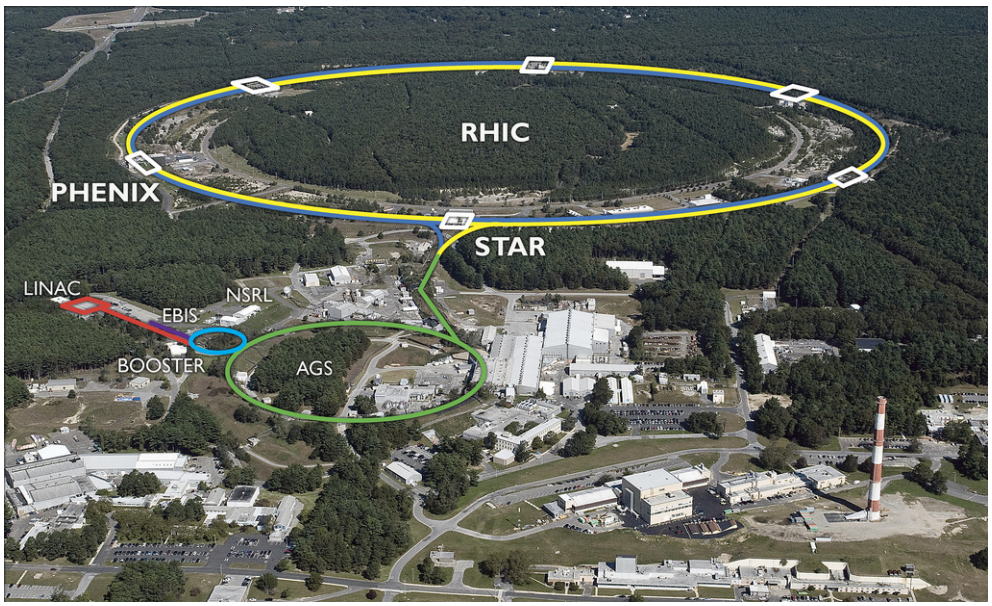


Figure 4.24: BNL accelerator complex.

### 4.4.2 AGS measurements

In the AGS accelerator the absence of a multi-turn BPM system allowed only for the measurement of the total effective impedance through the observation of the transverse tune shift with intensity. A measurement in the vertical plane could be performed while time constraints didn't allow for the horizontal one (which is anyway believed to be small due to the vacuum chamber elliptical shape).

The measurement has been performed at flat top before extraction with the machine parameters listed in App. B.4. The used beam parameters are reported in Tab. 4.5. Figure 4.25 shows the beam profile measured at the bunch shape monitor (BSM) and the rms bunch length $\sigma_b$ with a Gaussian fit is $\sigma_b = (5.8 \pm 0.1)$ ns, over 25 measurements.

| AGS beam | Parameter | Value |
|---|---|---|
| Intensity | $N_b$ | $5 \cdot 10^{10} \rightarrow 25 \cdot 10^{10}$ ppb |
| Momentum spread | $\mathrm{d}p/p_o$ | $2 \cdot 10^{-4}$ |
| Bunch length | $\sigma_t$ | 5.8 ns |
| Normalized 95% Horizontal emittance | $\varepsilon_{x_n}$ | 13.5 $\mu$rad |
| Normalized 95% Vertical emittance | $\varepsilon_{y_n}$ | 13.5 $\mu$rad |

Table 4.5: AGS beam parameters.

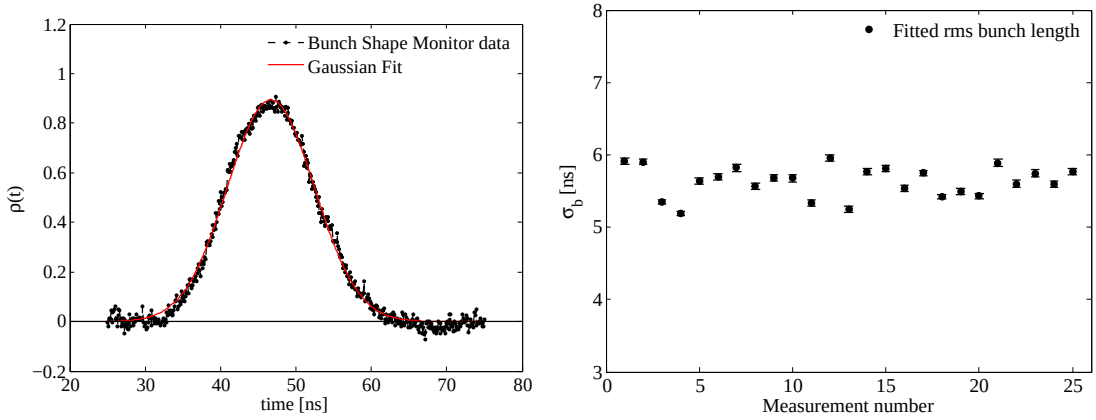


(a) (b)

Figure 4.25: Example of acquired bunch shape (a) and rms bunch length from Gaussian fit from 25 measurements (b) in the AGS.

An intensity scan was set up from $5 \cdot 10^{10}$ ppb up to $25 \cdot 10^{10}$ ppb and the beam was excited with a transverse kicker synchronized with a dedicated high-resolution BPM from which 300 turns of coherent betatron oscillation were stored. The acquired tune data are shown in Fig. 4.26: a tune shift of $5 \cdot 10^{-5}$ per $10^{11}$ ppb could be measured. Recurring to Eq. (3.43) in the smooth approximation we obtain

$$Z_y^{eff} = (1.3 \pm 0.1)\,\mathrm{M\Omega/m}. \tag{4.15}$$

From past measurements [78] it has been considered a longitudinal effective impedance $Z_l^{eff}/n = 10\,\Omega$ where we recall the longitudinal effective impedance definition

$$\frac{Z_l^{eff}}{n} = \frac{\displaystyle\int_{-\infty}^{\infty} \frac{Z_l(\omega)}{\omega/\omega_o} S(\omega)\,\mathrm{d}\omega}{\displaystyle\int_{-\infty}^{\infty} S(\omega)\,\mathrm{d}\omega}, \tag{4.16}$$

with $\omega_o = 2\pi f_{rev}$. Assuming the longitudinal impedance as prevalently due to the resistive wall, we can extrapolate the transverse effective impedance comparing the impedances from Tab 2.14 at the intermediate frequencies IF

$$Z_t(\omega) = \frac{\beta c}{\omega}\frac{2}{b^2} Z_l(\omega), \tag{4.17}$$

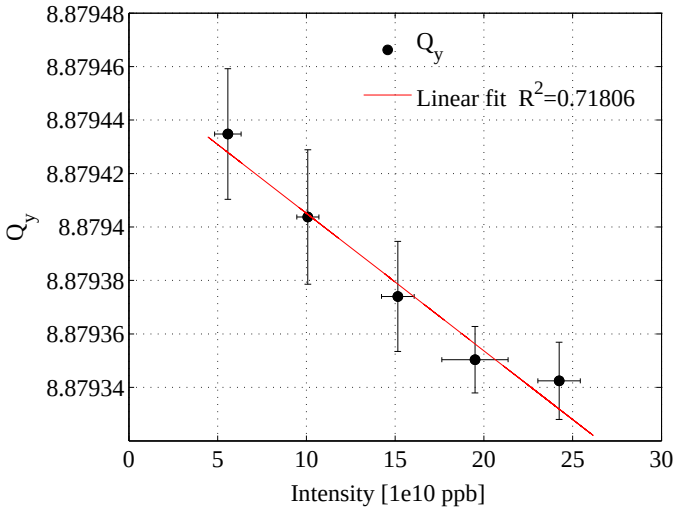


Figure 4.26: Example of acquired bunch shape (a) and rms bunch length from a Gaussian fit over 25 measurements (b) in the AGS.

where $b$ is the beam pipe radius of about 5 cm. Integrating over the beam spectrum $S(\omega)$ we get

$$Z_t^{eff} = \frac{2R}{b^2}\frac{Z_l^{eff}}{n} \simeq 1.5\,\mathrm{M\Omega/m} \tag{4.18}$$

which is very close to the measured one.

In case the value of the longitudinal effective impedance $Z_l^{eff}/n = 10\,\Omega$ is confirmed, most of the AGS impedance could be considered due to the resistive wall contribution.

### 4.4.3 RHIC measurements

The impedance measurements in RHIC were performed on 24-04-2013, 1-05-2013 and 15-05-2013 in collaboration with the machine operation team. Both total and local machine impedance could be in principle measured thanks to the high-performance of the BPM system. Focusing on the phase advance measurement for impedance localization, considering Eq. (3.64), the machine BPM system can be characterized as in Tab. 4.6. The phase advance slope accuracy $\sigma_{\Delta\mu/\Delta N_b}$ should be

| Best BPM performance | Parameter | Value |
|---|---|---|
| Maximum number of turns | $N$ | 1000 |
| Noise level | $\sigma_n$ | $15\,\mu$m |
| Kick amplitude | $A_{kick}$ | 2 mm |
| Number of measurements | $M$ | 100 |
| Intensity scan | $X$ | $0.5 \cdot 10^{11} \rightarrow 2 \cdot 10^{11}$ ppb |
| Phase advance slope accuracy | $\sigma_{\Delta\mu/\Delta N_b}$ | $6 \cdot 10^{-5}\,10^{-11}$ rad/$2\pi$ |

Table 4.6: Phase advance slope accuracy estimation for the RHIC BPM system.

compared to the impedance-induced phase advance beating amplitude $A_k$ from Eq. (3.67). Since Eq. (3.67) takes into account the tune shifts from the element by element impedance model of the accelerator $\Delta Q_{y_k}/\Delta N_b$, and are not always available, we could only assume a fraction of the whole accelerator tune shift $\Delta Q_y/\Delta N_b$ in order to assess the feasibility of the localization measurement.

**Total impedance measurements**

The total accelerator impedance could be derived from the tune shift with intensity for both accelerators, Blue and Yellow.

The measurements for Blue where performed on 24-04-2013 and 15-05-2013. The measurements were done injecting a train of bunches at different intensities, from $0.5 \cdot 10^{11}$ ppb to $1.8 \cdot 10^{11}$ ppb with average rms bunch length $\sigma_b \simeq 5\,\text{ns}$. The beam was excited with a transverse kick in both planes, and the betatron oscillations were recorded for 1024 turns. Chromaticity was set as close as possible to 0 on both planes, requiring a long machine set-up time. An example of betatron signal from a BPM is shown in Fig. 4.27 were we can see a fast damping after 100 turns and coherent oscillations up to 1024 turns. The signals are analyzed with SUSSIX after an SVD noise cleaning and the tune shift with intensity is therefore computed.

The tune shifts for both X an Y plane are presented in Fig. 4.28.

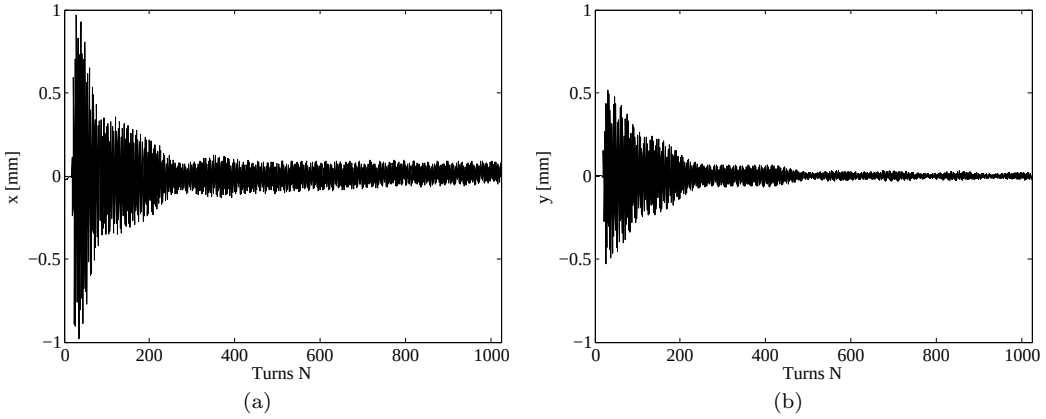


Figure 4.27: Example of recorded traces from 15-05-2013 from the "B06-BV15" BPM for X (a) and Y plane (b).

Analogously, on 01-05-2013, the same measurement was done in the Yellow ring injecting train of bunches at different intensities, from $0.5 \cdot 10^{11}$ to $2.5 \cdot 10^{11}$ ppb with average rms bunch length $\sigma_b \simeq 4\,\text{ns}$. The analyzed tune shifts are presented in Fig. 4.29 for a set of 2 good fills in Yellow. The deduced effective impedance is reported in Tabs. 4.7 and 4.8 and is calculated using Eq. (3.35).

| Measurement | $Z_x^{eff}$ [MΩ/m] | $Z_y^{eff}$ [MΩ/m] | $\mathrm{d}Q_x/\mathrm{d}N_b\,(\cdot 10^{-11})$ | $\mathrm{d}Q_y/\mathrm{d}N_b\,(\cdot 10^{-11})$ |
|---|---|---|---|---|
| 24-04-2013 | $(7.06 \pm 1.29)$ | $(9.06 \pm 1.56)$ | $(-4.74 \pm 0.86) \cdot 10^{-4}$ | $(-5.88 \pm 1.01) \cdot 10^{-4}$ |
| 15-05-2013 | $(20.51 \pm 1.98)$ | $(19.07 \pm 1.15)$ | $(-13.53 \pm 1.30) \cdot 10^{-4}$ | $(-12.16 \pm 0.73) \cdot 10^{-4}$ |
| Average | $(13.79 \pm 6.72)$ | $(14.01 \pm 5.00)$ | $(-9.13 \pm 4.39) \cdot 10^{-4}$ | $(-9.02 \pm 3.14) \cdot 10^{-4}$ |

Table 4.7: Tune slope and effective impedances measured in RHIC Blue ring.

We might notice that, for the tune shift measurement, the drift of the machine with time has been taken into account: at injection, the exponential decay for the current in the magnets affects the machine parameters as depicted in Fig. 4.30 resulting in wrong tune shift estimations (up to 10%).

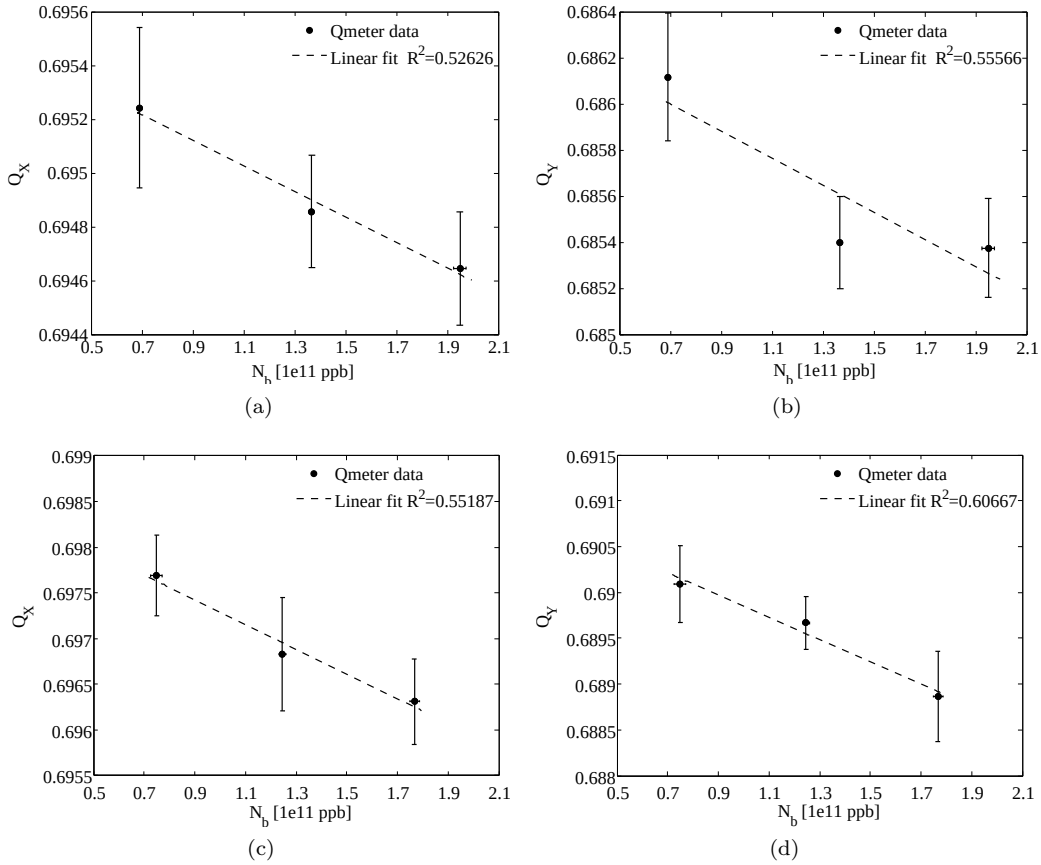


Figure 4.28: Tune shift measurements in RHIC Blue ring from 24-04-2013 X plane (a) and Y plane (b), 15-05-2013 X plane (c) and Y plane (d) with a bunch length $\sigma_b \simeq 5\,\text{ns}$.

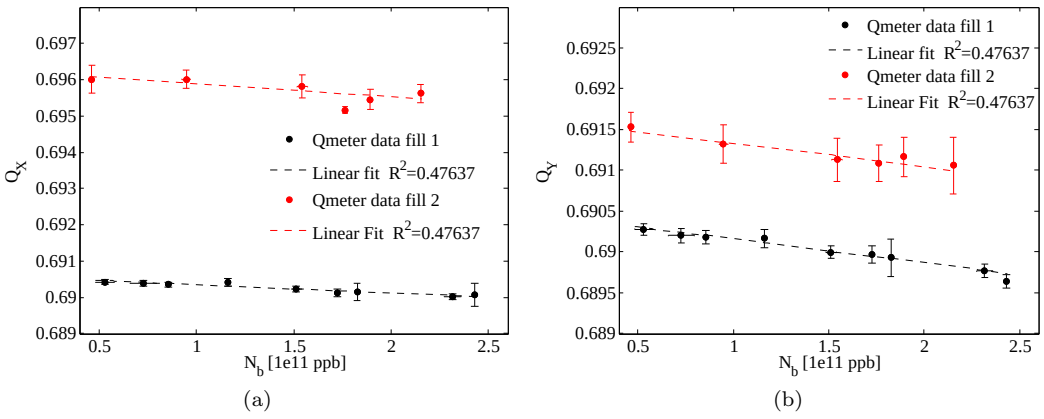


Figure 4.29: Tune shift measurements of two injection fills in the RHIC Yellow ring taken on 01-05-2013 X plane (a) and Y plane (b) with a bunch length $\sigma_b \simeq 4\,\text{ns}$.

| Measurement | $Z_x^{eff}$ [MΩ/m] | $Z_y^{eff}$ [MΩ/m] | $\mathrm{d}Q_x/\mathrm{d}N_b\,(\cdot 10^{-11})$ | $\mathrm{d}Q_y/\mathrm{d}N_b\,(\cdot 10^{-11})$ |
|---|---|---|---|---|
| 01-05-2013 #1 | $(2.47 \pm 0.30)$ | $(3.22 \pm 0.27)$ | $(-2.32 \pm 0.29) \cdot 10^{-4}$ | $(-2.92 \pm 0.25) \cdot 10^{-4}$ |
| 01-05-2013 #2 | $(3.87 \pm 0.85)$ | $(3.14 \pm 0.62)$ | $(-3.64 \pm 0.80) \cdot 10^{-4}$ | $(-2.85 \pm 0.56) \cdot 10^{-4}$ |
| Average | $(3.17 \pm 1.15)$ | $(3.18 \pm 0.89)$ | $(-2.98 \pm 1.09) \cdot 10^{-4}$ | $(-5.77 \pm 0.81) \cdot 10^{-4}$ |

Table 4.8: Tune slope and effective impedances measured in RHIC Yellow ring.

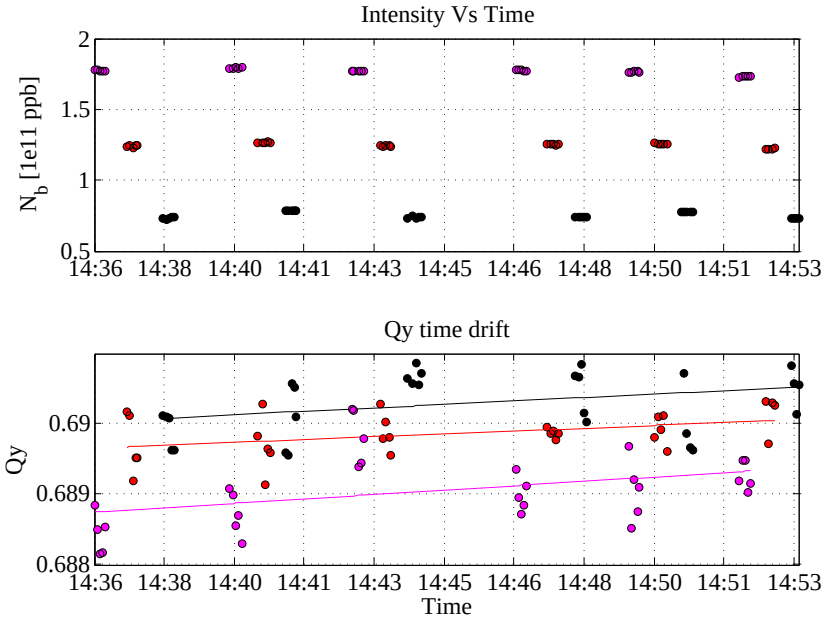


Figure 4.30: Example of tune drift with time for the vertical tune measured on 15-05-2013 on Blue. On top the train of injected bunches from high to low intensities; on bottom the correspondent measured tunes (dots) and the linear drift with time (thick lines).

### Localized impedance measurements

The RHIC BPM system [79], [80] consists in 160 23-cm cryogenic striplines per plane per ring. Most of the devices are made of by two opposite striplines oriented vertically or horizontally accordingly to the higher beta function. In critical areas, close to the interaction points, BPMs record both plane (i.e. two pairs of striplines). The system is able to record up to 1024 turns. During operation a noise of $\sigma_n \simeq 10\,\mu$m rms was measured in the turn by turn data.

From the measured tune shift with intensity we measured higher impedance for the Blue ring with respect to the Yellow one. We tried therefore to apply the impedance localization method in order to get an estimate of the main impedance sources in the Blue ring. The main Blue ring machine parameters used in the measurement are listed in App. B.5

The data recorded during 15-05-2013 were analyzed with SUSSIX and the integrated phase advance calculated starting from the STAR interaction point. At different intensities the phase advance was expected to shift linearly (analogously with the tune) as can be seen in Fig.4.31a. The measured data presented an average noise level $NSR \simeq 5\%$. Using Eq. (3.64) we can estimate the accuracy for the phase advance slope $\Delta\mu/\Delta N_b$ measurement and compare with the expected one. Figure 4.31b shows the measured and predicted accuracy compared with the tune shift with intensity (i.e. the total integrated phase advance slope with intensity). A high margin is present and suggests that an impedance of the order of 20% the total machine impedance could be localized.

Extrapolating the phase advance at 0-current $N_b = 0\,$ppb, we can study the machine optics

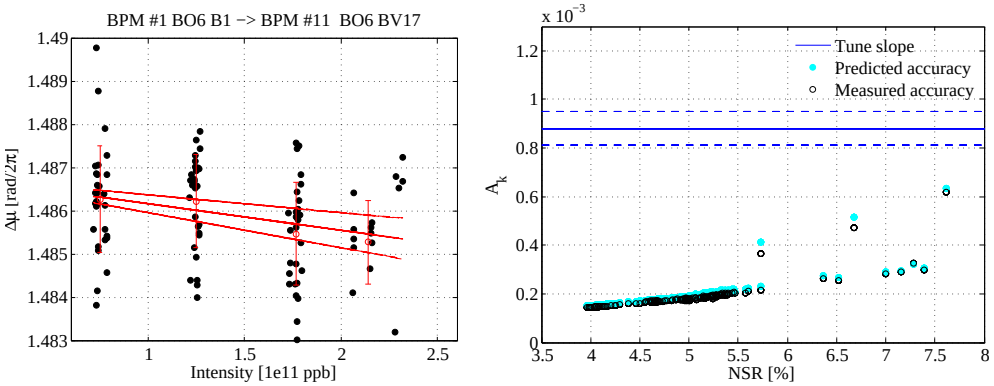


Figure 4.31: (a) example of phase advance slope with intensity measured in Blue; (b) comparison of the measured and predicted accuracy with the NSR level for all the measured phase advances (dots) and comparison with the tune slope (thick line) and its accuracy (dashed lines).

and quantify the accuracy of the MAD-X model used for its description. Figure 4.32 shows the comparison between model and measurement as well as their relative ratio. The model is in agreement within 30% to the measured one: this is a limitation for the impedance reconstruction algorithm, where the interpolation over a reliable (less than 5%) model is required in order to localize the most probable impedance sources.

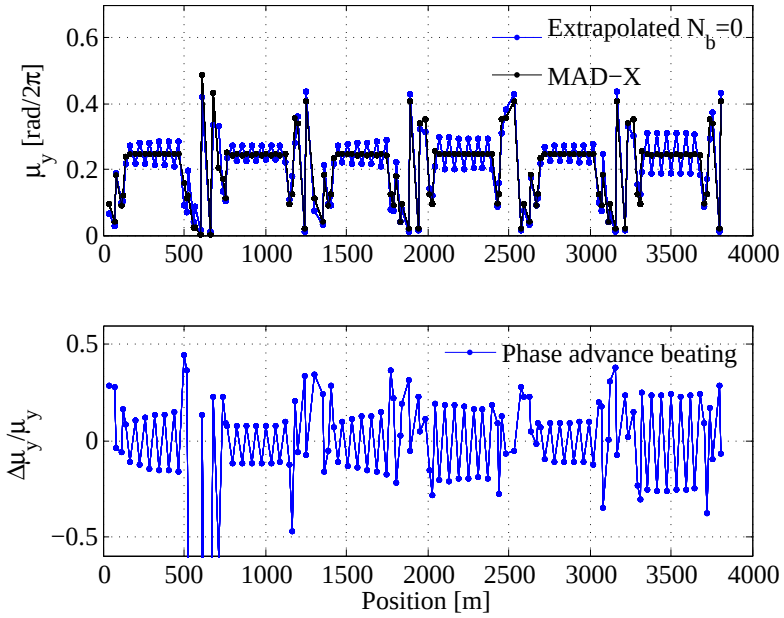


Figure 4.32: Measured phase advance in Blue compared with the MAD-X model (top) and relative beating (bottom).

The measured phase advance slope is shown in Fig. 4.33. In order to reconstruct the possible impedance positions we considered a set of impedance reconstruction points coincident with the BPM position. This choice is imposed by the model accuracy. As it has been shown, the model is accurate only within 30%: choosing the reconstruction points at the BPM position enables to calculate the response matrix $S$ by means of Eq. (3.54) using the measured phase advances in place of the model ones, being able to calculate a more reliable response matrix.

Measured and reconstructed slopes are shown in Fig. 4.34 as well as the impedance position. As we commented in Sec. 3.6 while the phase advance $\Delta\mu$ can be measured independently from

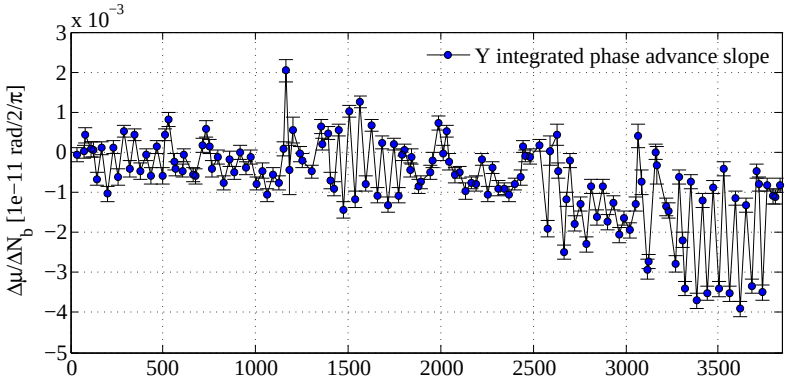


Figure 4.33: Measured phase advance slope in Blue.

the model, the $\beta$ function measurement is more involved: if derived from the measured oscillation amplitude it could be affected by the BPM gain calibration, if derived from the phase advance it depends on the model accuracy. Most of the impedance-induced phase advance beating is produced by localized impedance sources around $s \simeq 2500\,\mathrm{m}$ in the machine. This is only a preliminary conclusion due to the limited accuracy of the lattice model of the machine. It is known that part of the complication is due to the difficult modeling of the *Snakes*, special magnets used to preserve the beam spin direction along acceleration. For this reason new measurements are planned without the use of the Snakes and at flat top in order to mitigate te tune drift with time effect.

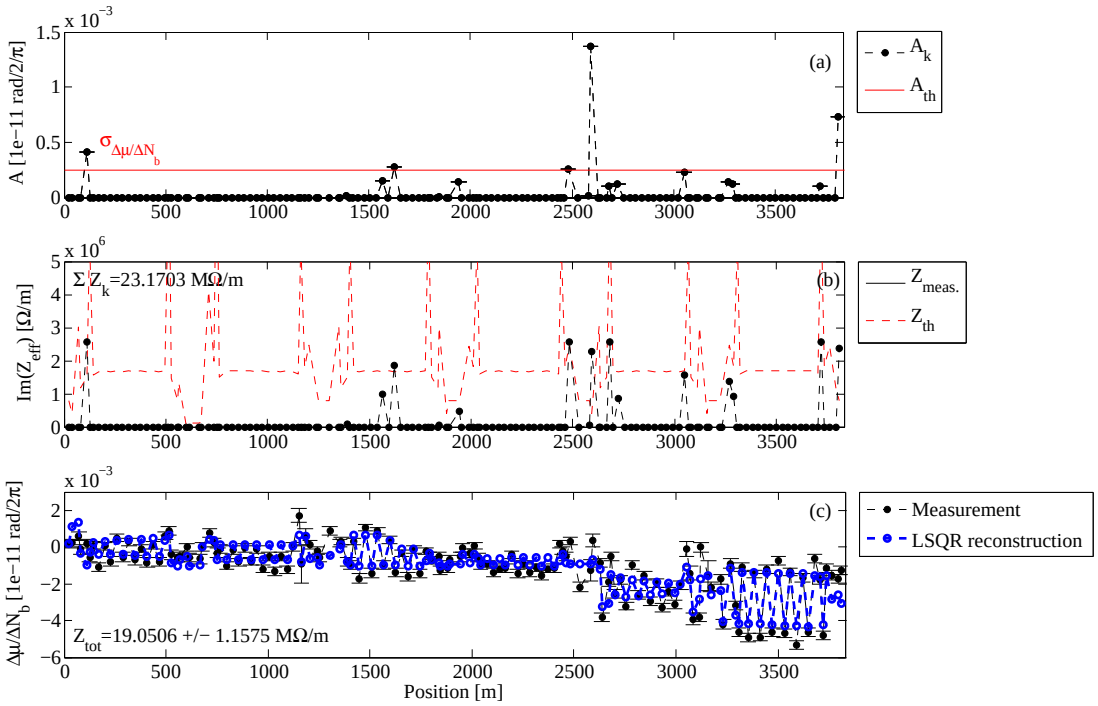


Figure 4.34: Measured phase advance slope in Blue placing reconstruction kicks at the BPM positions. (a) The reconstructed amplitude of the impedance-induced phase advance beating (in black) with accuracy threshold (in red); (b) The reconstructed impedance locations (in black) with corresponding accuracy threshold (in red); (c) Measured phase advance slope and LSQR reconstruction.

# Chapter 5

# Conclusions

In this thesis we presented a contribution for improved techniques of impedance calculation and localization in particle accelerators.

The Mode Matching technique was presented and applied to the calculation of the impedance of an azimuthally symmetric device of finite length loaded with a toroidal insert. This model was successfully benchmarked with theory, CST simulations and other already existing theories over a wide range of geometrical and electromagnetic parameters confirming the Mode Matching method as a powerful numerical tool.

The study of the impedance dependence on the device length with respect to the approaches which assume an infinite length, introduced two interesting effects: the increase of the transverse dipolar impedance for short highly conductive inserts at low frequencies, and the possible presence of a resonance at the beam pipe cut-off frequency.

The first effect is believed to be of academical interest because of the very low frequency range in which it is apparent: for longer devices there is indeed no appreciable difference between the infinite length approximation and the finite length approach studied in this thesis. Within the limits of our model we demonstrated that an impedance reduction by longitudinal segmentation of particle collimators is not effective and other methods should be considered (increase of collimator aperture, increase of conductivity, reduction of the $\beta$ function at the collimator positions, etc.) as shown in Fig. 2.12.

The second effect can be observed in short inserts like beam pipe flanges filled with dielectrics of equivalent conductivity in the order of $10^{-2}$ S/m. The presence of the resonant mode at cut-off was explained, for the longitudinal impedance case, with a simplified equivalent circuital model in which the reactive beam pipe impedance below cut-off resonates with the most nearby resonance produced in the insert as shown in Figure 2.29. It has also been demonstrated how the presence of the impedance kink at-cut off depends on the relative position of the insert resonances with respect to the cut off frequency. The existence of the mode has also been confirmed with CST Eigenmode Solver simulations. Since a high number of insulating beam pipe flanges is very common in particle accelerators, this effect could play a significant role in driving beam instabilities due to the beam interaction with the resonant impedance modes and should be taken into account.

The impedance localization method was also improved. With respect to the previously applied methods we studied the method accuracy considering the noise introduced by the BPM system on the measured signal, the range of intensity scan, the number of measurements and the number of recorded turns. The accuracy estimation has been benchmarked both with simulations and measurements showing good agreement.

The estimations of the impedance-induced phase advance signals was also studied in detail for the CERN PS machine where an impedance model of the accelerator was built taking into account the impedance of the beam pipe, the kickers, the cavities and other accelerator elements.

The PS impedance model was used for performing HEADTAIL simulations in order to validate the impedance localization method. This gave us the opportunity of refining the technique of impedance reconstruction taking into account the contribution of distributed localized impedances: the first are typically related to the beam pipe and indirect space charge, the second to high impedance elements such as kickers, collimators, etc. The reconstruction of a distributed impedance

would require in principle, infinite number of reconstructors all over the machine and for this reason it is suggested to calculate its contribution from the machine model, and subtract it from the measurement.

Measurements were done in the CERN PS. A first validation measurement varying the current in two quadrupoles demonstrated the impedance localization method in the case of two highly localized equivalent impedance sources. Measurements with beam were performed especially in the vertical plane at 2 GeV kinetic energy. The global impedance has been estimated to be about 9 MΩ/m, revealing that 40% is still missing with respect to the impedance model prediction. The impedance localization measurements were strongly affected by the high impact of noise as shown in Fig. 4.12. Choosing a working point closer to the half integer, we could enhance the impedance signal and have clearer impedance reconstructions at the kicker positions and in sections 16, 64 and 92. As a drawback, the machine $\beta$ functions strongly depend on the unavoidable presence of errors in the machine, complicating the impedance reconstruction. In order to complete the machine impedance model a series of new impedance localization measurements is planned at injection, flat bottom and extraction energies: the measurements at extraction, in particular, will reduce the contribution of the indirect space charge, i.e. the distributed impedance, helping the process of reconstructing localized impedance sources.

The method was applied in the CERN SPS where an accurate and almost complete impedance model has been recently developed. The highest impedance contributors in the machine are the kickers. Unfortunately the impedance localization measurements could not reconstruct the impedance positions due to the poor quality of the current BPM system. The substantial upgrade foreseen for the post-shutdown period will allow more accurate measurements.

A new method for the impedance localization was presented for the LHC machine were an AC dipole excitation is used. This device is used for optics measurements with highly coherent signals and could be used for very accurate measurements of the machine impedance. The proposed study demonstrates how the local and total impedance can be measured through phase advance measurement at the unperturbed 0-current natural tune. New measurements applying the AC dipole are foreseen for the LHC in the post-shutdown period. We remark the fact that, due to the small impedance-induced expected tune shifts, other effects, like the tune drift with time, should be taken into account and correctly compensated.

A campaign of impedance measurements was also done in the AGS and RHIC accelerators. In the AGS we could measure the total vertical imaginary part of the impedance estimated close to 1.3 MΩ/m. A rough estimation suggests that almost all the impedance could be due to the contribution of the beam pipe accordingly to past measurements of the longitudinal impedance.

A series of measurements was done in RHIC. The estimations of tune shift with intensity showed a strong difference between the two, in principle identical, accelerator rings, Blue and Yellow. Since the impedance in Blue seems to be much higher than the one in Yellow, we performed and impedance localization measurement revealing probable high impedance sources at about 2500 m from the STAR interaction point. The result is, by the way, only approximated due to the accuracy of the optics model ($\simeq 30\%$ beating) and new measurements are planned without the contribution of the Snakes that considerably complicate the machine optics. Since an AC dipole is available in the machine, it could be applied for impedance measurements as depicted in the case of the LHC.

# Appendix A

# Series summations

Here we list the sums of series used to simplify the mode matching in the longitudinal and transverse case:

## A.1 Longitudinal series

Sum of series in $s$.

$$\sum_{s=0}^{\infty} \frac{(-1)^s \, \epsilon_s}{\alpha_0^2 - \alpha_{p\,s}^2} = \frac{L}{b\,\tilde{\alpha}_p} \csc(\tilde{\alpha}_p L/b), \tag{A.1}$$

$$\sum_{s=0}^{\infty} \frac{\epsilon_s}{\alpha_0^2 - \alpha_{p\,s}^2} = \frac{L}{b\,\tilde{\alpha}_p} \cot(\tilde{\alpha}_p L/b), \tag{A.2}$$

$$\sum_{s=0}^{\infty} \frac{\epsilon_s}{\left(\alpha_b^2 - \alpha_s^2\right)\left(\alpha_o^2 - \alpha_{ps}^2\right)} = -\frac{L}{b\left(\alpha_b^2 - \tilde{\alpha}_p^2\right)} \left( \frac{\cot\left(\frac{L\alpha_b}{b}\right)}{\alpha_b} - \frac{\cot\left(\frac{L\tilde{\alpha}_p}{b}\right)}{\tilde{\alpha}_p} \right), \tag{A.3}$$

$$\sum_{s=0}^{\infty} \frac{(-1)^s \, \epsilon_s}{\left(\alpha_b^2 - \alpha_s^2\right)\left(\alpha_o^2 - \alpha_{ps}^2\right)} \to -\frac{L}{b\left(\alpha_b^2 - \tilde{\alpha}_p^2\right)} \left( \frac{\csc\left(\frac{L\alpha_b}{b}\right)}{\alpha_b} - \frac{\csc\left(\frac{L\tilde{\alpha}_p}{b}\right)}{\tilde{\alpha}_p} \right). \tag{A.4}$$

Sum of series in $p$ derived from the Kneser-Sommerfeld formula [26].

$$\sum_{p=1}^{\infty} \frac{\alpha_p}{J_1\left(\alpha_p\right)\left(\alpha_0^2 - \alpha_{p\,s}^2\right)} = -\frac{1}{2J_0\left(\tilde{\alpha}_s\right)}, \tag{A.5}$$

$$\sum_{p=1}^{\infty} \frac{1}{\alpha_o^2 - \alpha_{ps}^2} = -\frac{J_1\left(\tilde{\alpha}_s\right)}{2\tilde{\alpha}_s J_0\left(\tilde{\alpha}_s\right)}. \tag{A.6}$$

## A.2 Transverse series

Sum of series in $s$.

$$\sum_{s=0}^{\infty} \frac{\epsilon_s}{\alpha_0^2 - \alpha_{p\,s}^2} = \frac{L}{b\tilde{\alpha}_p} \cot\left(\frac{L\tilde{\alpha}_p}{b}\right), \tag{A.7}$$

$$\sum_{s=0}^{\infty} \frac{(-1)^s\,\epsilon_s}{\alpha_0^2 - \alpha_{p\,s}^2} = \frac{L}{b\tilde{\alpha}_p} \csc\left(\frac{L\tilde{\alpha}_p}{b}\right), \tag{A.8}$$

$$\sum_{s=0}^{\infty} \frac{\epsilon_s}{\beta_{p\,s}^2} = \frac{L}{b\beta_p} \coth\left(\frac{L\beta_p}{b}\right), \tag{A.9}$$

$$\sum_{s=0}^{\infty} \frac{(-1)^s\,\epsilon_s}{\beta_{p\,s}^2} = \frac{L}{b\beta_p} \operatorname{csch}\left(\frac{L\beta_p}{b}\right), \tag{A.10}$$

$$\sum_{s=0}^{\infty} \frac{\alpha_s^2}{\beta_{p\,s}^2\left(\alpha_0^2 - \beta_{p\,s}^2\right)} = \frac{L}{2b\,\alpha_0^2}\left(\tilde{\beta}_p \cot\left(\frac{L\tilde{\beta}_p}{b}\right) - \beta_p \coth\left(\frac{L\beta_p}{b}\right)\right), \tag{A.11}$$

$$\sum_{s=0}^{\infty} \frac{(-1)^s\,\alpha_s^2}{\beta_{p\,s}^2\left(\alpha_0^2 - \beta_{p\,s}^2\right)} = \frac{L}{2b\,\alpha_0^2}\left(\tilde{\beta}_p \csc\left(\frac{L\tilde{\beta}_p}{b}\right) - \beta_p \operatorname{csch}\left(\frac{L\beta_p}{b}\right)\right), \tag{A.12}$$

$$\sum_{s=0}^{\infty} \frac{(-1)^s \epsilon_s \left(\alpha_o^2 - \alpha_s^2\right)\left(-1 + (-1)^s e^{\frac{jL\alpha_b}{b}}\right)}{\left(\alpha_b^2 - \alpha_s^2\right)\left(\alpha_o^2 - \alpha_{ps}^2\right)} =$$

$$= \frac{L\left(i\tilde{\alpha}_p e^{\frac{jL\alpha_b}{b}}\left(\alpha_b^2 - \alpha_o^2\right) + \alpha_b\alpha_p^2\left(-\csc\left(\frac{L\tilde{\alpha}_p}{b}\right) + e^{\frac{jL\alpha_b}{b}}\cot\left(\frac{L\tilde{\alpha}_p}{b}\right)\right)\right)}{b\alpha_b\tilde{\alpha}_p\left(\alpha_b^2 - \alpha_o^2 + \alpha_p^2\right)}, \tag{A.13}$$

$$\sum_{s=0}^{\infty} \frac{\epsilon_s \left(\alpha_o^2 - \alpha_s^2\right)\left(-1 + (-1)^s e^{\frac{jL\alpha_b}{b}}\right)}{\left(\alpha_b^2 - \alpha_s^2\right)\left(\alpha_o^2 - \alpha_{ps}^2\right)} =$$

$$= \frac{L\left(\alpha_b\alpha_p^2\left(-\cot\left(\frac{L\tilde{\alpha}_p}{b}\right) + e^{\frac{jL\alpha_b}{b}}\csc\left(\frac{L\tilde{\alpha}_p}{b}\right)\right) + i\tilde{\alpha}_p\left(\alpha_b^2 - \alpha_o^2\right)\right)}{b\alpha_b\tilde{\alpha}_p\left(\alpha_b^2 - \alpha_o^2 + \alpha_p^2\right)}, \tag{A.14}$$

$$\sum_{s=0}^{\infty} \frac{\alpha_s^2\left(-1 + (-1)^s e^{\frac{jL\alpha_b}{b}}\right)}{\left(\alpha_b^2 - \alpha_s^2\right)\left(\beta_p^2 + \beta_s^2\right)} = \frac{L\left(i\alpha_b + \beta_p \operatorname{csch}\left(\frac{L\beta_p}{b}\right)\left(\cosh\left(\frac{L\beta_p}{b}\right) - e^{\frac{jL\alpha_b}{b}}\right)\right)}{2b\left(\alpha_b^2 + \beta_p^2\right)}, \tag{A.15}$$

$$\sum_{s=0}^{\infty} \frac{(-1)^s\alpha_s^2\left(-1 + (-1)^s e^{\frac{jL\alpha_b}{b}}\right)}{\left(\alpha_b^2 - \alpha_s^2\right)\left(\beta_p^2 + \beta_s^2\right)} = \frac{L\beta_p \operatorname{csch}\left(\frac{L\beta_p}{b}\right) + iLe^{\frac{jL\alpha_b}{b}}\left(\alpha_b + i\beta_p \coth\left(\frac{L\beta_p}{b}\right)\right)}{2b\left(\alpha_b^2 + \beta_p^2\right)}, \tag{A.16}$$

$$\sum_{s=0}^{\infty} \frac{\epsilon_s\left(-1 + (-1)^s e^{\frac{jL\alpha_b}{b}}\right)}{\left(\alpha_b^2 - \alpha_s^2\right)\left(\beta_p^2 + \beta_s^2\right)} = \frac{-L\alpha_b \coth\left(\frac{L\beta_p}{b}\right) + L\alpha_b e^{\frac{jL\alpha_b}{b}}\operatorname{csch}\left(\frac{L\beta_p}{b}\right) + iL\beta_p}{b\alpha_b^3\beta_p + b\alpha_b\beta_p^3}, \tag{A.17}$$

$$\sum_{s=0}^{\infty} \frac{\epsilon_s\left(e^{\frac{jL\alpha_b}{b}} - (-1)^s\right)}{\left(\alpha_b^2 - \alpha_s^2\right)\left(\beta_p^2 + \beta_s^2\right)} = \frac{jL\beta_p e^{\frac{jL\alpha_b}{b}} + L\alpha_b e^{\frac{jL\alpha_b}{b}}\coth\left(\frac{L\beta_p}{b}\right) - L\alpha_b \operatorname{csch}\left(\frac{L\beta_p}{b}\right)}{b\alpha_b^3\beta_p + b\alpha_b\beta_p^3}. \tag{A.18}$$

Sum of series in $p$.

$$\sum_{p=1}^{\infty} \frac{1}{\alpha_0^2 - \alpha_{p\,s}^2} = -\frac{1}{2\,\tilde{\alpha}_s} \frac{J_2\left(\tilde{\alpha}_s\right)}{J_1\left(\tilde{\alpha}_s\right)}, \tag{A.19}$$

$$\sum_{p=1}^{\infty} \frac{\beta_p^2}{\left(\beta_p^2 - 1\right) \beta_{p\,s}^2 \left(\alpha_0^2 - \beta_{p\,s}^2\right)} = \frac{1}{\alpha_0^2} \left( \frac{J_0\left(\alpha_s\right) - I_2\left(\alpha_s\right)}{2\,\left(I_0\left(\alpha_s\right) + I_2\left(\alpha_s\right)\right)} - \frac{J_0\left(\tilde{\alpha}_s\right) + J_2\left(\tilde{\alpha}_s\right)}{2\,\left(J_0\left(\tilde{\alpha}_s\right) - J_2\left(\tilde{\alpha}_s\right)\right)} \right), \tag{A.20}$$

$$\sum_{p=1}^{\infty} \frac{1}{\left(\beta_p^2 - 1\right) \beta_{p\,s}^2 \left(\alpha_0^2 - \beta_{p\,s}^2\right)} = \frac{1}{\alpha_0^2} \left( \frac{J_2\left(\tilde{\alpha}_s\right)/\tilde{\alpha}_s}{2\,\left(J_1\left(\tilde{\alpha}_s\right) - \tilde{\alpha}_s J_0\left(\tilde{\alpha}_s\right)\right)} + \frac{J_2\left(\alpha_s\right)/\alpha_s}{2\,\left(\alpha_s I_0\left(\alpha_s\right) - I_1\left(\alpha_s\right)\right)} \right), \tag{A.21}$$

$$\sum_{p=1}^{\infty} \frac{1}{\left(\beta_p^2 - 1\right) \left(\alpha_0^2 - \beta_{p\,s}^2\right)} = \frac{1}{2\,\tilde{\alpha}_s} \frac{J_2\left(\tilde{\alpha}_s\right)}{J_1\left(\tilde{\alpha}_s\right) - \tilde{\alpha}_s J_0\left(\tilde{\alpha}_s\right)}, \tag{A.22}$$

$$\sum_{p=1}^{\infty} \frac{\beta_p^2}{\left(\beta_p^2 - 1\right) \beta_{p\,s}^2} = \frac{1}{2} \frac{J_0\left(\alpha_s\right) - I_2\left(\alpha_s\right)}{I_0\left(\alpha_s\right) + I_2\left(\alpha_s\right)}, \tag{A.23}$$

$$\sum_{p=1}^{\infty} \frac{\beta_p^2}{\left(\beta_p^2 - 1\right) \left(\alpha_0^2 - \beta_{p\,s}^2\right)} = -\frac{1}{2} \frac{J_0\left(\tilde{\alpha}_s\right) + J_2\left(\tilde{\alpha}_s\right)}{J_0\left(\tilde{\alpha}_s\right) - J_2\left(\tilde{\alpha}_s\right)}, \tag{A.24}$$

$$\sum_{p=1}^{\infty} \frac{\beta_p^4}{\left(\beta_p^2 - 1\right) \beta_{p\,s}^2 \left(\alpha_0^2 - \beta_{p\,s}^2\right)} = -\frac{1}{2\,\alpha_0^2} \left( \frac{\tilde{\alpha}_s^2 \left(J_0\left(\tilde{\alpha}_s\right) + J_2\left(\tilde{\alpha}_s\right)\right)}{J_0\left(\tilde{\alpha}_s\right) - J_2\left(\tilde{\alpha}_s\right)} + \frac{\beta_s^2 \left(I_0\left(\alpha_s\right) - I_2\left(\alpha_s\right)\right)}{J_0\left(\alpha_s\right) + I_2\left(\alpha_s\right)} \right), \tag{A.25}$$

$$\sum_{p=1}^{\infty} \frac{1}{J_2\left(\alpha_p\right) \left(\alpha_o^2 - \alpha_{ps}^2\right)} = \frac{1}{\tilde{\alpha}_s^2} - \frac{1}{2\tilde{\alpha}_s J_1\left(\tilde{\alpha}_s\right)}, \tag{A.26}$$

$$\sum_{p=1}^{\infty} \frac{\beta_p^2}{\left(\beta_p^2 - 1\right) J_0\left(\beta_p\right) \beta_{ps}^2} \to -\frac{\beta_s^2}{2\beta_s I_1\left(\beta_s\right) - 2\beta_s^2 I_0\left(\beta_s\right)}, \tag{A.27}$$

$$\sum_{p=1}^{\infty} \frac{\beta_{p\,s}^2 - \alpha_f^2}{\left(\beta_p^2 - 1\right) J_0\left(\beta_p\right) \beta_{p\,s}^2} = 1 - \alpha_f^2 \left( \frac{1}{\beta_s^2} + \frac{1}{2\beta_s I_1\left(\beta_s\right) - 2\beta_s^2 I_0\left(\beta_s\right)} \right). \tag{A.28}$$

# Appendix B

# Machine parameters

In the following the main machine parameters used during the impedance quantification and localization measurements can be found.

## B.1 PS

Settings for the PS impedance measurements and budget at 2 GeV. These parameters were used during the measurements in 2012, and from the start of 2013 to the machine shutdown.

| | Parameter | Value |
|---|---|---|
| Circumference | $C$ | 628.318 m |
| Revolution period | $T_o$ | 2.212 $\mu$s |
| Vertical Tune | $Q_y$ | 6.23 |
| Horizontal Tune | $Q_x$ | 6.12 |
| Energy (total) | $E$ | 2.93 GeV |
| Energy (kinetic) | $T$ | 2 GeV |
| Gamma | $\gamma$ | 3.12 |
| Gamma transition | $\gamma_t$ | 6 |
| Average $\beta_x(s)$ | $\bar{\beta}_x$ | $\simeq 17.3$ m |
| Average $\beta_y(s)$ | $\bar{\beta}_y$ | $\simeq 16.8$ m |
| Vertical Chromaticity | $\xi_y$ | $\simeq 0$ |
| Horizontal Chromaticity | $\xi_x$ | $\simeq 0$ |
| Harmonic number | $h$ | 8 |
| RF frequency | $f_{RF}$ | 3.616 MHz |
| Synchronous phase | $\phi_s$ | 0 |
| RF voltage | $V_{RF}$ | 200 kV |
| Synchrotron tune | $Q_s$ | $2.69 \cdot 10^{-3}$ |

Table B.1: PS machine parameters.

## B.2 SPS

Settings for the SPS impedance measurements at $E = 26\,\text{GeV}$. These parameters were used during the measurements in 2012, and from the start of 2013 to the machine shutdown.

| | Parameter | Value |
|---|---|---|
| Circumference | $C$ | 6911.50 m |
| Revolution period | $T_o$ | 2.3 $\mu$s |
| Vertical Tune | $Q_y$ | 26.18 |
| Horizontal Tune | $Q_x$ | 26.13 |
| Energy (total) | $E$ | 26 GeV |
| Energy (kinetic) | $T$ | 25 GeV |
| Gamma | $\gamma$ | 27.72 |
| Gamma transition | $\gamma_t$ | 22.77 |
| Average $\beta_x(s)$ | $\bar{\beta}_x$ | $\simeq 54.6\,\text{m}$ |
| Average $\beta_y(s)$ | $\bar{\beta}_y$ | $\simeq 54.5\,\text{m}$ |
| Vertical Chromaticity | $\xi_y$ | $\simeq 0$ |
| Horizontal Chromaticity | $\xi_x$ | $\simeq 0$ |
| Harmonic number | $h$ | 4620 |
| RF frequency | $f_{RF}$ | 200 MHz |
| Synchronous phase | $\phi_s$ | $\pi$ |
| RF voltage | $V_{RF}$ | 3 MV |
| Synchrotron tune | $Q_s$ | $7 \cdot 10^{-3}$ |

Table B.2: SPS machine parameters.

## B.3 LHC

Settings for the LHC impedance measurements in the B1 ring at $E = 450\,\text{GeV}$. Set up of the 28-11-2012, fill n.3338.

| | Parameter | Value |
|---|---|---|
| Circumference | $C$ | 26658.88 m |
| Revolution period | $T_o$ | 88.92 $\mu$s |
| Vertical Tune | $Q_y$ | 59.3085 |
| Horizontal Tune | $Q_x$ | 64.2743 |
| Energy (total) | $E$ | 450 GeV |
| Energy (kinetic) | $T$ | 449.06 GeV |
| Gamma | $\gamma$ | 479.58 |
| Gamma transition | $\gamma_t$ | 55.75 |
| Average $\beta_x(s)$ | $\bar{\beta}_x$ | $\simeq 9.25$ m |
| Average $\beta_y(s)$ | $\bar{\beta}_y$ | $\simeq 101.36$ m |
| Vertical Chromaticity | $\xi_y$ | $\simeq 0.1$ |
| Horizontal Chromaticity | $\xi_x$ | $\simeq 0.09$ |
| Harmonic number | $h$ | 35640 |
| RF frequency | $f_{RF}$ | 400 MHz |
| Synchronous phase | $\phi_s$ | $\pi$ |
| RF voltage | $V_{RF}$ | 6 MV |
| Synchrotron tune | $Q_s$ | $4.89 \cdot 10^{-3}$ |

Table B.3: LHC machine parameters.

## B.4 AGS

These settings were used in the AGS tune shift measurements with protons. This set up refers to the MD of 17-04-2013.

| | Parameter | Value |
|---|---|---|
| Circumference | $C$ | 807.1 m |
| Energy (total) | $E$ | 23.81 GeV |
| Energy (kinetic) | $T$ | 22.87 GeV |
| Gamma | $\gamma$ | 25.38 |
| Gamma transition | $\gamma_t$ | 8.5 |
| Revolution period | $T_o$ | 2.69 $\mu$s |
| Vertical Tune | $Q_y$ | 8.87 |
| Horizontal Tune | $Q_x$ | 8.71 |
| Average $\beta_x(s)$ | $\bar{\beta}_x$ | 16 m |
| Average $\beta_y(s)$ | $\bar{\beta}_y$ | 16 m |
| Vertical Chromaticity | $\xi_y$ | $\simeq 0.16$ |
| Horizontal Chromaticity | $\xi_x$ | $\simeq -0.83$ |
| Harmonic number | $h$ | 8 |
| RF frequency | $f_{RF}$ | 2.969 MHz |
| Synchronous phase | $\phi_s$ | $\pi$ |
| RF voltage | $V_{RF}$ | 200 kV |
| Synchrotron tune | $Q_s$ | $3.6 \cdot 10^{-4}$ |

Table B.4: AGS machine parameters.

## B.5 RHIC

These settings were used in the RHIC tune shift and impedance localization measurements with protons. This set up refers to the MD of 24-04-2013 and 15-05-2013 in Blue ring and to the MD of 01-05-2013 of Yellow Ring. The two accelerator rings are in principle specular.

| | Parameter | Value |
|---|---|---|
| Circumference | $C$ | 3833.8451 m |
| Energy (total) | $E$ | 25 GeV |
| Energy (kinetic) | $T$ | 24.06 GeV |
| Gamma | $\gamma$ | 26.64 |
| Gamma transition | $\gamma_t$ | 23.50 |
| Revolution period | $T_o$ | 12.79 $\mu$s |
| Vertical Tune | $Q_y$ | 29.691 |
| Horizontal Tune | $Q_x$ | 28.695 |
| Average $\beta_x(s)$ | $\bar{\beta}_x$ | $\simeq$ 57.3 m |
| Average $\beta_y(s)$ | $\bar{\beta}_y$ | $\simeq$ 50.2 m |
| Vertical Chromaticity | $\xi_y$ | $\simeq$ 0.07 |
| Horizontal Chromaticity | $\xi_x$ | $\simeq$ 0.07 |
| Harmonic number | $h$ | 2520 |
| RF frequency | $f_{RF}$ | 197 MHz |
| Synchronous phase | $\phi_s$ | $\pi$ |
| RF voltage | $V_{RF}$ | 300 kV |
| Synchrotron tune | $Q_s$ | $6.47 \cdot 10^{-5}$ |

Table B.5: RHIC machine parameters.

# Appendix C

# PS impedance model at 2 GeV

PS impedance budget for each analyzed element. Within the kickers, starred elements have been studied with CST, the remaining ones with the Tsutsui's model.

| Element name | position [m] | $\beta_x[m]$ | $\beta_y[m]$ | $Z_x^{eff}$ [$\Omega$/m] | $Z_y^{eff}$ [$\Omega$/m] |
|---|---|---|---|---|---|
| PE.BFA09S | 57.33 | 22.85 | 13.14 | $-1.92 \cdot 10^4$ | $8.65 \cdot 10^4$ |
| PE.BFA09P | 57.33 | 22.85 | 13.14 | $-2.41 \cdot 10^4$ | $1.10 \cdot 10^5$ |
| PE.BFA21S | 132.17 | 19.27 | 12.75 | $-1.92 \cdot 10^4$ | $8.65 \cdot 10^4$ |
| PE.BFA21P | 132.17 | 19.27 | 12.75 | $-2.41 \cdot 10^4$ | $1.10 \cdot 10^5$ |
| PE.KFA04* | 25.86 | 12.11 | 22.47 | $8.33 \cdot 10^3$ | $7.38 \cdot 10^4$ |
| PE.KFA13* | 82.69 | 20.69 | 12.54 | $1.75 \cdot 10^4$ | $1.61 \cdot 10^5$ |
| PE.KFA21* | 133.51 | 18.82 | 12.81 | $1.75 \cdot 10^4$ | $1.61 \cdot 10^5$ |
| PE.KFA71 | 447.03 | 19.17 | 12.75 | $-9.33 \cdot 10^4$ | $3.85 \cdot 10^5$ |
| PE.KFA79* | 497.15 | 23.59 | 12.57 | $1.75 \cdot 10^4$ | $1.61 \cdot 10^5$ |
| PI.KFA28 | 176.99 | 14.64 | 20.33 | $-3.00 \cdot 10^4$ | $1.07 \cdot 10^5$ |
| PI.KFA45 | 283.24 | 23.00 | 11.60 | $-4.10 \cdot 10^4$ | $1.74 \cdot 10^5$ |
| PR.C8008 | 51.33 | 13.49 | 22.44 | $7.45 \cdot 10^2$ | $7.45 \cdot 10^2$ |
| PR.C8088 | 553.98 | 12.39 | 23.22 | $7.45 \cdot 10^2$ | $7.45 \cdot 10^2$ |
| PR.C8089 | 559.98 | 19.62 | 13.56 | $7.45 \cdot 10^2$ | $7.45 \cdot 10^2$ |
| PR.C4077 | 485.15 | 24.54 | 11.44 | $6.16 \cdot 10^2$ | $6.16 \cdot 10^2$ |
| PR.C4078 | 491.15 | 14.16 | 21.00 | $6.16 \cdot 10^2$ | $6.16 \cdot 10^2$ |
| PR.C1011 | 70.04 | 20.90 | 12.00 | $6.09 \cdot 10^2$ | $6.56 \cdot 10^2$ |
| PR.C1036 | 227.11 | 13.94 | 18.92 | $6.09 \cdot 10^2$ | $6.56 \cdot 10^2$ |
| PR.C1046 | 289.95 | 12.57 | 19.61 | $6.09 \cdot 10^2$ | $6.56 \cdot 10^2$ |
| PR.C1051 | 321.36 | 21.79 | 11.70 | $6.09 \cdot 10^2$ | $6.56 \cdot 10^2$ |
| PR.C1056 | 352.78 | 12.21 | 19.79 | $6.09 \cdot 10^2$ | $6.56 \cdot 10^2$ |
| PR.C1066 | 415.61 | 11.99 | 20.35 | $6.09 \cdot 10^2$ | $6.56 \cdot 10^2$ |
| PR.C1076 | 478.44 | 13.26 | 19.54 | $6.09 \cdot 10^2$ | $6.56 \cdot 10^2$ |
| PR.C1081 | 509.86 | 18.17 | 12.86 | $6.09 \cdot 10^2$ | $6.56 \cdot 10^2$ |
| PR.C1086 | 541.27 | 13.88 | 19.22 | $6.09 \cdot 10^2$ | $6.56 \cdot 10^2$ |
| PR.C1091 | 572.69 | 20.26 | 11.82 | $6.09 \cdot 10^2$ | $6.56 \cdot 10^2$ |
| PR.C1096 | 604.11 | 12.40 | 19.94 | $6.09 \cdot 10^2$ | $6.56 \cdot 10^2$ |
| PR.C02406 | 38.82 | 12.28 | 19.46 | $9.74 \cdot 10^2$ | $9.74 \cdot 10^2$ |
| PE.SMH16 | 101.45 | 12.36 | 20.15 | $7.25 \cdot 10^3$ | $1.86 \cdot 10^3$ |
| Rewall-RC-35mm-2GeV | - | 17.35 | 16.89 | $3.20 \cdot 10^6$ | $3.20 \cdot 10^6$ |
| Pumps | - | 17.35 | 16.89 | $1.37 \cdot 10^4$ | $1.63 \cdot 10^5$ |
| Bellows | - | 17.35 | 16.89 | $3.17 \cdot 10^2$ | $1.77 \cdot 10^5$ |
| Steps | - | 17.35 | 16.89 | $-2.33 \cdot 10^4$ | $1.43 \cdot 10^5$ |
| Total | - | - | - | $3.01 \cdot 10^6$ | $5.31 \cdot 10^6$ |

# Appendix D

# HEADTAIL configuration files

## D.1 PS configuration file

```
Flag_for_bunch_particles_(1->protons_2->positrons_3&4->ions):    1
Number_of_particles_per_bunch:                                   1e11
Machine                                                          PS
Observation_points:                                              PR.UHV
Interaction_points:                                              PE.KFA71
Custom_impedance:                                                REWALL1
ACdipole:                                                        NONE
Lump_impedance_(1->Yes,0->No):                                   0
Bunch_length_(rms_value)_[m]:                                    6.74533031
Normalized_horizontal_emittance_(rms_value)_[um]:                15
Normalized_vertical_emittance_(rms_value)_[um]:                  8
Longitudinal_momentum_spread:                                    0.002
Synchrotron_tune:                                                0.00270163997
Relativistic_gamma:                                              3.126961
Number_of_turns:                                                 1000
Longitud_extension_of_the_bunch_(+/-N*sigma_z)                   2.
Horizontal_tune:                                                 6.12
Vertical_tune:                                                   6.23
Horizontal_chromaticity_[Q'x]:                                   0
Vertical_chromaticity_[Q'y]:                                     0
Flag_for_synchrotron_motion:                                     1
Number_of_macroparticles_per_bunch:                              100000
Number_of_bunches:                                               1
Number_of_slices_in_each_bunch:                                  5000
Switch_for_bunch_table:                                          0
Switch_for_wake_fields:                                          1
Number_of_turns_for_the_wake:                                    1
Switch_for_initial_kick:                                         1
x-kick_amplitude_at_t=0_[m]:                                     0.001
y-kick_amplitude_at_t=0_[m]:                                     0.001
z-kick_amplitude_at_t=0_[m]:                                     0.
Switch_for_amplitude_detuning:                                   0
Linear_coupling_switch(1->on_0->off):                            0
Linear_coupling_coefficient_[1/m]:                               -
Sextupolar_kick_switch(1->on_0->off):                            0
Switch_for_losses_(0->no_losses_1->losses):                      0
Main_rf_voltage_[V]:                                             2e5
Main_rf_harmonic_number:                                         8
```

## D.2 LHC configuration file

```
Flag_for_bunch_particles_(1->protons_2->positrons_3&4->ions):    1
Number_of_particles_per_bunch:                                   1.8e11
Machine:                                                         LHCB1
Observation_points:                                              BPM
Interaction_points:                                              NONE
Custom_impedance:                                                BB_LHC
ACdipole:                                                        MKQA.6L4.B1
Lump_impedance_(1->Yes,0->No):                                   0
Bunch_length_(rms_value)_[m]:                                    0.108
Normalized_horizontal_emittance_(rms_value)_[um]:                2.5
Normalized_vertical_emittance_(rms_value)_[um]:                  2.7
Longitudinal_momentum_spread:                                    0.00032
Synchrotron_tune:                                                0.0048991
Relativistic_gamma:                                              479.5817
Number_of_turns:                                                 350
Longitud_extension_of_the_bunch_(+/-N*sigma_z)                   2.
Horizontal_tune:                                                 64.27
Vertical_tune:                                                   59.31
Horizontal_chromaticity_[Q'x]:                                   0
Vertical_chromaticity_[Q'y]:                                     0
Flag_for_synchrotron_motion:                                     41
Number_of_macroparticles_per_bunch:                              1000
Number_of_bunches:                                               1
Number_of_slices_in_each_bunch:                                  500
Switch_for_bunch_table:                                          0
Switch_for_wake_fields:                                          1
Number_of_turns_for_the_wake:                                    1
Switch_for_initial_kick:                                         1
x-kick_amplitude_at_t=0_[m]:                                     0.001
y-kick_amplitude_at_t=0_[m]:                                     0.001
z-kick_amplitude_at_t=0_[m]:                                     0.
Switch_for_amplitude_detuning:                                   0
Linear_coupling_switch(1->on_0->off):                            0
Linear_coupling_coefficient_[1/m]:                               -
Sextupolar_kick_switch(1->on_0->off):                            0
Switch_for_losses_(0->no_losses_1->losses):                      0
Main_rf_voltage_[V]:                                             6e6
Main_rf_harmonic_number:                                         35640
```

# List of Figures

# List of Tables

# Bibliography


[1]

[2] Oliver Sim Brning, Paul Collier, P Lebrun, Stephen Myers, Ranko Ostojic, John Poole, and Paul Proudlock. *LHC Design Report*. CERN, Geneva, 2004.

[3] Jean-Paul Burnet, Christian Carli, Michel Chanel, Roland Garoby, Simone Gilardoni, Massimo Giovannozzi, Steven Hancock, Helmut Haseroth, Kurt Hbner, Detlef Kchler, Julian Lewis, Alessandra Lombardi, Django Manglunki, Michel Martini, Stephan Maury, Elias Mtral, Dieter Mhl, Gnther Plass, Louis Rinolfi, Richard Scrivens, Rende Steerenberg, Charles Steinbach, Maurizio Vretenar, and Thomas Zickler. *Fifty years of the CERN Proton Synchrotron: Volume 1*. CERN, Geneva, 2011.

[4] Georges Aad et al. Observation of a new particle in the search for the Standard Model Higgs boson with the ATLAS detector at the LHC. *Phys.Lett.*, B716:1–29, 2012.

[5] Serguei Chatrchyan et al. Observation of a new boson at a mass of 125 GeV with the CMS experiment at the LHC. *Phys.Lett.*, B716:30–61, 2012.

[6] W. Herr. Concept of luminosity in particle colliders.

[7] V. G. Vaccaro L. Palumbo and M. Zobov.

[8] K Y Ng. *Physics of intensity dependent beam instabilities*. World Scientific, Hoboken, NJ, 2006.

[9] Alexander Wu Chao. *Physics of Collective Beam Instabilities in High Energy Accelerators*. John Wiley & Sons, Inc., New York, 1993.

[10] Cst, computer simulation technology.

[11] H. Tsutsui and L. Vos. Transverse coupling impedance of a simplified ferrite kicker magnet model.

[12] N Mounet and E Mtral. Electromagnetic fields and beam coupling impedances in a multilayer flat chamber. Dec 2010.

[13] N Mounet and E Mtral. Electromagnetic fields created by a macroparticle in an infinitely long and axisymmetric multilayer beam pipe. Technical Report CERN-BE-2009-039, CERN, Geneva, Nov 2009.

[14] Marco Panniello. *A numerical-analytical method for particle accelerators: a reworking mode matching technique s a testing tool for analytical and experimental methods in accelerators physics*. LAP Lambert, Saarbruecken, 2010.

[15]

[16] Robert E Collin. *Field theory of guided waves; 2nd ed.* IEEE, New York, NY, 1991.

[17] Jean G Van Bladel. *Electromagnetic Fields; 2nd ed.* Wiley, Newark, 2007.

[18] G. Franceschetti. *Campi elettromagnetici*. Programma di mat. fisica elettronica. Bollati Boringhieri, 1983.

[19] Robert L Gluckstern and B Zotter. Transverse impedance of a resistive cylinder of finite length. Technical Report CERN-AB-Note-2008-045, CERN, Geneva, Jul 2008.

[20] S. Krinsky, B. Podobedov, and R. L. Gluckstern. Impedance of finite length resistive cylinder. *Phys. Rev. ST Accel. Beams*, 7:114401, Nov 2004.

[21] Gennady Stupakov. Resistive wall impedance of an insert. *Phys. Rev. ST Accel. Beams*, 8:044401, Apr 2005.

[22] Yoshihiro Shobuda, Yong Ho Chin, and Koji Takata. Coupling impedances of a resistive insert in a vacuum chamber. *Phys. Rev. ST Accel. Beams*, 12:094401, Sep 2009.

[23] Alexander Wu Chao, Karl Hubert Mess, Maury Tigner, and Frank Zimmermann. *Handbook of accelerator physics and engineering; 2nd ed.* World Scientific, Singapore, 2013.

[24] N. Biancacci, G. Vaccaro, V. E. Métral, B. Salvant, M. Migliorati, and L. Palumbo. Impedance studies of 2d azimuthally symmetric devices of finite length. *Phys. Rev. ST Accel. Beams*, 17:021001, Feb 2014.

[25] R.L. Gluckstern. Analytic methods for calculating coupling impedances. 2000.

[26] V. G. Vaccaro and L. Verolino. Some remarks about the kneser-sommerfeld formula.

[27] Matlab, v.8.0.0.783 64-bit r2012b the mathworks inc., natick, massachusetts, 2012.

[28] K Y Ng. Transverse impedance of a coasting beam in a corrugated vacuum chamber at low frequencies. Technical Report FERMILAB-FN-389. FN-389, FERMILAB, Batavia, IL, 1983.

[29] G. V. Stupakov and S. S. Kurennoy. Trapped electromagnetic modes in a waveguide with a small discontinuity. *Phys. Rev. E*, 49:794–799, Jan 1994.

[30]

[31] C.G. Montgomery. *Technique of Microwave Measurements: In Two Volumes*. Dover Publications, 1966.

[32] Giovanni De Michele and Alexej Grudiev. EM characterization of Damping materials for CLIC RF accelerating structures. Technical Report CERN-OPEN-2013-029. CLIC-Note-988, CERN, Geneva, Aug 2013.

[33] Frank Zimmermann and Katsunobu Oide. Resistive-wall wake and impedance for nonultrarelativistic beams. *Phys. Rev. ST Accel. Beams*, 7:044201, Apr 2004.

[34]

[35] L Rossi. LHC Upgrade Plans: Options and Strategy. (CERN-ATS-2011-257):6 p, Dec 2011.

[36] L Rossi and O Brning. High Luminosity Large Hadron Collider A description for the European Strategy Preparatory Group. Technical Report CERN-ATS-2012-236, CERN, Geneva, Aug 2012.

[37] F J Sacherer. Transverse bunched beam instabilities: theory. (CERN-MPS-INT-BR-74-8):5 p, Apr 1974. Ninth international conference on high energy accelerators, Stanford, 2-7 May 1974. Proceedings, Springfield, Nat. Tech. Inf. Serv., 1974, CONF 740522, p. 347-351.

[38] D Brandt, P Castro, Karel Cornelis, A Hofmann, G Morpurgo, G L Sabbi, J Wenninger, and Bruno W Zotter. Measurements of impedance distributions and instability thresholds in LEP. (CERN-SL-95-34 AP):4 p, Jun 1995.

[39] V Kiselev and V Smaluk. A method for measurement of transverse impedance distribution along storage ring. 2000.

[40] L Emery, G Decker, and J Galayda. Local Bump Method for Measurement of Transverse Impedance of Narrow-Gap ID Chambers in Storage Rings. 2001.

[41] E Plouviez and L Farvacque. Probing the Transverse Impedance of the ESRF Storage Ring. 2002.

[42] Gianluigi Arduini, Christian Carli, and Frank Zimmermann. Localizing Impedance Sources from Betatron-phase Beating in the CERN SPS. (CERN-AB-2004-083):4 p, Aug 2004. revised version submitted on 2004-09-28 15:45:53.

[43] G. Arduini E. Métral G. Papotti D. Quatraro G. Rumolo B. Salvant R. Calaga and R. Tomás. Transverse impedance localization using intensity dependent optics. 2009.

[44] R. Calaga. Transverse impedance measurements in RHIC. 2010.

[45] J L Laclare. Bunched beam coherent instabilities. 1987.

[46] E. Métral and G. Rumolo. Uspas course.

[47] S Y Lee. *Accelerator physics; 3rd ed.* World Scientific, Singapore, 2012.

[48]

[49]

[50] R Bartolini and F Schmidt. SUSSIX: A computer code for frequency analysis of non-linear betatron motion. 1998.

[51] J. Laskar, C. Froeschlé, and A. Celletti. The measure of chaos by the numerical analysis of the fundamental frequencies. Application to the standard mapping. *Physica D Nonlinear Phenomena*, 56:253–269, May 1992.

[52] R. J. Barlow. *Statistics: A Guide to the Use of Statistical Methods in the Physical Sciences (Manchester Physics Series)*. WileyBlackwell, reprint edition, 1989.

[53] F. Caspers M. Giovannozzi A. Grudiev T. Kroyer E. Métral and L. Sermeus. Cern-ab-2006-051.

[54] C. Zannini et al. 2010.

[55] Giovanni Rumolo and Frank Zimmermann. Practical user guide for HEADTAIL. Technical Report SL-Note-2002-036-AP, CERN, Geneva, Nov 2002.

[56] Diego Quatraro, Giorgio Turchetti, and Giovanni Rumolo. *Collective Effects for the LHC Injectors: Non-ultrarelativistic Approaches*. PhD thesis, Bologna U., Bologna, 2011. Presented 06 Jun 2011.

[57] N. Biancacci. Headtail mad-x.

[58] Nicolas Mounet, Leonid Rivkin, and Elias Mtral. *The LHC Transverse Coupled-Bunch Instability*. PhD thesis, Ecole Polytechnique, Lausanne, Mar 2012. Presented 2012.

[59] P Castro. *Luminosity and beta function measurement at the electron-positron collider ring LEP*. PhD thesis, Valencia U., Geneva, 1996. Presented on 25 Nov 1996.

[60] H. Bartosik P. Freyermuth O. Hans S. Aumon and S. Gilardoni. Ats-note-2011-nnn.

[61] N Biancacci, G Arduini, T Argyropoulos, H Bartosik, R Calaga, K Cornelis, S Gilardoni, E Mtral, N Mounet, Y Papaphilippou, S Persichelli, G Rumolo, B Salvant, G Sterbini, R Toms, R Wasef, M Migliorati, and L Palumbo. Beam Coupling Impedance Localization Technique Validation and Measurements in the CERN Machines. (CERN-ACC-2013-0120):3 p, May 2013.

[62] Karl Leopold Freitag Bane, Y Cai, Franz Josef Decker, J Irwin, Michiko G Minty, G Stupakov, Frank Zimmermann, C X Wang, and Y T Yan. Model-Independent Analysis with BPM Correlation Matrices. 1998.

[63] R. Calaga and R. Tomás. Statistical analysis of rhic beam position monitors performance. *Phys. Rev. ST Accel. Beams*, 7:042801, Apr 2004.

[64] Carlo Zannini, Leonid Rivkin, and Giovanni Rumolo. *Electromagnetic Simulation of CERN accelerator Components and Experimental Applications*. PhD thesis, Ecole Polytechnique, Lausanne, Mar 2013. Presented 15 Apr 2013.

[65] H Bartosik, G Arduini, and Y Papaphilippou. Optics considerations for lowering transition energy in the SPS. (CERN-ATS-2011-088):3 p, Sep 2011.

[66] C. Zannini. Sps impedance model.

[67] M. Bai, L. Ahrens, J. Alessi, K. Brown, G. Bunce, P. Cameron, C. M. Chu, J. W. Glenn, H. Huang, A. E. Kponou, K. Krueger, W. Lamble, A. Luccio, Y. I. Makdisi, S. Y. Lee, M. Okamura, L. Ratner, K. Reece, T. Roser, H. Spinka, M. J. Syphers, N. Tsoupas, D. G. Underwood, W. van Asselt, N. Williams, and A. Yokosawa. Overcoming intrinsic spin resonances with an rf dipole. *Phys. Rev. Lett.*, 80:4673–4676, May 1998.

[68] S Peggs. Nonlinear Diagnostics using AC Dipoles. 1999.

[69] R. Tomás. Normal form of particle motion under the influence of an ac dipole. *Phys. Rev. ST Accel. Beams*, 5:054001, May 2002.

[70] F Schmidt, R Toms, N Catalan-Lasheras, G Crockford, M Hayes, Wolfgang Hfle, and Jean-Pierre Koutchouk. Measurement of resonant Terms using AC dipole in the SPS at 26 GeV. Technical Report AB-Note-2003-031-MD, CERN, Geneva, Apr 2003.

[71] R Toms, M Bai, R Calaga, W Fischer, A Franchi, and Giovanni Rumolo. Measurement of global and local resonance terms. *Phys. Rev. Spec. Top. Accel. Beams*, 8(2):024001, 2005.

[72] R. Miyamoto. *Diagnostics of the Fermilab Tevatron Using an Ac Dipole*. VDM Publishing, 2009.

[73] M. Bai G. Wang and L. Yang. Linear optics measurements and corrections using ac dipole in rhic.

[74] S White, E Maclean, and R Toms. Direct amplitude detuning measurement with ac dipole. *Phys. Rev. Spec. Top. Accel. Beams*, 16(7):071002. 12 p, 2013.

[75] R Miyamoto, S E Kopp, A Jansson, and M J Syphers. Parametrization of the Driven Betatron Oscillation. Technical Report arXiv:0709.4192. FERMILAB BEAMS-DOC-2816, Sep 2007. Comments: 8 pages, 8 figures, and 1 table.

[76] N Aquilina, M Lamont, R Steinhagen, E Todesco, J Wenninger, and N Sammut. Expected and measured behaviour of the tune in the LHC operation at 3.5 TeV. *Conf. Proc.*, C1205201(CERN-ATS-2012-196):THPPD025. 4 p, Aug 2012.

[77] Wolfram Fischer. RHIC Luminosity Upgrade Program. *Conf.Proc.*, C100523:TUXMH01, 2010.

[78] J Glenn, M Blaskiewicz, K A Brown, E Raka, and J Ryan. Spill Structure in Intense Beams. page 3 p, 2003.

[79] T. J. Shea and R. L. Witkover.

[80] Todd Satogata, Rama Calaga, Peter Cameron, Phil Cerniglia, John Cupolo, Anthony J Curcio, William C Dawson, Christopher Degen, Justin Gullotta, Joe Mead, Robert Michnoff, Thomas Russo, and Robert Sikora. RHIC BPM System Modifications and Performance. 2005.